Selected Standard Protocols for the Synthesis, Phase Transfer, and Characterization of Inorganic Colloidal Nanoparticles

Jonas Hühn,[†] Carolina Carrillo-Carrion,[‡] Mahmoud G. Soliman,[†] Christian Pfeiffer,[†] Daniel Valdeperez,[†] Atif Masood,[†] Indranath Chakraborty,[†] Lin Zhu,[†] Marta Gallego,[‡] Zhao Yue,[†] Monica Carril,[‡,§] Neus Feliu,[†,▼] Alberto Escudero,[†,∥] Alaaldin M. Alkilany,[⊥] Beatriz Pelaz,[†,#] Pablo del Pino,[†,#] and Wolfgang J. Parak*,[†,‡,▽]

[†]Fachbereich Physik, Philipps Universität Marburg, 35037 Marburg, Germany

[‡]CIC biomaGUNE, 20009 San Sebastian, Spain

[§]Ikerbasque, Basque Foundation for Science, 48011 Bilbao, Spain

[∥]Instituto de Ciencia de Materiales de Sevilla, CSIC − Universidad de Sevilla, 41092 Seville, Spain

[⊥]Faculty of Pharmacy, The University of Jordan, Amman 11942, Jordan

[#]Centro Singular de Investigación en Química Biológica y Materiales Moleculares (CiQUS) y Departamento de Física de Partículas, Universidade de Santiago de Compostela, 15782 Santiago de Compostela, Spain

[▽]Institute of Nano Biomedicine and Engineering, Key Laboratory for Thin Film and Microfabrication Technology of the Ministry of Education, Department of Instrument Science and Engineering, School of Electronic Information and Electrical Engineering, Shanghai Jiao Tong University, 800 Dongchuan Rd., Shanghai 200240, China

[▼]Experimental Cancer Medicine (ECM), Department of Laboratory Medicine, Karolinska Institutet, Huddinge, Stockholm, Sweden

ⓈSupporting Information

ABSTRACT: Synthesis, characterization, and applications of colloidal nanoparticles have been a prominent topic of current research interests within the last two decades. Available reports in the literature that describe the synthesis of colloidal nanoparticles are abundant with various degrees of reproducibility and simplicity. Moreover, different methods for the characterization of colloidal nanoparticle's basic properties are employed, resulting in conflicting results in many cases. Herein, we describe "in detail" selected standard protocols for the synthesis, purification, and characterization of various types of colloidal inorganic nanoparticles including gold nanoparticles, silver nanoparticles, iron oxide nanoparticles, and quantum dots. This report consists of five main parts: The first and the second parts are dedicated to describing the synthesis of various types of hydrophobic and hydrophilic nanoparticles in organic solvents and in aqueous solutions, respectively. The third part describes surface modification of nanoparticles with a focus on ligand exchange reactions, to allow phase transfer of nanoparticles from aqueous to organic solvents and vice versa. The fourth and the fifth parts describe various general purification and characterization techniques used to purify and characterize nanoparticles, respectively. Collectively, this contribution does not aim to cover all available protocols in the literature to prepare inorganic nanoparticles but rather provides detailed synthetic procedures for important inorganic nanocrystals with a full description of their purification and characterization process.
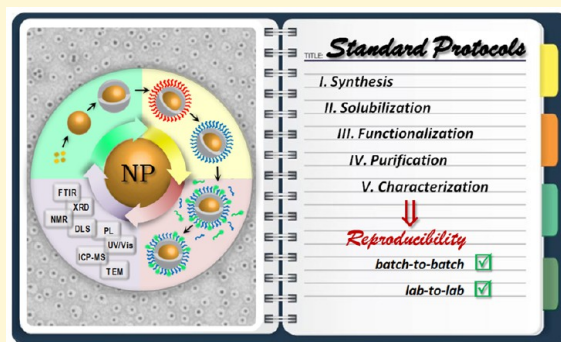
■ INTRODUCTION

Colloidal inorganic nanoparticles (NPs) gained an extensive interest recently due to their fascinating electronic, catalytic, optical, magnetic, and biological properties, which enable a novel material chemistry and a wide range of promising applications. Continuous development in understanding the fundamental physics, chemistry, and applications of these inorganic NPs originates from the availability of facile and reproducible synthetic protocols. The literature is abundant with a large number of synthetic protocols, which focus typically on controlling the nanoparticle (NP) size and shape in addition to purity, crystallinity, stability, and monodispersity.[1] However, the preparation of high quality inorganic NPs is still challenging and needs fine-tuning. For example, the widely used Frens protocol fails to prepare large citrate-capped gold NPs

(>50 nm) with acceptable monodispersity.[2] Recent modification to the Frens method by adapting the seed-mediated approach allowed for the synthesis of citrate-capped gold and silver NPs with excellent monodispersity and large diameter (up to 100 nm as described in Section 2).[3,4] More importantly, the reproducibility of available reports is an issue in some cases, which may originate from highly sensitive systems, and thus fluctuations of any variable, such as the source of some chemicals, may have a significant impact on the reaction products. Another reason for the observed irreproducibility is the unexpressed "critical details" and "tricks" in the published reports. With this in mind and based on our own experience, we aim in this contribution to compile reproducible, simple, and detailed synthetic protocols that enable the synthesis and characterization of high quality inorganic NPs. Accordingly, Sections 1 and 2 in this contribution focus on the synthesis of hydrophobic and hydrophilic inorganic NPs including gold, silver, iron oxide, and quantum dots.

Usually "as prepared" NPs need further modification to control their hydrophilicity, hydrophobicity, colloidal stability, biocompatibility, biological recognition, and many other properties. Powerful surface modification reactions and strategies are available in the literature, including ligand exchange, ligand modification, polymer coating, and silanization,[5,6] as well as controlled bioconjugation.[7] Due to the importance of surface functionalization, we describe ligand exchange reactions in three sections (Sections 3, 4, and 5) and a polymer coating strategy in Section 6. The described ligand exchange reactions might be employed to control the properties of the NPs such as (i) improving the colloidal stability and interaction with biological compartments (e.g., ligand exchange of citrate-capped Au = gold (Au) NPs with thiolated polyethylene glycol in Section 3); (ii) facilitating the phase transfer of NPs from water to organic solvent (e.g., ligand exchange of citrate-capped Au NPs with dodecylamine/ polyethylene glycol mix in Section 4); and (iii) facilitating the phase transfer of NPs from organic solvent to water (e.g., ligand exchange of alkanethiol capped Au NPs with 3-mercaptopropionic acid in Section 5). Another universal strategy of surface functionalization is detailed in Section 6, in which a polymer coating is employed to change hydrophobic inorganic NPs into highly charged NPs, rendering their surface hydrophilic and allowing their transfer to the aqueous solution. It is worth mentioning that the described surface functionalization strategies herein are general and can be applied to NPs of other materials, sizes, and shapes.

Similar to the synthesis of organic small molecules or polymers, the preparation of inorganic NPs requires a careful postsynthesis purification to get rid of "impurities", which can be any leftover reactants, free surfactant/capping agents, or undesired reaction products. The purification of NP solution is critical in many cases and should be considered as a vital step. For example, free cationic surfactants in gold nanorods (Au NRs) suspensions are responsible for cellular toxicity and in first order not the Au NRs themselves, highlighting the importance of using "purified" Au NR solution prior to biological evaluations/applications.[8] Another example is the presence of free recognition ligands (unbound) in NP solution, which should compete with bound ligand on the NPs for interaction with the designated target, which complicates interpretation of results and may result in serious artifacts. Despite the clear importance of the purification process, it is often overlooked in the literature and only briefly described in

many published reports. With this in mind, we tried to focus on this important topic through designating a separate section that describe various methods of NP purification including filtration, centrifugation, dialysis, size exclusion chromatography, and electrophoresis (see Section 7).

After synthesis and purification of NPs, proper characterization is essential to confirm the NP's structural, photophysical, and colloidal properties, as detailed in Sections 8, 9, and 10, respectively. Structural characterization of NPs involves probing the quantitative and qualitative composition of NPs, size and shape determination of inorganic core and organic shell using electron microscopy, analysis of NP crystallinity using X-ray diffraction (XRD), quantification of the organic shell weight percentage on single NPs using thermogravimetric analysis, and confirming the chemical structure of the organic shell on the surface of NPs using nuclear magnetic resonance (NMR) analysis and infrared spectroscopy.

Photophysical characterization of NPs is very important, since it is the basis of various applications. For example, plasmon absorption and scattering of Au NPs allow sensing, imaging, and analytical applications of these nanostructures. The fluorescence phenomenon of quantum dots (QDs) is the basis for their use in imaging, tracking, and cellular labeling applications. Considering the importance of careful evaluation to the photophysical properties of NPs, it is addressed separately in Section 9, which includes characterization of Au NP's optical absorption and determination of NP concentration based on their absorption spectra. Also fluorescence spectroscopy as a tool to characterize QDs and to calculate their quantum yields is detailed with examples.

Characterization of the colloidal properties of NPs such as hydrodynamic diameter using dynamic light scattering (DLS) and effective surface charge using laser Doppler anemometry is very critical and thus included in Section 10. For example, measuring hydrodynamic diameters is an effective tool to follow NP aggregation, dissolution, and interaction with proteins or other ligands. Moreover, evaluation of the effective surface charge of NPs can be employed to confirm specific surface functionalization, such as ligand exchange, polymer overcoating, and protein adsorption. In Section 10, following NP aggregation as a function of salt addition or the solution's pH is discussed and detailed with examples of gold and silver NPs with various surface chemistries. Finally, characterization of the acidity/basicity of NPs by determination of their pK_a and number of acidic or basic groups on single NPs using pH titration and laser Doppler anemometry is described.

1. SYNTHESIS AND CHARACTERIZATION OF HYDROPHOBIC INORGANIC NPs IN ORGANIC SOLVENT

1.1. General Considerations. All glassware was first cleaned with detergent followed by aqua regia and carefully rinsed with Milli-Q water and acetone to guarantee an extremely cleaned glass surface. Aqua regia oxidizes and dissolves residual organic and inorganic impurities, which may interfere with the synthesis of NPs. Aqua regia solution is prepared by mixing 3 volume parts of hydrochloric acid (HCl) with 1 volume part of nitric acid (HNO_3) and should be used fresh. Aqua regia is a corrosive and strong oxidizing agent that should be prepared with care in a well-ventilated fume cupboard with protective clothing, goggles, and gloves.

Sections 1.2−1.8 describe the detailed synthesis of various types of NPs (Au, Ag, FePt, Fe_3O_4, Sn, CdSe, CdSe/ZnS, and

CdS) in hydrophobic organic solvents. In these syntheses, the inorganic NP cores are stabilized by a shell of organic hydrophobic ligands (Figure 1), which ensures colloidal
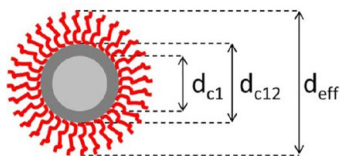

Figure 1. Scheme showing an inorganic NP, which consists of an inorganic core and an organic hydrophobic ligand shell (drawn in red). The inorganic core here is composed of a core/shell structure of two different materials (first material is the inner core drawn in light gray, and the second material is the inorganic shell drawn in dark gray).

stability of NPs in organic solvents such as toluene or chloroform. The effective NP diameter (d_{eff}) is the sum of the inorganic core diameter (d_c) and the thickness of the stabilizing ligand shell (l_{ligand}) as per eq 1. In case the NP core is comprised of (n) layers of different materials (e.g., core−shell NPs), the diameter of the first inner material is referred to as d_{c1} and the diameter of the core after the second material is referred to as d_{c12}. The diameter of the core after the nth material is referred to as $d_{c12...n}$).

$$d_{eff} = d_c + 2 \times l_{ligand} \tag{1}$$

1.2. Synthesis of Hydrophobic Au NPs (≈4 or 7 nm core diameter). *Dodecanethiol-Stabilized Au NPs (≈4 nm core diameter).* Hydrophobic Au NPs were synthesized according to the Brust−Schiffrin two-phase method,[9] with some modifications, as previously published.[10] The reaction was carried out at room temperature (RT) under ambient conditions. An aqueous phase with gold precursor (a yellow translucent solution containing $AuCl_4^-$ ions) was prepared by dissolving 300 mg (0.9 mmol) of hydrogen tetrachloroaurate (III) ($HAuCl_4$, 99.9%, Alfa Aesar no. 12325) in 25 mL of Milli-Q water. An organic phase containing 2.170 g (3.9 mmol) of tetraoctylammonium bromide (TOAB, $N(C_8H_{17})_4^+Br^-$, Sigma-Aldrich no. 294136) dissolved in 80 mL of toluene (Fluka 89682) was prepared immediately afterward.

The two solutions, i.e., the aqueous and the organic phases, were mixed in a 500 mL separation funnel (cf. Figures 2 and 3) and shaken vigorously for about 5 min. Upon mixing, $AuCl_4^-$ ions (in the aqueous yellow phase) were gradually transferred into the organic toluene phase, forming tetraoctylammonium tetrachloroaurate ion pairs ($N(C_8H_{17})_4^+AuCl_4^-$) as per eq 2. Within this process, the initial colorless toluene phase (tol)
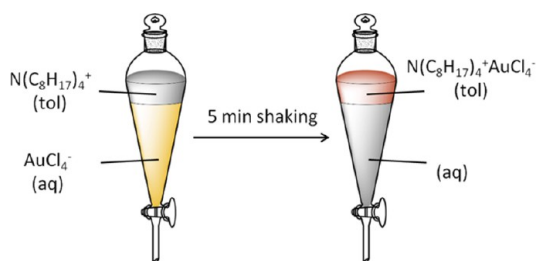

Figure 2. Scheme of the process of transferring $AuCl_4^-$ ions from the aqueous phase to the organic phase through the formation of tetraoctylammonium tetrachloroaurate ion pairs.
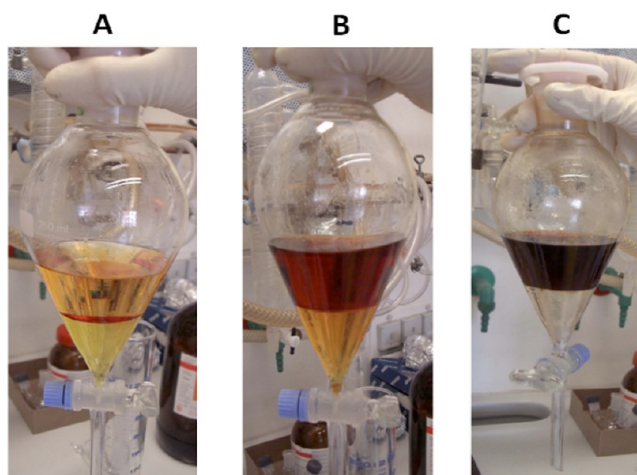

Figure 3. Photographs of the biphasic system showing the process of transferring $AuCl_4^-$ ions from the aqueous phase (lower phase) to the organic phase (upper phase) through the formation of tetraoctylammonium tetrachloroaurate ion pairs (dark red phase in C).

turned into a deep orange color, while the initial yellow color of the aqueous phase (aq) turned colorless (see Figure 3A−C).

$$HAuCl_4(aq) + N(C_8H_{17})_4^+Br^-(tol)$$
$$\rightarrow N(C_8H_{17})_4^+AuCl_4^-(tol) + HBr(aq) \tag{2}$$
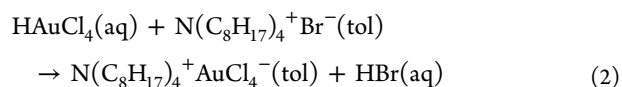
The aqueous solution (at the bottom) was discarded, and the organic phase containing gold precursors was transferred to a 250 mL round flask.

In addition to the gold precursor solution, a solution with a strong reducing agent was prepared as follows: In a beaker, 334 mg of sodium borohydride ($NaBH_4$, 98%, Sigma-Aldrich no. 452882) was dissolved in 25 mL of Milli-Q water under vigorous stirring. The prepared solution should be used immediately after preparation due to the fast decomposition of sodium borohydride as per eq 3. Observing small bubbles due to the formation of hydrogen is common.

$$BH_4^-(aq) + 3H_2O$$
$$\rightarrow B(OH)_3(aq) + 3H_2(\uparrow) + H^+ + e^- \tag{3}$$
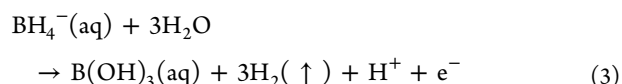
In order to obtain Au NPs, the freshly prepared solution of sodium borohydride was added dropwise within 1 min to the vigorously stirred organic phase containing the gold precursor (see Figures 4 and 5). Hereby the Au(III) precursor is reduced to Au(0) forming Au NPs. A few seconds after the addition of borohydride the color changed from deep orange (Au(III) precursor) to red-violet (tetraoctylammonium bromide capped Au NPs, TOAB-Au NPs).

$$n \times Au^{3+}(tol) + 3n \times e^- \rightarrow Au_n \tag{4}$$
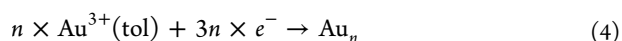
The solution was kept stirring for about 1 h in order to reduce remaining gold ions (Figure 5).

After 1 h of stirring at RT, the mixture was transferred into a separation funnel. The aqueous phase was discarded, and the organic phase was washed with 25 mL of 10 mM HCl (aq), 25 mL of 10 mM NaOH (aq), and 3 times with 25 mL Milli-Q water (cf. Figure 4). For the washing steps the solution used for washing (i.e., HCl, NaOH, or H$_2$O) was added in the funnel to the organic phase, and the mixture was shaken. After separation of the organic and aqueous phase the aqueous phase at the
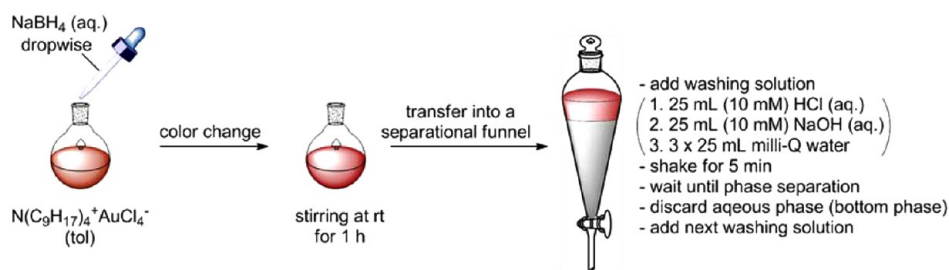
Figure 4. Synthesis of 4 nm TOAB-Au NPs is based on the reduction of Au(III) to elemental Au(0) by the addition of NaBH$_4$. After the formation of Au clusters, the NP suspension is washed several times with aqueous solutions.
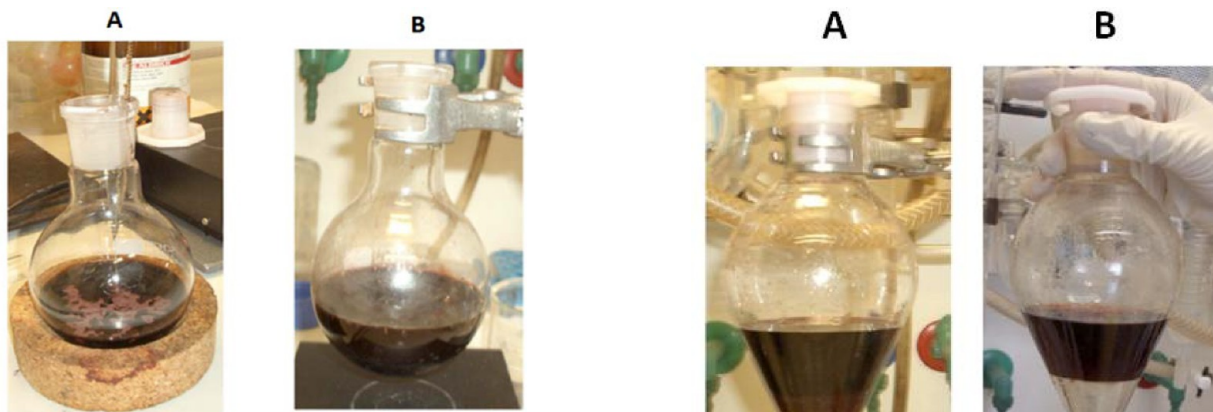

Figure 5. Reduction process of gold ions by sodium borohydride.

bottom was discarded. Washing steps are necessary to get rid of residual precursors and salts (Figure 6).

After discarding the aqueous phase from the last washing step, the remaining deep red, organic solution (ca. 80 mL) was transferred to a 250 mL round-bottom flask and stirred overnight to get thermodynamically stable NPs with narrow size distribution, mediated by Ostwald ripening[11−13] (cf. Figure 7).

After the synthesis of TOAB-Au NPs, a ligand exchange procedure was carried out, in order to obtain dodecanethiol-stabilized Au NPs (DDT-Au NPs). TOAB-Au NPs are stabilized by weakly adsorbed TOAB molecules at the surface of Au NPs, which can be desorbed by various stresses, such as dilution or repeated centrifugation. In order to get more stable Au NPs, TOAB can be exchanged with alkanethiols (e.g., dodecanethiol) that assemble strongly on the surface of gold due to the strong Au−S bond.[14,15]

For the ligand exchange procedure, 10 mL of 1-dodecanethiol (DDT, 98%, Sigma-Aldrich no. 471364) was added to the TOAB-Au NPs in toluene (ca. 80 mL) (Figures 8 and 9). The solution was heated to 65 °C and stirred for 2 h to facilitate the ligand exchange and finally stirred at RT to cool down. During this process, the mercapto group in dodeca-nethiol molecules displaces the TOAB,[16] yielding dodecane-thiol-stabilized Au NPs.

The solution of DDT-Au NPs was poured into several 40 mL vials and centrifuged at 900 rcf for 5 min, in order to remove larger agglomerates. The supernatant containing the well-dispersed DDT-Au NPs was collected and pooled, and the agglomerates (i.e., the precipitate) were discarded. DDT-Au NPs were then precipitated using methanol (99.8%, Sigma, no. 322415) as a nonsolvent. For this, about 20 mL of DDT-Au NPs solution was placed in 40 mL glass vials, followed by the

Figure 6. Purification of TOAB-Au NPs. Upper toluene phase containing TOAB-Au NPs is washed with aqueous solutions (HCl, NaOH, and Milli-Q water) in the lower phase to remove excess sodium borohydride and other residual chemicals. (A) Photograph of the two phases immediately after shaking: note that the two phases are not completely separated. (B) Photograph of the two phases after they were allowed to separate, forming a transparent aqueous phase at the bottom and a deep red organic phase at the top containing TOAB-Au NPs.
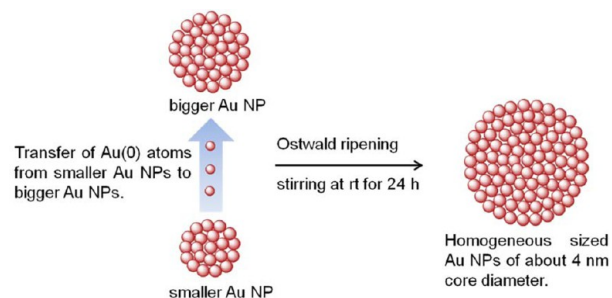

Figure 7. Ostwald ripening phenomena result in TOAB-Au NPs with a narrow size distribution. Smaller Au NPs in inhomogeneous population in terms of size dissolve and end up in bigger Au NPs.

gradual addition of methanol until the solution turned cloudy. The solution was then centrifuged at 900 rcf for 5 min, in order to precipitate the DDT-Au NPs. After this step of centrifugation, the supernatant turned colorless, and DDT-Au
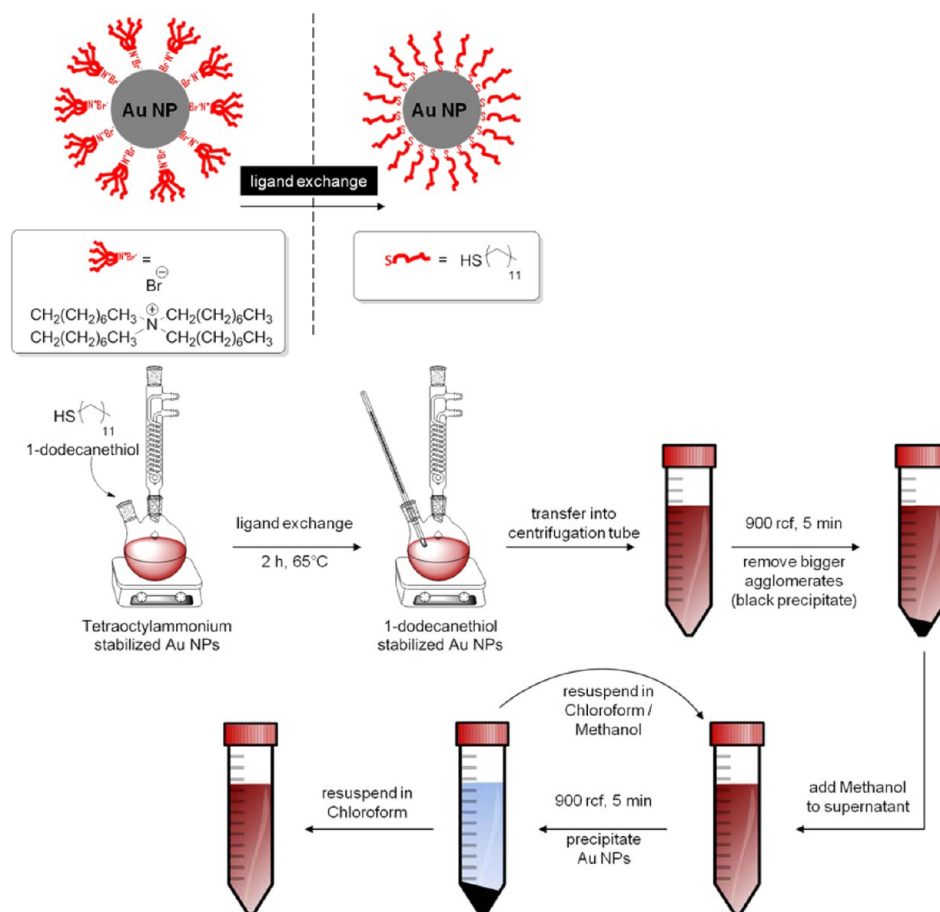
Figure 8. Ligand exchange on TOAB-Au NPs with dodecanethiol leading to the formation of DDT-stabilized Au NPs.

Figure 9. Au NPs are stirred after the addition of DDT while the temperature is controlled by a thermometer that is embedded in the reaction flask.

NPs were collected on the bottom of the centrifugation tube. In case of incomplete collection of DDT-Au NPs, additional methanol can be added, in order to increase the polarity of the medium and thus promoting the precipitation of the DDT-Au NPs, cf. Figure 10. After discarding the supernatant (which contains excess DDT and the replaced TOAB), the collected DDT-Au NPs were resuspended in chloroform. Similarly, DDT-Au NPs in chloroform were precipitated by the addition

of methanol (a large enough amount to induce turbidity), followed by centrifugation for 5 min at 900 rcf to precipitate and collect DDT-Au NPs. After discarding the supernatant, collected DDT-Au NPs were resuspended in chloroform, leading to the final solution of DDT-Au NPs.

The described cleaning procedure by the addition of methanol (i.e., nonsolvent) narrows the size distribution of the DDT-Au NPs. Upon the addition of only a little methanol, bigger Au NPs precipitate, whereas the smaller Au NPs remain in the supernatant. This size selective precipitation allows for collecting NPs with similar sizes and discarding extremely small NPs (Figure 10).[17] It is worth noting here that the use of excess methanol should be avoided, since this will coprecipitate excess ligand molecules in solution along with the collected NPs, and thus hinder the purification.[18]

Synthesis of Au NPs in the Presence of Hexanoic Acid: Hexanoic Acid-Stabilized Au NPs (≈4 nm core diameter). In a 25 mL round-bottom flask a solution of 29 μL (231 nmol) of hexanoic acid (Sigma-Aldrich, no. 153745) dissolved in 2 mL of toluene was mixed with 25 mg (97.2 mmol) of tetrabutylammonium borohydride (TBAB, 98%, Alfa Aesar, no. A17494) dissolved in 1 mL of didodecyldimethylammonium bromide (DDAB, 99%, Alfa Aesar, no. B22839) stock solution (100 mM in toluene) at RT. In addition, a solution of 500 μL (25 μmol) of HAuCl$_4$ (Sigma-Aldrich, no. 254169) (50 mM in DDAB stock) and 2 mL of DDAB stock was added fast under vigorous stirring. The solution was left for ripening for 1 h, stirring at RT before further use.
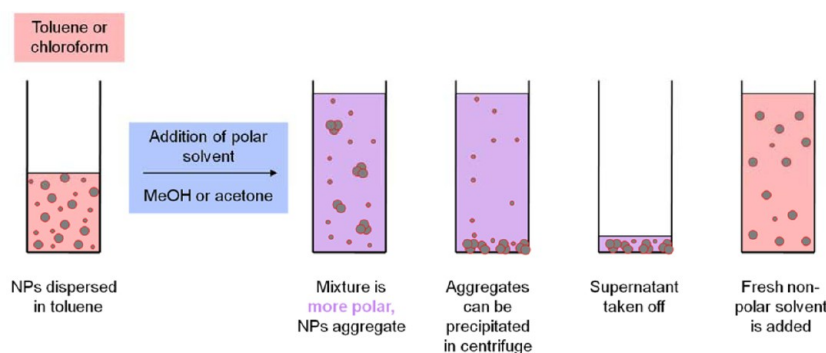
Figure 10. Size selective precipitation method to purify DDT-Au NPs and narrow their particle size distribution. The addition of a polar nonsolvent (methanol or acetone, drawn in blue) to DDT-Au NPs in hydrophobic solvent (e.g., toluene or chloroform, drawn in red) results in agglomeration and precipitation of large DDT-Au NPs. Collected precipitates of large DDT-Au NPs are redispersed in fresh hydrophobic solvent resulting in DDT-Au NPs with higher monodispersity. Smaller DDT-Au NPs remaining in supernatant are discarded.[17]

Synthesis of Au NPs in the Presence of Decanoic Acid: Decanoic Acid-Stabilized Au NPs (≈7 nm core diameter). For this purpose, a solution of 43 mg (250 μmol) of decanoic acid (Sigma-Aldrich, no. C1875) dissolved in 2.5 mL of toluene and a solution of 25 mg (97.2 mmol) of TBAB dissolved in 1 mL of DDAB stock solution (100 mM in toluene) were added in a 25 mL flask. Then a solution of 500 μL (25 μmol) of HAuCl$_4$ (50 mM in DDAB stock) and 2 mL of DDAB stock were added to the mixture quickly and under vigorous stirring and left for ripening for 1 h stirring at RT before further use.

It is worth noting that the synthesis of Au NPs in the presence of hexanoic or decanoic acid results in weakly capped NPs with these ligands, which can be considered as "intermediate NPs" ready for further ligand exchange with thiol capped molecules. However, the use of these fatty acids ensures a narrow size distribution of the prepared Au NPs as described by Jana et al.[19]

1.3. Synthesis of Hydrophobic Ag NPs (≈4 nm core diameter). Also silver NPs (Ag NPs) can be synthesized in organic solvents.[20] The herein described synthesis of Ag NPs is similar to the synthesis of Au NPs as described in Section 1.2. Mari et al. reported an effective protocol to prepare alkanethiol-stabilized Ag NPs (≈4.2 nm in core diameter).[21] The first step was the synthesis of an alkyl thiosulfate (namely, sodium S-dodecylthiosulfate) as a ligand precursor as per eq 5.

$$Na_2S_2O_3 \cdot 5H_2O + CH_3(CH_2)_{11}Br$$
$$\rightarrow CH_3(CH_2)_{11}S_2O_3^-Na^+ + NaBr + 5H_2O \quad (5)$$
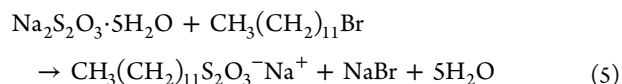
Sodium thiosulfate pentahydrate (6.21 g (25 mmol, 1.0 equiv), Sigma-Aldrich, no. 217247) was dissolved in 50 mL of Milli-Q water. In addition, 5.19 mL (25 mmol, 1.0 equiv) of 1-bromododecane (Sigma-Aldrich, no. B65551) was dissolved in 50 mL of ethanol. The combined solutions were stirred under reflux for 3 h. The mixture was cooled down to RT, and the resulting crystals of sodium S-dodecylthiosulfate were filtered using a funnel with a proper filter paper. Another crystallization step was performed, where sodium S-dodecylthiosulfate was dissolved in as little ethanol as possible under heating (~45 °C) and left in a crystallization beaker for cooling to RT. In this manner, purification of the product was obtained by allowing the solution to gradually cool and be saturated with the compound. The product of interest crystallized, and unwanted contaminations remained in the liquid phase. Finally, the sodium S-dodecylthiosulfate crystals were filtered as previously described, and the final product was dried in vacuum (cf. Figure

11). Importantly, the synthesis should be done in a fume hood and under controlled laboratory conditions.
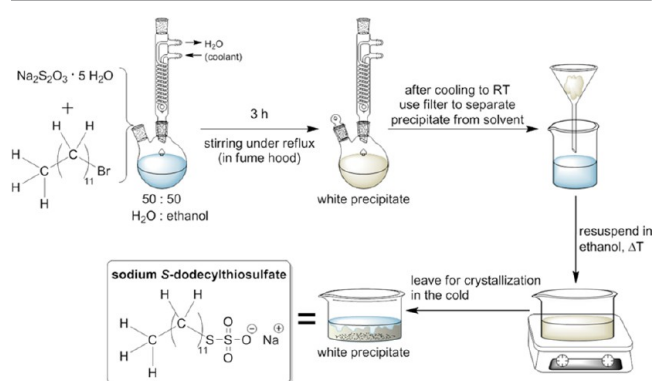

Figure 11. Schematic illustration of the chemical synthesis of sodium S-dodecylthiosulfate as a ligand precursor to stabilize Ag NPs.

For the synthesis of Ag NPs, 390 mg (1.26 mmol, 0.75 equiv) of sodium S-dodecylthiosulfate in 90 mL of ethanol was heated up to 50 °C. To this solution was added 282 mg (1.68 mmol, 1.0 equiv) of AgNO$_3$ (Sigma-Aldrich, no. 209139), and the resulting mixture was stirred for a further 10 min. A color change was observed; the white solution turned brown after a few minutes (cf. Figure 12). A total of 318 mg (8.4 mmol, 5.0 equiv) of sodium borohydride (NaBH$_4$ 98%, Sigma-Aldrich, no. 452882) was dissolved in 15 mL of ethanol and added to the mixture, which turned almost black immediately (cf. Figure 12). After 5 min, 74 mg (0.42 mmol, 0.25 equiv) of ascorbic acid (Sigma-Aldrich, no. 255564) was added, and the mixture was stirred at 50 °C for a further 3 h. As the reaction mixture reached RT, the solution with the Ag NPs was transferred into centrifuge tubes, and the Ag NPs were collected at the tube bottom by centrifuging at 3000 rcf for 15 min. After discarding the supernatant, the Ag NPs were resuspended in Milli-Q water and again collected by sedimentation (3000 rcf, 15 min). This washing step was repeated two more times using ethanol and then acetone (cf. Figure 12). After that, the Ag NPs were dried under reduced pressure, which led to gray powder. For further use, the NPs were resuspended in chloroform.

1.4. Synthesis of Hydrophobic FePt NPs (≈4 nm core diameter). The synthesis of ≈4 nm core diameter FePt NPs as carried out here was described first by Sun et al.[22] This reaction needs to be carried out in a water- and oxygen-free atmosphere
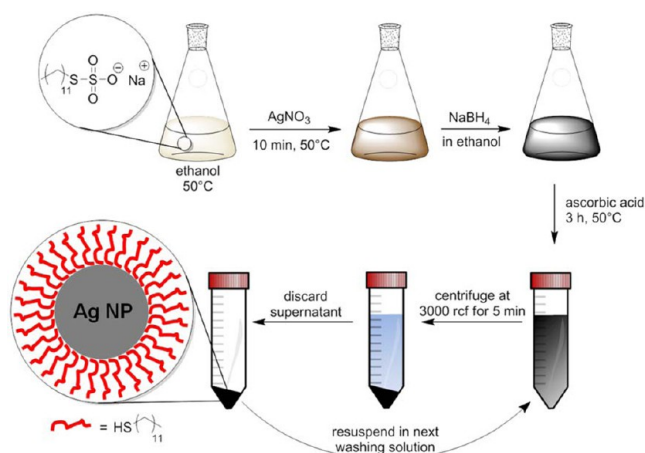
Figure 12. Graphic scheme of the synthesis and purification of dodecanethiol-stabilized Ag NPs (DDT-Ag NPs).

(e.g., Schlenk line and/or glovebox). In a typical synthesis, platinum(II) acetylacetonate (197 mg, 0.5 mmol, 1 eq, ABCR, no. AB 121416), 1,2-hexadecanediol (390 mg, 1.5 mmol, 3 equiv, Sigma-Aldrich, no. 213748) and dioctylether (20 mL, Sigma-Aldrich, no. 249599) were mixed in a three-neck flask, a magnetic bar was added, and the mixture was heated to 100 °C. The temperature was controlled by a temperature sensor immersed in the solution (cf. Figure 13). When the desired
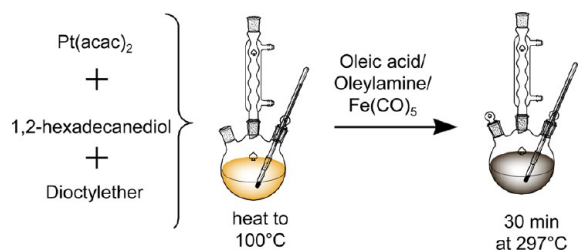

Figure 13. Schematic illustration of the chemical synthesis of 4 nm core diameter FePt NPs. The synthesis was carried out under water exclusion and N_2 atmosphere in a three neck flask equipped with seal septa to be able to add all reagents under oxygen and water free conditions.

temperature was reached, the solution presented a light yellow color. Then, oleic acid (OA, 0.16 mL, 0.5 mmol, 1 equiv, Sigma-Aldrich, no. O1008), oleylamine (OLA, 0.17 mL, 0.5 mmol, 1 equiv, Sigma-Aldrich, no. O7805), and $Fe(CO)_5$ (0.13 mL, 1 mmol, 2 equiv, Sigma-Aldrich, no. 481718) were added. After the addition of the Fe precursor, the color of the solution turned to light brown. The reaction was heated under reflux (297 °C) for 30 min (cf. Figure 13). At this temperature, the solution started to boil, and some fumes were observed. Moreover, the color of the solution changed to deep brown, indicating the formation of NPs. After 30 min of heating, the reaction mixture was allowed to cool down to RT by removing the heating source.

For purification, the solution of FePt NPs was transferred to two centrifuge tubes of 50 mL, and ethanol (40 mL, Carl Roth, no. 64-17-5) was added to induce precipitation of the NPs. The NPs were separated by centrifugation (5 min, 2700 rcf) (cf. Figure 14). The brown colored supernatant containing byproducts was discarded, and the black NP precipitate was dispersed in hexane (25 mL) in the presence of OA (0.05 mL)
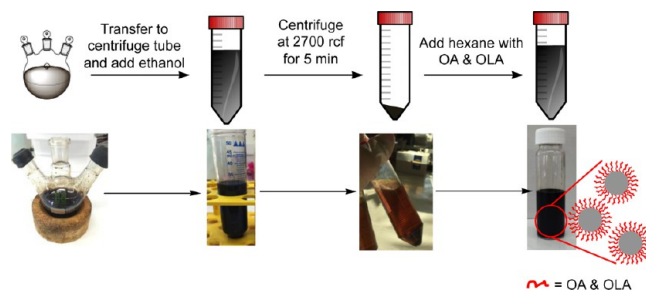

Figure 14. Graphic scheme (upper panel) and photographs (lower panel) of FePt NP purification steps after synthesis.

and OLA (0.05 mL), in order to provide the NP colloidal stability for long storage periods.

1.5. Synthesis of Hydrophobic Fe_3O_4 NPs ($\approx$4 nm core diameter). The synthesis of Fe_3O_4 NPs as outlined here was initially published by Sun et al. in 2003,[23] with a procedure to obtain monodisperse NPs with variable composition: MFe_2O_4, M being a metal that can be iron, cobalt, or manganese, allowing variation in the magnetic properties. This protocol allows for the synthesis of NPs with a tunable diameter from 3 to 20 nm by changing the initial reaction conditions, or via a postsynthesis seed-mediated approach. In the present report only the synthesis of 4 nm core size Fe_3O_4 NPs is presented and detailed (cf. Figure 15). To prepare these NPs, 706.4 mg (2
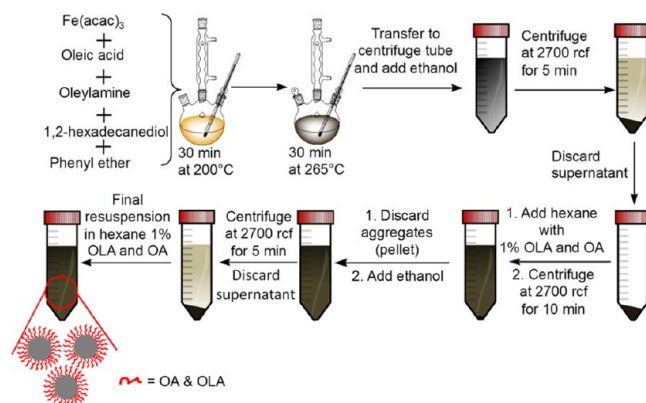

Figure 15. General scheme of the synthesis and purification of Fe_3O_4 NPs. After the initial synthesis, both large aggregates and solvent impurities are removed by centrifugation, obtaining NPs that are finally stabilized by OLA and OA.

mmol, 1 equiv) of the metal precursor iron(III) acetylacetonate ($Fe(acac)_3$; 99%, Strem Chemicals, no. 26-2300) was dissolved in 20 mL of diphenyl ether (Sigma-Aldrich, no. P24101) in the presence of 6 mmol of OA (3 equiv, 90%, Sigma-Aldrich, no. 364525), 6 mmol of OLA (3 equiv, Aldrich, no. O7805), and 10 mmol of 1,2-hexadecanediol (5 equiv, Sigma-Aldrich, no. 52270). The process needs to be carried out in an oxygen- and water-free atmosphere (glovebox and/or Schlenk line), where the mixture was stirred at 200 °C for 30 min. The mixture was then heated up to 265 °C for another 30 min to induce thermal decomposition and thus the formation of NPs (cf. Figure 15). The Fe_3O_4 NP dispersion was then cooled down to RT and was taken away from the water- and oxygen-free ambient. In this preparation, 1,2-hexadecanediol acts as reducing agent to reduce the metal precursor into Fe_3O_4 NPs that are stabilized with oleic acid and oleylamine. For purification, the dark brown dispersion was equally distributed into two 50 mL centrifuge

tubes, and then 25 mL of ethanol (Roth, no. 5054.2) was added to each tube, and the NPs were centrifuged at 2700 rcf for 5 min. Supernatants were discarded, and the Fe_3O_4 NPs were collected at the bottom of the centrifugation vial. The Fe_3O_4 NPs were resuspended in a mixture of hexane with 1% (v/v) OA and OLA. Additional centrifugation at 2700 rcf for 10 min is necessary to get rid of any undispersed residue/aggregates. The resulting supernatants were transferred to clean vials, and a new washing step with ethanol was performed at 2700 rcf for 5 min (cf. Figure 15). The final Fe_3O_4 NPs with a core diameter of ≈4 nm forming the pellet were finally redispersed into hexane supplemented with 1% OA and OLA.

1.6. Synthesis of Hydrophobic Sn NPs (≈11 nm core diameter). The synthesis of monodisperse Sn NPs with a core diameter of 11 nm as reported here was first published by Kravchyk et al. in 2013.[24] The protocol employs the reaction of $LiN(Si(CH_3)_3)_2$ with a solution of oleylamine (OLA) and $SnCl_2$ at 180 °C, followed by the reduction of Sn(II) to elemental tin using diisobutylaluminum hydride (DIBAH) (Figure 16). The reaction was completely performed inside a
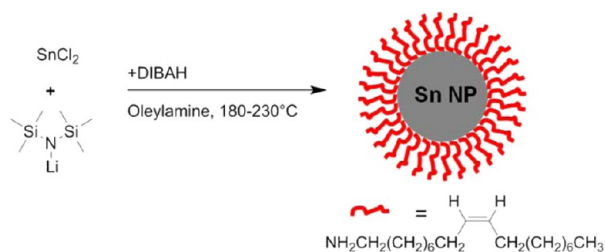

Figure 16. Synthesis of monodispersed Sn NPs.

glovebox under N_2 atmosphere. Importantly, all glassware should be dried using heat and vacuum as the reaction is sensitive to water. The described reaction is violent; thus, it should be carried out with caution, and safety regulations should be considered.

A 250 mL three neck flask was equipped with a reflux condenser, stirring bar, and two additional seal septa with one thermal sensor connected to a magnetic stirrer with heating capability. A total of 24.6 mL of OLA (Sigma-Aldrich, ≥98%, no. HT-OA100) was filled into the flask using a 20 mL syringe and was stirred under vacuum at 140 °C for 1.5 h. After cooling the solvent down to 50 °C, 94.8 mg (0.5 mmol, 1.0 equiv) of $SnCl_2$ (Sigma-Aldrich, no. 208256) was added, and the mixture was again dried under vacuum at 140 °C for 30 min. Meanwhile, 601 mg (3.6 mmol, 7.2 equiv) of $LiN(Si(CH_3)_3)_2$ (Sigma-Aldrich, no. 324620) was dissolved in 3 mL of toluene using a small beaker. The mixture of OLA and $SnCl_2$ was heated up to 180 °C under N_2 atmosphere, followed by the injection of $LiN(SiMe_3)_2$ in toluene solution. After 10 s, 0.6 mL (0.6 mmol, 1.2 equiv) of a 1.0 M solution of DIBAH dissolved in tetrahydrofuran (THF, Sigma-Aldrich, no. 214981) was injected, which induced a color change to dark brown. The reaction mixture was further stirred for 1 h before putting the flask into an ice bath to cool it down. During this, at about 150 °C, 10 mL of toluene were added, and the flask was extracted out of the glovebox and immediately held into an ice bath to speed up the cooling process (cf. Figure 17).

When the Sn NP solution had cooled to RT, it was transferred into two 50 mL centrifuge tubes and mixed with 40 mL of ethanol, which led to precipitation of the Sn NPs. The sample was centrifuged at 3000 rcf for 5 min, in order to
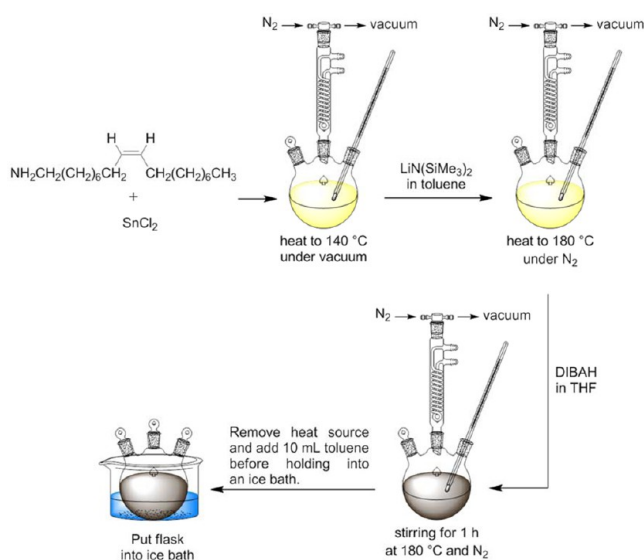

Figure 17. Schematic illustration of the chemical synthesis of 11 nm Sn NPs. The synthesis was carried out under water exclusion and N_2 atmosphere in a three neck flask equipped with a seal septa to be capable of adding all reagents and guarantee oxygen- and water-free conditions. For drying the solvent OLA and $SnCl_2$, the reflux condenser was equipped with a three-way valve to be able to switch between N_2 and vacuum. Before extracting the flask out of the glovebox, the thermal sensor and reflux condenser were removed, and all three necks were closed using the seal septa.

separate the NPs from the solvent. The NPs were collected, and the supernatant was discarded. Next, the Sn NPs were resuspended in a solution of oleic acid (OA) in chloroform (∼6 mL, 1 mL OA/50 mL $CHCl_3$), which led to a ligand exchange from OLA to OA. Finally, a second precipitation step was performed by adding 10 mL of ethanol to the solution and centrifugation at 3000 rcf for 5 min and resuspension in 10 mL of $CHCl_3$ to generate a long-term stable solution of Sn NPs (cf. Figure 18).
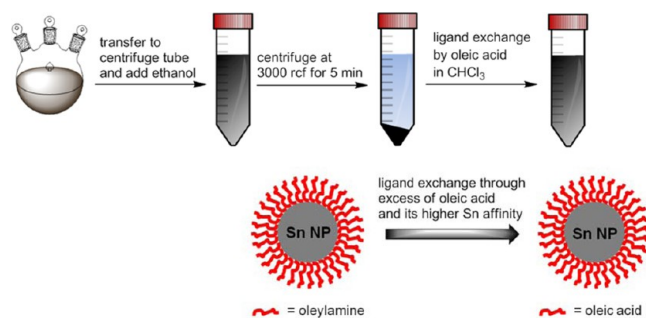
Figure 18. Purification of Sn NPs and OLA ligand exchange with OA.

1.7. Synthesis of Hydrophobic CdSe and CdSe/ZnS NPs (≈2−10 nm core diameter). CdSe NPs, so-called quantum dots (QDs), of different sizes were synthesized using CdO as a precursor, via the procedure described by Peng's group,[25] with minor modification in reaction temperature/time, in order to achieve a better control of the size of the NPs. To improve the quantum yield and long-term stability of these fluorescent NPs, coating of the CdSe NPs with a shell of ZnS was employed[26,27] using diethylzinc and hexamethyldisilathiane as zinc and sulfur sources, respectively.[28]

Synthesis of CdSe cores: In a typical synthesis, 0.03 g of cadmium oxide (CdO, Sigma-Aldrich no. 202894), 0.11 g of hexylphosphonic acid (HPA, Sigma-Aldrich no. 750034), and 3.5 g of trioctylphosphine oxide (TOPO, Sigma-Aldrich no. 223301) were loaded into a 100 mL glass three-neck flask connected to a nitrogen line (see Figure 19). The mixture was

Figure 19. Setup for the synthesis of CdSe/ZnS NPs. The photo shows a three-neck flask equipped with a heating mantle, a reflux condenser, an addition funnel, a thermometer connected to a temperature controller, and a nitrogen flow.

degassed at 120 °C for 20 min and then heated to 300−320 °C under nitrogen atmosphere for 15 min to allow the complete dissolution of CdO in HPA and TOPO leading to a clear and colorless solution, which indicates that a Cd−HPA/TOPO complex has been formed. In case the CdO did not dissolve completely, (i.e., the solution did not turn transparent), some more HPA needs to be added.

Then, the temperature of the solution was cooled down to 270 °C by setting the temperature controller to this temperature and waiting for around 10−15 min. When the desired temperature was reached, 1.2 mL of selenium stock solution was swiftly injected with a syringe. The selenium stock solution was prepared by dissolving 0.0255 g of selenium powder (Se, Sigma-Aldrich no. 229865) in 1.5 mL of trioctylphosphine (TOP, Sigma-Aldrich no. 718165), to produce a 0.215 M stock solution of trioctylphosphine selenide (Se−TOP). After injection, the temperature dropped by roughly 20 °C and was maintained then at 250 °C throughout the synthesis of the CdSe cores. At 3−5 min after the injection, the color of the solution turned from colorless to yellow, indicating the nucleation of CdSe NPs. Upon further grown of the NPs this color gradually turned to yellow-orange, orange, red, and finally dark red 30−40 min after the injection.

CdSe NP growth was monitored by taking aliquots from the reaction flask every 5 min. Aliquot solutions were diluted with chloroform, and their UV/visible absorption spectra were recorded (cf. Figure 20). Even when the growth rate varied slightly from synthesis to synthesis, it was always sufficiently
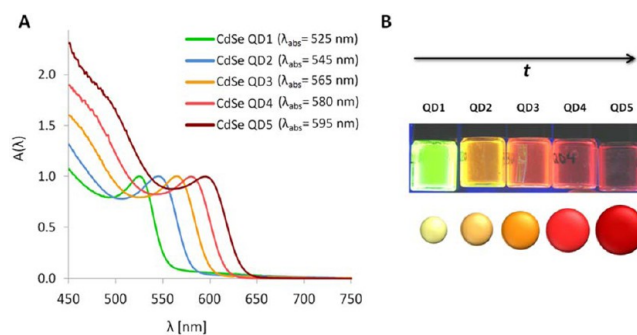

Figure 20. Monitoring the growth of CdSe NPs by (A) recording the UV/visible absorption spectra $A(\lambda)$ of aliquot samples that were taken from the reaction flask at different time intervals followed by dilution with chloroform. The peak in the spectrum at wavelength λ_{abs} is due to the excitation of the first exciton.[30] The spectra were normalized to the absorption at the first exciton peak. Upon growth of CdSe NPs, the absorption peak shifts to higher wavelength, as shown here in the five spectra recorded after different time points (t = 5 min, 10 min, 15 min, 20 min, 30 min). (B) The solutions of the CdSe NPs are fluorescent with tunable excitation wavelength that were red upon growth of NPs.

slow so that the synthesis could be stopped whenever the first exciton peak in the absorption spectrum reached the desired value, which could be easily correlated to the NPs' average size through calibration curves available in the literature.[29] Once the cores had reached the desired size, either the reaction could be stopped by removing the heating mantle to let the solution cool down to RT with the resulting NPs purified as described below or optionally the temperature could be maintained at 250 °C and the synthesis was continued further to grow a ZnS shell on the prepared CdSe cores.

For ZnS shell growth, a shell of ZnS can be optionally grown around the CdSe cores; see Figure 21. Once CdSe NPs have reached the desired size, they can be directly passivated by growing a ZnS shell, without the need of isolating the CdSe NPs from the crude solution.[31] For CdSe cores with a size of d_c = 3.82 nm in diameter, 1.5 mL of the overcoating stock solution (Zn/S/TOP solution) was added dropwise to the mixture under vigorous stirring through the addition funnel over a period of ≈10 min. It is important that the addition is done dropwise in order to avoid nucleation of ZnS NPs. The Zn/S/TOP stock solution was prepared by adding equimolar amounts of the Zn and S precursors in TOP, that is, 1.75 mL of diethylzinc solution (ZnEt$_2$ 1 M in hexane, Sigma-Aldrich no. 296112) and 0.37 mL of hexamethyldisilathiane ((TMS)$_2$S, Sigma-Aldrich no. 283134) in 10.38 mL of trioctylphosphine (TOP, Sigma-Aldrich no. 718165). Note that the Zn/S/TOP stock solution can be separated and frozen into aliquots to be used in the next synthesis, being stable once frozen for at least six months. After the addition of Zn/S/TOP solution, the mixture was left to cool down to 90 °C by removing the heating mantle, and then this temperature was maintained and the solution stirred for 3 h more. Finally, the solution was cooled down to RT by turning the heating off, and the NP suspension was transferred to a glass vial and diluted with 10 mL of anhydrous chloroform.

The amount of added Zn/S/TOP stock solution depends on the CdSe core size and the desired thickness of the ZnS shell. The amount of Zn and S precursors (i.e., Zn/S/TOP stock solution) needed for growing a ZnS shell of desired thickness can be estimated. First, from the wavelength of the first exciton peak λ_{abs} in the absorption spectrum of the CdSe cores, the
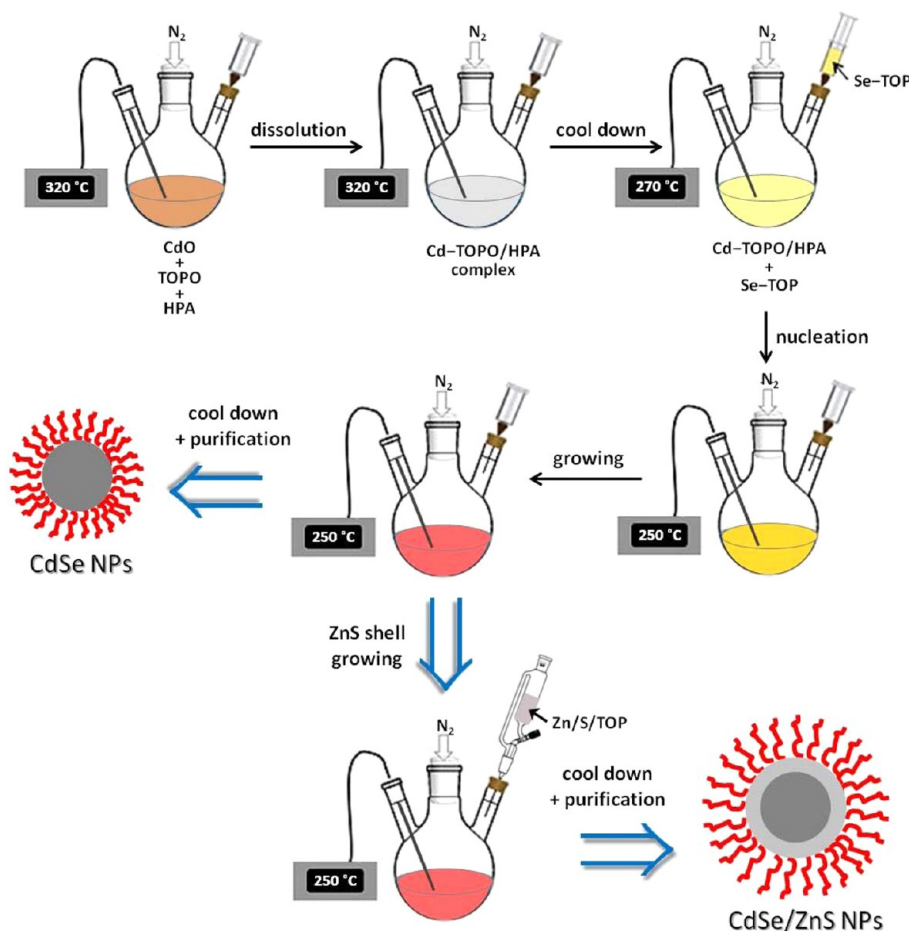
Figure 21. Schematic illustration of the synthesis of CdSe and CdSe/ZnS NPs.

diameter of the cores d_c is estimated via an empirical formula by Yu et al.,[29] which correlates CdSe NPs core size (d_c) with the corresponding wavelength of the first exciton peak (λ_{abs}):

$$d_c = (1.6122 \text{ nm} \times 10^{-9} \text{nm}^{-4}) \times \lambda_{abs}^4 - (2.6575 \times 10^{-6} \text{nm}^{-3})$$
$$\times \lambda_{abs}^3 + (1.6242 \times 10^{-3} \text{nm}^{-2}) \times \lambda_{abs}^2 - 0.4277 \times \lambda_{abs}$$
$$+ 41.57 \text{ nm} \tag{6}$$

According to the literature, a number of ZnS monolayers between 1 and 2 is usually the optimum for getting the maximum quantum yield in CdSe/ZnS NPs.[26,31,32] In case of too thin layers, the passivation effect is not significant. In case of too thick layers, the ZnS shell may crack due to differences in the lattice constants between CdSe and ZnS, resulting in poor quantum yields. In this work 1.2 monolayers were selected as the desired thickness of ZnS on CdSe NPs. According to the bulk lattice parameters of ZnS, the thickness of one single ZnS monolayer is 0.31 nm, defined as the distance between consecutive planes along the [002] axis in bulk wurtzite ZnS.[26] Therefore, the thickness of the ZnS shell corresponding to 1.2 monolayers is 0.37 nm (cf. Figure 1).

By knowing the diameter of the CdSe core (d_{c1}) from eq 6 (as the inorganic part comprises here a core and a shell the innermost core is termed d_{c1} instead of d_c) and the desired thickness of the ZnS shell ($d_{c12} - d_{c1}$) = 2 × 0.37 nm = 0.74 nm, the diameter d_{c12} of the CdSe/ZnS core/shell NP can be calculated ($d_{c12} = d_{c1} + 0.74$ nm). The volume of the ZnS shell V_{c2} around one CdSe core thus is the volume of one CdSe NP

($V_{c1} = (\pi/6)d_{c1}^3$), subtracted from the volume of one CdSe/ZnS NP ($V_{c12} = (\pi/6)d_{c12}^3$), cf. eq 22.

For example, sample QD4 in Figure 20 corresponds to CdSe NPs with $\lambda_{abs} = 580$ nm. According to eq 6, $d_{c1} = 3.82$ nm, and thus $d_{c12} = 3.82$ nm + 0.74 nm = 4.56 nm. This leads to volumes $V_{c1} = 29.19$ nm^3 and $V_{c2} = V_{c12} - V_{c1} = 20.46$ nm^3 of the CdSe core and the ZnS shell, respectively. The ratio of the shell volume to the core volume thus is $V_{c2}/V_{c1} = 0.70$. As there are Cd atoms only in the core ($N_{Cd/NP}$ per NP) and Zn atoms only in the shell ($N_{Zn/NP}$ per NP), the amount of Cd and Zn in one NP scales according to eqs 7, 8, 28, and 29 with the volume of the CdSe core (ratio of Cd:Se = x:y = 1) and the ZnS shell (ratio of Zn:S = x:y = 1), respectively:

$$N_{Cd/NP} = \rho_{CdSe} \times V_{c1} \frac{N_A}{\left(M_{Cd} + \left(\frac{1}{1}\right) \times M_{Se}\right)} \tag{7}$$

$$N_{Zn/NP} = \rho_{ZnS} \times V_{c2} \frac{N_A}{\left(M_{Zn} + \left(\frac{1}{1}\right) \times M_S\right)} \tag{8}$$

Hereby $M_{Cd} = 112.4$ g/mol, $M_{Se} = 79.0$ g/mol, $M_{Zn} = 65.4$ g/mol, and $M_S = 32.1$ g/mol are the molar masses of cadmium, selenium, zinc, and sulfur, respectively. $\rho_{CdSe} = 5.82$ g/cm^3 and $\rho_{ZnS} = 4.09$ g/cm^3 are the bulk densities of CdSe and ZnS, respectively. Thus, the ratio of Zn to Cd atoms in one CdSe/ZnS NP is

$$\frac{N_{Zn/NP}}{N_{Cd/NP}} = \left(\frac{V_{c2}}{V_{c1}}\right) \times \left(\frac{\rho_{ZnS}}{\rho_{CdSe}}\right) \times \left(\frac{M_{Cd} + M_{Se}}{M_{Zn} + M_S}\right)$$

$$= 1.38 \times \left(\frac{V_{c2}}{V_{c1}}\right) \tag{9}$$

In the case of the sample QD4 in Figure 20 with λ_{abs} = 580 nm this leads to N_{Zn}/N_{Cd} = 1.38 × 0.70 ≈ 0.96. The amount n_{Cdsol} of Cd added in form of CdO as precursor during the synthesis of the CdSe cores is known. In the particular case of the synthesis described here it was n_{Cdsol} = 0.234 mmol (mass of added CdO = 0.03 g, M_W(CdO) = 128.4 g/mol). The amount of Zn needed in the reaction solution thus is $n_{Znsol} = n_{Cdsol} \times (N_{Zn}/N_{Cd})$ = 0.234 mmol × 0.96 ≈ 0.22 mmol. Note that this calculation assumes that all added Cd ends up in the CdSe core. The Zn concentration in the Zn/S/TOP stock solution is c_{Zn} = 1 M × 1.75 mL/(1.75 mL + 0.37 mL + 10.38 mL) = 0.14 M. Thus, in order to inject n_{Znsol} = 0.22 mmol Zn, the volume $V_{Zn/S/TOPsol} = n_{Znsol}/c_{Zn}$ = 0.22 mmol/0.14 M ≈ 1.5 mL needs to be dropwise injected.

Note that this calculation only provides a rough estimate of the amount of Zn/S/TOP stock solution, which is needed for growing the ZnS shell. In fact, during growth of the ZnS shell small aliquots may be taken and the fluorescence analyzed. Shell growth is continued until the quantum yield of the NPs no longer increases.

Purification of CdSe or CdSe/ZnS NPs: 10 mL of anhydrous methanol were added to 10 mL of the NP suspension, which caused flocculation of the NPs. The NPs were then precipitated by centrifugation (5000 rcf, 5 min). Then, the supernatant was discarded and the NP precipitate at the bottom of the vial was resuspended in chloroform. This purification process was repeated two more times (cf. Figure 22). After the last
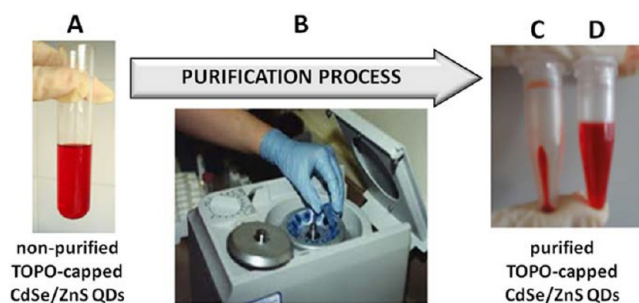

Figure 22. Purification process of the CdSe or CdSe/ZnS QDs by centrifugation and washing with methanol. (A) Vial with NPs dispersed in chloroform. (B) Centrifugation of the NP suspension after the addition of methanol. (C) Precipitated QDs after centrifugation. (D) QDs solution after removal of supernatant in C and redispersion in chloroform.

centrifugation, the supernatant should be colorless and the NPs should be all precipitated on the bottom of the Eppendorf tube in which centrifugation had been carried out. If the supernatant is still colored, the addition of more methanol is needed in order to increase the polarity of the medium, promoting the precipitation of the NPs. Finally, the purified QD NPs (TOPO-capped CdSe or CdSe/ZnS QDs) were dispersed in 10 mL of anhydrous chloroform and stored in the dark.

1.8. Synthesis of Hydrophobic CdS NPs (≈2 nm core diameter). Hydrophobic CdS NPs were synthesized by adapting the original method described by Yu and Peng.[33]

For the synthesis, a mixture of 4 g including 12.8 mg (0.10 mmol, 2 equiv) of cadmium oxide (Sigma, no. 202894), 85 mg (0.30 mmol, 6 equiv) of oleic acid (OA, Sigma, no. 364525), and 3.90 g (15.3248 mmol, 306.5 equiv) of octadecane (ODE, Technical grade 90%, Alfa Aesar, no. L11004) were weighed and mixed in a 50 mL three-neck round-bottom flask. Then, the mixture was heated to 120 °C and stirred under nitrogen environment, followed by degassing under vacuum for 5 min, cf. Figure 23.
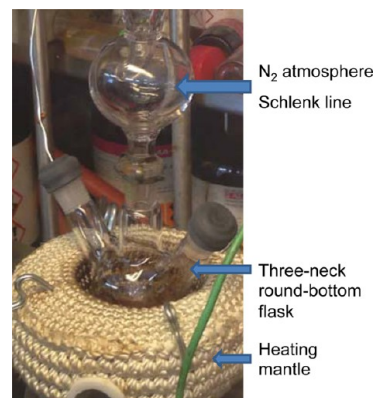
Figure 23. Reaction setup used for heating the mixture of CdO, oleic acid, and ODE.

This mixture was then heated to 300 °C, while a solution of sulfur (0.0016 g, 0.05 mmol, 1 equiv, Sigma, no. 414980) in 2 g of ODE was prepared in a separated glass vial. Since it is very difficult to measure such a small quantity of sulfur, a stock solution was prepared instead by dissolving 8 mg of sulfur in 10 g of octadecane (ODE, Technical grade 90%, Alfa Aesar, no. L11004). To efficiently dissolve the sulfur in ODE, the mixture was heated to 85 °C under stirring.

When the mixture of CdO, OA, and ODE reached 300 °C, the CdO started to decompose, and the initial brownish colored solution started turning into a transparent solution, cf. Figure 24. When the solution became completely transparent, the previously prepared sulfur solution was quickly injected using a syringe, cf. Figure 25.

After injection of the sulfur-ODE solution, the temperature of the mixture dropped to 240 °C. In the case that the required size of the QDs was d_c ≈ 2 nm, the heating mantle was

Figure 24. Color change of the mixture before (A) and after (B) decomposition of CdO.

Figure 25. Injection of the sulfur−ODE solution at 300 °C.

Figure 27. Growth of CdS QDs. Absorption spectra (A) and emission spectra (B) were recorded by taking small aliquots from the reaction solution at different time points (QD1−8). The spectra were normalized to the exciton peak, $A(\lambda_{abs})$ for absorbance and $I(\lambda_{em})$ for emission. Note that upon growth of the QDs, the peak shifts toward higher wavelength.

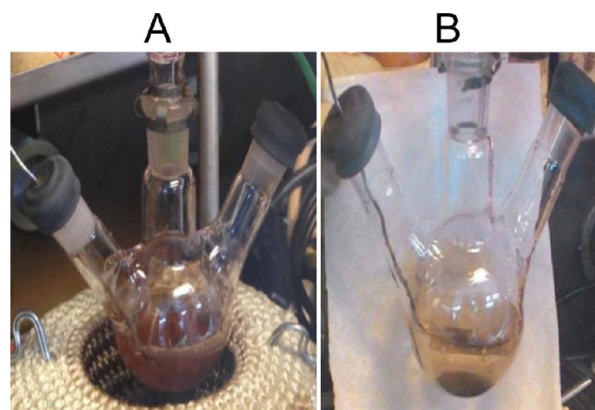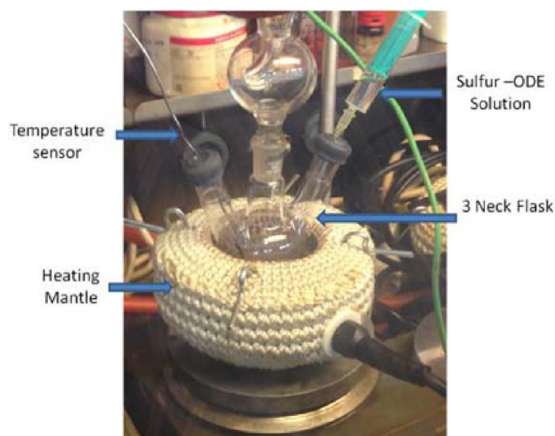removed just before injecting the sulfur−ODE solution, and the solution was left undisturbed to cool down to RT under the same stirring conditions, cf. Figure 26. In the case the required size of the QDs was bigger than 2 nm, the temperature of the solution was allowed to recover up to 250 °C after injection of the sulfur−ODE solution. Depending on the required size of the QDs, the solution was kept for 1−15 min at 250 °C (i.e., longer times for bigger QDs), cf. Figure 27. The formation of the QDs could be observed by the change of the solution color, from transparent to light yellow. When the desired size (i.e., the envisaged absorption/emission wavelength of the QDs) was achieved, the heating mantle was removed and the solution was allowed to cool down to RT.

After cooling down to RT, the solution was transferred into a centrifuge tube. To purify the QDs from ODE, OA, and nonreacted Cd or CdO, 20 mL of acetone was added and mixed together until the mixture became cloudy. The cloudy mixture was then centrifuged at 2500 rcf for 10 min. The QDs were precipitated, and the supernatant was discarded. The precipitated QDs could be redispersed in organic solvent (e.g., chloroform, toluene, etc.). For further cleaning of the QDs, a 1:1 volumetric ratio of chloroform and methanol was used to precipitate the QDs. This process was repeated 1−3 times, until the precipitated QDs were like white powder, in order to ensure the purity of the QDs. Finally, the solvent was evaporated and the QDs were dissolved in toluene.
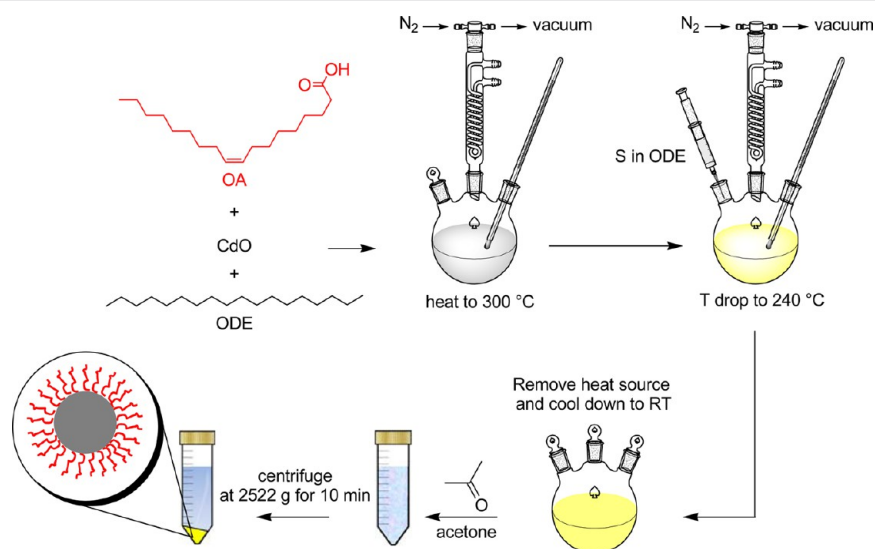
Figure 26. Schematic illustration of the chemical synthesis of hydrophobic CdS NPs ($d_c \approx 2$ nm) is shown. OA, CdO, and ODE were mixed and heated at 300 °C resulting in a color change from brown to transparent. The sulfur solution in ODE was rapidly injected to induce the formation of NPs as evident from the change from transparent to light yellow (QDs). The QDs were purified (1−3 times) by addition of acetone or methanol followed by precipitation and centrifugation.

2. SYNTHESIS OF INORGANIC NPs IN AQUEOUS SOLUTION LEADING TO HYDROPHILIC NPs

2.1. General Considerations. As detailed in Section 1.1, all glassware was first cleaned with detergent followed by aqua regia and carefully rinsed with Milli-Q water and acetone to guarantee extremely clean glass surfaces.

In this chapter NPs are prepared in aqueous media and thus capped by a shell of hydrophilic ligands to maintain their colloidal stability; see Figure 28. In particular, in this chapter

$$L_{eff} = L_c + 2 \times l_{ligand} \qquad \text{(Equation 10)}$$
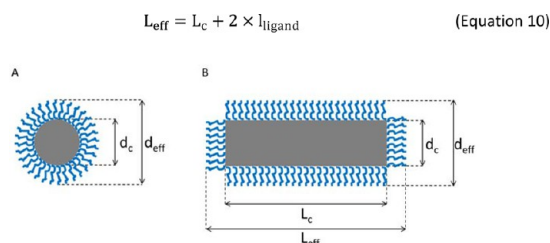
Figure 28. Sketch of (A) spherical and (B) rod-shaped inorganic NPs, comprising an inorganic core (drawn in gray) and an organic hydrophilic ligand shell (drawn in blue). In the case of nanorods, their shape is described by a cylinder with length L_c of the inorganic core and L_{eff} of the NP including the organic ligand shell and with diameter d_c of the inorganic core and d_{eff} of the whole NP.

the synthesis of different materials such as Au and Ag with different shapes is described. In case the NP cores are not of spherical shape, their geometry needs to be described by parameters other than just the core diameter (cf. Figure 28). While this is complex in the form of irregularly shaped NP cores, some other cores can be described best by simple three-dimensional objects such as tubes, ellipsoids, cubes, etc. As described in Section 1.1 the ligand shell adds to the size of the whole NP. Thus, in the case of an elongated object, apart from the diameter also the effective length is higher than the core lengths; see eq 1 and eq 10.

$$L_{eff} = L_c + 2 \times l_{ligand} \qquad (10)$$

2.2. Synthesis of Hydrophilic Au NPs ($\approx$5–100 nm core diameter). Since the first systematic preparation of Au NPs in aqueous media by Turkevich[34] and then by Frens,[2] significant efforts have been exerted during the past decade to fabricate monodisperse Au NPs with controlled size and shape using wet chemical methods.[35−39] In the following sections we will detail recent synthetic protocols that present improved outcomes compared to the traditional Frens method in several aspects: higher monodispersity and reaction yield of prepared Au NPs, as well as superior tunability and control over NP size and size distribution.

Citrate-capped spherical Au NPs (Cit-Au NPs) can be prepared in aqueous media by reducing gold ions using sodium citrate (SC) as reducing agent and stabilizer. Turkevich et al. and Frens were the first to prepare monodisperse Cit-Au NPs in aqueous solution in a controlled way.[2,40] However, these protocols fail to produce Au NPs with large diameters ($d_c > 50$ nm) with acceptable monodispersity. By controlling the reaction conditions (temperature, pH, stirring speed, etc.), stoichiometry of the reagents (gold salt to SC ratio), and addition of additives, recent protocols produce different sizes of Cit-Au NPs (up to 200 nm with excellent monodispersity) as reported by Bastus et al.[3] Synthetic protocols for spherical Cit-

Au NPs with core diameter of 5 nm, 13 nm, 20 nm, 25 nm, 50 nm, and 100 nm are described below.

Synthesis of Cit-Au NPs (5 nm core diameter). Cit-Au NPs with a core diameter of around 5 nm were synthesized by following the protocol reported by Piella et al.[38] Briefly, 150 mL of 2.2 mM sodium citrate (SC, 0.33 mmol, 13.2 equiv, Sigma-Aldrich, no. W302600), 0.1 mL of 2.5 mM tannic acid (TA, 0.25 μmol, 0.01 equiv, Alfa Aesar, no. A17022) (the use of traces of tannic acid helps for the growing of homogeneous seeds; as tannic acid is used at a very small concentration, the predominant capping agent is citric acid), and 1 mL of 150 mM potassium carbonate (K_2CO_3, 0.15 mmol, 6 equiv, Sigma-Aldrich, no. P5833) were placed in a 250 mL three-necked round-bottomed flask connected with a condenser to prevent the evaporation of the solvent and were heated up with a heating mantle under vigorous stirring. When the temperature reached 70 °C, 1 mL of 25 mM tetrachloroauric acid ($HAuCl_4$, 25 μmol, 1 equiv, Strem Chemicals, no. 16903-35-8) was quickly injected. The color of the solution changed quickly to purple and then to red in 2 min (see Figure 29). The solution was kept at 70 °C for 5 min more, in order to ensure a complete reduction of gold ions.

Figure 29. Synthesis of Cit-Au NPs of $\approx$5 nm in diameter. Photographs showing the reaction flask. (A) Before gold injection (note the yellow gold salt solution inside the syringe). (B) Immediately after injection of gold salt solution (the solution color changed from pale to purple in less than 10 s after the gold addition). (C) Few minutes (ca. 2 min) after injection of gold salt solution; the red color indicates the formation of the Cit-Au NPs.

The reduction of a gold salt by sodium citrate in general is described in eq 11. This equation represents all the following methodologies to obtain spherical Cit-Au NPs. A sketch of the reaction is shown in Figure 30.

$$n \cdot HAuCl_4(aq) + n \cdot (^-OCOCH_2)_2C(OH)COO^-)(aq)$$
$$\rightarrow 4n \cdot Cl^-(aq) + 4n \cdot H^+(aq) + Au^0{}_n + n$$
$$\cdot (^-OCOCH_2)_2CO(aq) + n \cdot CO_2(\uparrow) \qquad (11)$$

Synthesis of Cit-Au NPs (13 nm core diameter). Cit-Au NPs with a core diameter of $\approx$13 nm were synthesized by following the protocol reported by Schulz et al.[37] Briefly, 144 mL of Milli-Q water were placed in a 250 mL three-necked round-bottomed flask connected with a condenser and heated up until boiling (ca. 100 °C) with a heating mantle. Then, a mixture of sodium citrate (3.5 mL of 60 mM, 0.21 mmol, 8.4 equiv) and citric acid (1.5 mL of 60 mM, Acros, no. A0350656) was added and kept under vigorous stirring (450 rpm) for 30 min. Two parameters are crucial in this reaction to get a narrow
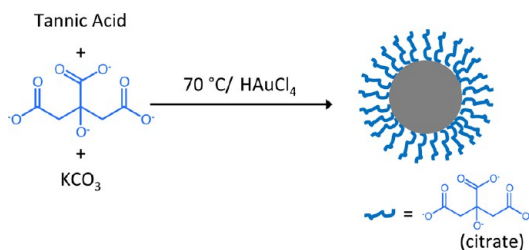
Figure 30. Schematic representation of the synthesis of 5 nm Cit-Au NPs in water.

size distribution: the final pH (which is kept constant by the addition of the buffer citrate/citric) and the heating time (30 min), in which citrate is partially oxidized. To this solution, 0.1 mL of 30 mM ethylenediaminetetraacetic acid (EDTA, 0.003 mmol, 0.12 equiv, Sigma-Aldrich, no. EDS) was injected quickly, followed by the addition of 1 mL of 25 mM hydrogen tetrachloroaurate(III) dissolved in water (0.025 mmol, 1 equiv). After ca. 60 s the color of the mixture changed from pale yellow to dull blue and then to wine-red, which is indicative of the formation of Cit-Au NPs (see Figure 31). After
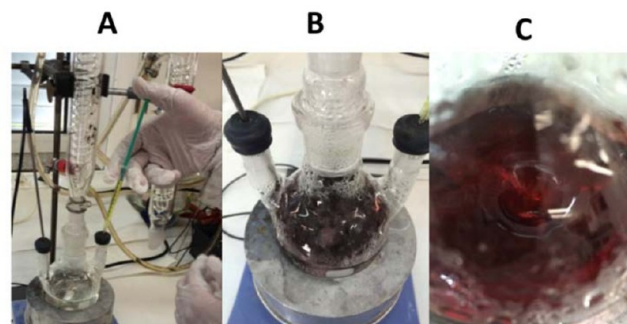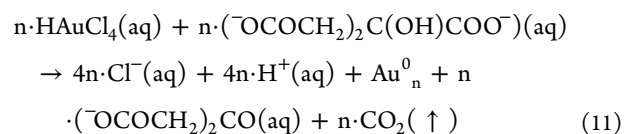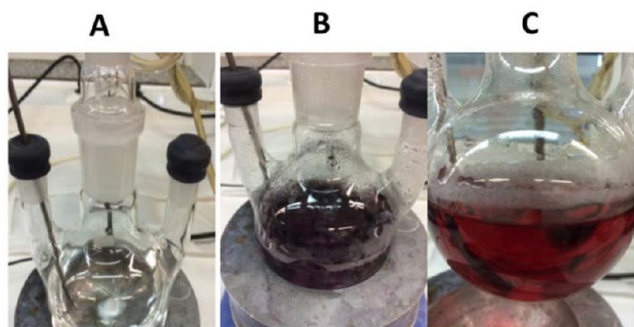

Figure 31. Synthesis of Cit-Au NPs of ≈13 nm in diameter. Photographs showing the reaction flask (A) before gold injection, (B) after injection of gold salt and EDTA solutions when the solution color changed to purple/blue, and (C) shortly (ca. 1 min) after injection, when the red color showed up, indicating the formation of Cit-Au NPs.

that, the heating was switched off (but not the stirring). When the temperature of the mixture had cooled down to 95 °C, the flask with the NP suspension was immersed in ice in order to stop the reaction. It is worth mentioning that this method allows for a fine-tuning of Cit-Au NP size by employing a seed-

mediated approach to grow larger NPs. For example, after the synthesis of Au NPs with 13 nm core diameter as described above, the NP suspension may be cooled down to 95 °C, and upon injection of 1 mL of HAuCl$_4$ (25 mM) to this seed solution in the same flask bigger NPs may be grown, similar to using 18 nm seeds, as explained in more detail later in this section.

Synthesis of Cit-Au NPs (18 nm core diameter). Spherical NPs were synthesized following a modified protocol reported by Bastus et al.[3] Briefly, 150 mL of a 1.32 mM sodium citrate solution (0.2 mmol, 8 equiv) was added to a 250 mL three-necked round-bottom flask connected with a condenser and heated up until boiling with a heating mantle under vigorous stirring. After 5 min of boiling, 1.5 mL of 25 mM tetrachloroauric acid (HAuCl$_4$, 0.025 mmol, 1 equiv) was injected. A color change was immediately observed from pale yellow to light blue and then to soft red (see Figure 32). The solution was further boiled for 10 min to allow the NPs to grow and then cooled down with stirring to RT. The resultant Cit-Au NPs had a core diameter of $d_c \approx 18$ nm.

Synthesis of Cit-Au NPs (18 < d_c < 100 nm core diameter). Cit-Au NPs (18 nm core diameter) were used as seeds to prepare larger Cit-Au NPs. After preparing 18 nm Cit-Au NPs as described above, the solution was cooled down to 90 °C, and 1 mL of 25 mM HAuCl$_4$ (0.025 mmol, 1 equiv) was injected (see Figure 33). The solution was stirred for 30 min, and this
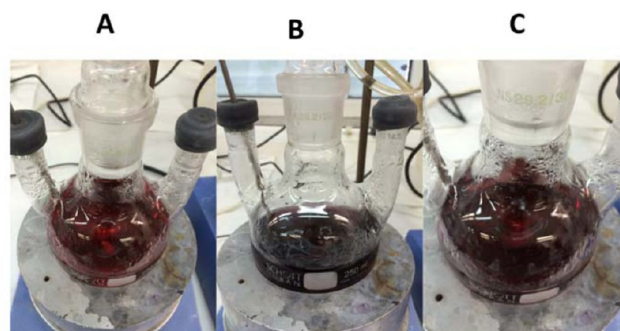
Figure 33. Synthesis of Cit-Au NPs of ≈25 nm in diameter using 18 nm seeds and the seed-mediated approach. Real photographs showing the color change at different stages: (A) 18 nm Au NPs seeds; (B) after injection of gold salt solution where the solution color changed to purple; and (C) after three injections (30 min reaction time between injections) to prepare Cit-Au NPs of 25 nm in diameter.

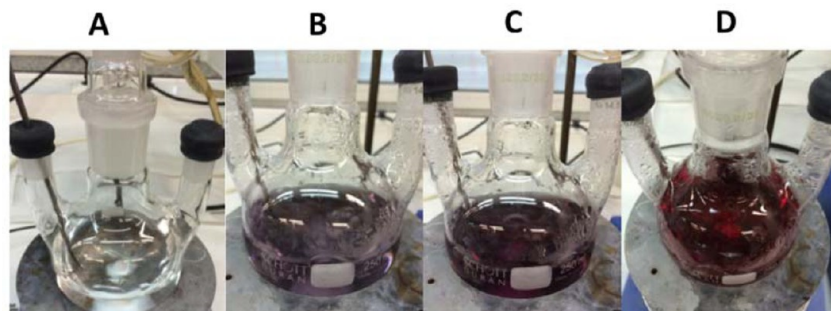**Figure 32.** Synthesis of Cit-Au NPs of ≈18 nm in diameter. Real photographs showing the color change at different stages: (A) before gold injection; (B) after injection of gold salt solution where the solution color changed to light blue and then to purple in (C), and finally to red color indicating the formation of Cit-Au NPs in (D).

process was repeated twice (total three injections of gold salt *per* growth step). Importantly, the temperature was set constant to 90 °C during the whole growing steps. Notice that the temperature is minimally affected by the addition of 1 mL into the 150 mL reaction. After that, the sample was diluted by extracting 55 mL of sample and adding 53 mL of Milli-Q water and 2 mL of 60 mM sodium citrate (0.12 mmol, 4.8 equiv), which temporarily drops the temperature, and thus, the mixture requires ca. 15 min to reach the temperature set in the heating mantle (i.e., 90 °C). Then, by three consecutive gold additions (0.025 mmol, 1 equiv, each) separated by 30 min intervals as described above, Cit-Au NPs with 25 nm were obtained. Likewise, 25 nm Cit-Au NPs were grown to 50 nm, and later they were grown to 100 nm, by using the approach described above (i.e., growing from 18 to 25 nm Cit-Au NPs; see Figure 90 for UV/vis absorption spectra of different growing steps). After the synthesis, the Cit-Au NPs can be stored for further modification in the presence of free citrate in the solution to ensure colloidal stability of Cit-Au NPs for long time periods (months).

2.3. Synthesis of Hydrophilic Ag NPs (≈15 nm core diameter). Ag NPs can be synthesized with different capping agents in aqueous solution to yield a Ag core of different sizes and shapes.[41] Citric acid has been used as the most common capping agent. Synthesizing highly monodisperse citrate-capped silver NPs (Cit-Ag NPs) has been a challenge for long time. There are plenty of synthetic routes developed to synthesize Cit-Ag NPs.[4,41−44] In this section, we briefly describe the synthesis of Cit-Ag NPs (15 nm in diameter) as developed by Bastus et al.[4] The described procedure employs tannic acid (TA) (basically its phenolic hydroxyl groups) as well as citric acid as reducing agents. The use of a small amount of tannic acid controls the size during the growth process, yielding unprecedented narrow size distributions. TA acts as both a reducing agent and a size control agent. The advantage of this method is that, by varying the concentration of TA, a wide size range of highly monodisperse Cit-Ag NPs can be synthesized.

$$Ag^+ + e^- \rightarrow Ag^0 \tag{13}$$
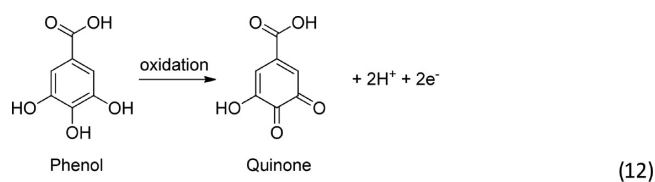
To synthesize 15 nm Cit-Ag NPs, 100 mL of aqueous solution of sodium citrate (SC) and tannic acid (TA) were taken in a three-neck round-bottom flask such that the final concentration of SC and TA are 5 mM and 0.1 mM, respectively. At this stage the solution looks colorless, as it can be seen in the photographs given in Figure 34A. The flask was heated with a heating mantle (with a magnetic stirrer), and a condenser was used to avoid the evaporation of solvent. When the solution started boiling, 1 mL of an aqueous solution of 25 mM AgNO₃ was rapidly injected into the solution. The color of the solution immediately turned to bright yellow (cf. Figure 34B), confirming the formation of NPs. After cooling down the solution, it was centrifuged at 5000 rcf for 10 min in order to precipitate the NPs. Then, the supernatant was removed and the NP precipitate was redispersed in 0.25 mM sodium citrate solution to get the purified Cit-Ag NPs.
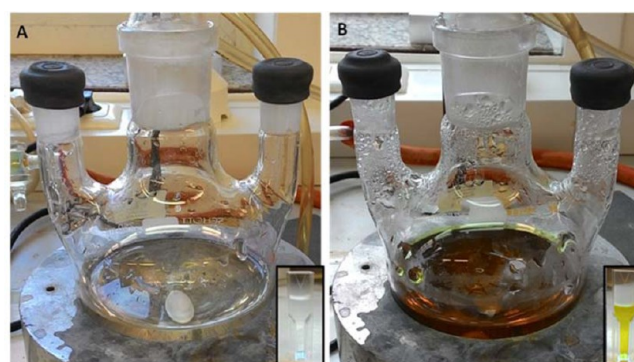

Figure 34. Synthesis of Cit-Ag NPs of ≈15 nm in core diameter. Photographs showing the solution color (A) before and (B) after injection of silver nitrate solution. Yellow solution color in B indicates the formation of Cit-Ag NPs. For more clarity, a photograph of a cuvette containing the solution is given in the inset.

2.4. Synthesis of Rod-Shaped Au NPs (variable size). Rod-shaped Au NPs (gold nanorods, Au NRs) with the longitudinal surface plasmon resonance (SPR) located at λ_{SPR} = 650, 800, 830, and 1050 nm were prepared by a seed-mediated method following previously published protocols.[35,45]

The wet-synthesis method to prepare Au NRs was pioneered by the groups of Murphy[46] and El Sayed[47] in the early 2000s. In general, a solution of small gold seeds (NPs of $d_c \approx 3-4$ nm in diameter) is synthesized in the presence of the cationic surfactant hexadecyltrimethylammonium bromide (CTAB), and silver ions. These seeds are further grown in a growth solution that contains more gold ions, silver ions, and CTAB. The gold ions in the growth solution are partially reduced to Au(I) to allow complete reduction to Au(0) only at the surface of the added seeds, in order to promote growth of Au NRs and to prevent undesired nucleation and formation of nanospheres as side product. The presence of silver ions improves the shape yield and controls the final aspect ratio (length to width ratio) of the nanorods. CTAB is the shape-directing agent that promotes the unidirectional growth and acts simultaneously as a capping agent to form CTAB-capped gold nanorods (CTAB-Au NRs).[48] The shape and size of the prepared Au nanorods can be tuned primarily by varying silver nitrate levels, but generally by controlling the reaction conditions and the level of used chemicals (cf. Table 1 and Table 2).

The traditional protocols to prepare CTAB-Au NRs indicate the use of a high concentration of CTAB (0.1 M), which is cytotoxic and thus limits the use of CTAB-Au NRs in biomedical applications.[49] Significant effort has been done to prepare CTAB-Au NRs in low-CTAB growth solution. In 2012, Murray's group proved that the presence of aromatic additives

Table 1. Synthesis of CTAB-Au NRs in the Presence of 5-Bromosalicylic Acid, with Different SPR Wavelengths λ_{SPR} As Detailed in the Text[a]

λ_{SPR} [nm]	V_{HCl_sol} [mL]	pH	V_{AgNO3_sol} [mL]	V_{AA_sol} [mL]	V_{NP_sol} [mL]
650	0	3.05	6	1	0.8
825	0	2.00	18	2	0.4

[a]V_{HCl_sol} refers to the volume of HCl, which was used to optimize the pH of the growth solution. V_{AgNO3_sol} refers to the volume of added AgNO₃ solution. V_{AA_sol} refers to the volume of added ascorbic acid solution. V_{NP_sol} refers to the volume of added NP seed solution.

Table 2. Synthesis of CTAB-Au NRs in the Presence of Sodium Oleate, with Different SPR Wavelengths λ_{SPR} Using Protocol 2 As Detailed in the Text[a]

λ_{SPR} [nm]	V_{HCl_sol} [mL]	pH	V_{AgNO3_sol} [mL]	V_{AA_sol} [mL]	V_{NP_sol} [mL]
790	2.4	1.68	18	1.25	0.4
1050	5	1.2	24	1.25	0.8

[a]V_{HCl_sol} refers to the volume of HCl, which was used to optimize the pH of the growth solution. V_{AgNO3_sol} refers to the volume of added AgNO$_3$ solution. V_{AA_sol} refers to the volume of added ascorbic acid solution. V_{NP_sol} refers to the volume of added seed NP solution.

in the growth solution reduces the required amount of CTAB to half (this procedure will be termed Protocol 1 below).[35] In 2013, the same group published a modified method in which the CTAB concentration was reduced to 0.037 M. This methodology employs a binary surfactant mixture: CTAB and sodium oleate (NaOL) (this procedure will be termed Protocol 2 below).[45]

Synthesis of the Seed Solution. A seed solution was prepared by mixing 5 mL of 0.5 mM HAuCl$_4$ (0.5 mmol, 1 equiv) with 5 mL of 0.2 M CTAB (200 mmol, 396 equiv, Sigma-Aldrich, no. H9151) in a 40 mL tube. To this solution, 0.6 mL of 0.01 M freshly prepared NaBH$_4$ (10 mmol, 19.8 eq, Sigma-Aldrich no. 71321) was added under stirring. The solution color changed immediately to brownish-yellow (cf. Figure 35). The seed solution, containing ~4 nm core diameter Au NPs capped with CTAB, was vigorously stirred at 1200 rpm for 2 min and kept at 25 °C.
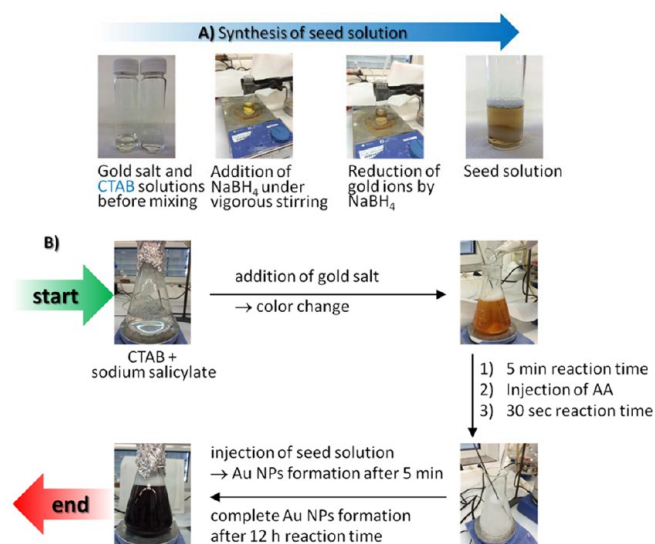

Figure 35. Photographs of steps involved in the preparation of CTAB-Au NRs, using wet chemical seed-mediated method (in the presence of sodium salicylate). (A) Preparation of CTAB-capped seeds. (B) Growth of CTAB-Au NRs.

Protocol 1: Synthesis of CTAB Capped Gold Nanorods (CTAB-Au NRs) in the Presence of 5-Bromosalicylic Acid. This protocol[35] was used to prepare CTAB-Au NRs with longitudinal surface plasmon resonance at λ_{SPR} = 650 and 825 nm. For this purpose, 9.0 g of CTAB (24.6 mmol, 98.5 equiv) and 0.8 g of sodium salicylate (5 mmol, 20 equiv, Sigma, no. S3007) in the case of λ_{SPR} = 650 nm or 1.1 g of 5-bromosalicylic acid (5 mmol, 20 equiv, Sigma, no. 461814) in

case of λ_{SPR} = 825 nm were dissolved in 250 mL of warm water (60 °C) in a 500 mL Erlenmeyer flask. The solution was allowed to cool to 30 °C, and then silver nitrate dissolved in water (AgNO$_3$, 4 mM) was added as per Table 1. The mixture was kept undisturbed at 30 °C for 15 min, after which 250 mL of aqueous 1 mM HAuCl$_4$ solution (0.25 mmol, 1 equiv) was added. After 15 min of slow stirring (400 rpm), ascorbic acid solution was added (64 mM) as per Table 1. The solution was stirred for 30 s, until it became colorless. The color change is due to the incomplete reduction of Au(III) to Au(I) by ascorbic acid. Finally, seed solution (freshly prepared as described above) was injected into the growth solution as per Table 1. The solution was mixed gently and left undisturbed overnight, to allow for a compete growth of CTAB-Au NRs. CTAB-Au NRs were collected by centrifugation, and the supernatant was discarded. The centrifuged CTAB-Au NRs pellets were finally redispersed in water.

(Protocol 2): Synthesis of CTAB Capped Gold Nanorods (CTAB-Au NRs) in the Presence of Sodium Oleate. This protocol[45] was used to prepare CTAB-Au NRs with longitudinal surface plasmon resonance at λ_{SPR} = 790 and 1050 nm. For this purpose, 7.0 g of CTAB (19.1 mmol, 76.6 equiv) and 1.234 g of sodium oleate (NaOL, 4 mmol, 16.2 equiv, Sigma-Aldrich, no. O7501) were dissolved in 250 mL of Milli-Q water at 50 °C. After dissolving the reactants, the solution was cooled down to 30 °C; then, a specific amount of AgNO$_3$ (4 mM) was added as per Table 2, and the solution was kept at 30 °C for 15 min. To this solution, 250 mL of 1 mM HAuCl$_4$ (0.25 mmol, 1 equiv) were added, and the solution color changed from dark yellow to colorless during 90 min of stirring at 700 rpm. To control the aspect ratio of Au NRs, HCl (37 wt % in water, 12.1 M, Sigma-Aldrich, no. 320331) was added to adjust the pH as per Table 2. The solution was stirred at 400 rpm for 15 min. After this, 1.25 mL of 0.064 M ascorbic acid (0.08 mmol, 0.32 equiv) was added, and the solution was vigorously stirred for 30 s. Finally, a small amount of seed solution was injected into the growth solution as per Table 1. The solution was stirred for 30 s and kept at 30 °C, without stirring overnight, to allow a compete growth of CTAB-Au NRs. Finally, the CTAB-Au NRs were collected by centrifugation, and the supernatant was discarded. The centrifuged CTAB-Au NRs pellets were redispersed in water.

2.5. Synthesis of Star-Shaped Au NPs (≈70 nm diameter, distance from tip to tip). Gold nanostars can be prepared following an unpublished modification of the protocol reported by Vo-Dihn.[50] Typically, gold nanostars are grown using spherical gold NPs as seeds and using Ag$^+$ ions as blocking facet agents. These Ag$^+$ ions promote the tip growth on the surface of the spherical NPs. The reduction of the gold salt at RT using ascorbic acid promotes the seed growth instead of independent nucleation.[20]

Briefly, in a clean glass vial, 20 mL of an aqueous solution of 0.25 mM HAuCl$_4$ (5 μmol, 1 equiv) was mixed with 0.03 mL of 1 M HCl (0.03 mmol, 6 equiv) and 1.5 mL of Au NPs of 13 nm diameter, as prepared according to the protocol given in Section 2.2. To this mixture, 0.15 mL of 1 mM AgNO$_3$ (0.15 μmol, 0.03 equiv) and 0.15 mL of 66.67 mM ascorbic acid (10 μmol, 2 equiv) were added simultaneously. After 1 min, 1 mL of an aqueous solution of 10 mg/mL α-metoxy-ω-thiol-poly(ethylene glycol (mPEG-SH; molecular weight M_w = 750 Da, 13.3 μmol, 2.67 equiv, Rapp polymer, no. 12750-40) and 0.05 mL of 2 M sodium hydroxide (NaOH, 0.1 mmol, 20 equiv, Carl Roth no. 6771.3) were added simultaneously (cf. Figure

36). After that, the solution was immersed in ice in order to stop the reaction. The NPs can be stored as prepared or purified by centrifugation (15 min, 4000 rcf).
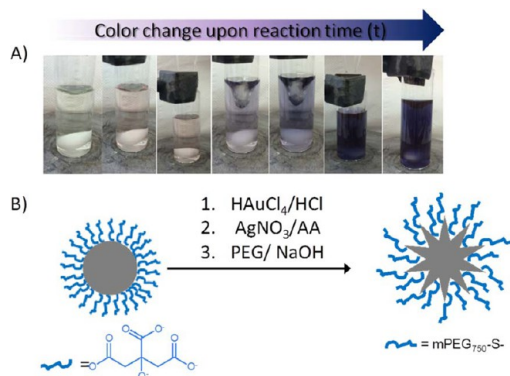

Figure 36. (A) Synthesis process of PEG-coated star-shaped Au NPs. After addition of AgNO$_3$ and AA, the solution color changed from soft red to light blue in a few seconds and then to dark blue, which is indicating the formation of gold nanostars. (B) The cartoon demonstrates the seed mediated growth of spherical gold NPs (seeds) into star-shaped Au NPs. The final surface functionalization of the resulting NPs is PEG-SH, as mediated by displacement of physically adsorbed citrate ions by chemically assembled PEG-S$^-$ molecules via the strong S−Au bond.

3. LIGAND EXCHANGE PROCEDURES FOR HYDROPHILIC NPs MAINTAINING THEIR HYDROPHILIC CHARACTER

3.1. General Considerations.
Often the original hydrophilic ligands used for the synthesis of NPs in aqueous solutions are not adequate to maintain excellent colloidal stability and/or not the ligand of choice for a desired application. The original ligands can be replaced in a ligand exchange procedure based on a superior affinity of the displacing ligand and/or concentration difference.[51] The general scheme of the ligand exchange process is depicted in Figure 37. Despite the availability of various examples in the literature, this section will describe a few selected examples.

3.2. Ligand Exchange on Citrate-Capped Au NPs with Bis(p-sulfonatophenyl)-phenylphosphine.
The citrate ions are physically adsorbed on the surface of citrate-caped Au NPs; i.e., the ligands are only weakly associated with the Au NPs' surface. For example, citrate ligands tend to desorb from the
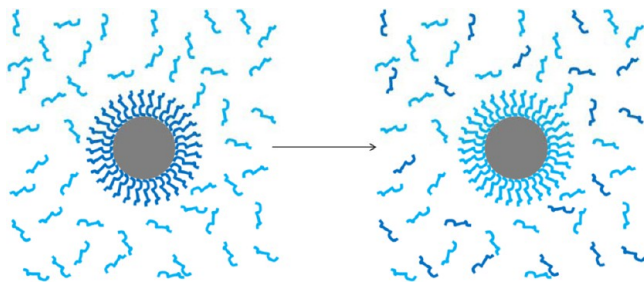

Figure 37. Ligand exchange reaction at the surface of Au NPs. After synthesis, the depicted Au NP core is capped by hydrophilic ligands (drawn in dark blue). In the case Au NPs are incubated with new ligands in excess (drawn in light blue), the new ligands can displace the original ones.

surface of Cit-Au NPs upon dialysis, dilution, or repeated centrifugation, resulting in irreversible aggregation. In other words, Cit-Au NPs are not stable for a long time and further processing/applications. There are many strategies to improve the colloidal stability of Cit-Au NPs, including exchanging citrate molecules with ligands that provide superior stability or specific functionality. Au NPs of 5 and 10 nm core diameter were used to perform the ligand exchange reaction by displacing citrate ions on the gold surface with bis(p-sulfonatophenyl)-phenylphosphine as described previously by Pellegrino et al.[52,53]

In order to perform the ligand exchange, bis(p-sulfonatophenyl)phenylphosphine dihydrate dipotassium salt (150 mg (281 μmol, 1.0 equiv; Strem Chemicals, no. 15-0463) was dissolved in 500 mL of suspension of Cit-Au NPs (d_c = 5 nm (c_{NP} = 8.3 nM) or d_c = 10 nm (c_{NP} = 9.0 nM), BBI Solutions, no. 15702 and no. 15703, or synthesized according to Section 2.2). The resulting solution was stirred at RT for 2 days, cf. Figure 38. After this, the mixture was concentrated to
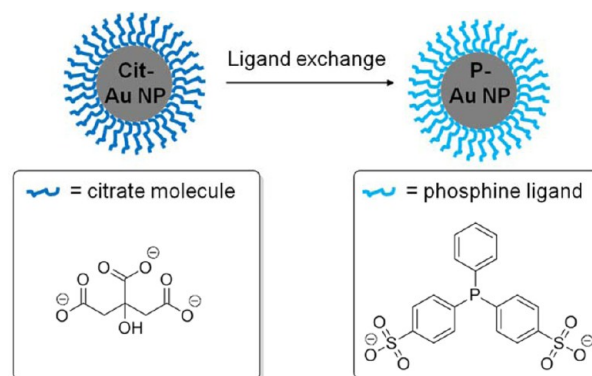
Figure 38. Scheme of the ligand exchange on Cit-Au NPs of different size with bis(p-sulfonatophenyl)-phenylphosphine. Spherical Cit-Au NPs of d_c = 5 and 10 nm core size stabilized by citrate molecules (drawn as dark blue ligands) were modified by bis(p-sulfonatophenyl)-phenylphosphine molecules (drawn as light blue ligands). The resulting P-Au NPs have improved colloidal stability.

approximately 2 mL, cf. Section 7.2. For that, the solution was centrifuged at 3000 rcf for 5 min using centrifuge filters (Merck Millipore, 100 kDa, 15 mL). Next, the concentrated Cit-Au NP suspension was diluted in phosphine solution (3 mg of bis(p-sulfonatophenyl)phenylphosphine dihydrate dipotassium salt per 10 mL of Milli-Q water) to 15 mL. Then, the solution was concentrated to 2 mL using centrifuge filters as described previously. Importantly, in order to ensure an excess of phosphine (by decreasing the amount of citrate molecules), the dilution and concentration step was repeated three times. Finally, this leads to phosphine-capped Au NPs (P-Au NPs) that are suspended in 3 mg/10 mL phosphine solution.

3.3. Ligand exchange of citrate-capped Au NPs with thiolated polyethylene glycol.
PEGylation, i.e., coating the surface of NPs with an organic shell composed of polyethylene glycol (PEG), is among the most used strategies to improve the colloidal stability of Au NPs in both polar and nonpolar solvents, due to the amphiphilic character of PEG. Moreover, PEGylation is essential for various biomedical applications as it enhances the biocompatibility of NPs and alters their in vitro cellular interaction and in vivo pharmacokinetics.[54] Usually, linear thiolated PEG polymers with molecular weight in the range of 0.75 to 10 kDa are employed to PEGylate Cit-Au

NPs.[55−57] Thiol moieties are necessary to ensure strong attachment of PEG chains to the surface of Au NPs via the strong Au−S bond forming a self-assembled monolayer of PEG on the Au NP surface. In a typical experiment, PEG-SH is dissolved in distilled water (e.g., 10 mg·mL^{-1}) and added in excess (ca. 5−15 PEG per nm^2 of NP surface A_c) to ensure full coverage of PEG on the surface of Au NPs.[56] After ca. 2 min stirring, NaOH (2 M) is added dropwise to increase the pH value to 8−9 (to deprotonate thiol groups in PEG-SH and thus increase their reactivity). Samples are stirred overnight at RT, followed by centrifugation (at least three steps) to collect the PEG-capped Au NPs (PEG-Au NPs). Notice that the centrifugal force has to be adapted to d_c (bigger colloids require less centrifugal force). For instance, for PEG-Au NPs with $d_c \approx 14$ nm, 30 min at ca. 15 000 rcf was sufficient to obtain clear supernatants and to pellet all PEG-Au NPs containing excess. Purified PEG-Au NPs can be stored (ideally at 4 °C) for extended periods of time (years) without losing their colloidal stability and preserving the initial optical properties (i.e., UV/vis absorption spectrum). Figure 39 illustrates the PEGylation method for Cit-Au NPs with thiolated PEG molecules, resulting in PEG-Au NPs.
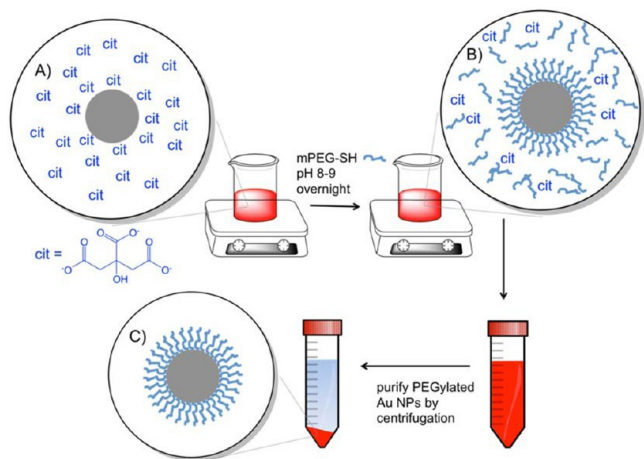

Figure 39. (A) Cit-Au NPs in solution with physically adsorbed and excess free citrate molecules. (B) Addition of mPEG-SH at basic pH to promote displacement of citrate molecules by mPEG-SH. (C) Purification by centrifugation in which PEGylated NPs are purified from free citrate molecules and mPEG-SH in the supernatant.

4. LIGAND EXCHANGE PROCEDURES TO TRANSFER HYDROPHILIC NPs FROM AQUEOUS SOLUTION TO ORGANIC SOLVENT AND THUS TO RENDER THEM HYDROPHOBIC

4.1. General Considerations.
The synthesis of Au NPs with complex shapes and/or large size is usually carried out in aqueous media. However, some applications require hydrophobic Au NPs, for example, in the cases the NPs are to be embedded into an organic matrix as in the case of molecular electronics. With this in mind, a significant effort was devoted to developing facile postsynthesis surface functionalization protocols that modify the surface of hydrophilic Au NPs with hydrophobic ligands (surface hydrophobization) (Figure 40).[58] In this section we will describe three examples in which Au NPs were typically prepared in water (Cit-Au NPs, CTAB-Au NRs, and star-shaped PEG-Au NPs as per Section 2.3), followed by
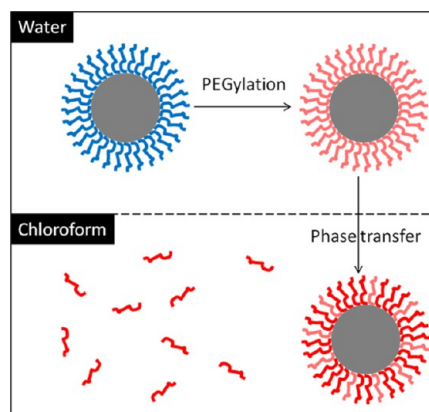
Figure 40. Hydrophobization of Au NPs via two-stage functionalization: (1) PEGylation in water (upper panel) by displacement of hydrophilic ligands (drawn in blue) by PEG-SH molecules (drawn in light red), followed by phase transfer into chloroform containing alkylamines (drawn in dark red).

surface PEGylation, which is an intermediate step prior to phase transfer of the NPs to organic solvent containing alkylamines.[57,59] We found that PEGylation is crucial to initiate phase transfer without NP aggregation due to the unique solubility of PEG in both aqueous and organic media, which provides excellent colloidal stability for NPs in both media. For more insights into the mechanism of phase transfer, the original references should be consulted as cited.

4.2. Ligand Exchange on Citrate-Capped Au NPs with PEG-SH Followed by Phase Transfer of PEG-Capped Au NPs to Chloroform Containing Dodecylamine.
Herein, a protocol to transfer Cit-Au NPs, as prepared in Section 2.2, from water to chloroform is detailed.[57] As prepared Cit-Au NPs were first coated with mPEG-SH ($M_W = 750$ Da, Rapp Polymer, no. 12750-40), as described in detail in Section 3.3, followed by purification and concentration (range of ca. $c_{NP} = 50-200$ nM in distilled water). Then, typically 1 mL of the concentrated solution of PEG-Au NPs was mixed with 5 mL of chloroform (Carl Roth, no. Y015.2) containing dodecylamine (DDA) as per Table 3. DDA was added in excess of ∼2.5 × 10^6 DDA molecules *per* NP, in order to promote partial/full exchange of PEG by DDA. This resulted in a two-phase system with the aqueous phase containing the PEGylated NPs on top and the organic phase with the DDA at the bottom (cf. Figure 41A). Both phases were mixed by magnetic stirring (ca. 800 rpm), until the NPs were transferred to the chloroform phase

Table 3. Phase Transfer of Spherical Cit-Au NPs with Various Core Diameters (d_c)^a

d_c [nm]	c_{NP} [nM]	c_{DDA} [M]	c_{PEG}/c_{NP}	c_{DDA}/c_{NP}
5	200	0.1	1 × 10^4	2.5 × 10^6
13	200	0.2	2 × 10^4	5 × 10^6
20	200	0.4	3 × 10^4	10 × 10^6
25	150	0.4	3 × 10^4	13 × 10^6
50	100	0.4	20 × 10^4	20 × 10^6
100	50	0.4	50 × 10^4	40 × 10^6

^{a}c_{NP} and c_{DDA} refer to the concentration of NPs and DDA, respectively. The ratios c_{PEG}/c_{NP} and c_{DDA}/c_{NP} describe the number of PEG and DDA molecules added per Au NP, respectively. Detailed procedure to determine Au NP concentration c_{NP} can be found in Sections 8.2 and 9.2.

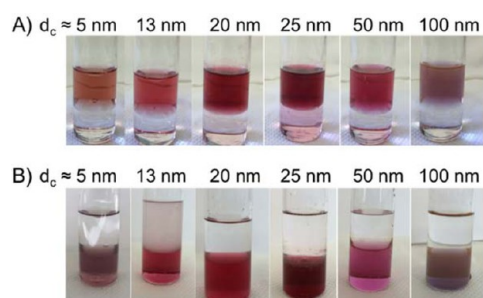**Figure 41.** Phase transfer of PEG-Au NPs from water (upper layers in all vials) to chloroform containing DDT (lower layers in all vials). (A) Photographs of biphasic system after ligand exchange of Cit-Au NPs with PEG in water. (B) Photographs of biphasic system after phase transfer of PEG-Au NPs to the chloroform layer with DDT. Different vials correspond to Au NPs with different core diameters as labeled.

Figure 42. Phase transfer of PEG-Au NRs from water (upper layers in all vials) to chloroform containing DDT (lower layers in all vials). (A) Photographs of the biphasic system after ligand exchange of CTAB-Au NRs with PEG in water. (B) Photographs of the biphasic system after phase transfer of PEG-Au NRs to the chloroform layer with DDT. Different vials correspond to Au NRs with different aspect ratios and λ_{SPR} as labeled.

(Figure 41B). The transferred Au NPs were cleaned twice by centrifugation in order to remove free DDA and PEG molecules (i.e., the supernatant was discarded, and the NP pellet was redispersed in chloroform). The same protocol can be employed to phase transfer Cit-Au NPs with various core diameters as per Table 3.

4.3. Ligand Exchange on CTAB-Capped Au NRs with PEG-SH Followed by Phase Transfer of PEG-Capped Au NPs to Chloroform Containing Dodecylamine. CTAB-Au NRs can be transfered to the chloroform phase using a similar protocol as for Cit-Au NPs as described in Section 4.2.[57] Initially, free CTAB in excess in "as prepared" CTAB-Au NRs suspensions was removed by centrifugation (5000 rcf, 30 min), and the supernatant was discarded. The resultant NP pellets were then resuspended in water, and another round of purification was performed. To the purified CTAB-Au NRs, PEG-SH (mPEG-SH, M_W = 750 Da, Rapp Polymer, no. 12750-40) was added as per Table 4 and mixed for 2 min. Then, the

Table 4. Phase Transfer of CTAB-Au NRs with Various Aspect Ratios and λ_{SPR}[a]

λ_{SPR} [nm]	c_{PEG}/c_{NR}	c_{DDA} [M]
650	3×10^4	0.4
790	8×10^4	0.4
825	8×10^4	0.4
1050	8×10^4	0.4

[a]c_{NR}, c_{PEG}, and c_{DDA} refer to the concentrations of Au NRs, PEG, and DDA, respectively. The ratio c_{PEG}/c_{NR} describes the number of PEG molecules added per Au NR. A detailed procedure to determine the Au NR concentration c_{NP} can be found in Section 8.2.

pH was adjusted to ca. 8−9 by dropwise addition of NaOH (2 M). The solution was left under stirring at RT overnight, to allow for self-assembly of PEG-SH on the Au NRs to form PEG-Au NRs. The PEG-Au NRs were then purified by centrifugation (5000 rcf, 30 min, twice). A significant decrease in ζ-potential, from 40 mV (CTAB-Au NRs) to 10 mV (PEG-Au NRs), was observed, confirming a partial ligand exchange.[57] Finally, a solution of DDA in chloroform (volume ratio 5:1 chloroform to aqueous solution of NPs) was added (cf. Table 4), leading to a two-phase system, which was stirred overnight at RT. After stirring for ca. 12 h, PEG-Au NPs transferred to the chloroform phase (Figure 42). Au NRs in chloroform were cleaned twice by centrifugation to remove free DDA and PEG molecules and were finally redispersed in chloroform. The same
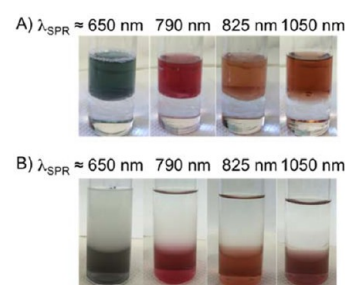
protocol can be employed to phase transfer CTAB-Au NPs with various aspect ratios as per Table 4.

4.4. Phase Transfer of Star-Shaped PEG-Capped Au NPs to Chloroform Containing Dodecylamine. The protocol in Section 2.5 describes the synthesis of star-shaped Au NPs, which are capped with PEG molecules as prepared. Thus, these NPs can be directly transferred from aqueous media to chloroform containing DDA (0.2 M), similar to the phase transfer of PEG-Au NPs and PEG-Au NRs as detailed in Section 4.2 and Section 4.3. The phase transfer is shown in Figure 43.
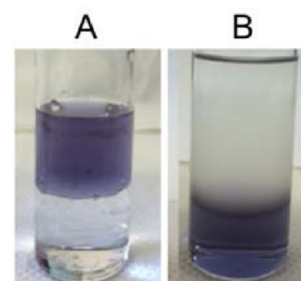
Figure 43. Phase transfer of star-shaped Au NPs from water (upper layers) to chloroform containing DDT (lower layers). Photographs of biphasic system before (A) and after (B) phase transfer from water to chloroform.

5. LIGAND EXCHANGE PROCEDURES TO TRANSFER HYDROPHOBIC NPs INTO AQUEOUS SOLUTION AND THUS TO RENDER THEM HYDROPHILIC

5.1. General Considerations. For most biological applications, dispersion of NPs in the aqueous phase is required. Thus, proper surface modification of hydrophobic NPs, which have been originally synthesized in organic solvent, is needed to allow their stable dispersion in aqueous media. Ligand exchange is a powerful approach to displace the original hydrophobic ligands by hydrophilic versions (Figure 44).[19,60] This section describes procedures to modify the surface of hydrophobic Au NPs and Ag NPs with hydrophilic ligands.

5.2. Ligand Exchange on DDT-Au NPs with 3-Mercaptopropionic Acid (MPA) or 11-Mercaptoundecanoic Acid (MUA). Here we describe the detailed procedure for synthesizing Au NPs, protected by weakly bound ligands, and
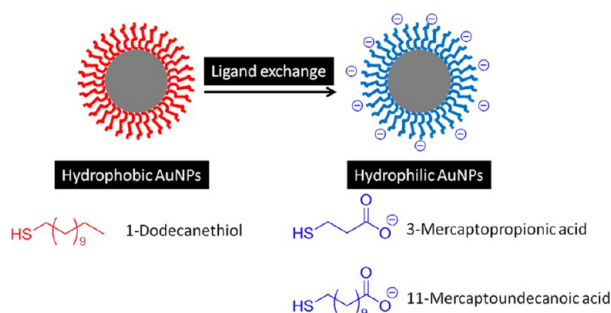
Figure 44. Ligand exchange on hydrophobic NPs (capped with hydrophobic ligands drawn in red) with hydrophilic ligands (drawn in blue). The chemical structures of 1-dodecanethiol, 3-mercaptopropionic acid, and 11-mercaptoundecanoic acid are shown.

how to perform the following ligand exchange to mercapto-carbonic acids like mercaptopropionic acid (MPA) or mercaptoundecanoic acid (MUA), which due to their mercapto-groups are strong ligands, cf. Figure 45. The protocol
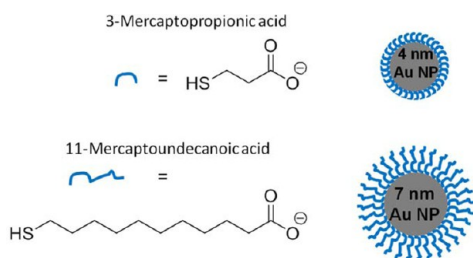
Figure 45. Sketch of the final Au NPs stabilized by MPA in case of d_c = 4 nm Au NPs and MUA in case of 7 nm Au NPs.

for synthesizing precursor Au NPs stabilized by hexanoic or decanoic acid (cf. Section 1.2), as well as the additional ligand exchange to MPA or MUA, was previously described, and we refer to the original protocols for more information.[19,61]

Ligand Exchange on DDT-Au NPs (4 nm) with Mercaptopropionic Acid. To DDT-Au NPs (d_c = 4 nm) in chloroform (as synthesized per Section 1.2) was added MPA dissolved in CH_2Cl_2 (dichloromethane) (500 μL in 2 mL), and the mixture was left to react in an ultrasonic bath for 90 min at RT to allow for ligand exchange. The MPA-Au NPs were then transferred into a 50 mL centrifuge tube, 20 mL of methanol was added, and the mixture was centrifuged at 3000 rcf for 5 min. The supernatant was removed, and the sedimented Au NPs were resuspended in 20 mL of methanol and centrifuged. The washing procedure was done four times in total. After the last washing step, the supernatant was discarded, and the Au NP pellet (at the bottom of the centrifugation tube) was dispersed in 15 mL of Milli-Q water, which led to a dark red solution. Finally, the MPA-Au NPs were washed twice using centrifuge filters (Merck Millipore, 100 kDa, 15 mL) and a speed of 3000 rcf for 5 min to get rid of free MPA (cf. Section 7.2).

Ligand Exchange on DDT-Au NPs (7 nm) with Mercaptoundecanoic Acid. To DDT-Au NPs (d_c = 7 nm) in chloroform (as synthesized per Section 1.2) was added 91 mg (417 μmol) of MUA, and the resulting mixture was first stirred at 60 °C for 30 min and then put into an ultrasonic bath at RT for another hour to allow for ligand exchange. MUA-Au NPs were precipitated by the addition of 40 mL of methanol, transferred into a centrifuge tube, and sedimented at 3000 rcf

for 10 min to collect the MUA-Au NPs. The supernatant was discarded, and the solid Au NP pellet was resuspended in another 40 mL of methanol and again centrifuged. This washing procedure was repeated 3 times, and the MUA-Au NPs were finally purified by column chromatography using a Sepharose (CL-4B) column and 25 mM aqueous sodium hydroxide as the mobile phase (cf. Section 7.3).

5.3. Phase Transfer of DDT-Ag NPs from Chloroform to Water Using 3-Mercaptopropionic Acid (MPA) or 11-Mercaptoundecanoic Acid (MUA). This protocol implies the phase transfer of DDT-Ag NPs with MPA or MUA to render Ag NPs with a hydrophilic surface and thus to resuspend them in aqueous solution with satisfactory colloidal stability (Figure 46).[62] Briefly, DDT-Ag NPs in chloroform (10 mL of
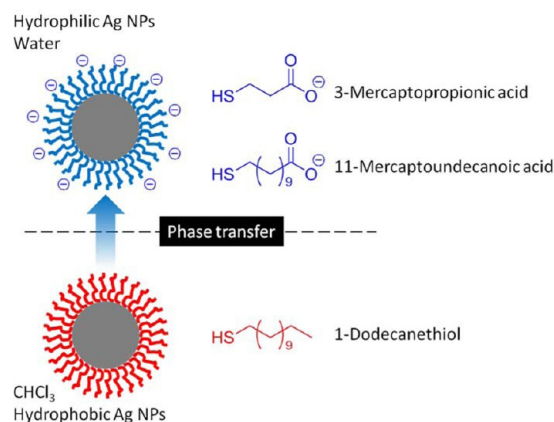
Figure 46. Phase transfer of DDT-Ag NPs from chloroform to water using 3-mercaptopropionic acid (MPA) or 11-mercaptoundecanoic acid (MUA).

0.5 mg/mL, cf. Section 1.3) were placed in a 250 mL round-bottom flask. MPA (7.3 mmol, 636 μL) or MUA (7.3 mmol, 1.59 g) was dissolved in 130 mL of Tris-Borate-EDTA (TBE) buffer (0.5×) (Sigma-Aldrich, no. T3913). In the case of MUA, the buffer mixture had to be dissolved by placing it into an ultrasonic bath for 45 min. Then aqueous buffer solution was added to the chloroform organic phase, and both phases were mixed thoroughly until a phase transfer of Ag NPs to the aqueous layer at the top of the vial was observed. The two phases were then transferred into a 40 mL glass vial and centrifuged at 900 rcf for 20 min to precipitate the excess ligands as white solid on the bottom of the vial and simultaneously to separate the two liquid layers. The aqueous phase, including the MPA-Ag NPs or MUA-Ag NPs on top of the biphasic system, was removed by a pipet and further washed three times with Milli-Q water using centrifuge filters (Merck Millipore, 100 kDa, 15 mL) at 3000 rcf for 5 min.

6. POLYMER COATING TO TRANSFER HYDROPHOBIC NPs INTO AQUEOUS SOLUTION AND THUS TO RENDER THEM HYDROPHILIC

6.1. General Considerations. This section describes the phase transfer of hydrophobic alkanethiol-capped NPs to the aqueous phase by overcoating the NPs with an amphiphilic polymer that interacts strongly with the self-assembled alkane monolayer on the NPs' surface and provides a hydrophilic character that enables efficient transfer of NPs from organic solvent to water phase (cf. Figure 47). In other words, the hydrophobic NPs are encapsulated inside the hydrophobic

cavity of the polymer micelles with independence on the type of the inorganic core material.[63,64]
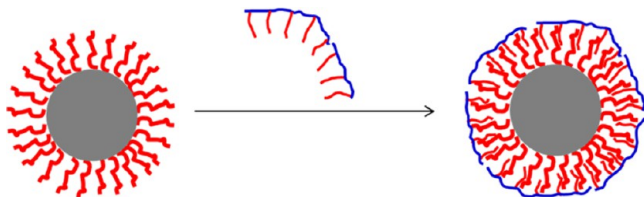
Figure 47. NP cores (drawn in gray) that are capped with hydrophobic ligands (drawn in red) are modified with an amphiphilic polymer (hydrophilic backbone drawn in blue and hydrophobic side chains drawn in red). The NP core is embedded in the resulting polymer micelle, resulting in a hydrophilic nanoparticle surface.

6.2. Synthesis of the Amphiphilic Polymer: Poly-(isobutylene-*alt*-maleic anhydride)-*graft*-dodecyl, PMA-*g*-dodecyl.

In principle, there are many potential amphiphilic polymers which can be used for polymer coating of NPs. In this section emphasis is given to an amphiphilic polymer which is based on a backbone of poly(isobutylene-*alt*-maleic anhydride), functionalized with dodecylamine, yielding dodecylamine hydrophobic side chains through formation of amide bonds upon reaction with the maleic anhydride rings (PMA). The anhydride rings that have not been reacted with dodecylamine open in contact with water, forming negatively charged carboxyl groups and, thus, providing colloidal stability to the NPs in aqueous solutions. This chemistry allows for preparation of the amphiphilic polymers with additional functionalities (e.g., by attaching organic fluorophores).[65]

The synthetic PMA has been reported in previous work.[10,66] A 250 mL round-bottom flask received 3.084 g (20 mmol expressed as monomer, cf. Figure 48) of poly(isobutylene-*alt*-maleic anhydride) (average $M_w \sim$ 6000 g/mol of whole polymer, molecular weight of one PMA monomer unit $M_{PMA} \sim$ 154 g/mol, Sigma, no. 531278). Then, 2.70 g (15 mmol) of dodecylamine (DDA, ≥ 98%, Fluka, no. 44170) was dissolved

in 100 mL of anhydrous tetrahydrofuran (THF, ≥99.9%, Aldrich, no. 186562). Note, each polymer monomer unit comprises an anhydride ring. The ratio of dodecylamine/anhydride rings was chosen in a way that $R_{chain/mon}$ = 75% (15 mmol out of 20 mmol), to allow for 75% anhydride rings coupled with dodecylamine and 25% intact anhydride rings. It is very important to use anhydrous organic solvents in order to maintain the maleic anhydride rings active during the synthesis, i.e., to prevent hydrolysis. This solution was then added to the poly(isobutylene-*alt*-maleic anhydride), and the mixture was sonicated for ca. 20 s, followed by heating to 55−60 °C for 3 h under stirring. This mixture was initially cloudy, and only after a while of heating it turned transparent. Next, the solution was concentrated to 30−40 mL by evaporation of THF under reduced pressure in a rotary evaporator, and the mixture was heated under reflux overnight. Finally, the solvent was completely evaporated under reduced pressure in a rotary evaporator, and the dried polymer powder was dissolved in V_{P_sol} = 40 mL of anhydrous chloroform (≥99%, Sigma, no. 372978), yielding a solution 0.5 M in monomer concentration, c_P. It is important to keep this polymer solution under anhydrous conditions so that the remaining maleimide rings do not yet hydrolyze.

The final molar mass of one polymer unit M_P comprises the molar mass M_{PMA} of one PMA monomer and the molar mass M_{DDA} = 185 g/mol of one DDA side chain times the number of side chains per monomer; see eq 14.

$$M_P = M_{PMA} + R_{chain/mon} \times M_{DDA} \qquad (14)$$

For $R_{chain/mon}$ = 0.75, the value of M_P = 154 g/mol + 0.75 × 185 g/mol ≈ 293 g/mol is obtained.

During the polymer synthesis molecules that are soluble in THF and which bear a −NH$_2$ group can be integrated into the polymer. This can be done by adding those amine-containing molecules (like dyes or spacer molecules like polyethylene glycol) together with the dodecylamine to the PMA. By this $R_{chain/mon}$ = 75% of the anhydride rings will react with the NH$_2$ group of the dodecylamine, as described above, and some of the
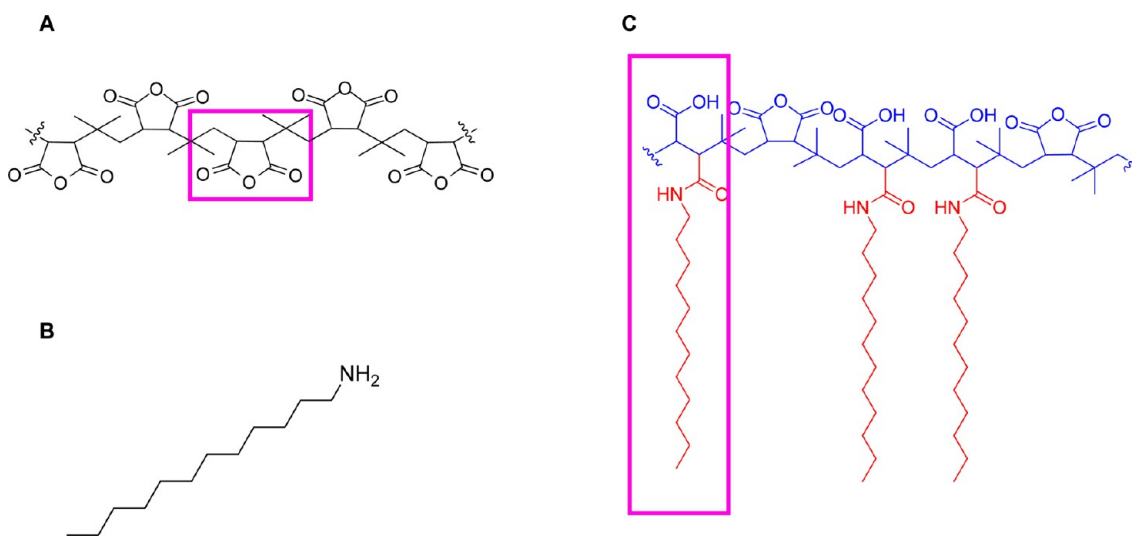
Figure 48. Synthesis of poly(isobutylene-*alt*-maleic anhydride)-*graft*-dodecyl, PMA-*g*-dodecyl. (A) Poly(isobutylene-*alt*-maleic anhydride) is used as hydrophilic backbone (the purple box shows one monomer unit). (B) Dodecylamine is used as hydrophobic side chain. The amphiphilic polymer was obtained by reaction of the hydrophilic backbone with hydrophobic side chains. (C) Structure of the amphiphilic polymer (PMA-*g*-dodecyl). The purple box in C shows a monomer unit with attached side chain (of molar mass M_P). The hydrophobic and hydrophilic parts are drawn in red and blue, respectively.

remaining PMA monomers with the additional functional molecules. Typically not more than $R_{func/mon}$ = 5% of the anhydride rings should be modified with functional molecules, as otherwise the polymer coating procedure as described in Section 6.3 may no longer work. A list with modified polymers that has been reported in literature is provided in Section 6.3.

6.3. Phase Transfer of Alkanethiol-Capped NPs from Chloroform to Water Using PMA-*g*-dodecyl Polymer.

DDT-Au NPs in chloroform were mixed with PMA-*g*-dodecyl dissolved in chloroform. The mixture was stirred manually for 5 min at RT, and then the solvent (i.e., chloroform) was completely evaporated in a rotary evaporator under heating at 40 °C to force the polymer to wrap around the NPs, as illustrated in Figure 49. A few milliliters of anhydrous
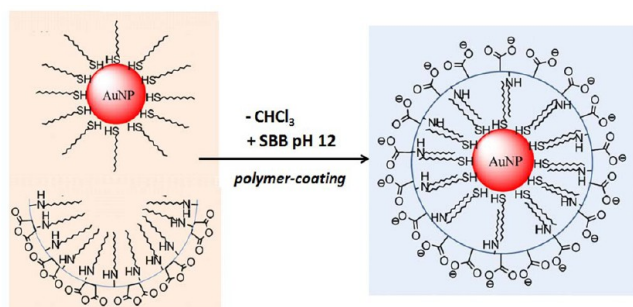
Figure 49. Phase transfer of DDT-Au NPs from chloroform (left) to water (right) using PMA-*g*-dodecyl polymer.

chloroform were added to the flask to reconstitute the solid film, and again the solvent was removed under reduced pressure. This step was carried out 3 times in order to obtain a homogeneous coating. After the last step, the remaining solid film in the flask film was reconstituted in alkaline sodium borate buffer (50 mM, pH 12 adjusted with NaOH) under vigorous stirring until the solution turned clear, cf. Figure 50. Sonication
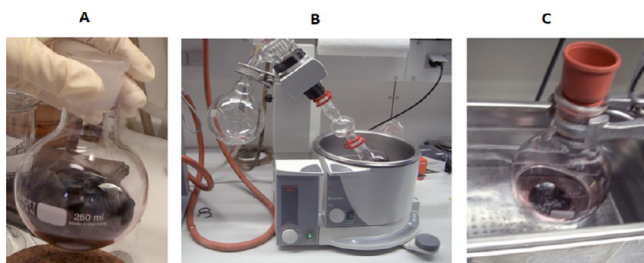
Figure 50. Phase transfer of DDT-Au NPs (d_c = 4.2 nm) from chloroform to water using PMA-*g*-dodecyl polymer. Photographs of (A) DDT-Au NPs in chloroform after addition of the polymer solution dissolved in chloroform, (B) chloroform evaporated using a rotary evaporator, and (C) sonication after the addition of sodium borate buffer (pH 12).

can be optionally used to facilitate the dispersion. In the last step, the remaining anhydride rings get hydrolyzed in alkaline conditions resulting in carboxylate groups that allow reconstitution in water with excellent colloidal stability. This approach can be employed to transfer various types of NPs with different sizes from water to chloroform as per Table 5.

A key point in this procedure is the calculation of the amount of polymer N_P (in terms of monomer units), which needs to be added to the NPs. The amount of polymer per NP scales with the effective surface area A_{eff} of one NP and with the amount of

NPs. In the case of spherical NPs A_{eff} is given as the surface of a sphere (cf. Figure 1):

$$A_{eff} = 4\pi \times \left(\frac{d_{eff}}{2}\right)^2 = \pi \times d_{eff}{}^2 \tag{15}$$

Nanorods were considered as cylinders with diameter d_{eff} and length L_{eff} to simplify the calculations (cf. Figure 2), and thus the effective surface of one rod-shaped NP becomes

$$A_{eff} = 2\pi \times \left(\frac{d_{eff}}{2}\right) \times L_{eff} = \pi \times d_{eff} \times L_{eff} \tag{16}$$

In a solution with volume V_{NP_sol} and NP concentration c_{NP} the number of moles of NPs is $n_{NP} = c_{NP} \cdot V_{NP\_sol}$; i.e., the total number of NPs $N_{NP} = n_{NP} \times N_A$ (N_A = Avogadro's number). The total effective surface area of all NPs in solution thus is

$$A_{total\_eff} = N_{NP} \times A_{eff} = c_{NP} \times V_{NP\_sol} \times N_A \times A_{eff} \tag{17}$$

The number of monomer units that needs to be added per nm² of effective surface area ($R_{P/Area}$) is an important value that should be determined experimentally for any polymer coating protocol, as it may depend on the core material, core diameter, surface capping, etc. of the NPs. The number of polymer monomers N_P that needs to be added to the NP suspension thus is

$$N_P = R_{P/Area} \times A_{total\_eff} \tag{18}$$

For a polymer stock solution of monomer concentration c_P, the volume V_{P_sol} needs to be added to the NP suspension.

$$
\begin{aligned}
V_{P\_sol} &= \frac{n_P}{c_P} = \frac{N_P/N_A}{c_P} = \frac{R_{P/Area} \times A_{total\ eff}}{N_A \times c_P} \\
&= \frac{R_{P/Area} \times A_{eff} \times c_{NP} \times V_{NP\_sol}}{c_P}
\end{aligned}
\tag{19}
$$

The polymer coating procedure should be carried out in sufficiently diluted NP suspension. In the case of NPs with $d_c <$ 10 nm we typically use a NP concentration of around c_{NP} = 1 μM. In case of bigger NPs, lower NP concentrations should be used.

To give an example of the above calculation: A batch of hydrophobic Au NPs synthesized according to Section 1.2 have a core diameter of d_c = 4.2 nm, and a ligand length of dodecanethiol of l_{ligand} = 1 nm was assumed. The Au NPs were suspended at a concentration of c_{NP} = 1 μM in a volume of V_{NP_sol} = 7.1 mL. For the polymer coating procedure the amount of polymer added per effective NP surface was chosen as $R_{P/Area}$ = 100 nm^{-2}. The polymer was dissolved in a stock solution with monomer concentration c_P = 0.05 M. In this way with the help of eq 1, eq 15, and eq 19 the amount V_{P_sol} of polymer solution, which needs to be added to the NP suspension of volume V_{NP}, can be calculated:

$$d_{eff} = d_c + 2 \times l_{ligand} = 4.2 \text{ nm} + (2 \times 1 \text{ nm}) = 6.2 \text{ nm}$$

$$A_{eff} = \pi \times d_{eff}{}^2 = \pi \times (6.2 \text{ nm})^2 = 121 \text{ nm}^2$$

$$
\begin{aligned}
V_{P\_sol} &= (R_{P/Area} \times A_{eff} \times c_{NP} \times V_{NP\_sol})/c_P \\
&= (100 \text{ nm}^{-2} \times 121 \text{ nm}^2 \times 1 \text{ }\mu\text{M} \times 7.1 \times \text{mL}) \\
& /0.05 \text{ M} = 1.7 \text{ nm}
\end{aligned}
$$

Table 5. List of Parameters Used To Overcoat Various NPs with PMA-*g*-dodecyl Polymer[a]

NP material	shape	d_c [nm]	L_c [nm]	l_{ligand} [nm]	synthesis described in section	$R_{chain/mon}$	$R_{P/Area}$ [nm^{-2}]	ref
Au	sphere	4.2	-	1.0	1.2	75%	100	10
Au	sphere	25	-	1.0	2.2, 4.2	75%	3000	57
Au	sphere	50	-	1.0	2.2, 4.2	75%	3000	57
Au	sphere	50	-	1.0	2.2, 4.2	75%	3000	57
Au	sphere	100	-	1.0	2.2, 4.2	75%	4000	-
Au	rod	15	40	1.0	2.4, 4.3	75%	3000	-
Au	rod	15	63	1.0	2.4, 4.3	75%	3000	57
Au	rod	30	100	1.0	2.4, 4.3	75%	3000	-
Au	rod	12	83	1.0	2.4, 4.3	75%	3000	57
Ag	sphere	4.2		1.0	1.3	75%	100	62
FePt	sphere	4	-	1.0	1.4	75%	100	67
Fe$_3$O$_4$	sphere	4	-	1.0	1.5	75%	100	-
CdSe/ZnS	sphere	2−10		1.2	1.7	75%	100	64, 68

[a]In some of the examples[57] the original NPs were not capped with hydrophobic ligands and thus were capped with DDT previous to the polymer coating procedure.

A list of polymer coating conditions for a variety of NP materials is given in Table 5. Parameters for NPs coated with functionalized polymers are listed in Table 6 and Table 7.

7. PURIFICATION OF HYDROPHILIC NPs

7.1. General Considerations. Generally, NPs should be purified from excess of free reactants, byproducts, and ligand molecules in the solution. The selection of a purification technique for a NP solution depends on many variables such as colloidal stability of NPs during purification, efficiency of the purification process, the desired purity level, size and nature of molecules/ligands to be removed, and availability of the respective purification techniques. Unfortunately, there is no universal purification tool for any generic NP solution, but indeed proper purification techniques should be carefully selected for each reaction, to ensure efficient separation between NPs (products) and free excess reactants (impurities). Purification, on the other hand, also may change the properties of the NPs, e.g., modify their ligand shell.[18]

As an xample, the polymer coating procedure in Section 6.3 employs excess polymer in the reaction, which must be removed afterward (post-synthesis purification). It is worth mentioning that avoiding excess addition of polymer may result in incomplete coating and thus induce NP aggregation. The free residual polymer in aqueous solution forms polymeric micelles, with a hydrophobic cavity and a hydrophilic surface, cf. Figure 51.[100] They are stable assemblies of several polymer molecules, in which the hydrophobic tails point toward the inside of the micelle, and the hydrophilic backbones are exposed to the outside. Thus, they can be thought of as "empty" polymer shells without embedded inorganic NPs. The polymer micelles have the size of a few nanometers, and thus it is hard to be separated from NPs with similar size using size exclusion chromatography. However, efficient separation could be achieved by other separation methods such as gel electrophoresis and ultracentrifugation (cf. Section 7.5).

Purification is paramount for many applications. In case of cytotoxicity studies it is required to ensure that any effect is related to the NPs and not to residuals in solution. Also, for quantitative labeling, empty micelles will compete with polymer coated NPs for binding to the same target; however, without any label (i.e., the NP core) inside and, thus, without being detected. Note that polymeric micelles are hard to detect, as the amphiphilic polymer itself does not have any specific absorption of light and also is not fluorescent. In case the polymer has been modified with organic fluorophores, these micelles can be detected by their fluorescence.[100] In addition negative staining of the polymer allows for visualizing empty polymer micelles with transmission electron microscopy, cf. Section 7.5.

7.2. Filtration, Ultrafiltration, and Dialysis. The synthesis of NP synthesis in many occasions is associated with the formation of large aggregates/agglomerates due to NP aggregation, which can be removed from solution by simple filtration via a syringe membrane filter (0.22 μm pore size, Carl Roth, no. KY62.1) as per Figure 52. In case the NP solution does not pass easily through the filter, addition of water to the NP solution, i.e., dilution, may help.

Ultrafiltration can be employed to purify and to concentrate NPs. Ultrafiltration also allows for exchange of the suspending media, for example, from buffer to water or vice versa. Briefly, NP suspension is placed in the centrifuge filter (available from various suppliers, e.g., Vivaspin 20 from Sartorius or Amicon Ultra 4 mL Centrifugal Filters), with typically 100 000 Da molecular weight cutoff (MWCO). The pores of the filter are big enough to be passed through by small molecules but retain the NPs. Upon centrifugation the filtrate that contains free ligands/reactants is collected in the outer vial below the filter membrane, and the NP suspension is concentrated in the inner vial. Fresh solvent can be added to the NP concentrate, and the filtration can be repeated for several rounds of clean up as required (Figure 53 and Figure 54). Note that excessive purification/concentration may induce NPs aggregation, which can also block the filter.

Dialysis is a widely used method to purify NP suspensions from free impurities. The method is described in Figure 55. The NP suspension is put in a semipermeable membrane dialysis bag with defined pore size and molecular weight cutoff (MWCO), which then is placed in a beaker filled with a large volume of fresh buffer/solvent. Molecules smaller than the MWCO can penetrate the membrane and diffuse out from the dialysis bag to the bulk solution in the beaker. Dialysis is driven by the concentration gradient between the dialysis bag and the concentration in the beaker. Thus, the process occurs until equilibrium is achieved. At this point, the bath needs to be replaced with fresh solvent. Dialysis is easy to perform and in fact is a "gentle" treatment for the NPs, since no mechanical stress is placed on NPs (the case of centrifugation as an

Table 6. List of Parameters Used for Overcoating Various NPs with PMA-*g*-dodecyl or Functionalized PMA-*g*-dodecyl Polymers[a]

NP core material	shape	d_c [nm]	L_c [nm]	l_{ligand} [nm]	$R_{chain/mon}$	$R_{cross/mon}$	$R_{func/mon}$	added functionality	$R_{P/Area}$ [nm^{-2}]	d_h [nm]	ζ [mV]	ref
Au	sphere	2.36 ± 0.48	-	1.0	75%	0	0	-	200	-	-	61
Au	sphere	3.2 ± 0.5	-	-	75%	0	0	-	100–200	13.9	-	66
Au	sphere	3.2 ± 0.5	-	-	100%	0	0	-	100–200	-	-	66
Au	sphere	3.2 ± 0.5	-	-	100%	0	0	-	100–200	-	-	66
Au	sphere	3.2 ± 0.5	-	-	100%	0	0	-	100–200	-	-	66
Au	sphere	3.2 ± 0.5	-	-	100%	0	0	-	100–200	11.4	-	66
Au	sphere	3.8	-	1.2	75%	0	0	-	200	9.0	−45	69
Au	sphere	4.0	-	1.0	100%	7%	0	-	147, 295	-	-	64
Au	sphere	4.0	-	1.0	100%	8%	0	-	310	-	-	64
Au	sphere	4.0	-	1.0	100%	10%	0	-	92, 100	-	-	64
Au	sphere	4.0	-	1.0	100%	10%	0	-	92, 100	-	-	70
Au	sphere	4.0	-	-	100%	10%	0	-	100	-	-	17
Au	sphere	4.0	-	-	100%	10%	0	-	100	-	-	17
Au	sphere	4.0	-	1.0	75%	0	0	-	100	-	-	10
Au	sphere	4.0	-	1.0	75%	0	1%	Fluoresceinamine	100	-	-	10
Au	sphere	4.0	-	1.0	75%	0	4%	Galactose	100	-	-	10
Au	sphere	4.0	-	1.0	75%	0	4%	Biotin	100	-	-	10
Au	sphere	4.0	-	-	75%	0	2%	Amino-MQAE + CV	50–100	9.6 ± 0.6	-	71
Au	sphere	4.0	-	-	75%	0	2%	NH$_2$-PEG-Amino-MQAE + CV	50–100	10.6 ± 0.6	-	71
Au	sphere	4.0	-	-	75%	0	2%	NH$_2$-PEG-Amino-MQAE + CV	50–100	11.0 ± 0.6	-	71
Au	sphere	4.0	-	-	75%	0	2%	NH$_2$-PEG-Amino-MQAE + CV	50–100	13.2 ± 0.6	-	71
Au	sphere	4.0	-	-	75%	0	-	NH$_2$-PEG-NH-SNARF	100	-	-	72
Au	sphere	4.0	-	1.0	75%	0	4%	Cresyl violet	100	-	-	73
Au	sphere	4.0	-	1.2	75%	0	0	-	100	13.2	-	74
Au	sphere	4.0	-	1.2	75%	0	0	-	100	24.6	-	74
Au	sphere	4.0	-	1.6	75%	0	0	-	100	13.9 ± 1.2	−27.6 ± 5.6	75
Au	sphere	4.0	-	-	75%	0	0	-	100	26.8	−61.1	76
^{198}Au (neutron irradiated)	sphere	4.2 ± 0.5	-	1.1	75%	0	2%	ATTO590	100	-	-	65
^{198}Au (neutron irradiated)	sphere	4.2 ± 0.5	-	1.1	75%	0	3%	ABz-DOTA + Gd^{3+}	100	-	-	65
^{198}Au (neutron irradiated)	sphere	4.2 ± 0.5	-	1.1	75%	0	3%	ABz-DOTA +^{111}In^{3+}	100	-	-	65
Au	sphere	4.4 ± 0.6	-	-	75%	0	0	-	100	-	-	77
Au	sphere	4.4 ± 1.1	-	1.2	75%	0	1%	Dy647	200	11.7	−38	78
Au	sphere	4.4 ± 0.6	-	1.2	75%	0	2%	ATTO633	100	-	-	79
Au	sphere	4.6	-	3.25	100%	10%	0	Crystal Violet	100	11.7	-	80
Au	sphere	4.6	-	6.9	100%	10%	0	-	100	-	-	80
Au	sphere	4.6	-	9.95	100%	10%	0	-	100	-	-	80
Au	sphere	4.6	-	12.65	100%	10%	0	-	100	-	-	80
Au	sphere	4.6	-	8.5	100%	10%	0	-	100	-	-	80
Au	sphere	4.6	-	12.35	100%	10%	0	-	100	-	-	80
Au	sphere	4.6	-	11.55	100%	10%	0	-	100	-	-	80
Au	sphere	4.6	-	17.8	100%	10%	0	-	100	-	-	80
Au	sphere	4.6	-	3.95	100%	10%	0	-	100	13.5	-	80

Table 6. continued

NP core material	shape	d_c [nm]	L_c [nm]	l_{ligand} [nm]	$R_{chain/mon}$	$R_{cross/mon}$	$R_{func/mon}$	added functionality	$R_{P/Area}$ [nm^{-2}]	d_h [nm]	ζ [mV]	ref
Au	sphere	4.6	-	5.95	100%	10%	0	-	100	15.6	-	80
Au	sphere	4.6	-	8.2	100%	10%	0	-	100	17.9	-	80
Au	sphere	4.6	-	12.1	100%	10%	0	-	100	18.5	-	80
Au	sphere	4.6	-	15.1	100%	10%	0	-	100	18.6	-	80
Au	sphere	4.6	-	2.2	100%	10%	-	-	100	-	-	81
Au	sphere	4.6	-	1.0	75%	0	-	-	100	-	-	82
Au	sphere	4.6 ± 1.1	-	1.6	75%	0	-	-	50	12.6 ± 1.1	−31.9 ± 5.2	83
Au	sphere	4.6 ± 1.0	-	1.0	75%	0	-	-	100	19 ± 1	−(55 ± 6)	84
Au	sphere	4.6 ± 1.0	-	1.0	75%	0	2%	Cresyl violet + PEG	100	40 ± 5	−(10 ± 5)	84
Au	sphere	4.6 ± 1.0	-	1.0	75%	0	2%	Cresyl violet + PEG-CPP1	100	60 ± 7	−(11 ± 5)	84
Au	sphere	4.6 ± 1.0	-	1.0	75%	0	2%	Cresyl violet + PEG-CPP2	100	35 ± 5	−(13 ± 4)	84
Au	sphere	4.7 ± 0.8	-	-	75%	0	0	-	-	-	-	85
Au	sphere	4.8 ± 0.7	-	1.2	75%	0	2%	ATTO590	50	-	-	86
Au	sphere	4.8 ± 0.9	-	1.2	75%	0	3%	ABz-DOTA	100	13.0 ± 0.8	−46 ± 16	87
Au	sphere	5	-	-	100%	0	0	-	-	21 ± 3	−(19.1 ± 0.4)	54
Au	sphere	5	-	-	100%	0	0	-	-	31.0 ± 0.2	−(10.1 ± 0.6)	54
Au	sphere	5	-	1	75%	0	0	-	100	24.2 ± 2.6	−42.7 ± 2.3	88
Au	sphere	6.0	-	-	75%	0	0	-	100	-	-	10
Au	sphere	6.89 ± 1.25	-	1.0	75%	0	0	-	600	-	-	61
Au	rod	11 ± 2	77.3 ± 12.8	-	75%	0	0	-	3000	29.6 ± 0.5	−(33.5 ± 0.3)	57
Au	sphere	12.6	-	1.2	75%	0	1%	ATTO-590	400	20.9 ± 1.2	-	89
Au	sphere	24 ± 3	-	-	75%	0	0	-	3000	27.0 ± 0.2	−(25.7 ± 0.5)	57
Au	rod	24 ± 5	92.3 ± 14.8	-	75%	0	0	-	3000	9.0 ± 0.2	−(29.2 ± 0.4)	57
Au	sphere	50 ± 7	-	-	75%	0	0	-	3000	43 ± 1	−(34 ± 2)	57
Au	sphere	60 ± 8	-	-	75%	0	0	-	3000	47 ± 1	−(28.4 ± 0.3)	57
Au	star	-	-	-	75%	0	2%	Tamra	150	-	-	90
Ag	sphere	3.8	-	1.2	75%	0	0	-	200	8.9	−35	69
Ag	sphere	4.2 ± 0.4	-	1.0	75%	0	0	-	100	12 ± 3	−(31 ± 1)	62
Ag	sphere	4.2 ± 0.4	-	1.0	75%	0	0	-	100	13 ± 4	−(41 ± 1)	62
Ag	sphere	4.2 ± 0.4	-	1.0	75%	0	0	-	100	12 ± 3	−(10.9 ± 0.4)	62
Ag	sphere	4.2	-	-	75%	0	0	-	-	12 ± 2.7	−31 ± 1.3	91
CdSe	sphere	2.6	-	1.2	75%	0	0.1−5%	ATTO590	50	-	-	92
CdSe	sphere	4.7	-	-	100%	10%	0	-	100	-	-	80
CdSe (Q dot 705 ITK)	sphere	9.4 ± 0.7	-	-	75%	0	4%	EuC + PEG-Cy5-biotin	130	-	-	93
CdSe (Q dot 655 ITK)	sphere	9.6 ± 0.6	-	-	75%	0	4%	EuC + PEG-Cy5-biotin	125	-	-	93
CdSe/ZnS	sphere	-	-	-	100%	10%	0	-	-	5.5 ± 1.3	-	94
CdSe/ZnS	sphere	-	-	-	100%	10%	0	-	-	10.8 ± 1.4	-	94
CdSe/ZnS (Evindent QD490)	sphere	-	-	-	100%	0	0	-	100−200	16.9	-	66
CdSe/ZnS (Evident QD610)	sphere	-	-	-	100%	0	0	-	100−200	23.6	-	66
CdSe/ZnS	sphere	-	-	-	75%	0	0	-	-	-	-	85
CdSe/ZnS	sphere	-	-	-	75%	0	0	-	-	-	-	85
CdSe/ZnS	sphere	2.1	-	1.2	75%	0	2%	ATTO590	100	-	-	86
CdSe/ZnS	sphere	2.35	-	1.7	75%	0	0	-	100	-	-	10

Table 6. continued

NP core material	shape	d_c [nm]	L_c [nm]	l_{ligand} [nm]	$R_{chain/mon}$	$R_{cross/mon}$	$R_{func/mon}$	added functionality	$R_{P/Area}$ [nm^{-2}]	d_h [nm]	ζ [mV]	ref
CdSe/ZnS	sphere	2.56	-	-	75%	0	2%	ATTO590	100	-	-	65
CdSe/ZnS	sphere	2.56	-	-	75%	0	3%	ABz-DOTA + Gd^{3+}	100	-	-	65
CdSe/ZnS	sphere	2.56	-	-	75%	0	3%	ABz-DOTA + ^{111}In^{3+}	100	-	-	65
CdSe/ZnS	sphere	2.7 ± 0.4	-	1.2	75%	0	2 to 0.06%	ATTO590	100	-	-	68
CdSe/ZnS	sphere	2.8	-	1.1	75%	0	0.1–5%	ATTO590	50	-	-	92
CdSe/ZnS	sphere	2.9 ± 0.3	-	1	75%	0	0	-	500	16.5 ± 0.3	−18.1 ± 0.4	95
CdSe/ZnS (Evidot 490)	sphere	3.2	-	-	75%	0	0	-		10	-	96
CdSe/ZnS (Evidot 520)	sphere	3.3	-	-	75%	0	0	-		12	-	96
CdSe/ZnS (Evidot 540)	sphere	3.4	-	-	75%	0	0	-		12.4	-	96
CdSe/ZnS	sphere	4.2	-	1.0	100%	10%	0	-		-	-	97
CdSe/ZnS	sphere	4.4	-	1.0	100%	10%	0	-		-	-	97
CdSe/ZnS (Evidot 580)	sphere	4.4	-	-	75%	0	0	-		13.4	-	96
CdSe/ZnS	sphere	4.6 ± 0.9	-	1.2	75%	0	0	-	100	11.9 ± 5.6	−29.0 ± 5.6	98
CdSe	sphere	4.7	-	-	100%	10%	0	-	100	-	-	80
CdSe/ZnS	sphere	4.7 ± 0.9	-	-	75%	0	0	-	100	11.4 ± 3.2	18.3 ± 1.4	99
CdSe/ZnS	sphere	4.7 ± 1	-	1.1	75%	0	2%	Dy495	70	-	−28 ± 4	87
CdSe/ZnS	sphere	4.7 ± 1	-	1.1	75%	0	2%	Dy636	70	-	−33 ± 3	87
CdSe/ZnS	sphere	5.3	-	7.6	100%	10%	0	-	100	13.3	-	80
CdSe/ZnS	sphere	5.3	-	8.75	100%	10%	0	-	100	-	-	80
CdSe/ZnS	sphere	5.3	-	9.55	100%	10%	0	-	100	-	-	80
CdSe/ZnS	sphere	5.3	-	10.3	100%	10%	0	-	100	-	-	80
CdSe/ZnS	sphere	5.3	-	13.75	100%	10%	0	-	100	-	-	80
CdSe/ZnS	sphere	5.3	-	10.25	100%	10%	0	-	100	-	-	80
CdSe/ZnS	sphere	5.3	-	10.65	100%	10%	0	-	100	-	-	80
CdSe/ZnS	sphere	5.3	-	10.5	100%	10%	0	-	100	-	-	80
CdSe/ZnS	sphere	5.3	-	11.95	100%	10%	0	-	100	-	-	80
CdSe/ZnS	sphere	5.3	-	10.05	100%	10%	0	-	100	16.8	-	80
CdSe/ZnS	sphere	5.3	-	10.15	100%	10%	0	-	100	17.7	-	80
CdSe/ZnS	sphere	5.3	-	11.15	100%	10%	0	-	100	18	-	80
CdSe/ZnS	sphere	5.3	-	12.45	100%	10%	0	-	100	18.2	-	80
CdSe/ZnS	sphere	5.3	-	14.45	100%	10%	0	-	100	18.4	-	80
CdSe/ZnS	sphere	5.3	-	-	75%	5%	1%	ATTO590	70	-	-	100
CdSe/ZnS	sphere	5.3	-	-	75%	5%	0	-	70	-	-	100
CdSe/ZnS	sphere	5.3	-	-	75%	0	5%	ATTO590	70	-	-	73
CdSe/ZnS	sphere	5.6	-	1.0	100%	10%	0	-	-	-	-	97
CdSe/ZnS	sphere	6.2 ± 0.3	-	1	75%	0	0	-	500	21.7 ± 0.4	−20.4 ± 1.4	95
CdSe/ZnS	sphere	6.4	-	1.0	100%	10%	0	-	-	19 ± 2	-	97
CdSe/ZnS	sphere	7.0	-	1.0	100%	6%	0	-	10, 15; 20, 60	24 ± 2	-	64
CdSe/ZnS	sphere	7.0	-	1.0	100%	10%	0	-	100	19 ± 2	-	64
CdSe/ZnS	sphere	7.0	-	1.0	100%	10%	0	-	100	24 ± 2	-	70

Table 6. continued

NP core material	shape	d_c [nm]	L_c [nm]	l_{ligand} [nm]	$R_{chain/mon}$	$R_{cross/mon}$	$R_{func/mon}$	added functionality	$R_{P/Area}$ [nm^{-2}]	d_h [nm]	ζ [mV]	ref
CdSe/ZnS	sphere	7.0	-	-	100%	10%	0	-	100	-	-	17
CdS/Mn:ZnS/ZnS	sphere	4.4 ± 0.7	-	1.2	75%	0	2%	ATTO633	150	-	-	101
CdS/ZnS/ZnS	sphere	4.5 ± 0.8	-	1.2	75%	0	2%	ATTO633	150	-	-	101
CdTe	sphere	6.3	-	2.8	100%	10%	0	-	-	-	-	80
Co	rod	5.0 ± 1.1	52.3 ± 7.9	-	75%	0	0	0	5200	-	-	102
Co$_{0.5}$Fe$_{2.5}$O$_3$	sphere	15.3 ± 1.6	-	-	75%	0	-	-	300	19.8 ± 2.1	−30.5 ± 0.6	103
Co$_{0.5}$Fe$_{2.5}$O$_3$/Mn$_{0.3}$Fe$_{2.7}$O$_3$	sphere	12.9 ± 1.4	-	-	75%	0	-	-	300	19.5 ± 0.4	−31.9 ± 1.4	103
CoPt$_3$	sphere	8.0	-	1.0	100%	10%	0	-	100	-	-	64
Fe$_3$O$_4$	sphere	3.8	-	1.2	75%	0	0	-	200	12.3	−54	69
Fe$_3$O$_4$	sphere	5.5	-	-	75%	0	0	-	200	9.0	-	104
Fe$_3$O$_4$	sphere	8.0	-	-	75%	0	0	-	200	12.0	-	104
Fe$_3$O$_4$	sphere	8	-	-	75%	0	0	-	-	145 ± 2	-	105
Fe$_3$O$_4$	sphere	8	-	-	75%	0	0	-	-	178 ± 7	-	105
Fe$_3$O$_4$	sphere	8.0 ± 1.1	-	1.0	75%	0	0.75%	DY-636	100	6.2 ± 0.2	−(55 ± 3)	67
Fe$_2$O$_3$	sphere	9.2	-	1.0	100%	10%	0	-	100, 519	-	-	64
Fe$_2$O$_3$	sphere	9.2	-	1.0	100%	13%	0	-	93, 182, 260	-	-	64
Fe$_2$O$_3$	sphere	10.8 ± 0.12	-	-	75%	0	0	-	50	22.1 ± 7.1	−38.0 ± 5.6	106
Fe$_2$O$_3$	sphere	10.8 ± 0.5	-	1.2	75%	0	2%	ATTO590	50	-	-	65
Fe$_2$O$_3$	sphere	10.8 ± 0.5	-	1.2	75%	0	3%	ABz-DOTA + Gd^{3+}	50	-	-	65
Fe$_2$O$_3$	sphere	10.8 ± 0.5	-	1.2	75%	0	3%	ABz-DOTA + ^{111}In^{3+}	50	-	-	65
Fe$_3$O$_4$	sphere	10.8 ± 0.12	-	-	100%	0	0	-	100–200	-	-	66
Fe$_3$O$_4$	sphere	12.0	-	-	75%	0	0	-	200	15.0	-	104
Fe$_2$O$_3$	sphere	13.0	-	1.0	75%	0	0	-	100	-	-	10
FePt	sphere		-	-	75%	0	2%	DY-636	300	-	-	107
FePt	sphere	3.1 ± 0.4	-	1.0	75%	0	0.75%	DY-636	100	4.2 ± 0.2	−(44 ± 3)	67
FePt	sphere	3.1 ± 0.4	-	1.0	75%	0	0.75%	DY-636 + Glucose	100	4.6 ± 0.6	−(25 ± 3)	67
FePt	sphere	3.1 ± 0.4	-	1.0	75%	0	0.75%	DY-636 + PEG (750 Da)	100	4.8 ± 0.5	−(17.8 ± 0.5)	67
FePt	sphere	3.1 ± 0.4	-	1.0	75%	0	0.75%	DY-636 + PEG (5 kDa)	100	6.5 ± 0.7	−(28 ± 1)	67
FePt	sphere	3.1 ± 0.4	-	1.0	75%	0	0.75%	DY-636 + PEG (10 kDa)	100	10.6 ± 0.9	−(14.3 ± 0.4)	67
FePt	sphere	3.1 ± 0.4	-	1.0	75%	0	0.75%	DY-636	100	4.2 ± 0.2	−(44 ± 3)	67
FePt	sphere	3.2 ± 0.4	-	1.1	75%	0	0–2%	ATTO590	200	11.2	-	108
FePt	sphere	3.2 ± 0.4	-	1.2	75%	0	2%	ATTO633	100	-	-	79
FePt	sphere	3.5 ± 0.6	-	-	75%	0	0	Crystal Violet	-	9 ± 5	−(66 ± 2)	109
Mn$_{0.3}$Fe$_{2.7}$O$_3$	sphere	13.9 ± 1.9	-	-	75%	0	-	-	300	16.8 ± 0.9	−32.4 ± 1.6	103
Mn$_{0.3}$Fe$_{2.7}$O$_3$/Co$_{0.5}$Fe$_{2.5}$O$_3$	sphere	13.8 ± 1.3	-	-	75%	0	-	-	300	17.1 ± 0.58	−30.7 ± 1.5	103
Mn$_{0.3}$Fe$_{2.7}$O$_3$/Co$_{0.5}$Fe$_{2.5}$O$_3$	sphere	14.3 ± 1.5	-	-	75%	0	-	-	300	17.8 ± 0.9	−31.8 ± 1.3	103
MnFe$_2$O$_3$	sphere	4.5	-	1.0	100%	10%	0	-	100	-	-	110
MnFe$_2$O$_3$	sphere	6.0	-	1.0	100%	10%	0	-	100	-	-	110
MnFe$_2$O$_3$	sphere	7.5	-	1.0	100%	10%	0	-	100	-	-	110
PbS	sphere	3.0 ± 0.4	-	1.2	75%	0	2%	Rhodamine 123 / Rhodamine 6G / Rhodamine B	100	-	-	79

Table 6. continued

NP core material	shape	d_c [nm]	L_c [nm]	l_{ligand} [nm]	$R_{chain/mon}$	$R_{cross/mon}$	$R_{func/mon}$	added functionality	$R_{P/Area}$ [nm^{-2}]	d_h [nm]	ζ [mV]	ref
								Oregon Green				
								cadaverine				
								Cresyl Violet				
								Crystal Violet				
								amino-ATTO590				
								amino-DY636				
								Nile Red				
								amino-ATTO633				
NaYF$_4$;Yb^{3+}, Er^{3+}	sphere	22.7	-	-	1.1	75%	0	75%	-	100	34	−53	111
ZnO	sphere	6.9 ± 1.5	-	-	1.1	75%	0	-	-	100	18 ± 2	−(35 ± 4)	112

[a]$R_{chain/mon}$ describes the percentage of anhydride rings of PMA that has been used for linking hydrophobic side chains (dodecyl chains). Note that in some references a slightly different polymer was used, in which there is one hydrophobic side chain in addition to each anhydride ring, and thus $R_{chain/mon} = 100\%$[17,64,80,94,100,110] and thus $R_{chain/mon} + R_{cross/mon} + R_{func/mon} > 100\%$. $R_{cross/mon}$ describes the percentage of anhydride rings that have been used for addition of a crosslinker.[64] $R_{func/mon}$ describes the percentage of anhydride rings that have been used to add organic functionalities such as fluorophores. The following fluorophores have been integrated into PMA, as given together with their excitation wavelength and the extinction coefficient at their excitation wavelength: (i) ATTO590 ($\lambda_{ext} = 590$ nm, $\varepsilon = 1.2 \times 10^5$ M^{-1} cm^{-1}), (ii) DY-636 ($\lambda_{ext} = 645$ nm, $\varepsilon = 1.9 \times 10^5$ M^{-1} cm^{-1}), (iii) SNARF ($\lambda_{ext} = 514$ nm, $\varepsilon = $ depends on pH), (iv) Amino-MQAE ($\lambda_{ext} = 350$ nm, $\varepsilon = 2.8 \times 10^3$ M^{-1} cm^{-1}), (v) Cresyl Violet (CV) ($\lambda_{ext} = 590$ nm), (vi) Oregon Green ($\lambda_{ext} = 494$ nm, $\varepsilon = 7.02 \times 10^4$ M^{-1} cm^{-1}), (vii) 3-hydroxyflavone dye (FE) ($\lambda_{ext} = 410$ nm), (viii) Fluoresceinamine ($\lambda_{ext} = 515$ nm), (ix) Cy5-biotin ($\lambda_{ext} = 649$ nm), (x) Rhodamine 123 ($\lambda_{ext} = 505$ nm, $\varepsilon = 8.52 \times 10^4$ M^{-1} cm^{-1}), (xi) Rhodamine 6G ($\lambda_{ext} = 530$ nm, $\varepsilon = 1.16 \times 10^5$ M^{-1} cm^{-1}), (xii) Rhodamine B ($\lambda_{ext} = 555$ nm, $\varepsilon = 1.07 \times 10^5$ M^{-1} cm^{-1}), (xiii) Nile Red ($\lambda_{ext} = 555$ nm, $\varepsilon = 3.8 \times 10^4$ M^{-1} cm^{-1}), (xiv) Crystal Violet ($\lambda_{ext} = 590$ nm, $\varepsilon = 8.7 \times 10^4$ M^{-1} cm^{-1}), (xv) ATTO633 ($\lambda_{ext} = 630$ nm, $\varepsilon = 1.3 \times 10^5$ M^{-1} cm^{-1}), and (xvi) Tamra ($\lambda_{ext} = 544$ nm). Hydrodynamic diameter (d_h) and zeta-potential ζ values are provided (cf. Section 10).

Table 7. List of Amphiphilic Polymers Other than PMA Which Have Been Used for the Overcoating of Hydrophobic NPs[a]

NP core material	d_c [nm]	polymer	M_w(polymer) [g/mol]	$R_{P/Area}$ [nm^{-2}]	d_h [nm]	ζ [mV]	ref
Au	4.0	PEO	600000				113
Au	3.8	PDMAEMA-*stat*-PLMA (11:89)	9950	≥ 50			114
Au	3.8	PDMAEMA-*stat*-PLMA (19:81)	11000	≥ 50			114
Au	3.8	PDMAEMA-*stat*-PLMA (20:80)	8650	≥ 50			114
Au	3.8	PDMAEMA-*stat*-PLMA (38:62)	9500	≥ 50	22 ± 13	$+(28 \pm 15)$	114
Au	3.8	PDMAEMA-*stat*-PLMA (47:53)	46200	≥ 50			114
Au	3.8	PDMAEMA-*stat*-PLMA (51:49)	47000	≥ 50			114
Au	3.8	PDMAEMA-*stat*-PLMA (53:47)	11000	≥ 50	7 ± 2	$+(30 \pm 14)$	114
Au	3.8	PDMAEMA-*stat*-PLMA (64:36)	12000	≥ 50			114
Au	3.8	PDMAEMA-*stat*-PLMA (73:27)	6500	≥ 50			114
Au	3.8	PDMAEMA-*stat*-PLMA (75:25)	46000	≥ 50			114
Au	3.8	PDMAEMA-*stat*-PLMA (76:24)	7000	≥ 50	28 ± 21	$+(31 \pm 6)$	114
Au	3.8	PMAPHOS(OMe)$_2$-*stat*-PLMA (21:79)	10500	≥ 50			114
Au	3.8	PMAPHOS(OMe)$_2$-*stat*-PLMA (25:75)	8000	≥ 50			114
Au	3.8	PMAPHOS(OMe)$_2$-*stat*-PLMA (35:65)	11800	≥ 50	13 ± 3	$-(25 \pm 5)$	114
Au	3.8	PMAPHOS(OMe)$_2$-*stat*-PLMA (40:60)	9500	≥ 50	11 ± 4	$-(21 \pm 9)$	114
Au	3.8	PMA-*g*-D1 (68:32)	6000	≥ 50	10.6 ± 0.7	$-(24 \pm 4)$	114
CdSe/ZnS	4	PDMAEMA-*stat*-PLMA (38:62)	9500	50			114
CdSe/ZnS	4	PDMAEMA-*stat*-PLMA (53:47)	11000	50			114
CdSe/ZnS	4	PDMAEMA-*stat*-PLMA (76:24)	7000	50			114
CdSe/ZnS	4	PDMAEMA-*stat*-PLMA (35:65)	11800	50			114
CdSe/ZnS	4	PDMAEMA-*stat*-PLMA (40:60)	9500	50			114
CdSe/ZnS	4	PDMAEMA-*stat*-PLMA (68:32)	6000	50			114
Au	4.6 ± 1.1	PMAPHOS-*stat*-PLMA	9000	50	11 ± 3	$-(40 \pm 10)$	115
Au	4.6 ± 1.1	PTMAEMA-*stat*-PLMA	16300	50	13 ± 3	$+(10 \pm 9)$	115
Au	4.6 ± 1.1	PMAPHOS-*stat*-PLMA-*stat*-PDI	9500	50	13 ± 6	$-(23 \pm 8)$	115
Au	4.6 ± 1.1	PTMAEMA-*stat*-PLMA-*stat*-PDI	17800	50	7 ± 2	$+(17 \pm 1)$	115

[a]For the polymer materials the ratio of charged (x) to uncharged (y) monomer units in the polymer is noted as (x:y).
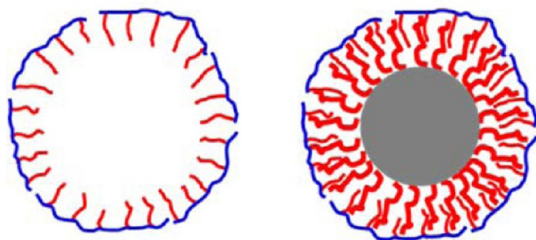
Figure 51. Empty polymer micelles (left) versus polymer-coated Au NPs (right). Due to similar size, separation using size exclusion chromatography is not efficient.
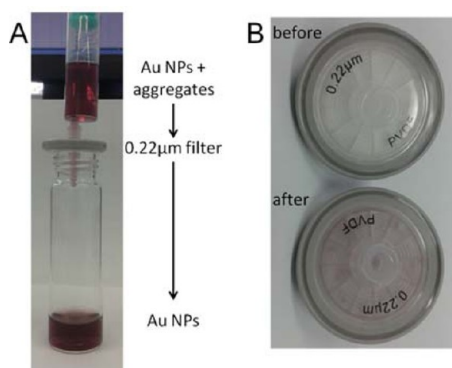
Figure 52. (A) Purification of PMA-*g*-dodecyl capped Au NPs (≈4 nm core diameter, cf. Section 1.2, Section 6.3) from aggregates via filtration using a syringe filter. (B) After filtration the aggregates can be seen in the filter by the naked eye.
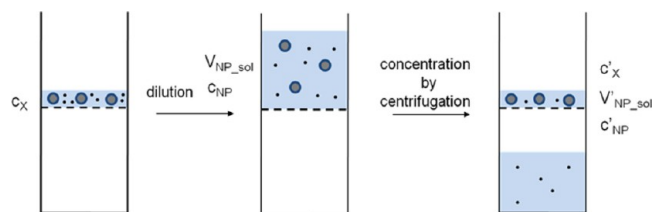
Figure 53. Ultrafiltration of hydrophilic NPs (drawn as gray spheres with blue surface) using a centrifugal filter. The NP suspension contains impurities (small black dots) of concentration c_X. First, the NP suspension is diluted with fresh solvent to a volume (V_{NP_sol}), resulting in NP concentration of c_{NP}. Upon centrifugation only solvent and the small impurities pass through the filter membrane, which results in an increase in NP concentration ($c'_{NP} = c_{NP} \cdot V'_{NP\_sol}/V_{NP\_sol}$) and a decrease in impurities concentration ($c'_X = c_X \cdot V_{NP\_sol}/V'_{NP\_sol}$).

example). However, it is time-consuming and has lower efficiency compared to ultrafiltration. In addition, due to osmotic pressure upon dialysis, the volume of the NP suspension in the dialysis bag may increase, resulting in dilution of the NP suspension.

7.3. Size Exclusion Chromatography. In size exclusion chromatography (SEC), a NP suspension is run through a porous gel matrix driven by gravity or by pressure. The separation mechanism is based on the interaction between the NPs and the pores of the gel: "small" NPs can enter the pores and are thus retained, whereas "large" NPs are excluded from the pores and thus pass the gel faster without interaction. In this way "large" NPs are eluted first, and "small" NPs take longer to diffuse into and out of the pores and thus are eluted later, cf. Figure 56. "Small" and "large" sizes of NPs are relative
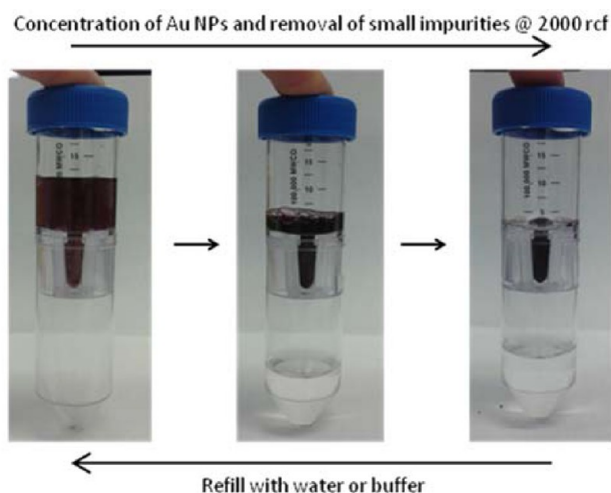
Figure 54. Ultrafiltration using a centrifugal filter to purify and concentrate Au NPs. (PES (Polyethersulfon-membrane centrifugal filter with 100 kDa MWCO, Sartorius Stedim, no. VS2042).
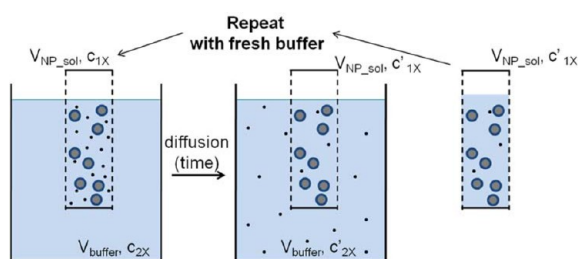

Figure 55. Dialysis of hydrophilic NPs (drawn as gray spheres with blue surface) using dialysis bag of volume V_{NP_sol}. Besides the NPs there are also small impurities of concentration c_{1X} in the NP suspension. The dialysis bag is placed into a bath solution of volume V_{buffer}, in which there are no impurities, i.e., $c_{2X} = 0$. Upon diffusion impurities move from the dialysis bag into the bath. At equilibrium, concentration of impurities in the dialysis bag is reduced to c'_{1X} ($c'_{1X} = c_{1X} \times V_{NP\_sol}/(V_{NP\_sol} + V_{buffer})$).
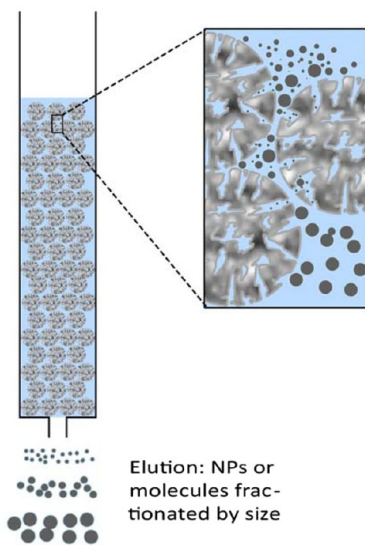
Figure 56. Principle of size exclusion chromatography. Small impurities enter the pores of gel beads and are thus retarded, whereas larger NPs are eluted faster.

to the size of the pores of the gel; i.e., the pore size has to be selected based on the size of the NPs in the sample. The gel beads used to form the gel matrix have to be inert, i.e., the NPs must not react and/or stick to them. SEC is frequently used for desalting, i.e., small ions are retained, whereas the sample, such as proteins, is eluted.[116,117] In this way SEC can be also be used to purify NPs from smaller excess molecules (e.g., salt or capping agent) in solution. For quantitative analysis, SEC columns need to be calibrated to estimate the hydrodynamic diameter d_h of NPs.[80]

The possibility of assembling a SEC column in a high performance liquid chromatography (HPLC) system (cf. Figure 57) allows for an automatic sample injection and
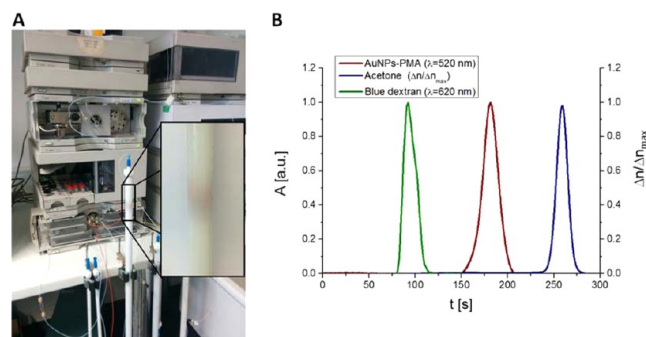
Figure 57. (A) Elution of PMA-*g*-dodecyl-capped Au NPs (≈4 nm core diameter, cf. Section 1.2, Section 6.3) via high performance liquid chromatography (HPLC; Agilent 1100 Series) on a size exclusion chromatography column (75 cm length and 1.5 cm diameter) filled with Sephacryl S400HR as stationary phase and sodium borate buffer pH = 9 as mobile phase. The flow rate was set as 0.5 mL·min⁻¹. The inset shows the red band of eluted Au NPs. (B) Size exclusion chromatograph of PMA-*g*-dodecyl-capped Au NPs (≈4 nm diameter, cf. Section 1.2, Section 6.3) using similar conditions in A. The normalized absorption A at 520 nm is plotted versus the elution time of the Au NPs (dark red curve). For column calibration, peaks of blue dextran shown as normalized absorption at 620 nm (drawn in green) and acetone shown as normalized changes of the refractive index (blue) are also represented on the chromatogram as reference of the range of the column retention time at these working conditions. In the case of the acetone the changes of the refractive index are measured via an internal reference cell and a sample cell set in the instrument. Both are initially flushed with the mobile phase until the refractive index is the same in both cells, and at this moment the zero value is adjusted. Once the measurement starts, the reference cell stays closed and the column eluate flows through the sample cell. The final signal is expressed as Refractive Index Units (RIU), being the difference Δn between the refractive index in the sample cell and the refractive index in the reference cell.

collection, a customizable constant pressure all over the sample run, and the possibility of multiple programmed detectors. Optimizing parameters related to the stationary phase, the column dimensions, the mobile phase, or the process flow allows fine-tuning of the separation quality. It is important to note that a prefiltering step of NP suspension prior to sample injection is important.

7.4. Gel Electrophoresis. Gel electrophoresis is based on the mobility of charged molecules in a gel matrix under applied electric field. The higher the charge of the molecules, the faster they migrate through the gel.[118] The bigger the molecules, the slower they can pass the pores in the gel and the slower they migrate.[53] In this way, assuming similar surface charge density, "large" NPs run slower in gel than "small" NPs.[52] Separation of

NPs with various particle sizes can be optimized by adjusting the concentration of the gel and thus the gel mean pore size.[52]

For gel preparation (here 2% (w/v) agarose), 3 g of agarose powder (Invitrogen, no. 15510027, "Agarose UltraPure") was dissolved in 150 mL of 0.5× TBE buffer (44.5 mM Tris-borate and 1 mM ethylenediaminetetraacetic acid (EDTA), pH = 8.3, Sigma-Aldrich, no. T3913) in a 500 mL Erlenmeyer flask. The solution was then covered with a watch—glass and heated in a microwave oven at 380 W for 8 min until the solution started to boil. The flask was swirled to help all agarose powder to dissolve and was then heated again to the boiling point. The hot and clear agarose solution was poured in a 10 × 15 cm gel tray leveled in a gel caster (BioRad). A comb (1, 2, 15, 20, or 30 wells) was placed into the gel, and the whole device was covered with an alumina or polyethylene foil. The gel was allowed to cool down to RT and to solidify, which typically takes 1 h, cf. Figure 58. After solidification the comb was
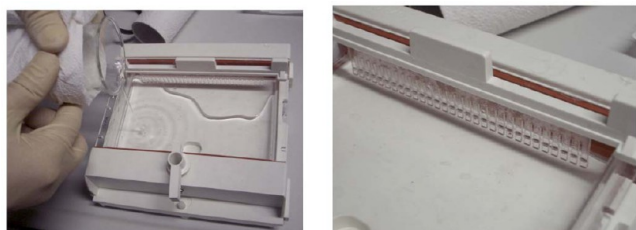
Figure 58. Boiling agarose solution is poured in the gel tray, and a template comb is inserted. The gel then is allowed to cool down and solidify at RT.

removed and the gel was taken out of the casting device and placed into the electrophoresis device (BioRad Subcell GT wide mini), which was filled with 0.5× TBE buffer until the whole gel was covered.

Prior to loading into the wells of the gel, the NPs were first mixed with about 20% by volume with loading buffer (30% glycerol in 0.5× TBE with 0.3% Orange G). Glycerol increases the viscosity so that the NP suspension can be better filled into the wells of the gel. The yellow/orange color of Orange G allows for observing a fast migrating band as control on the gel. The NP suspension was carefully pipetted into the wells of the gel, i.e., into the holes made by the removed template comb, cf. Figure 59A. The wells should not be filled too high, and the NP suspension should not be too concentrated, as otherwise the band upon running electrophoresis may be smeared out. Once the gel had been loaded with NP suspension the electrophoresis devices were connected to a power source (BioRad Power Pac 1000) and run at a constant voltage of typically 100 V, corresponding to a potential gradient of 10 V/cm. The NPs were then run on the 2% agarose gels for 30−100 min under the following conditions: 100 V, 500 mA, 250 W, 0.5× TBE buffer. In case the NPs are charged, they migrate toward the oppositely charged pole, cf. Figure 59B. The speed of migration depends on the charge and hydrodynamic diameter of the NPs. In this way different NP species can be separated as different bands on the gel. The more homogeneous the size and charge distribution of one NP species, the sharper the corresponding NP band is. The longer the running time, the better the separation of the NP bands.

Afterward, the gel was taken out from the tray and a digital picture was taken (BioRad Gel Doc), showing the gel under visible or UV light. In the case the NPs did not migrate
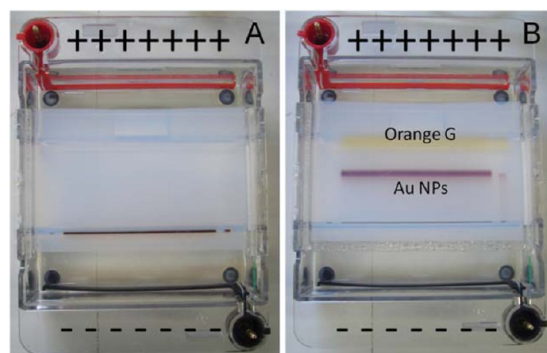
Figure 59. Photographs of an agarose gel filled with anionic Au NPs (≈4 nm diameter, cf. Section 1.2, Section 6.3) (A) before and (B) after electrophoresis. The NP sample is loaded in the well seen on the bottom of the image and can be seen by the red color of the Au NPs as labeled. PMA-coated Au NPs are negatively charged, and thus they migrate toward the positive pole when an electric field is applied, i.e., in the shown image toward the top of the image. Orange G is a small negatively charged molecule and thus migrates faster than Au NPs toward the positive pole. Yellow and red bands in the gel correspond to the Orange G and Au NPs, respectively.

sufficiently, the gel was run for another 30 min and another photograph was taken after the additional running time. For imaging, the gel was placed on a white plastic plate to enhance the contrast and was inserted into the chamber of the imaging device, cf. Figure 60.
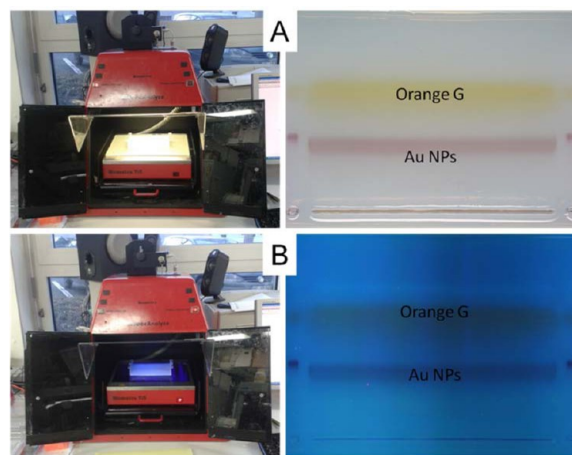

Figure 60. Photographs of the BioRad Gel Doc imaging device, which was used to take pictures of gel containing Orange G and Au NPs bands (in Figure 59), under white light (A) or under UV illumination (B). In both A and B: The gel inside the imaging device is shown on the left and the resulting images on the right. In case of white light illumination the yellow band of Orange G and the red band of Au NPs can be seen. Since Orange G and the Au NPs are nonfluorescent, no fluorescence can be observed under UV illumination.

Gel electrophoresis can be used for purification of NP samples. Free impurities such as surfactants, molecules, or polymer micelles typically migrate faster than NPs. By taking out the NP band from the gel, an NP suspension purified from empty polymer micelles can be obtained. The band of the NPs was cut with a knife and then put into a dialysis bag tube (Spectra/Pro 6 dialysis tubing, 50 kDa MWCO, 34 mm flat width, Spectralabs, no. 132544). The gel-filled bag was then put into the electrophoresis cell filled with fresh 0.5× TBE buffer,

and voltage (100 V) was applied, typically for 20 min. Due to the applied voltage the NPs migrated out of the gel, but they remained trapped inside the dialysis bags. Once the NPs had been migrated out of the gel pieces and the voltage was switched off, the dialysis bags were taken out of the electrophoresis cell, and the suspension of NPs was pipetted out of the bags, cf. Figure 61. For concentration and buffer exchange of this NP suspension ultrafiltration was applied as reported in Section 7.2.
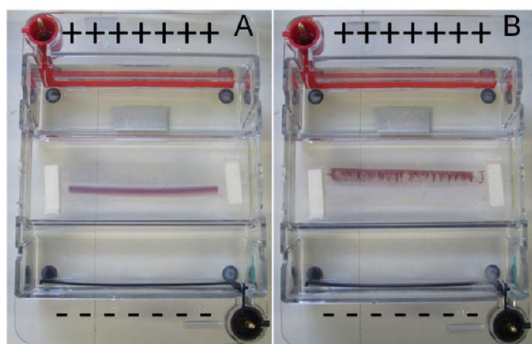

Figure 61. Recovering Au NPs from a gel band. (A) The extracted band contains Au NPs (≈4 nm diameter, cf. Section 1.2, Section 6.3) and was placed inside a dialysis bag, which was placed into the electrophoresis cell. (B) After applying an electric field the Au NPs migrated out of the gel band but remained trapped inside the dialysis bag.

7.5. Ultracentrifugation. A major method for NP purification is centrifugation. NPs with density higher than the density of the solvent may be precipitated by gravity or centrifugal forces, whereas lighter impurities (surfactants, ions, capping agents, polymers, etc.) remain in the supernatant and thus can be removed by supernatant decantation. The NP pellet is then resuspended in fresh medium/solvent, cf. Figure 62. This procedure works well for NPs that are large or dense
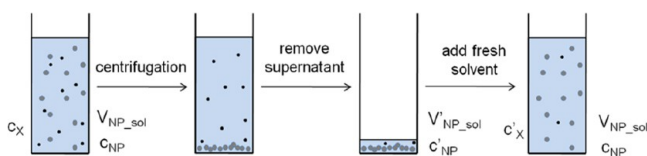
Figure 62. Purification via repeated centrifugation of a suspension of NPs (drawn in gray) of initial volume V_{NP_sol} and a concentration of c_{NP}. Small impurities (drawn in black) with concentration c_X are presented initially in the suspension. Upon centrifugation the NPs form a pellet, whereas the impurities remain in solution. The supernatant with the impurities is removed. Fresh solvent is added to result in a decreased final concentration of impurities $c'_X = c_X \cdot V'_{NP\_sol}/V_{NP\_sol}$.

enough to be precipitated by using a tabletop centrifuge (e.g., Au NPs of $d_c > 15$ nm at 10000 rcf). In the case of smaller NPs, ultracentrifugation with much higher centrifugation speed is needed. The duration and centrifugal forces depend on the NPs' size, shape, and density, as well as on solvent-related parameters such as solvent density/viscosity. Moreover, the colloidal stability of NPs during centrifugation is a very important parameter to be considered when selecting the centrifugation settings. Collectively, optimum centrifugation settings for a specific NP suspension should be evaluated

experimentally. For example, PMA-*g*-dodecyl capped Au NPs (≈4 nm core diameter, cf. Section 1.2, Section 6.3) required centrifugation at 85 000 rcf (Thermo Scientifiv ultracentrifuge equipped with a SureSpin 630 rotor in combination with 36 mL PET thin-walled tubes (Thermo Scientific, no. 75000471)) for 3 h. After centrifugation, a red pellet was observed, and the supernatant was discarded. Three centrifugation cycles were found to be necessary to purify PMA-*g*-dodecyl capped Au NPs from empty PMA-*g*-dodecyl micelles (cf. Figure 62). After the third centrifugation step, the Au NPs were suspendet in Milli-Q water and filtered through a hydrophilic syringe filter (0.22 *μ*m, cf. Section 7.2).

Various purification methods may result in different purification efficiencies. For example, we did find that purification of PMA-*g*-dodecyl capped Au NPs using ultra-centrifugation is more efficient than the gel electrophoresis method. Interestingly, some empty polymer micelles may remain in solution after electrophoresis, whereas the NP sample was virtually free of empty micelles after three ultra-centrifugation cycles, cf. Figure 63.

8. CHARACTERIZATION OF STRUCTURAL PROPERTIES OF THE NPS

8.1. General Comments about the Composition of the NPs. As outlined in Sections 1−6, NPs described in this report are composed of an inorganic core and an organic shell. The total mass of one NP (m_{NP}) involves the mass of the inorganic core (m_c) and the mass of the organic surface coating. As inorganic cores can be conveniently imaged with transmission electron microscopy (TEM, cf. Section 8.3), the mass of one NP core can be obtained. In addition to the NPs' core material density, the NP core volume V_c should be calculated using NP dimensions as obtained from TEM images (core diameter (d_c) in the case of spherical NPs and core diameter (d_c) and length (L_c) in the case of rod-shaped NPs). Note that without additional staining (cf. Section 8.4) the organic shell does not provide contrast in regular TEM, and thus only the inorganic cores are visible. In the case of spheres and rods (assumed to have the shape of a cylinder) the volume of one NP core is

$$V_c(\text{sphere}) = \left(\frac{4\pi}{3}\right) \times \left(\frac{d_c}{2}\right)^3 = \left(\frac{\pi}{6}\right) \times d_c^{\ 3} \tag{20}$$

$$V_c(\text{rod}) = \pi \times \left(\frac{d_c}{2}\right)^2 \times L_c = \left(\frac{\pi}{4}\right) \times d_c^{\ 2} \times L_c \tag{21}$$

If the core is built in core/shell geometry (cf. Figure 1), the volume V_{c2} of the shell is

$$V_{c2}(\text{sphere}) = V_{c12}(\text{sphere}) - V_{c1}(\text{sphere})$$
$$= \left(\frac{\pi}{6}\right) \times (d_{c12}^{\ 3} - d_{c1}^{\ 3}) \tag{22}$$

In the case the core is composed out of material of density ρ_c, the mass of one NP core is

$$m_c = \rho_c \times V_c \tag{23}$$

For most inorganic NP materials their densities can be found in the literature. In first order the bulk densities of the materials can be assumed. The molar mass of an NP core thus is
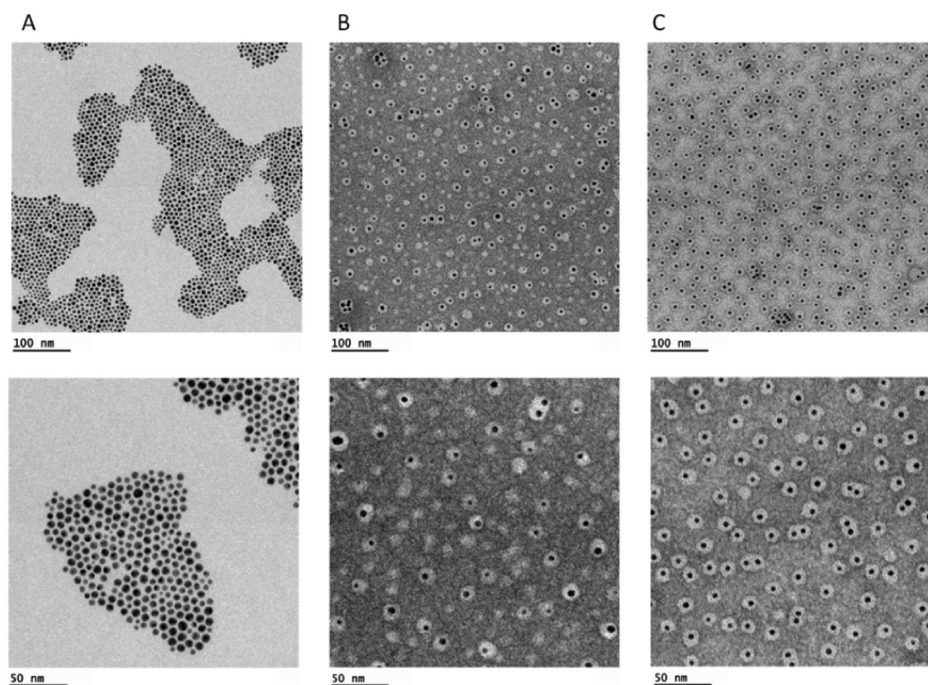
$$M_c = m_c \times N_A \tag{24}$$

Figure 63. Transmission electron microscopy (TEM) images of PMA-*g*-dodecyl capped Au NPs (≈4 nm core diameter, cf. Section 1.2). (A) TEM images of the DDT-Au NPs (cf. Section 8.3) before coating with PMA-*g*-dodecyl polymer at two magnifications in upper and lower panels. (B) TEM images after negative staining (cf. Section 8.4) of the PMA-*g*-dodecyl capped Au NPs purified by gel electrophoresis (cf. Section 7.4) at two magnifications in upper and lower panels (Note: some empty polymer micelles can be seen (gray spots without black NP inside)). (C) TEM images of the PMA-*g*-dodecyl capped Au NPs purified by ultracentrifugation at 65 000 × *g* three times at two magnifications in upper and lower panels (Note: the sample is virtually free of empty polymer micelles). The scale bars in the top and bottom rows represent 100 and 50 nm, respectively.

In the case the core is composed out of one element X, then each NP core includes $N_{X/NP}$ atoms of X. M_X is the molar mass of element X.

$$N_{X/NP} = \frac{M_c}{M_X} = \rho_c \times V_c \times \frac{N_A}{M_X} \qquad (25)$$

To give an example, for a spherical Au NP with core diameter d_c = 4.2 nm, $V_c = (\pi/6) \times (4.2 \text{ nm})^3 \approx 38.8 \text{ nm}^3$. Given the bulk density of Au of ρ_{Au} = 19.3 g/cm^3, the mass of one Au core thus is m_c = 19.3 g/cm^3 × 38.8 nm^3 ≈ 750 g·$(10^{-9}$ m/10^{-2} m$)^3$ = 7.5×10^{-19} g. The molar mass of a Au core thus is $M_c = m_c \times N_A = 7.5 \times 10^{-19}$ g $\cdot 6.02 \times 10^{23}$ mol^{-1} ≈ 4.5×10^5 g/mol. Given the molar mass of Au M_{Au} = 197 g/mol, one Au core thus comprises approximately $N_{Au/NP} = M_c/M_{Au}$ = 4.5×10^5 g·mol^{-1} /197 g·mol^{-1} ≈ 2284 ≈ 2300 Au atoms.

In the case the core is composed out of two elements X and Y with the stoichiometry X_xY_y (i.e., for Fe$_3$O$_4$, x = 3 and y = 4), then each NP core includes $N_{X/NP}$ and $N_{Y/NP}$ atoms of X and Y, respectively. M_X and M_Y are the molar masses of the two elements.

$$M_c = N_{X/NP} \times M_X + N_{Y/NP} \times M_Y \qquad (26)$$

$$\frac{N_{X/NP}}{N_{Y/NP}} = \frac{x}{y} \qquad (27)$$

Thus, $M_c = N_{X/NP} \times M_X + N_{X/NP} \times (y/x) \times M_Y$, leading to

$$N_{X/NP} = \frac{M_c}{M_X + \left(\frac{y}{x}\right) \times M_Y}$$

$$= \rho_c \times V_c \times \frac{N_A}{M_X + \left(\frac{y}{x}\right) \times M_Y} \qquad (28)$$

$$N_{Y/NP} = \frac{M_c}{M_Y + \left(\frac{x}{y}\right) \times M_x}$$

$$= \rho_c \times V_c \times \frac{N_A}{M_y + \left(\frac{x}{y}\right) \times M_x} \qquad (29)$$

To give an example, for a spherical Fe$_3$O$_4$ NP with core diameter d_c = 4.2 nm, $V_c = (\pi/6) \times (4.2 \text{ nm})^3 \approx 38.8 \text{ nm}^3$. Given the bulk density of Fe$_3$O$_4$ of ρ_{Fe3O4} = 5 g/cm^3, the mass of one Fe$_3$O$_4$ core thus is m_c = 5 g/cm^3 × 38.8 nm^3 = 194 g × $(10^{-9}$ m/10^{-2} m$)^3$ ≈ 1.9×10^{-19} g. The molar mass of a Fe$_3$O$_4$ core thus is $M_c = m_c \times N_A = 1.9 \times 10^{-19}$ g·6.02×10^{23} mol^{-1} ≈ 1.2×10^5 g/mol. Given the molar masses of iron M_{Fe} = 55.8 g/mol and of oxygen M_O = 16 g/mol, one Fe$_3$O$_4$ core thus comprises approximately $N_{Fe/NP} = M_c/(M_{Fe} + (4/3) \times M_O)$ = 1.2×10^5 g·mol^{-1}/(55.8 g·mol^{-1} + (4/3) × 16 g·mol^{-1}) = 1556 ≈ 1600 iron atoms, and $N_{O/NP} = M_c/(M_O + (3/4) \times M_{Fe})$ = 1.2×10^5 g·mol^{-1}/(16 g·mol^{-1} + (3/4) × 55.8 g·mol^{-1}) = 2074 ≈ 2100 oxygen atoms.

8.2. Determination of NP Concentrations by Elemental Analysis. With inductively coupled plasma coupled with either mass spectrometry (ICP-MS) or optical emission spectroscopy (ICP-OES), quantitative elemental analysis can be performed. Dilution and acid digestion are required prior to analysis. For example, in the case of metal NPs, such as Au or

Ag, 50 μL of the sample was added to 200 μL of aqua regia (i.e., concentrated HCl (35 wt %) and HNO$_3$ (67 wt %) in 3:1 volume ratio), and then it was left for digestion (oxidation of metallic cores into their corresponding ions) for about 30 min. The digestion step diluted the sample by a dilution factor of 5× prior to further dilution by a factor of 10× with HCl solution (2 wt % HCl) prior to their injection into ICP-MS (total dilution factor of 50×). A high dilution factor in acidic media is required to stabilize metallic ions and to improve the analytical detection limit, as well as to ensure a qualitative and quantitatively equal background signal for all samples. Samples with high levels of acid might harm the ICP-MS machinery.

For calibration, the autotuning solution from Agilent for ICP-MS 7500cs with a standard concentration of 1 μg/L of Ce, Co, Li, Mg, Tl, and Y was used to set the general background, as well as to calibrate the electrical field of the lenses and the magnetic quadrupole field in strength and frequency before the actual run. The oxidation level (less than 0.8%) and double charge rate (less than 1.8%) were also measured using this tuning solution.

All vials and working materials either were cleaned using freshly prepared aqua regia for 2 h followed by boiling in Milli-Q water or consisted of sterile and clean nonreusable consumables. The samples were introduced into the ICP-MS setup through a Perfluoroalkoxy-Alkane (PFA) based microflow spray chamber, where the aqueous sample was nebulized, introduced to the argon gas flow, and transported to the torch, where it was ionized in an argon-plasma of around 6000 °C. After ionization the sample was presorted using an omega lens, element-wise separated in the quadrupole field through the mass to charge ratio, again sorted using kinetic barriers and a charged lens system, and finally detected with either an analog or a digital detector depending on the count rate. It is important to mention that the working mode of the instrument and flow of Ar gas also affected the analysis.

Before each run, a proper calibration was needed with an appropriate standard. The ICP-MS setup was calibrated by using an Agilent standard of corresponding ions (all the standards of corresponding ions should be available prior to the measurement). For example, in the case of Au NPs the element to be detected is Au. The Agilent Au standard has 1000 mg/L Au concentration from which eight solutions of concentration 2500, 1000, 500, 250, 100, 50, 25, and 10 parts per billion (1 ppb = 10^{-9} = 1 μg detected Au/1 kg water (density ρ_{H2O} = 1 kg/L), corresponding to a gold concentration C_{Au} = 1 μg/L) were prepared along with a blank using the same low matrix (aqueous 2 wt % HCl) as diluent. The calibration curve was constructed using concentration points of the aforementioned standard solutions. The syringe and tubings were washed thoroughly at the end of each run (for gold, extensive rinsing is needed as it often sticks to the tube). The calibration curve and the sample results were used to calculate the concentration of measured elements in the corresponding samples considering the used dilution factor (Final concentration = dilution factor × measured concentration).

With TEM studies the volume of one NP core V_c (the core that contains the detected element) can be determined, leading to the total number of atoms X per NP ($N_{X/NP}$) (cf. Section 8.3). By knowing the elemental concentration of metallic ions X in a sample c_X, the concentration of NPs in the sample can be determined:

$$c_{NP} = c_X / N_{X/NP} \qquad (30)$$

For example, to determine the concentration of Fe$_3$O$_4$ NP in a sample (c_{NP}) we need to determine the elemental concentration of iron c_{Fe} in the sample and the number of Fe atoms per NP as per eq 28: $N_{Fe/NP} = \rho_{Fe3O4} \times V_c \times N_A / (M_{Fe} + (4/3) \times M_O) = \rho_{Fe3O4} \times (\pi/6) \times d_c^3 \times V_c \times N_A / (M_{Fe} + (4/3) \cdot M_O)$. The concentration of Fe$_3$O$_4$ NP in the sample now can be calculated as follows: $c_{NP} = c_{Fe} / N_{Fe/NP}$.

8.3. Transmission Electron Microscopy of NP Cores. Transmission electron microscopy (TEM) analysis allows a direct measure of the size and shape of NPs. The organic ligand shell typically does not provide sufficient electron contrast, and thus in TEM images only the inorganic part of the NPs can be seen. However, special techniques can be employed to visualize the organic shell around NPs as described in Section 8.4.

All images in this section were obtained using a Philips CM 100 electron microscope operated at an accelerating voltage of 100 kV or on a JEOL JEM-1400PLUS TEM operated at an accelerating voltage of 120 kV. The NPs were deposited from a dilute solution onto a 3−4 nm thick film of amorphous carbon supported on a 400 mesh copper grid (Ted Pella Inc., no. 01822-F). One drop (2 μL) of NP suspension was deposited onto the grid, and the solvent was evaporated at RT. In the case of NPs suspended in water, the grids were kept under ethanol vapor for 1−2 days prior to sample deposition. This treatment made the carbon film more hydrophilic and improved the adsorption of the NPs on it. The microscope magnification was calibrated with a calibration grid (Grating Replica, Waffle, 2160 l/mm, on 3 mm grid, Ted Pella Inc., no. 607).

From TEM images several parameters can be extracted. First, the shape of the NPs can be determined, which is important in the case of nonspherical NPs such as rods, stars, etc. Second, the frequency distribution (histograms) of NP core diameter d_c (and length L_c in case of rod-shaped NPs) can be determined to calculate the NP's dimensions. Figures 64−76 show TEM
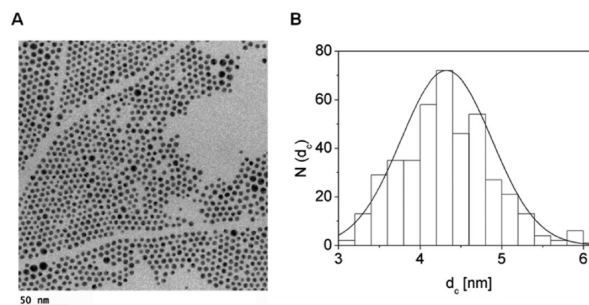

Figure 64. (A) TEM image of hydrophobic DDT-Au NPs (capped with dodecanethiol, ≈4 nm core diameter, cf. Section 1.2) dried on a grid from a chloroform suspension. The scale bar corresponds to 50 nm. (B) Size distribution histogram, plotted as number of NPs $N(d_c)$ that have a core diameter of d_c. From this histogram the mean NP diameter and its standard deviation was determined to be d_c = (4.3 ± 0.4) nm.

images of NP samples prepared in this work, along with their size distribution histograms. To determine the size distribution histograms, dimensions of several NPs were measured from their TEM images using ImageJ 1.42 (freely available software from https://imagej.nih.gov/ij/). As a representative sample, at least 100 NPs were analyzed for each size distribution histogram, from which the mean diameter of the NPs (d_c) and its standard deviation (as indicator of polydispersity) could be calculated. Third, the state of agglomeration can be observed
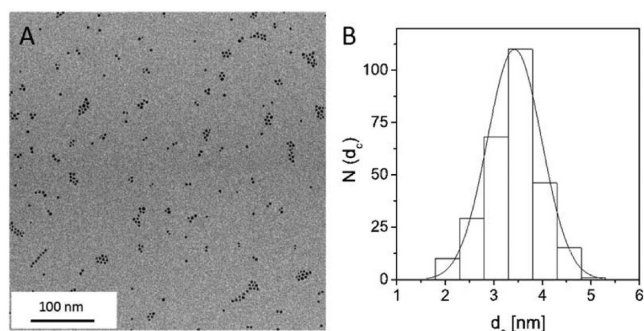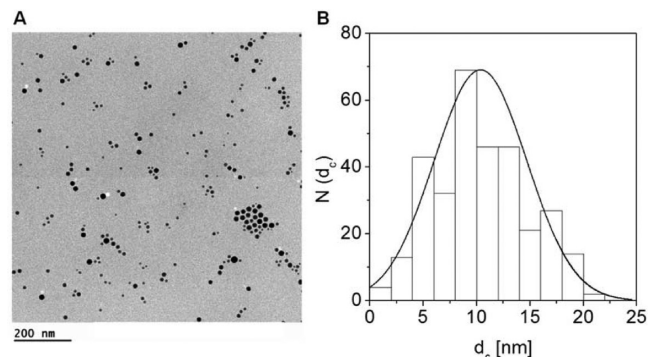
Figure 65. (A) TEM image of hydrophobic FePt NPs (capped with OA and OLA, ≈4 nm core diameter, cf. Section 1.4) dried on a grid from a chloroform suspension. The scale bar corresponds to 100 nm. (B) Size distribution histogram, plotted as number of NPs $N(d_c)$ that have a core diameter of d_c. From this histogram the mean NP diameter and its standard deviation were determined to be $d_c = (3.4 \pm 0.6)$ nm.

Figure 67. (A) TEM image of hydrophobic Sn NPs (capped with oleic acid, ≈ 11 nm core diameter, cf. Section 1.6) dried on a grid from a chloroform suspension. The scale bar corresponds to 200 nm. (B) Size distribution histogram, plotted as number of NPs $N(d_c)$ that have a core diameter of d_c. From this histogram the mean NP diameter and its standard deviation were determined to be $d_c = (10 \pm 4)$ nm.

(note that TEM works with dried samples, and thus even NPs, which are individually dispersed in solution, may cluster on the TEM grids due to drying-induced assembly). Drying-induced clustering on the TEM grids can be reduced by depositing diluted NP suspensions on the TEM grids, using treated grids (cationic or anionic surfaces), or optimizing the rate of drying. In contrast, when TEM grids are prepared with higher concentration of NPs, the NPs can self-assemble into 2-dimensional lattices, cf. Figure 64. Fourth, from TEM images with self-assembled NPs the thickness of the organic coating/shell around the inorganic NP cores can be estimated as half the minimum distance between the two adjacent inorganic NP cores.[80,85,119] However, for TEM imaging the NPs have to be deposited on a substrate, and the solution in which the NPs are dispersed must be evaporated. The thickness of the organic layer is likely to be reduced due to the drying-induced shrinkage. For example, organic hydrophobic tails of two adjacent NPs can intercalate, and polymeric shells on NPs can shrink upon desolvation. For these reasons, the measured thickness of the organic coating around the NP cores as determined from TEM is likely to be underestimated, and therefore, the values obtained in this way have to be interpreted as lower limits.

8.4. Transmission Electron Microscopy of NPs Including Their Organic Shell. As shown in the previous sections, TEM imaging is used to determine the size (d_c) and shape (rods, spheres, stars, etc.) of NP cores composed of

various materials such as Au, Ag, Fe_3O_4, FePt, etc. The inorganic cores of the NPs appear almost black due to the strong electron-scattering character of these materials. However, as it has been previously discussed, these NPs are modified with different organic ligands, which increase the effective diameter of the NPs (e.g., d_{eff}). Such organic shells have low electron scattering character and thus do not show sufficient contrast to be visible in regular TEM images. In order to investigate the thickness of these organic coatings (e.g., l_{ligand}), negative staining is needed. Heavily electron-scattering compounds (e.g., uranyl acetate, ammonium molibdate, or osmium tetroxide) may be used to stain the background of TEM grids and indirectly allow the visualization of the organic shell around NPs.[120] Ideally, negative staining contrast agents form a homogeneous dark background, and thus the organic shells around NPs appear as bright corona (i.e., negative staining) around the dark inorganic cores (cf. Figure 77)

The technique can be visualized as to balance the competition between the sample and the staining agent to reach the grid surface. Therefore, for a successful negative staining it may be important to take into account several sample parameters such as, for example, the overall particle charge or its diffusion rate together of the chosen stain. This translates into the need of different approaches to achieve homogeneous negative contrast for different samples. For PEGylated Au NPs (cf. Section 2.2 and Section 3.3), as shown in Figure 77, a sample preparation protocol reported by Harris[120] was
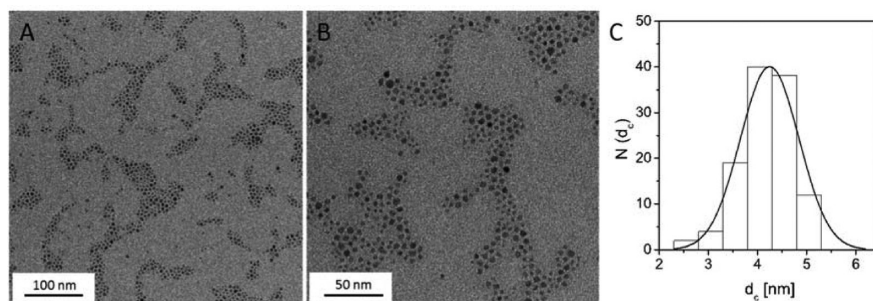

Figure 66. TEM image of hydrophobic Fe_3O_4 NPs (capped with OA and OLA, ≈4 nm core diameter, cf. Section 1.5) dried on a grid from a chloroform suspension. (A) The scale bar corresponds to 100 nm, and (B) the scale bar corresponds to 50 nm. (C) Size distribution histogram, plotted as number of NPs $N(d_c)$ that have a core diameter of d_c. From this histogram the mean NP diameter and its standard deviation were determined to be $d_c = (4.2 \pm 0.6)$ nm.
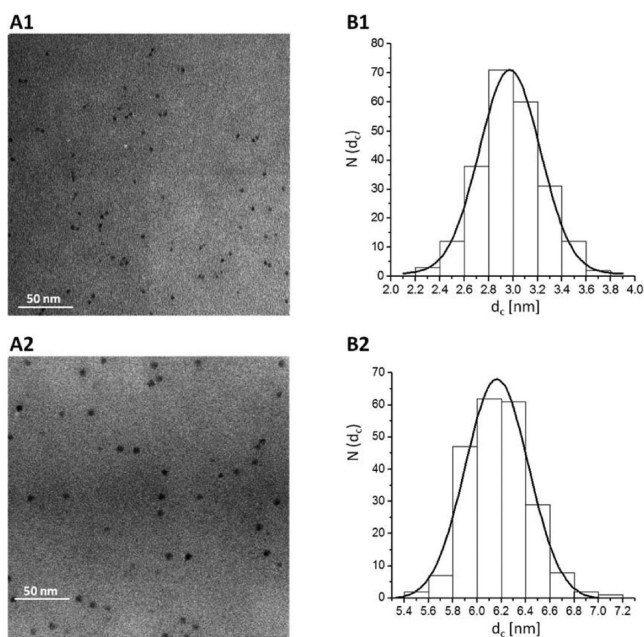
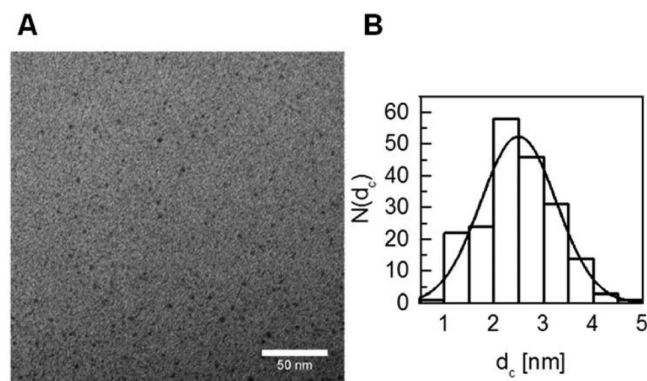**Figure 68.** (A) TEM image of hydrophobic CdSe/ZnS NPs (capped with TOPO, ≈4 nm core diameter, cf. Section 1.7) dried on a grid from a chloroform suspension. The scale bar corresponds to 50 nm. (B) Size distribution histogram, plotted as number of NPs $N(d_c)$ that have a core diameter of d_c. A1 and B1 correspond to CdSe/ZnS NPs of ≈3 nm in diameter. From the histogram in B1, the mean NP diameter and its standard deviation were determined to be $d_c = (3.0 \pm 0.2)$ nm. A2 and B2 correspond to CdSe/ZnS NPs of ≈6 nm in diameter. From the histogram in B2, the mean NP diameter and its standard deviation were determined to be $d_c = (6.2 \pm 0.3)$ nm.

Figure 69. (A) TEM image of hydrophobic CdS NPs (capped with oleic acid and to some extent with octadecane, ≈2 nm core diameter, cf. Section 1.8) dried on a grid from a chloroform suspension. The scale bar corresponds to 50 nm. (B) Size distribution histogram, plotted as number of NPs $N(d_c)$ that have a core diameter of d_c. From this histogram the mean NP diameter and its standard deviation were determined to be $d_c = (2.5 \pm 0.8)$ nm. Note that for NPs of such a very small size, the size measurement as determined by TEM has to be interpreted with care, as NPs with ultrasmall size may not provide sufficient contrast and thus are not counted.

optimized as follows:[56] Samples were prepared on carbon film 400 copper mesh grids purchased from Electron Microscopy Sciences (Hatfield, U.S.A.). To enhance the hydrophilicity of grids and to impart them with negative charge, the specimen grids were exposed to glow-discharge treatment under air plasma for 20 s (2.0×10^{-1} atm and 30 mA), using a MED 020 modular high vacuum coating system (BAL-TEC AG, Balzers,

Fürstentum Liechtenstein). Negatively charged carbon grids were used within 5 min after treatment to ensure hydrophilicity. 0.35 μL sample droplet of NP solution with NP concentration ranging from 10 nM (for Au cores of 14 nm diameter) to 1.5 nM (for Au cores of 30 nm diameter) of PEGylated Au NPs was placed on the grid, allowed to incubate for 20 s to 1 min (the smaller the particle size, the lower the incubation time) followed by 0.35 μL droplet of 0.25% weight/volume (w/v) uranyl acetate aqueous solution. The grid was air-dried overnight before actual TEM imaging.

8.5. X-ray Diffraction. With X-ray diffraction (XRD) the diameter d_{crys} of the crystalline part of the NP core can be determined. For this, a diffractogram has to be recorded. Briefly, and in most of the cases, a NP powder solid sample is irradiated with monochromatic X-ray radiation, and the diffraction (i.e., the change of the direction of the elastically scattered radiation) is recorded. For a crystalline material, diffraction occurs only for several angles, named Bragg's angles (Θ). Such angles are associated with crystallographic planes, which depend on the unit cell parameter of the analyzed material. In a typical XRD experiment, the intensity (i.e., number of counts in the detector for a determined Θ) is plotted versus the double of the diffraction angle (2Θ). The number and position of peaks in a powder diffractogram can be used for phase identification, since every individual crystalline compound has its own "fingerprint", which is determined by its crystallographic structure. The intensity of the peaks (i.e., the number of counts in the detector for a determined 2Θ) is related to the atomic positions in the crystalline unit cell, and the width of every peak is connected with the crystallite size and microstrain in the corresponding crystallographic direction.

The crystallite size for a crystalline direction, determined by a crystallographic plane and a Bragg's angle (Θ), can be estimated with the Scherrer equation:

$$d_{\mathrm{crys}} = \frac{K\lambda}{\beta \cos \Theta} \tag{31}$$

where d_{crys} is the crystallite size. K is the shape factor or Scherrer constant, which varies in the range $0.89 < K < 1$, and usually $K = 0.9$. λ is the wavelength of the X-ray (for Cu Kα = 0.15418 nm). β is the line broadening at half the maximum intensity (fwhm). Θ is the Bragg's angle of the analyzed peak.

For single crystal NPs, the crystallite size d_{crys} estimated by the Scherrer equation is expected to be very similar to the geometric particle size d_c as determined by other characterization techniques such as TEM.[122] In the case of polycrystalline NPs, the obtained crystalline sizes are much smaller than the actual NP size.

Here, X-ray diffraction (XRD) studies were carried out using a Panalytical X'Pert Pro diffractometer equipped with an X-Celerator detector. The NPs were deposited on a silicon sample holder. In this instrument a $\Theta:\Theta$ Bragg–Brentano geometry is used, in which the sample is fixed, the tube rotates at a rate $\Theta°$/min, and the detector rotates at the same rate of $\Theta°$/min. In Figure 78 data obtained with dodecanethiol-capped Au NPs (≈4 nm core diameter, cf. Section 1.2) overcoated with PMA (cf. Section 6.3) are shown. The XRD pattern indicates that the analyzed NPs consisted of *fcc* Au crystals (PDF card number: 00-004-0784).

The peak corresponding to the (111) plane (2Θ around 38.5°) was used to determine the crystallite size. It should be taken into account that Θ values (and not 2Θ) should be used, as well as radian units (and not degrees), especially for the β
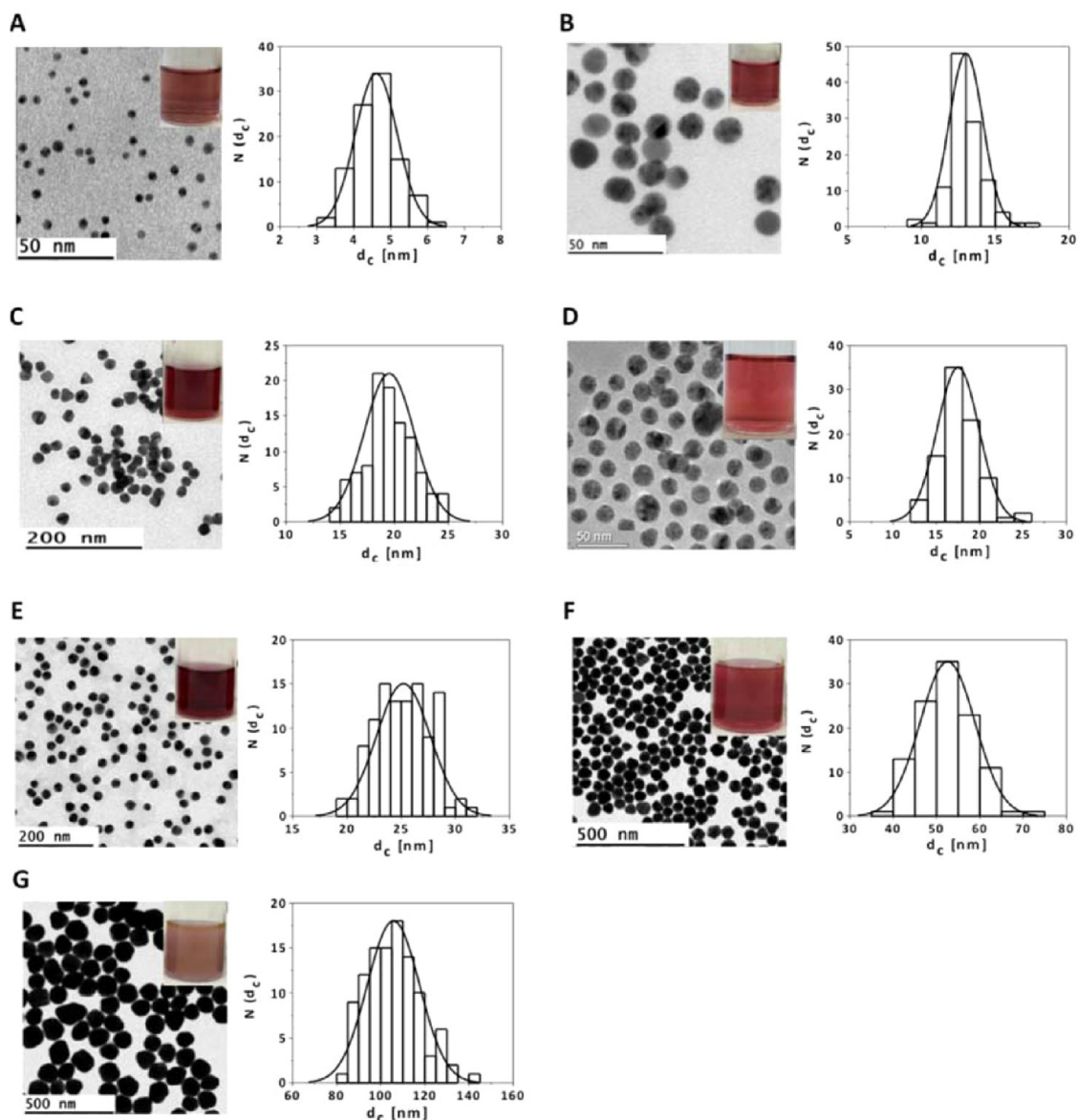
Figure 70. TEM images of Cit-Au NPs (cf. Section 2.2) dried on a grid from a suspension of NPs in water and their corresponding size distribution histograms, plotted as number of NPs $N(d_c)$ that have a core diameter of d_c. From these histograms, the mean NP diameter d_c and its standard deviation were determined for each preparation. Insets show images of glass vials filled with Cit-Au NPs suspension of each preparation. (A) Cit-Au NPs with $d_c = (4.6 \pm 0.5)$ nm; the scale bar corresponds to 50 nm. (B) Cit-Au NPs with $d_c = (13 \pm 1)$ nm; the scale bars correspond to 50 nm. (C) Cit-Au NPs with $d_c = (19 \pm 2)$ nm; the scale bar corresponds to 200 nm. (D) Cit-Au NPs with $d_c = (17 \pm 3)$ nm; the scale bar corresponds to 50 nm. (E) Cit-Au NPs, ≈25 nm core diameter, grown on 18 nm seeds, $d_c = (25 \pm 2)$ nm; the scale bar corresponds to 200 nm. (F) Cit-Au NPs with $d_c = (53 \pm 6)$ nm, the scale bar corresponds to 500 nm. (G) Cit-Au NPs with $d_c = (106 \pm 12)$ nm; the scale bar corresponds to 500 nm.

(fwhm) value. The first step consisted of the appropriate plot of the desired peak (intensity I versus Θ). The determination of the full width at half-maximum (fwhm) value was carried out by fitting the peak. In most of the cases a GauSamp function provides accurate results (cf. Figure 79).

In the presented case, the following values were obtained: $\Theta = 19.198°$; fwhm = 1.457° = 0.0255 rad. Thus, according to eq 31, $d_{crys} = (K \times \lambda)/(\beta \cdot \cos(\Theta)) = (0.9 \times 0.15418$ nm$)/(0.0255 \times \cos(19.198°)) = 5.7$ nm. In this way the crystallite size determined from the width of the (111) peak was $d_{crys} = 5.7 \pm 0.2$ nm, in acceptable agreement with the TEM data (cf. Figure 64 and the actually determined value for the batch used here was $d_c = 4.3$ nm).

8.6. Thermogravimetric Analysis of NPs. Thermogravimetric analysis (TGA) measures the mass of a sample, while its

temperature is continuously increased. Upon decomposition of parts of the sample its mass decreases and thus allows for analyzing the composition of the sample. In the case of inorganic NPs upon heating the solvent may be evaporated, as the organic shell around the NP surface may decompose. In this section, calculation of the weight contribution of the organic coating on NPs to the total weight of the NPs will be detailed.

In Figure 80A the TGA analysis carried out on DDT-Au NPs (≈ 4 nm core diameter, cf. Section 1.2) is shown. A suspension of the hydrophobic NPs in chloroform was added dropwise to an alumina sample holder, and the solvent was evaporated in an oven at 40 °C. The process was repeated until around $m_{NP\_pel} \approx 2$ mg of NPs were deposited on the sample holder. TGA was performed in air at a heating rate of 5 °C·min^{-1}, using a Q600 TA Instrument.
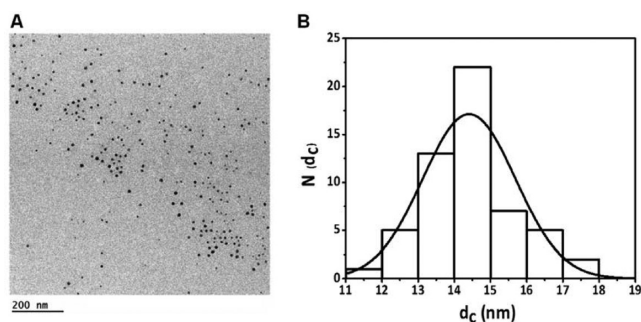
Figure 71. (A) TEM image of Cit-Ag NPs (cf. Section 2.3) dried on a grid from a suspension of NPs in water. The scale bar corresponds to 200 nm. (B) Size distribution histogram, plotted as number of NPs $N(d_c)$ that have a core diameter of d_c. From this histogram the mean NP diameter d_c and its standard deviation were determined to be $d_c = (15 \pm 1)$ nm.

The TGA curve corresponding to the dodecanethiol-capped Au NPs (Figure 80A) showed a very slight loss (<1%) in the 25−150 °C range, as expected from hydrophobic NPs. An abrupt loss (around 18%) took place between 150 and 300 °C, which should be caused by the decomposition of the DDT. No changes in the mass were observed at higher temperatures. Based on these data, an estimation of the amount of the organic coating ($m_{NP,org}$, comprising the original DDT ligand in this case) deposited on the NPs surface can be determined. The diameter of the inorganic Au core of this batch of Au NPs had been determined to be $d_c = 4.3$ nm. The mass m_{NP} of one NP comprises the mass of the inorganic core m_c and the mass of the organic coating $m_{NP,org}$:

$$m_{NP} = m_c + m_{NP,org} \tag{32}$$

In the present case according to eq 20 and eq 23 the volume V_c and the mass m_c of one NP core could be calculated. For a spherical Au NP with core diameter $d_c = 4.3$ nm, $V_c = (\pi/6) \times (4.3 \text{ nm})^3 \approx 41.6 \text{ nm}^3$. Given the bulk density of Au of $\rho_{Au} = 19.3 \text{ g/cm}^3$, the mass of one Au core thus is $m_c = 19.3 \text{ g/cm}^3 \times 41.6 \text{ nm}^3 \approx 803 \text{ g} \times (10^{-9} \text{ m}/10^{-2} \text{ m})^3 \approx 8.0 \times 10^{-19} \text{ g}$ (cf. Section 8.1).

In the data shown in Figure 80A, the absolute weights for the NP pellet ($m_{NP\_pel}(T)$) were $m_{NP\_pel}(25 \text{ °C}) = 1.744$ mg (mass at RT), $m_{NP\_pel}(150 \text{ °C}) = 1.730$ mg, $m_{NP\_pel}(340 \text{ °C}) = 1.424$ mg, and $m_{NP\_pel}(700 \text{ °C}) = 1.421$ mg (final mass). We considered that at 700 °C only the NP cores were present. The number of cores (and thus of NPs) in the sample thus was $N_c = m_{NP\_pel}(700 \text{ °C})/m_c = 1.421 \times 10^{-3} \text{ g}/8.0 \times 10^{-19} \text{ g} = 1.77 \times 10^{15} \approx 1.8 \times 10^{15}$. We attributed the mass of the organic coating (DDT) to the mass lost upon heating from 150 to 340 °C: $m_{NP,org\_pel} = m_{NP\_pel}(150 \text{ °C}) − m_{NP\_pel}(340 \text{ °C}) = 1.730$ mg − 1.424 mg = 0.306 mg. Thus, the mass of the organic coating around one NP is $m_{NP,org} = m_{NP,org\_pel}/N_c = 0.306 \times 10^{-3} \text{ g}/1.8 \times 10^{15} \approx 1.7 \times 10^{-19} \text{ g}$. Therefore, the whole mass of one Au NP is according to eq 32 $m_{NP} = m_c + m_{NP,org} = 8.0 \times 10^{-19} \text{ g} + 1.7 \times 10^{-19} \text{ g} \approx 9.7 \times 10^{-19} \text{ g}$. The organic coating thus contributed $m_{NP,org}/m_{NP} = 1.7 \times 10^{-19} \text{ g}/9.7 \times 10^{-19} \text{ g} \approx 17\%$ of the mass of one NP.

The TGA analysis of the DDT-Au NPs overcoated with PMA (cf. Section 6.3) is shown in Figure 80B. The PMA-Au NPs, which were suspended in water were cleaned by ultracentrifugation (cf. Section 7.2). In this case, the sample was dried before analysis, and around $m_{NP\_pel} \approx 1$ mg of pelleted PMA coated NPs were placed in an alumina sample

holder. TGA was also performed in air at a heating rate of 5 °C·min^{-1}, using the same Q600 TA Instrument.

The TGA curve of the DDT-Au NPs overcoated with PMA showed a slight weight loss (around 5%) in the 25−150 °C range, which can be ascribed to the release of absorbed water. An additional abrupt loss (around 26%) took place between 150 and 300 °C, which should be caused by the decomposition of the dodecanethiol and/or the amphiphilic polymer poly-(isobutylene-*alt*-maleic anhydride)-*graft*-dodecyl (PMA). Almost no changes in the mass were observed at higher temperatures. As in the previous hydrophobic sample, the TGA data could be used to estimate the mass of organic coating $m_{NP,org}$ of one Au NP. The mass of an Au NP core was calculated as described above to be 8.0×10^{-19} g.

The absolute weights $m_{NP\_pel}(T)$ in Figure 80B were $m_{NP\_pel}(25 \text{ °C}) = 1.032$ mg (mass at RT), $m_{NP\_pel}(150 \text{ °C}) = 0.990$ mg, $m_{NP\_pel}(340 \text{ °C}) = 0.711$ mg, $m_{NP\_pel}(700 \text{ °C}) = 0.693$ mg (final mass). As in the previous sample, we considered that at 700 °C only the NP cores were present. The number of cores (and thus of NPs) in the sample thus was $N_c = m_{NP\_pel}(700 \text{ °C})/m_c = 0.693 \times 10^{-3} \text{ g}/8.0 \times 10^{-19} \text{ g} = 8.66 \times 10^{14} \approx 8.7 \times 10^{14}$. We attributed the mass of the organic coating to the mass lost upon heating from 150 to 340 °C: $m_{NP,org\_pel} = m_{NP\_pel}(150 \text{ °C}) − m_{NP\_pel}(340 \text{ °C}) = 0.990$ mg − 0.711 mg = 0.279 mg. Thus, the mass of the organic coating around one NP was $m_{NP,org} = m_{NP,org\_pel}/N_c = 0.279 \times 10^{-3} \text{ g}/8.7 \times 10^{14} = 3.21 \times 10^{-19} \text{ g} \approx 3.2 \times 10^{-19} \text{ g}$. Thus, the whole mass of one Au NP was according to eq 32 $m_{NP} = m_c + m_{NP,org} = 8.0 \times 10^{-19} \text{ g} + 3.2 \times 10^{-19} \text{ g} \approx 11.2 \times 10^{-19} \text{ g}$. The organic coating thus contributed $m_{NP,org}/m_{NP} = 3.2 \times 10^{-19} \text{ g}/11.2 \times 10^{-19} \text{ g} \approx 29\%$ of the mass of one NP. The contribution of the organic coating for the dodecanethiol-capped Au NPs over-coated with PMA was thus higher than for the hydrophobic DDT-Au NPs, as expected. Note that for bigger NP cores the percentage contribution of the organic coating would be much lower, but in the case of very small NPs it is highly relevant.

The TGA analysis of dried PMA (cf. Section 6.2) is shown in Figure 81. Note that PMA decomposed from 200 to ca. 500 °C; however, in the PMA-coated Au NPs (Figure 80B) the main mass loss took place from 200 to 300 °C, and the mass of the sample remained almost constant above this temperature. The mass loss observed in the PMA polymer above ca. 350 °C may thus have corresponded to the evaporation of impurities, which may have originated from the precursors used for its synthesis. By using ultracentrifugation (cf. Section 7.2), such impurities can be removed from the coated NPs.

Based on these data some quantitative analysis concerning the organic surface coating can be performed. In the case of the DDT capped Au NPs the number $N_{DDT/NP}$ of DDT molecules per Au NP can be calculated, by assuming that the organic surface coating only comprises DDT.

$$m_{NP,org} = m_{NP,DDT} \tag{33}$$

Using the molar mass of DDT $M_{ligand} = M_{DDT} = 202.40$ Da thus leads to

$$N_{DDT/NP} = (m_{NP,org}/M_{ligand}) \times N_A \tag{34}$$

For the DDT-Au NPs ($d_c = 4.3$ nm) as analyzed here with TGA the following result was obtained as described above: $m_{NP,org} = 1.7 \times 10^{-19}$ g. Thus, $N_{DDT/NP} = (m_{NP,org}/M_{DDT}) \times N_A = (1.7 \times 10^{-19} \text{ g}/202.40 \text{ g·mol}^{-1}) \times 6.02 \times 10^{23} \text{ mol}^{-1} = 506$ DDT molecules are assumed to be situated at the surface of the DDT-Au NPs. The surface of one Au core is
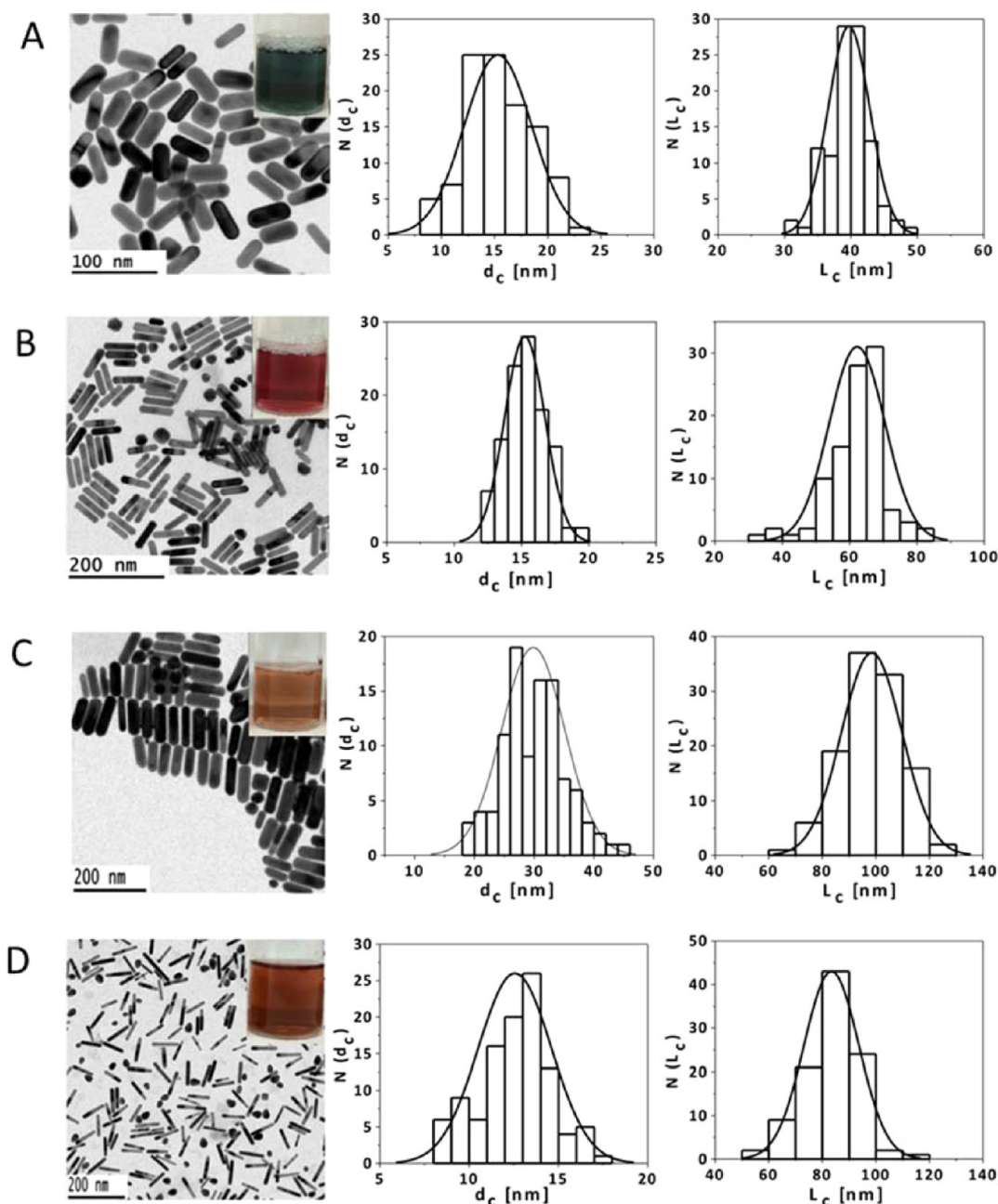
Figure 72. TEM images of CTAB- Au NRs (cf. Section 2.4) dried on a grid from a suspension of NPs in water and the corresponding size distribution histograms, plotted as number of NPs $N(d_c)$ that have a core diameter of d_c (histograms to the left) or as number of NPs $N(L_c)$ that have a core length of L_c (histograms to the right). From these histograms the mean NP diameter d_c and its standard deviation, as well as the mean length L_c and its standard deviation, were determined for each preparation. Insets show images of glass vials filled with CTAB-Au NRs suspension of each preparation. (A) λ_{SPR} = 650 nm, d_c = (16 ± 5) nm, and L_c = (40 ± 3) nm; the scale bar corresponds to 100 nm. (B) λ_{SPR} = 825 nm, d_c = (15 ± 1) nm, and L_c = (62 ± 8) nm; the scale bar corresponds to 200 nm. (C) λ_{SPR} = 790 nm, d_c = (30 ± 5) nm, and L_c = (98 ± 11) nm; the scale bar corresponds to 200 nm. (D) λ_{SPR} = 1050 nm, d_c = (13 ± 2) nm, and L_c = (83 ± 10) nm; the scale bar corresponds to 200 nm. λ_{SPR} corresponds to their surface plasmon peak.

$$A_c = 4\pi \times (d_c/2)^2 = \pi \cdot d_c^2 \qquad (35)$$

and thus in the present case $A_c = \pi \cdot (4.3 \text{ nm})^2 \approx 58.1 \text{ nm}^2$. In this way the surface area which is occupied by each DDT molecule is

$$A_{c,DDT} = A_c / N_{DDT/NP} \qquad (36)$$

In the present case each DDT molecule covers $A_{c,DDT}$ = 58.1 nm²/506 ≈ 0.11 nm² surface area. This is less than observed for

the highest packing density of alkanethiols on the regular smooth Au(111) surface of 0.214 nm².[123] The discrepancy might be explained by several arguments. Due to the highly curved surface more thiols may be bound per surface area according to a radius-of-curvature effect, which leaves more space for the alkyl chains pointing toward solution.[53] Due to the typical size distribution of Au cores (such as shown in Figure 64), there is a part of the NPs with d_c smaller than the average value and thus with a higher surface-to-volume ratio,
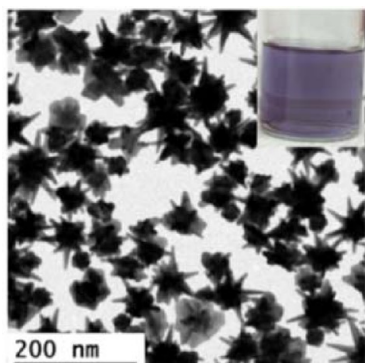
Figure 73. TEM image of hydrophilic star-shaped Au NPs (cf. Section 2.5) dried on a grid from a suspension of NPs in water. The scale bar corresponds to 200 nm. The inset shows glass vials filled with a suspension of star-shaped Au NPs.

and thus more thiols can bind. Despite purification there still may be excess ligand (DDT) in solution. The ligand exchange from TOAB-Au NPs to DDT-Au NPs may have been incomplete, leading to the presence of ligands others than DDT on the Au surface. In addition, the assumed monolayer formation of DDT may not be completely true, and some more DDT may be attached to the NPs, for example, due to intercalation. TGA thus helps to verify assumptions about the structure of NPs.

Also for the PMA coated Au NPs some quantitative analysis can be performed.[124] In this case the mass of the organic surface coating around one NP comprises the underlying DDT layer $m_{NP,DDT}$ and the PMA-based polymer $m_{NP,P}$ wrapped around it.

$$m_{NP,org} = m_{NP,DDT} + m_{NP,P} \qquad (37)$$

According to the TGA results in this section the DDT contributes to 17% of the mass of one DDT-Au NP, whereas the DDT plus PMA-based polymer contributes to 29% of the mass of one PMA-Au NP. Thus, based on the TGA data of $m_{NP,org} = 3.2 \times 10^{-19}$ g for PMA-Au NPs the following contributions can be calculated: $m_{NP,DDT} = (17\%/29\%) \times m_{NP,org} = (17/29) \times 3.2 \times 10^{-19}$ g $\approx 1.9 \times 10^{-19}$ g and $m_{NP,P} = ((29\%-17\%)/29\%) \times m_{NP,org} = (12/29) \times 3.2 \times 10^{-19}$ g $\approx 1.3 \times 10^{-19}$ g. By using the molar mass of one polymer monomer (cf. eq 14), the number of polymer monomers bound per NP can be calculated as

$$N_{P/NP} = (m_{NP,P}/M_P) \times N_A \qquad (38)$$

Using the value of $M_P = 293$ g/mol for PMA-based polymers as calculated in Section 6.2 leads to $N_{P/NP} = (m_{NP,P}/M_P) \times N_A = (1.3 \times 10^{-19}$ g/293 g/mol$) \times 6.02 \times 10^{23}$ mol$^{-1} \approx 270$ polymer monomer units bound to each PMA-Au NP. This value can be now compared to the number of polymer monomer units $N_{P/NP(added)}$ that have been added to each DDT-Au NP during the formation of PMA-Au NPs.

$$N_{P/NP(added)} = R_{P/Area} \times A_{eff} \qquad (39)$$

In the present case the following parameters were used: $l_{ligand} = l_{DDT} = 1$ nm (cf. Table 5), resulting in $d_{eff} = d_c + 2 \times l_{ligand} = 4.3$ nm + 2×1 nm = 6.3 nm, and thus according to eq 15 in $A_{eff} = \pi \cdot d_{eff}^2 = \pi \cdot (6.3$ nm$)^2 \approx 124$ nm^2. Therefore, $N_{P/NP(added)} = R_{P/Area} \times A_{eff} = 100$ nm$^{-2} \times 124$ nm$^2 = 12\,400$ polymer monomer units had been added per NP upon the polymer coating procedure. The fact that $N_{P/NP} \ll N_{P/NP(added)}$ demonstrates that most added polymer actually has not bound to the NPs, and thus purification of NP solutions from excess polymer is crucial.
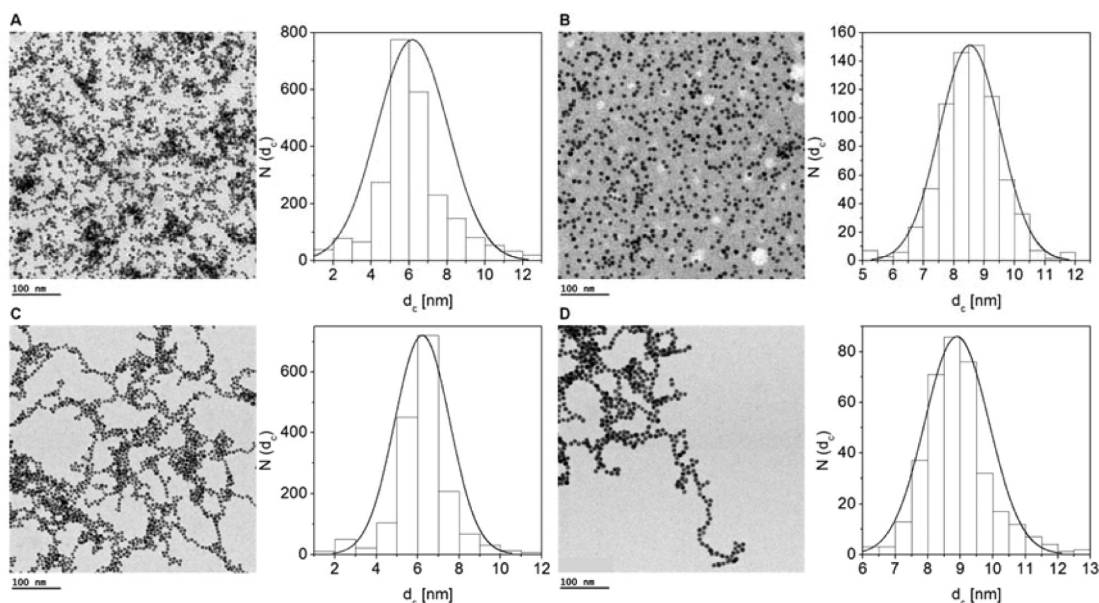

Figure 74. TEM images of Cit-Au NPs (cf. Section 2.2) dried on a grid from a suspension of NPs in water and their corresponding size distribution histograms before (A zand C) and after (B and D) ligand exchange with bis(p-sulfonatophenyl)-phenylphosphine (cf. Section 3.2). Histograms are plotted as number $N(d_c)$ of NPs which have a core diameter d_c. From these histograms the mean NP diameter d_c and its standard deviation were determined. All scale bars correspond to 100 nm. (A) Cit-Au NPs before ligand exchange with $d_c = (6.0 \pm 1.1)$ nm. (B) Au NPs after exchanging the original citrate capping ions with bis(p-sulfonatophenyl)-phenylphosphine with, $d_c = (8.7 \pm 1.0)$ nm. (C) Cit-Au NPs before ligand exchange with $d_c = (6.3 \pm 0.8)$ nm. (E) Au NPs after exchanging the original citrate capping ions with bis(p-sulfonatophenyl)-phenylphosphine with $d_c = (8.9 \pm 0.8)$ nm.
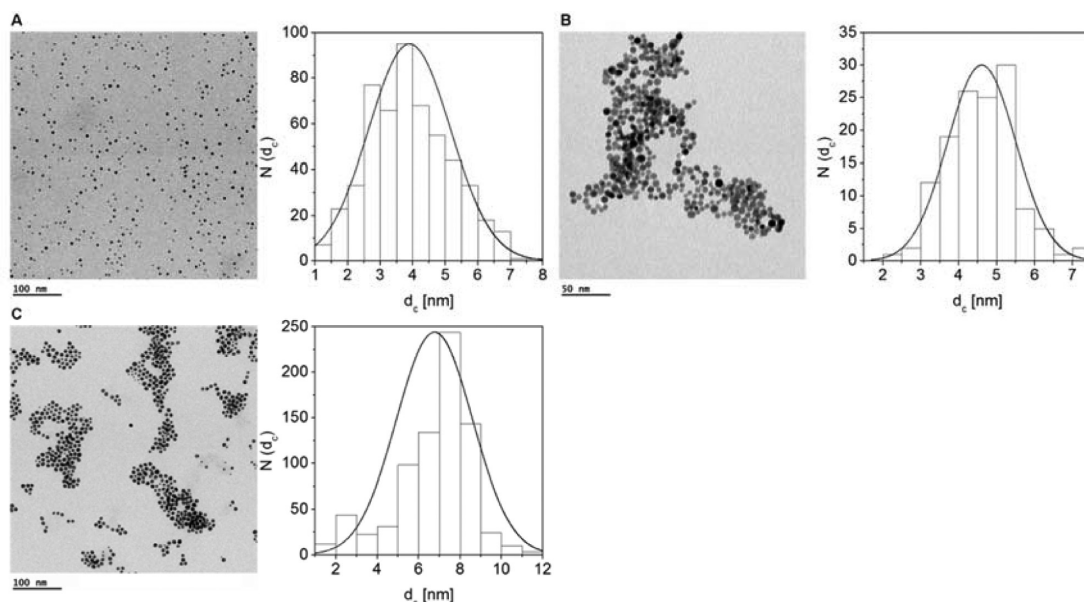
Figure 75. TEM images of PMA-Au NPs, made by DDT-Au NPs (cf. Section 1.2), which have been transferred to aqueous solution using PMA-*g*-dodecyl polymer coating or ligand exchange method (cf. Section 6.3 and Section 5.2, respectively) and dried on a grid from a suspension of NPs in water, along with corresponding size distribution histograms. Histograms are plotted as number of NPs $N(d_c)$ that have a core diameter d_c to calculate the mean NP diameter d_c and its standard deviation. (A) PMA-Au NPs (DDT-Au NPs after coating with PMA-*g*-dodecyl polymer, Section 6.3) with $d_c = (4.1 \pm 1.1)$ nm; the scale bar corresponds to 100 nm. (B) Au NPs originally capped with hexanoic acid, ≈4 nm core diameter, after ligand exchange with mercaptopropionic acid (cf. Section 5.2), $d_c = (4.4 \pm 0.9)$ nm; the scale bar corresponds to 50 nm. (C) Au NPs originally capped with decanoic acid, ≈7 nm core diameter, after ligand exchange with mercaptoundecanonic acid (cf. Section 5.2), $d_c = (7.1 \pm 1.3)$ nm; the scale bar corresponds to 100 nm.
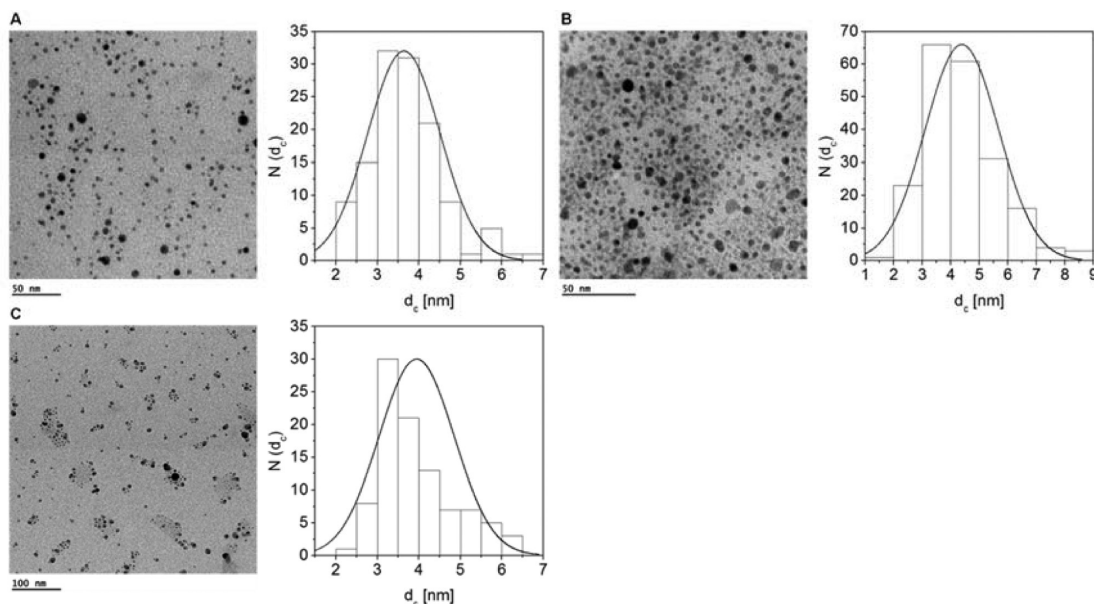
Figure 76. TEM images of hydrophobic Ag NPs originally capped with dodecanethiol of ≈4 nm core diameter (cf. Section 1.3), which have been transferred to aqueous solution using PMA-*g*-dodecyl polymer coating or the ligand exchange method (cf. Section 6.3 and Section 5.2, respectively) and dried on a grid from a suspension of NPs in water. Histograms are plotted as number of NPs $N(d_c)$ that have a core diameter d_c to calculate the mean NP diameter d_c and its standard deviation. (A) PMA-Ag NPs (DDT-Ag NPs after coating with PMA-*g*-dodecyl polymer, Section 6.3) with $d_c = (3.6 \pm 0.9)$ nm; the scale bar corresponds to 50 nm. (B) Ag NPs after ligand exchange with mercaptopropionic acid (cf. Section 5.3), $d_c = (4.4 \pm 1.3)$ nm; the scale bar corresponds to 50 nm. (C) Ag NPs after ligand exchange with mercaptoundecanonic acid (cf. Section 5.3), $d_c = (4.4 \pm 1.3)$ nm; the scale bar corresponds to 100 nm.

8.7. Infrared Spectroscopy.

Fourier transform infrared spectroscopy (FTIR) allows for analyzing the chemical structure of the organic shell around NP cores. As a vibrational spectroscopy with a specific vibrational fingerprint for specific functional groups, FTIR can be used to qualitatively describe the organic shell around NPs and thus can be employed to follow up surface functionalization or ligand exchange. Moreover, deviations in typical vibrational features of adsorbing functional groups on the surface of NPs can be used to describe the type and orientation of organic ligand−core interaction. In
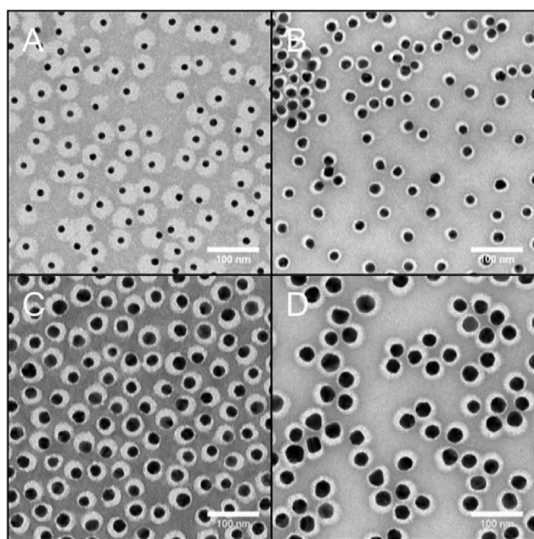
Figure 77. Visualizing the PEG shell around PEG-Au NPs using TEM imaging and the negative staining technique with uranyl acetate[56] (cf. Section 2.2 and Section 3.3). (A) Au cores (d_c = 13.7 ± 0.7 nm) plus an organic shell of PEG (10 kDa, l_{ligand} = 11.8 ± 1.2 nm) results in d_{eff} = 37.4 ± 2.5 nm. (B) Au cores (d_c = 18.9 ± 1.9 nm) plus an organic shell of PEG (1 kDa, l_{ligand} = 3.2 ± 0.4 nm) results in d_{eff} = 25.4 ± 2.1 nm. (C) Au cores (d_c = 23.5 ± 1.7 nm) plus an organic shell of PEG (5 kDa, l_{ligand} = 11.8 ± 1.5 nm) results in d_{eff} = 37.4 ± 1.5 nm. (D) Au cores (d_c = 30.1 ± 2.6 nm) plus an organic shell of PEG (3 kDa, l_{ligand} = 7.7 ± 1.0 nm) results in d_{eff} = 45.6 ± 3.6 nm. Mean and corresponding standard deviation values of the core (d_c), ligand shell (l_{ligand}), and the effective size (d_{eff}) were obtained by analyzing several negative staining TEM micrographs (>1000 NPs) as described by del Pino et al.[56] TEM images were segmented using Matlab (Mathworks) and Cellprofiler.[121] The scale bars are 100 nm.
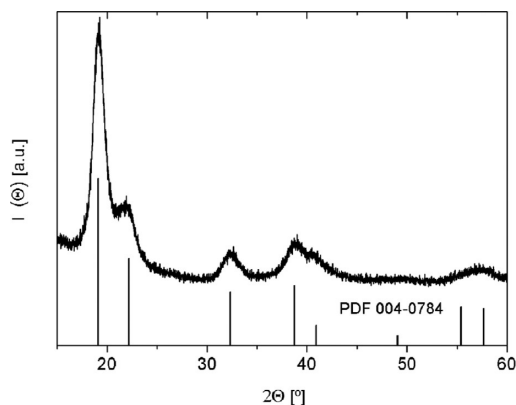
Figure 78. XRD diagram $I(\Theta)$ of polymer coated Au NPs (≈4 nm core size, cf. Section 1.2 and Section 6.3). The PDF pattern of cubic gold has also been included.

the present work FTIR analysis of DDT-Au NPs (≈4 nm core diameter, cf. Section 1.2) before and after overcoating with PMA (cf. Section 6.3), as well as for free PMA as control, were carried out and compared. Spectra were measured with a Thermo Nicolet 6700 FT-IR. Sample purity is essential, and thus initial the DDT-Au NP sample was purified as described above (cf. Section 1.2) and PMA-coated Au NPs (cf. Section 6.3) were purified following the protocol mentioned above (cf. Section 7.5), while PMA was used directly as-synthesized (cf. Section 6.2). DDT-Au NPs and PMA solutions were dissolved in chloroform, and they were left to evaporate to get solid
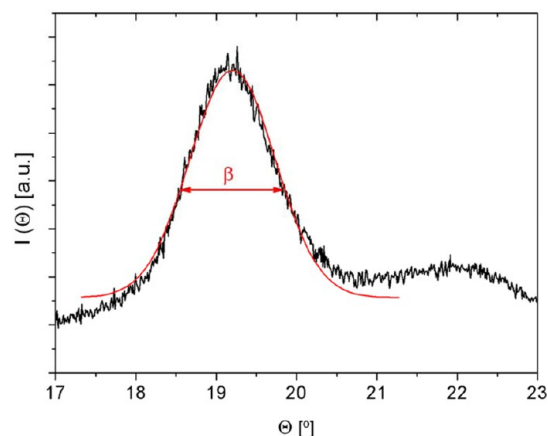

Figure 79. XRD diagram $I(\Theta)$ of the (111) plane of polymer coated Au NPs (≈4 nm core size, cf. Section 1.2 and Section 6.3). The red line represents the GauSamp fit of the peak. This graph is a part of the graph shown in Figure 78.
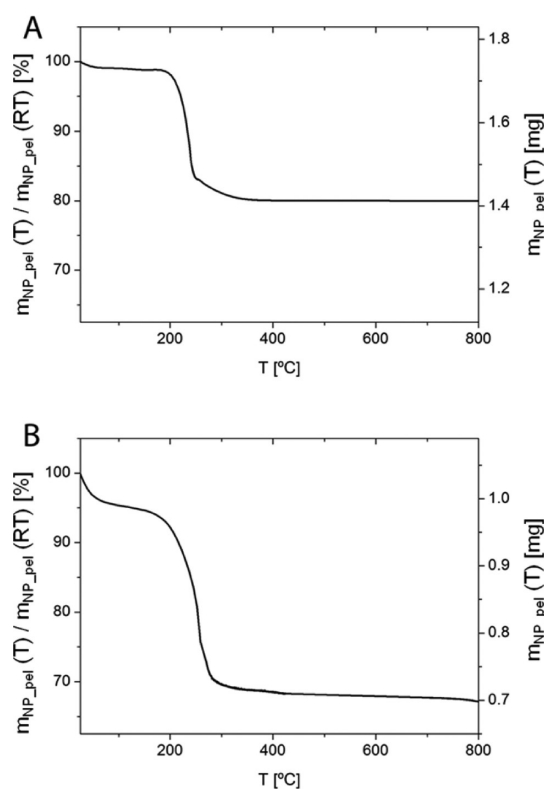

Figure 80. TGA analyses of DDT-Au NPs (A) and DDT-Au NPs overcoated with PMA (B). In both graphs, $m_{NP\_pel}(T)$ describes the mass of the NP pellet at temperature T. The masses are normalized to the mass $m_{NP\_pel}(RT)$ at RT. The same scale in the left y-axis is used to facilitate the comparison. For both samples d_c = 4.3 nm.

samples, whereas the aqueous solution of PMA-coated Au NPs was lyophilized prior to the preparation of the KBr pellets. These pellets were prepared at a 1% concentration of the sample, i.e., m_{NP_pel} = 2 mg of the dried NP sample was mixed with 200 mg of KBr, grinding until a homogeneous mixture was obtained, and finally the pellet was formed by using a hand press. For the measurements, 50 scans were recorded with a Thermo Nicolet 6700 FT-IR, and the presented FTIR spectra of 50 scans at 4 cm^{-1} resolution were averaged. Data are presented in Figure 82.
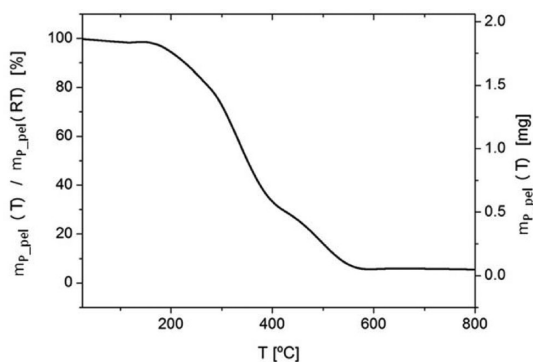
Figure 81. TGA analysis of PMA. $m_{P\_pel}(T)$ describes the mass of the PMA at temperature T. The mass is normalized to the mass $m_{P\_pel}(RT)$ at RT.
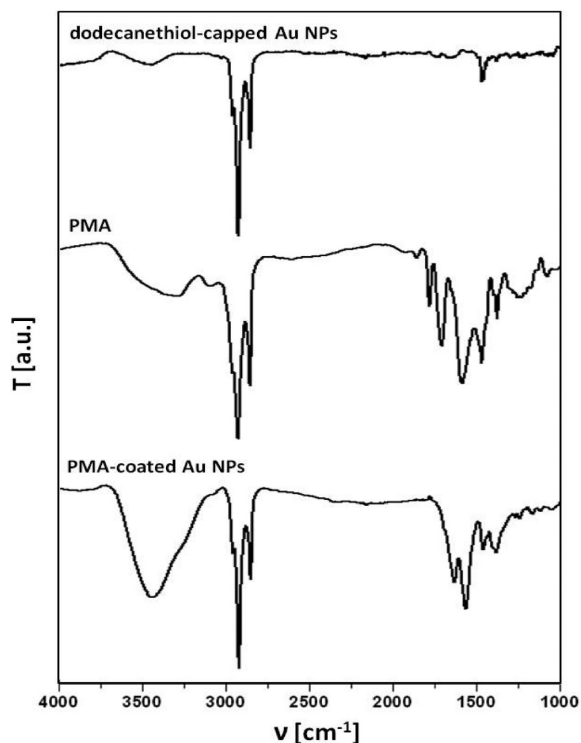

Figure 82. FTIR spectrum (transmission mode $T(\nu)$, i.e., transmission T versus wavenumber ν) of DDT-Au NPs of ≈ 4 nm core diameter before and after overcoating with PMA. The spectrum of free PMA is shown as control.

The DDT-Au NPs exhibited only three significant peaks. The strong peaks at 2923 and 2853 cm^{-1} were assigned to the asymmetric and symmetric C−H stretching of the alkyl chain, respectively, and the peak at 1460 cm^{-1} was assigned to the bending vibrations of C−H. In contrast, the PMA polymer (cf. Figure 48) presented more peaks. The strong peaks at 2925 and 2854 cm^{-1} were assigned to the asymmetric and symmetric C−H stretching of the alkyl chains. The broad and weak adsorption peak from 3200−3600 cm^{-1} corresponded to the presence of the O−H stretching resonance of the carboxylic acids formed after the anhydride opening. The two peaks at 1780 and 1705 cm^{-1} were characteristic of the cyclic anhydride with 5-membered rings. The peak of the symmetric stretching vibrations of C=O from the carboxylic groups overlapped with the peak at 1705 cm^{-1}. At 1583 cm^{-1} the symmetric stretching

vibrations of N−C=O of the amide groups appeared. The 1468 and 1375 cm^{-1} peaks were assigned to the angular deformation of CH$_2$ and CH$_3$, respectively. When the DDT-Au NPs were overcoated with the amphiphilic PMA polymer, the IR spectrum of the resulting PMA-coated Au NPs had the same peaks as the DDT-Au NPs and some additional peaks from the PMA, such as the peaks at 1635 and 1565 cm^{-1} assigned to the symmetric stretching vibrations of C=O from the carboxylic groups and N−C=O from the amide groups, respectively. Here, again the 1466 and 1384 cm^{-1} peaks from the angular deformation of CH$_2$ and CH$_3$ appeared, respectively. Additionally, there was a broad and intense band from 3000−3600 cm^{-1} corresponding the O−H stretching resonance of the carboxylic acids formed when the NPs had been transferred to water and then all the anhydride rings had been opened. Collectively, FTIR results indicated the surface modification (overcoating) of DDT-Au NPs with PMA.

In summary, FTIR analysis of NPs allows for knowing which ligands and chemical groups are present on the NP surface. This serves to confirm that the functionalization strategy (e.g., polymer coating or ligand exchange/displacement) worked properly.

8.8. Nuclear Magnetic Resonance. Nuclear magnetic resonance spectroscopy (NMR) is a powerful tool to probe the chemical structure of the organic shell around the inorganic NP core. NMR is mainly used to provide evidence on the presence and orientation of organic molecules/ligands around NPs. NMR works well to analyze small molecules, but it may get complicated in the case of large constructs, due to the heterogeneity and reduced flexibility of the analyzed constructs.

In the present work we analyzed the NMR spectra of PMA before and after the coating of ≈ 4 nm DDT-Au NPs (cf. Section 1.2 and Section 6.3). A ^{1}H NMR spectrum of PMA in CDCl$_3$ (i.e., chloroform where the proton ^{1}H was substituted by a deuteron D = ^{2}H) was first measured. As expected nonresolved broad bands were observed as a result of the size distribution of the starting poly(isobutylene-*alt*-maleic anhydride)-*graft*-dodecyl and the random distribution of dodecylamine moieties along the polymer chain. In this situation it was possible to distinguish broad singlets (br s) between 3.66 and 2.63 ppm corresponding to −C*H*− protons, 1.69−0.92 ppm corresponding to −C*H$_2$*− protons, and 0.90−0.80 ppm corresponding to −C*H$_3$*− protons (cf. Figure 83A). A ^{13}C NMR spectrum was also measured observing good resolution for nonquaternary carbon atoms due to their higher signal intensity compared to quaternary ones such as *C*=O, for instance (cf. Figure 83B). The peak assignment both in ^{1}H and ^{13}C NMR was based on the chemical shift (δ) and was aided by 2D HSQC experiment (heteronuclear single quantum correlation) edited for distinguishing CH$_2$ signals from CH and CH$_3$.

^{1}H NMR of PMA coated Au NPs (≈ 4 nm core diameter, cf. Section 1.2) was measured in water with 15% of deuterium oxide, using a sequence for suppressing water signal. When PMA was coating the Au NPs, there were no longer cyclic anhydrides present and two separate peaks were observed for −C*H* protons: those linked to amide groups and kept inside the hydrophobic core, and those linked to carboxylic groups and exposed to the water phase. Those nuclei had very different environments and hence different chemical shifts. Interestingly, when this spectrum was compared with that of PMA treated with NaOH to open all the anhydride groups and measured under the same conditions (H$_2$O with 15% D$_2$O) a somehow
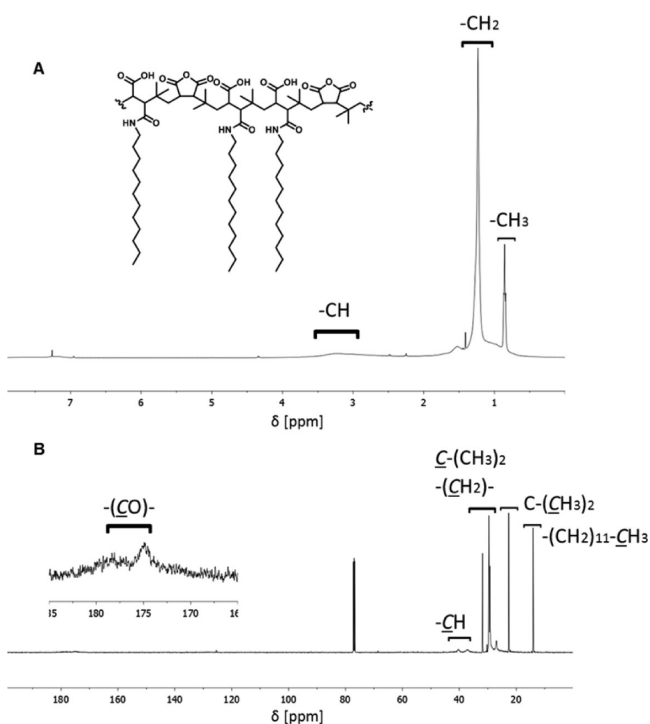
Figure 83. (A) ^{1}H NMR spectrum of PMA in CDCl$_3$. (B) ^{13}C NMR spectrum of PMA in CDCl$_3$; the zoomed area shows the peaks for the carbonyl groups.

different profile was observed. The CH peak was barely visible, and only the CH$_2$ and CH$_3$ peaks were clearly visible, although the ratio between them was modified (CH$_2$/CH$_3$ ≈ 2 in PMA coated Au NPs vs CH$_2$/CH$_3$ ≈ 1 in PMA after NaOH treatment). This shows that PMA molecules arranged differently when free in solution (i.e., forming empty polymer micelles) or when on the surface of Au NPs, but it is difficult to extract further structural information from these experiments.

In summary, NMR spectroscopy can give further evidence of the presence of PMA on the surface of Au NPs of ≈4 nm and can also be used to check the purity of those NPs by confirming the absence of other organic molecules such as organic solvents or glycerol from the filters. However, the heterogeneity of PMA polymer and the poor ability of some of the protons to resonate when linked to Au NPs led to poor resolution spectra that could only be interpreted from a qualitative point of view.

^{1}H and ^{13}C spectra were recorded in a Bruker 500 MHz spectrometer. Chemical shifts are reported in parts per million (ppm) relative to the residual signal of the solvent used, and are listed below:

PMA (cf. Figure 83). ^{1}H NMR (500 MHz, CDCl$_3$) δ 3.66–2.63 (br s, CH), 1.69–0.92 (m, CH$_2$), 0.90–0.80 (m, CH$_3$). ^{13}C NMR (126 MHz, CDCl$_3$) δ 178.08, 174.80, 173.92, 77.00, 40.36, 37.19, 31.86, 30.25, 29.59, 29.30, 29.14, 28.78, 26.98, 22.62, 14.05.

PMA coated Au NPs (cf. Figure 84A). ^{1}H NMR (500 MHz, D$_2$O) δ 3.66 (br s, CH), 2.64 (br s, CH), 1.68 (br s, CH$_2$), 1.31 (br s, CH$_2$), 0.89 (br s, CH$_3$).

PMA after basic treatment (cf. Figure 84B). ^{1}H NMR (500 MHz, D$_2$O) δ 2.40 (br s, CH), 1.08 (br s, CH$_2$), 0.67 (br s, CH$_3$).

9. CHARACTERIZATION OF THE PHOTOPHYSICAL PROPERTIES OF NPs

9.1. UV/Vis Absorption Spectroscopy. UV/vis absorption spectroscopy is an easy and simple method to characterize important properties of colloidal NPs. Several types of NPs, such as quantum dots or plasmonic NPs, have particular features (i.e., resonance peaks) in their absorption spectra, which provide important information regarding NP size, size distribution, and shape. Moreover, UV/vis absorption spectroscopy can be used to determine the concentration of NPs (cf. Section 9.2) and to follow colloidal growth and stability (cf. Section 10.1).

To record absorption spectra for NPs, several issues need to be considered. First, a blank has to be recorded for the pure solvent, which needs to be subtracted from the NP absorption spectrum. Typically (unless, for example, IR absorbing NPs such as gold nanorods are investigated) NP suspensions are transparent at high wavelengths. Spherical Au NPs of a few nm in size have their plasmon absorption peak around 520 nm (cf. Table 8) and do not absorb light at higher wavelengths of ca. 800–1200 nm. In case the measured "absorption" in this range does not converge to zero, in fact scattering and not absorption has been detected. This most likely is due to partial agglomeration of the NP sample (cf. Section 10.1). Thus, before further analysis based of the UV/vis absorption spectra of a NP solution, it has to be made sure that the absorption in the spectra converges toward zero in this range (ca. 800–1200 nm). In case the NPs are well dispersed this should be automatically the case after automated subtraction of the offset. However, in case the offset function does not work, a constant offset may be subtracted manually, until the absorption for high wavelengths (ca. 800–1200 nm, in case there are no absorption
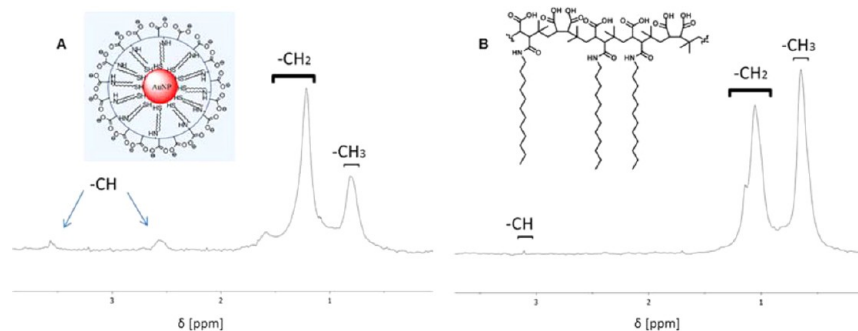

Figure 84. (A) ^{1}H NMR spectrum of PMA coated Au NPs of ≈4 nm core diameter in 15% D$_2$O/H$_2$O mixture. (B) ^{1}H NMR of PMA in 15% D$_2$O/H$_2$O mixture after treatment with base to open all anhydride groups.

Table 8. Values of Surface Plasmon Resonance Maximum Wavelength (λ_{max}) and Molecular Extinction Coefficients, ε_{NP}, (cf. Section 9.2) of Cit-Au NPs of Different Sizes in Water[a]

d_c [nm]	source	λ_{SPR} [nm]	ε_{NP} [M$^{-1}\cdot$cm^{-1}]
4.2	Section 1.2, Section 6.3	516	8.70×10^6
5	BBI solutions	518	9.70×10^6
10	BBI solutions	520	9.55×10^7
15	BBI solutions	523	3.64×10^8
30	BBI solutions	526	3.58×10^9
50	BBI solutions	532	1.93×10^{10}

[a]Extinction coefficients were provided from the manufacturer.

features of the NPs in this range) converges to zero; see Figure 85.
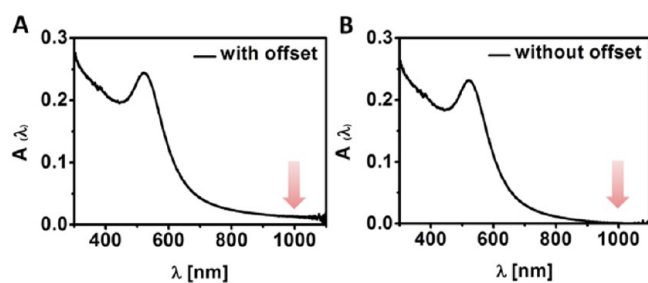
Figure 85. Absorption spectra (absorption (A) as a function of the wavelength λ) of $\approx$4 nm core diameter Au NPs (cf. Section 1.2) coated with PMA in water (cf. Section 6.3). (A) The "raw spectra" include an offset at higher wavelengths. (B) Processed spectra by subtracting the absorption at higher wavelengths from the whole spectra. Processed spectra provide more accurate comparison between different spectra with different offset levels.

Next, it is important to use a cuvette of an appropriate material. Plastic cuvettes may be incompatible with organic solvents (e.g., acetone and chloroform), which should be avoided to eliminate artifacts in recording absorption spectra of NPs. Moreover, cuvettes are not transparent in the whole UV/vis absorption spectrum. In case that the absorbance at small wavelengths (<300 nm) is important, the material of the used cuvette plays an important role. Plastic cuvettes are not transparent at short wavelengths (<250 nm) and thus should be avoided in these cases. Even glass cuvettes show significant absorption at short wavelengths. The use of quartz cuvettes is standard practice to minimize cuvette-related absorption at short wavelengths (see Figure 86).

Proper sample dilution is essential to record accurate UV/vis spectra of NP solutions. If the sample is very concentrated, the recorded spectra will be noisy, due to saturation of the instrument detector. Moreover, quantification will not be possible since absorbance readings will be out of the linear range of the concentration−absorbance relationship.

The absorption $A(\lambda)$ is the logarithmic ratio of the intensity of the incident light beam I_0 to the intensity of the transmitted light beam $I_t(\lambda)$. For this reason the absorption also has no units. In the case the path length of the cuvette is $l_{sol} = 1$ cm, the absorption is also referred to as optical density (OD) of the solution.

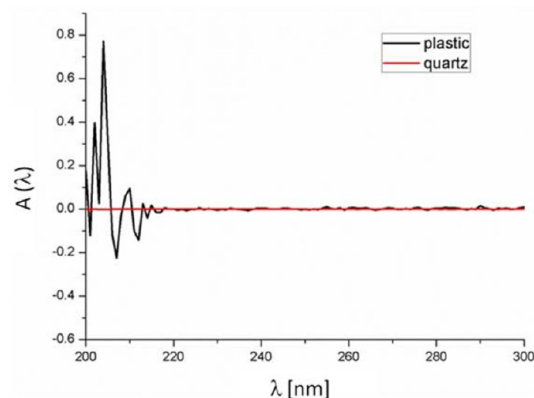$$A(\lambda) = \log(I_0/I_t(\lambda)) \tag{40}$$

Figure 86. Absorption spectrum $A(\lambda)$ of water (with water as blank) recorded in plastic or quartz cuvette. Note the cuvette-related absorption when a plastic cuvette was used at short wavelength.

In the case the transmitted light is ten times less, due to the decadic logarithm, the absorption is a factor of 2 higher. Thus, for high absorption rates the intensity of the transmitted light becomes very low and can no longer be correctly detected.

Figure 87 shows the UV/vis absorption spectra of Au NPs as a function of sequential dilution, as recorded on an Agilent
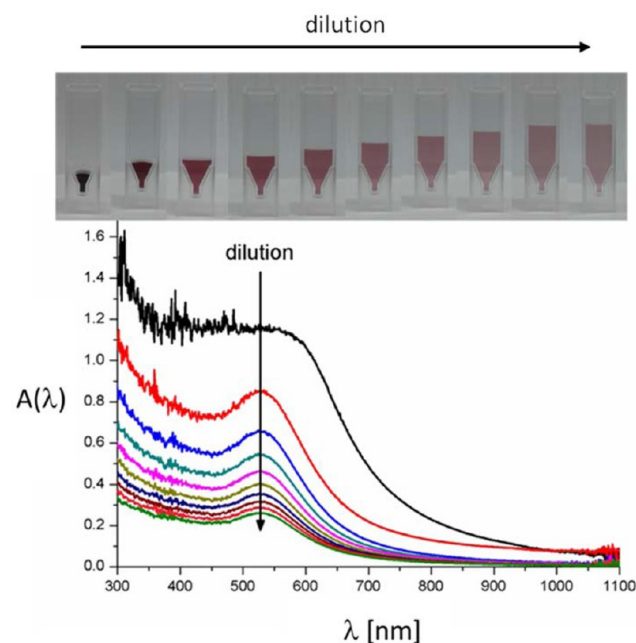

Figure 87. Concentrated aqueous solution of Au NPs was stepwise diluted, which can be seen by the fading color in the solution (upper panel) and deceasing absorption intensity (lower panel). High NP concentration (black curve) resulted in high absorption, and thus λ_{max} cannot even be identified due to detector saturation that results in peak broadening and distortion.

8450 UV/vis spectrometer. At high NP concentrations, the absorption spectrum is noisy and distorted at lower wavelengths, where the absorption is high and exceeding the capacity of the detector. Thus, absorption spectra need to be recorded at sufficiently low concentrations by accurate dilution with solvent. Typical optical densities should not exceed 0.5, and at higher absorption the shape of the spectrum may be an artifact.

443

Despite the strong plasmon optical extinction of Ag NPs and Au NPs, NPs from other materials may have no features in their UV/vis absorption spectra. Figure 88 shows as examples of
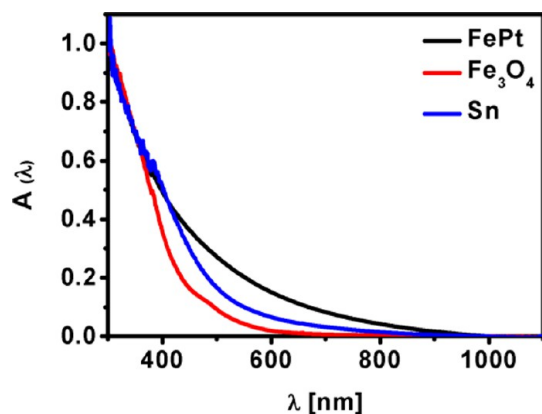

Figure 88. Normalized absorption spectra $A(\lambda)$ of FePt NPs (black curve) (cf. Section 1.4), Fe_3O_4 NPs (red curve) (cf. Section 1.5), and Sn NPs (blue curve) (cf. Section 1.6). All NPs are dispersed in chloroform. Due to the absence of plasmon resonance, the absorption spectra do not contain defined peaks or characteristics.

such cases the absorption spectra for ≈4 nm FePt (cf. Section 1.4), ≈4 nm Fe_3O_4 (cf. Section 1.5), and ≈11 nm Sn (cf. Section 1.6) NPs dispersed in organic solvent. These NP solutions have higher absorption in the UV region (with no peaks), which converges to zero in the IR.

Plasmonic NPs (such as Au NPs, Ag NPs) have characteristic absorption peaks due to the surface resonance plasmon (SPR) phenomenon in the UV/vis−NIR region. Plasmonic NPs may have one or even more SPR peaks, depending on the shape and architecture of the NPs.[125−127] The characteristic absorption peaks are responsible for the distinctive bright color of NP solutions. The spectral position and shape of the surface plasmon absorption peak depends on a variety of factors, such as NP material, size, size-distribution, shape, surface chemistry, and state of aggregation, as well as of the solvent. Figure 89A
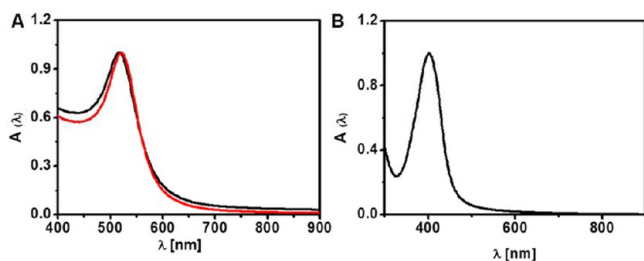

Figure 89. Normalized UV/vis absorption spectra of (A) Cit-Au NPs ≈ 13 nm core diameter (black line) versus Cit-Au NPs ≈ 20 nm core diameter (red line). (B) Cit-Ag NPs ≈ 15 nm core diameter. Au NPs and Ag NPs suspensions in water were prepared as detailed in Section 2.2 and Section 2.3, respectively.

shows a red shift of the SPR maximum (λ_{SPR}) to higher wavelength when the size of Au NPs is increased from 13 to 20 nm (size dependency). Figure 89B shows the absorption spectra of citrate capped spherical Ag NPs in the violet/UV (λ_{SPR} = 415 nm) as compared to Au NPs with the same size (15 and 13 nm respectively) that absorb green light (λ_{SPR} = 520 nm) (NP material dependency).

The size-dependency of λ_{SPR} for Au NPs is well documented with a general trend predicting a red shift of the absorption (λ_{SPR}) as the NP diameter increases. Figure 90 shows a red shift
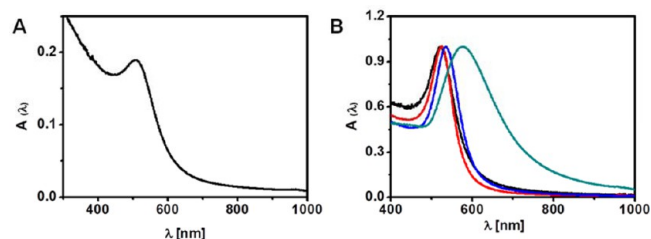

Figure 90. Normalized UV/vis absorption spectra of Cit-Au NPs (cf. Section 2.2) with core diameters of ≈5 nm (A), 18 nm (B, black line), 25 nm (B, red line), 50 nm (B, blue line), and 100 nm (B, green line). The corresponding TEM images of these NPs are shown in Figure 70 A,D−G.

of the SPR maximum (λ_{SPR}) to higher wavelength, when Cit-Au NPs increase in size from 5 to 100 nm. In case of Cit-Au NPs (green curve in B), the size distribution of the NPs is poor, i.e., there are NPs of different sizes in solution, and the absorption peak becomes broader. Thus, a sharp SPR peak is a good indication of narrow size distribution of the core diameter d_c. Figure 91 and Table 8 show a red shift of the SPR maximum wavelength (λ_{SPR}) to higher wavelengths, when commercially available Cit-Au NPs increased in size from 5 to 50 nm.
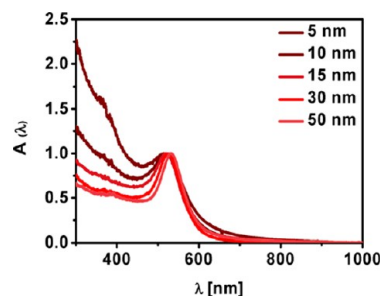

Figure 91. Normalized UV/vis absorption spectra of commercial Cit-Au NPs in water from BBI solutions (cf. Section 2.2) with core diameters of 5, 10, 15, 30, and 50.

The shape dependence of the SPR peak is well documented and reported in the literature. For example, rod-shaped Au NPs have two SPR peaks, as the oscillation of electrons in the conduction band can occur around either the short axis or the long axis, resulting in the so-called transverse and longitudinal peaks, respectively. While in case of Au NPs the transverse plasmon peak is located generally in the visible region (∼520 nm), the longitudinal peak can be tuned to be in the visible−near infrared (vis−NIR) region of the spectrum (600−1200 nm) as shown in Figure 92A. Spectra for star-shaped Au NPs exhibit one peak in the vis−NIR as shown in Figure 92B.

Finally, the surface plasmon peak can change dramatically upon agglomeration due to the plasmon coupling of aggregated NPs.[128] This will be discussed in more detail in Section 10.1.

The UV/vis absorption spectrum of NPs may also change in dependence of the surface capping, as well as on the solvents in which the NP are suspended. This is demonstrated in Figure 93.

Quantum dots have a characteristic absorption peak in their spectrum due to the formation of electron−hole pairs
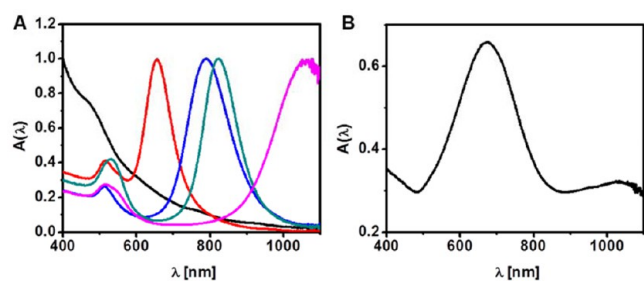
Figure 92. Normalized UV/vis absorption spectra of (A) Au NRs (cf. Section 2.4), with λ_{SPR} = 650 nm (red curve), 790 nm (blue curve), 825 nm (green curve), 1050 nm (pink curve), and the original spherical Au seeds used to grow the nanorods (black curve). For TEM images of these Au NRs cf. Figure 72. (B) Star-shaped Au NPs with λ_{SPR} = 690 nm (cf. Section 2.5). For TEM images of these NPs cf. Figure 73.
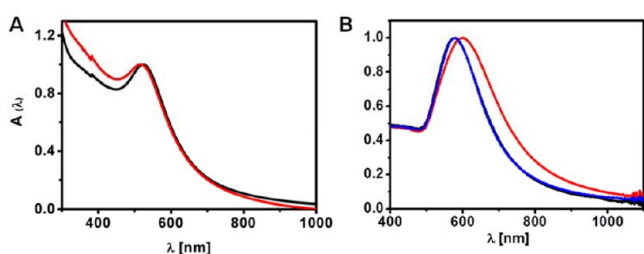

Figure 93. Normalized UV/vis absorption spectrum of Au NPs capped with different surface coatings and suspended in different solvents. (A) Au NPs with core diameter of ≈4 nm (cf. Section 1.2), either capped with DDT and suspended in chloroform (black curve) or after being overcoated with PMA (cf. Section 6.3) and suspended in water (red curve). (B) Au NPs with core diameter of ≈100 nm (cf. Section 2.2) either with the original citrate capping as recorded in water (black) or after their phase transfer to chloroform by ligand exchange with dodecylamine and PEG (cf. Section 4.3) (red curve), and finally after retransfer to water by PMA coating (cf. Section 6.3) (blue curve). The black and blue curves are almost superimposed in B.

(excitons) upon absorption.[129−132] In the case of semiconductor NPs with very sharp size distribution, multiple exciton peaks can be observed.[133−135] The absorption spectra of CdSe/ZnS and CdS NPs are shown in Figure 94.

The spectral position of the first exciton peak, which corresponds to the energy gap between the ground states of the valence and conduction band, is extremely size dependent. This is due to the quantum confinement of light-generated
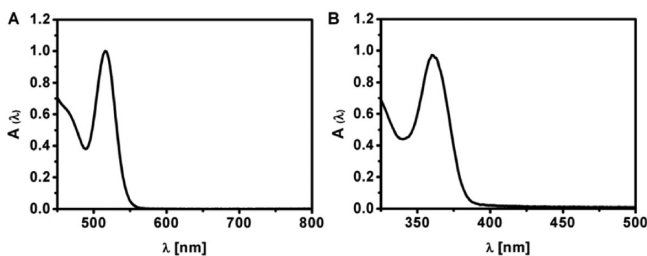

Figure 94. (A) Normalized UV/vis absorption spectrum of CdSe/ZnS quantum dots with core diameter of ≈4 nm (cf. Section 1.7; Figure 68) as recorded in toluene with λ_{max} = 516 nm. (B) Normalized UV/vis absorption spectrum of CdS quantum dots with core diameter of ≈2 nm (cf. Section 1.8; Figure 69) as recorded in toluene with λ_{max} = 360 nm.

electron−hole pairs.[136−139] The smaller a QD becomes, the bigger the energy gap and thus the shorter the wavelength of the first exciton peak. Equation 6 correlates the wavelength λ_{max} of the first exciton peak in the absorption spectrum with the core NP diameter d_c. Values have been listed for several QD materials.[29,140] Note that in Yu et al. data are only provided for QDs with a single semiconductor core. However, as demonstrated in Section 1.7, quantum dots can also be grown with several semiconductor shells around the semiconductor core. For example, the values for CdSe NPs in the Yu et al. table cannot be directly applied for CdSe/ZnS NPs, as the ZnS shell will shift the absorption peak λ_{abs} to higher wavelength. If this wavelength is used with eq 6, the resulting d_c for the CdSe core in CdSe/ZnS is overestimated. However, and since the ZnS shell contributes to the size of the inorganic part of the NPs, this error in the calculation is often tolerated.

9.2. Determination of NP Concentrations from Absorption Spectra. The NP concentration of NP suspension c_{NP} can be obtained from the Beer−Lambert's law, which correlates the absorption A (from the UV/vis absorption spectrum) with c_{NP} as follows:

$$A(\lambda) = \varepsilon_{NP}(\lambda) \times l_{sol} \times c_{NP} \tag{41}$$

Both the molar extinction coefficient $(\varepsilon_{NP}(\lambda))$ and thus the absorption $(A(\lambda))$ depend on the wavelength λ and the solvent. l_{sol} is the path length of the cuvette in which the absorbance has been measured, i.e., the distance that the light passes in the NP suspension during measurements. As mentioned in Section 9.1, a blank spectrum of the solvent should be measured first and subtracted from the sample spectrum, in order to eliminate absorption from the cuvette and the solvent. In order to determine the NP concentration c_{NP} of a sample, the absorption $A(\lambda)$ is measured at wavelength λ in a cuvette of path length l_{sol}. It is important to correct the offset of the absorption spectra as detailed in Figure 85). In the case that $\varepsilon_{NP}(\lambda)$ is known, the NP concentration can be calculated according to eq 41.

In the case of NPs which do not have specific peaks in their absorption spectra (such as FePt, Fe_3O_4, Sn, etc.), $\varepsilon_{NP}(\lambda)$ usually is not reported in the literature. In this case the absorption $A(\lambda)$ of an NP suspension is recorded, and then the NP concentration c_{NP} in this solution is determined by ICP-MS (cf. Section 8.2). The molar extinction coefficient can then be calculated as $\varepsilon_{NP}(\lambda) = A(\lambda)/(c_{NP} \times l_{sol})$. Once $\varepsilon_{NP}(\lambda)$ is known, the NP concentration in the following samples can be determined by absorption instead of ICP-MS analysis, which is less time-consuming and cheaper.

For plasmonic NPs or QDs, values for the molar extinction at λ_{SPR} (wavelength of the surface plasmon resonance) or λ_{max} (first exciton peak), respectively, are available in the literature. For Au NPs some molar extinction values λ_{SPR} are given in Table 8. An extended table has been reported by Haiss et al.[141] Also in the case of QDs, lists of molar extinction values are reported in literature.[29,142] In Figure 95 an example for the concentration determination of a solution of Au NPs is given.

NP concentration values obtained via absorption measurements have to be interpreted with care, as they may be prone to significant errors. With this in mind, published reports should clearly detail calculation of NP concentration stating the used molar extinction values and the selected absorption wavelength.

In the case the molar extinction coefficient for a NP sample is recorded at one wavelength λ_1 but the extinction coefficient at
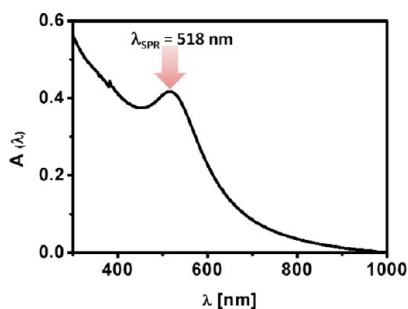
Figure 95. Absorption spectrum of $\approx$4 nm Au NPs (cf. Section 1.2) recorded in chloroform. The absorption at their surface plasmon peak λ_{SPR} = 518 nm is measured to be $A(\lambda_{SPR})$ = 0.42. The path length of the used cuvette was l_{sol} = 1 cm. The molar extinction coefficient $\varepsilon(\lambda_{SPR})$ = 8.7 × 10^6 M^{-1} × cm^{-1} is obtained from Table 8. Thus, the concentration of Au NPs in this solution was calculated using eq 41 as c_{NP} = $A(\lambda_{SPR})/(\varepsilon_{NP}(\lambda_{SPR}) \times l_{sol})$ = 0.42/(8.7 × 10^6 M^{-1} × cm^{-1} × 1 cm) = 0.048 × 10^{-6} M = 48 nM.

another wavelength λ_2 is needed, this can be calculated from the absorption spectrum $A(\lambda)$ according to eq 42 as

$$\varepsilon(\lambda_2) = \varepsilon(\lambda_1) \times A(\lambda_2)/A(\lambda_1) \tag{42}$$

For homogeneous NPs with characteristic features, such as Au NPs, the extinction coefficients of the Au cores are known with relatively good precision.[141] However, these values refer to the absorption related to the NP core, with an assumption that the organic coating does not contribute significantly to the total absorption (as the absorption of the inorganic core is much stronger). Thus, the extinction coefficient for the core is used for the whole NP. In the case of thin transparent ligand shells this approximation works well at higher wavelengths (vis−NIR) but not at lower wavelengths (UV) where most organic ligands possess significant absorption. Also in the case the inorganic part comprises a core and (several) shell(s), such as already mentioned in the case of CdSe/ZnS NPs, the absorption of the shell often is neglected and the extinction values for the core are used for the whole core/shell NP.

The organic shell can be modified intentionally with "absorbers", for example, in the case organic fluorophores are integrated into the polymer shell around a NP (cf. Section 6.2). In this case the absorption spectrum shows the absorption of the inorganic NP core, the absorption of the organic shell (which can be in general neglected), and the absorption of the integrated fluorophores; see Figure 96. Obviously, it is important to determine the number of fluorophores per NP, for which several methods have been proposed.[68,79,92] One of these methods is based on determining both the concentration of NP cores c_{NP} and the concentration of dyes c_{dye} from the UV/vis absorption spectra, leading to the number $N_{dye/NP}$ = c_{dye}/c_{NP} of fluorophores per NP. An example of the calculation is shown in Figure 96.

Typically the absorption spectrum of the dye will overlap with the absorption spectrum of the NP core. Thus, the dye absorption part needs to be deconvoluted from the NP core absorption part. For this purpose three UV/vis absorption spectra need to be recorded: (i) from solutions of the NPs with integrated fluorophores, (ii) of the NPs alone, and (iii) of the fluorophores alone, cf. Figure 96.[52,86] The fluorophores typically absorb only in a small spectral band, whereas the NP cores absorb continuously, optionally until a maximum wavelength. Thus, the NP core concentration can be
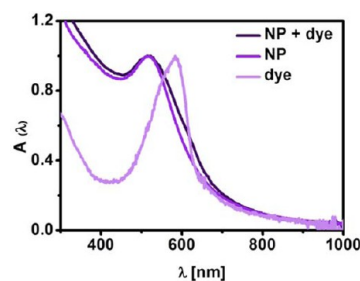

Figure 96. Normalized absorption spectra of $\approx$4 nm Au NPs (cf. Section 1.2; blue curve) recorded after their PMA coating and functionalization with a dye (cresyl violet perchlorate, CV) versus the spectrum free of the dye (red curve). The absorption at surface plasmon peak λ_{SPR} = 519 nm of the NPs is normalized to $A(\lambda_{SPR})$ = 1.0. The absorption of the free dye at their emission maximum $\lambda_{dye,max}$ = 583 nm is normalized to $A(\lambda_{dye,max})$ = 1.0 as well. To calculate the concentration c_{dye} of the conjugated dye, the absorption of the NPs at $\lambda_{dye,max}$ is first subtracted from the absorption of dye-modified NPs at $\lambda_{dye,max}$ ⇒ $A_{dye}(\lambda_{dye,max})$ = $A_{NP+dye}(\lambda_{dye,max}) - A_{NP}(\lambda_{dye,max})$ = 0.73−0.63 = 0.1. The molar extinction coefficient of NPs $\varepsilon_{NP}(\lambda_{SPR})$ = 8.7 × 10^6 M^{-1}·cm^{-1} is obtained from Table 8, and the one of CV is $\varepsilon_{dye}(\lambda_{max})$ = 8.3 × 10^4 M^{-1}·cm^{-1}. The path length of the used cuvette was l_{sol} = 1 cm. Now both concentrations can be calculated according to eq 41. For the dye c_{dye} = $A_{dye}(\lambda_{dye,max})/(\varepsilon_{dye}(\lambda_{dye,max}) \times l_{sol})$ = 0.1/(8.3 × 10^4 M^{-1}·cm^{-1} × 1 cm) = 1.21 × 10^{-6} M = 1.21 μM. For the NPs c_{NP} = $A_{NP}(\lambda_{SPR})/(\varepsilon_{NP}(\lambda_{SPR}) \times l_{sol})$ = 1.0/(8.7 × 10^6 M^{-1}·cm^{-1} × 1 cm) = 0.115 × 10^{-6} M = 115 nM. By this the ratio of $N_{dye/NP}$ = c_{dye}/c_{NP} = 1.21 × 10^{-6} M/0.115 × 10^{-6} M = 10.5 dye molecules per NP can be estimated.

determined at a wavelength where the NP core, but not the fluorophore, absorbs. This can be directly done by the known molar extinction coefficient $\varepsilon_{NP}(\lambda)$ at this wavelength by measuring the absorption from the NP spectrum, leading to the concentration of NP cores c_{NP}. On the other hand, at the absorption peak of the dye there is typically also absorption of the NP core. Thus, the absorption spectrum of the NP cores only is scaled by multiplication with an appropriate factor to match the absorption spectrum of the NPs with integrated dyes at the parts, where the dyes do not absorb. Then, at the absorption peak of the dye the appropriately scaled absorption of the nonmodified NPs is subtracted from the absorption of the NPs with integrated dyes, leading to the absorption of only the dyes. In the case the molar extinction coefficient of the dyes $\varepsilon_{dye}(\lambda)$ at this absorption wavelength is known, then the dye concentration can be calculated using Lambert−Beer's law:

$$A(\lambda) = \varepsilon_{dye}(\lambda) \times c_{dye} \times l_{sol} \tag{43}$$

This methodology works better the more the characteristic absorption peaks of the NP cores and the more the dyes are spectrally shifted. An example for a calculation is shown in Figure 96.

Also data from TGA (cf. Section 8.6) can be used for estimating the number of dyes attached per NP. In the case the number of polymer units bound to the NP ($N_{P/NP}$) is known, the number of dyes bound per NP ($N_{dye/NP}$) can be derived from the amount of dye that has been added per monomer ($R_{dye/mon}$):

$$N_{dye/NP} = R_{dye/mon} \times N_{P/NP} \tag{44}$$

In the case of the PMA-Au NPs with d_c = 4.3 as discussed in Section 8.6, addition of dye to 2% of the anhydride rings ($R_{dye/mon}$ = 0.02) leads to $N_{dye/NP}$ = 0.02 × 270 = 54. This value

can now be compared to the values determined with other methods. In Kaiser et al.[68] Evidot540/Catskill Green QDs ($d_c = 2.7 \pm 0.4$ nm determined by TEM, value provided by company: 2.6 nm) were modified with 2% dye ($R_{dye/mon} = 0.02$), and the value $N_{dye/NP} = 7 \pm 0.7$ was determined from time-resolved photoluminescence spectra. Assuming that the number of dye molecules per NP scale with the effective surface area A_{eff}, this value can be compared to the TGA data of Au: $N_{dye/NP(1)} = N_{dye/NP(2)} \times ((R_{P/Area(1)} \times A_{eff(1)})/(R_{P/Area(2)} \times A_{eff(2)})) = N_{dye/NP(2)} \times (R_{P/Area(1)}/R_{P/Area(2)}) \times ((d_{c(1)} + 2 \times l_{ligand(1)})/(d_{c(2)} + 2 \times l_{ligand(2)}))^2$. In both cases the same amount of polymer per surface area had been added, $R_{P/ligand(1)} = R_{P/ligand(2)} = 100$ nm^2, but the diameters are different. In the case of CdSe/ZnS, $d_{c(1)} = 2.7$ nm and $l_{ligand(1)} = 1.2$ nm, and in the case of Au, $d_{c(2)} = 4.3$ nm and $l_{ligand(2)} = 1.0$ nm. Thus, this leads to $N_{dye/NP(1)} = N_{dye/NP(2)} \times ((d_{c(1)} + 2 \times l_{ligand(1)})/(d_{c(2)} + 2 \times l_{ligand(2)}))^2 = 54 \times ((2.7 \text{ nm} + 2 \times 1.2 \text{ nm})/(4.3 \text{ nm} + 2 \times 1.0 \text{ nm}))^2 = 54 \times (5.1/6.3)^2 \approx 35$. Thus, TGA analyses leads to a value of $N_{dye/NP} = 35$ dye molecules per CdSe/ZnS NP, as compared to the optically determined value of $N_{dye/NP} = 7$. For this reason, in order to estimate the error, it is convenient to use several methods in parallel for the determination of $N_{dye/NP}$.

9.3. Fluorescence Spectroscopy. NPs can be fluorescent for two reasons. First, NPs may be intrinsically fluorescent, such in the case of QDs,[143] upconverting NPs,[111] ultrasmall Au,[144] or Ag clusters.[145] Examples for fluorescence spectra of CdSe/ZnS and CdS NPs are shown in Figures 97 and 98, respectively.

Figure 97. Normalized absorption spectrum $A(\lambda)$ (black solid line, cf. Figure 94A) and emission spectrum $I(\lambda)$ (blue solid line) of hydrophobic CdSe/ZnS NPs ($d_c \approx 4$ nm, cf. Section 1.7) in toluene. The absorption and emission peaks are at $\lambda_{abs} \approx 516$ nm and $\lambda_{em} \approx 530$ nm respectively, and correspond to CdSe/ZnS NPs of ≈ 4 nm.
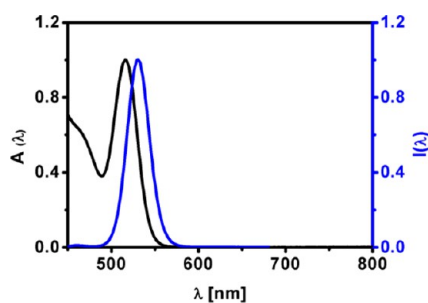
Figure 98. Normalized absorption spectrum $A(\lambda)$ (black solid line, cf. Figure 94B) and emission spectrum $I(\lambda)$ (blue solid line) of hydrophobic CdS NPs ($d_c \approx 2$ nm, cf. Section 1.8) in toluene. The absorption and emission peaks, respectively, at $\lambda_{abs} \approx 360$ nm and $\lambda_{em} \approx 390$ nm correspond to CdS NPs of ≈ 2 nm.

Second, organic fluorophores can be integrated in the organic surface coating (cf. Section 6.2) around nonfluorescent inorganic NP cores. An example is shown in Figure 99. In
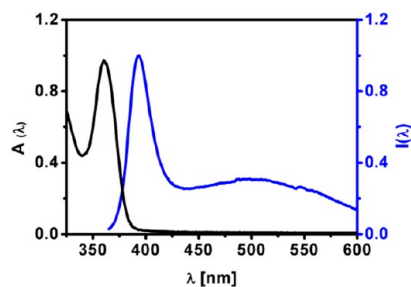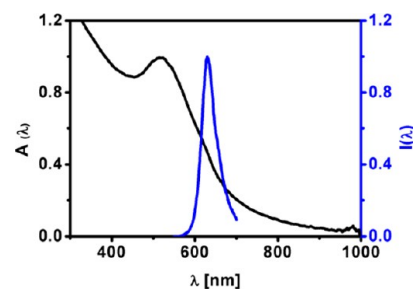
Figure 99. Normalized absorption spectrum $A(\lambda)$ (black solid line, cf. Figure 96) and emission spectrum $I(\lambda)$ (blue solid line) of hydrophilic Au NPs coated with PMA modified with cresyl violet (CV) ($d_c \approx 4$ nm, cf. Section 1.2) as recorded in water. The absorption and emission peaks are at $\lambda_{abs} \approx 519$ nm and $\lambda_{em} \approx 630$ nm, respectively.

this case the underlying inorganic NP core may affect the fluorescence emission of the organic fluorophores. In the case of plasmonic NPs the fluorescence of adjacent dyes may be quenched,[146] and in the case of QDs, fluorescence resonance energy transfer (FRET) may occur with the linked dyes.[86,100,147] In both cases the effects strongly depend on the distance between the organic fluorophores and the NP cores.

9.4. Determination of Quantum Yields. A major characteristic of fluorescent NPs is their quantum yield (Φ_F). This feature represents the ratio of the number of photons emitted through fluorescence to the number of absorbed photons. In other words, the quantum yield describes the probability that a photoexcited state gets relaxed by fluorescence rather than by another, nonradiative mechanism. As photons may be emitted in all directions, in principle, a 4π-detection geometry is required to detect absolute quantum yields.[148,149] Instead, often relative quantum yields are measured in standard 90° detection geometry. For this purpose fluorescence intensities of a dilution series of the sample (s) and a dilution series of a reference fluorophore (ref) with known absolute quantum yield Φ_{ref} are determined. From the slopes $\Delta I_{int}/\Delta A_\lambda$ of the integrated emission (I_{int}) versus absorption (A_λ) curves of the sample and the reference fluorophore, the absolute quantum yield of the NP sample can be calculated, cf. eq 45. A good description of this methodology is detailed by Horiba Jobin Yvon.[150,151]

$$\frac{\Phi_s}{\Phi_{ref}} = \frac{(\Delta I_{int}/\Delta A_\lambda)_s}{(\Delta I_{int}/\Delta A_\lambda)_s} \cdot \frac{n_s^2}{n_{ref}^2} \quad (45)$$

$[\Phi_s, \Phi_{ref}]$, $[(\Delta I_{int}/\Delta A_\lambda)_s, (\Delta I_{int}/\Delta A_\lambda)_{ref}]$, and $[n_s, n_{ref}]$ refer to the quantum yield, slope of the integrated emission versus absorption curve, and refractive index of the sample and reference fluorophore, respectively. An example for determining the quantum yield of Au NPs with the attached fluorophore is provided in Figure 100.[115]

To demonstrate how to determine the quantum yield of NPs (Φ_{NP}), hydrophobic Au NPs ($d_c \approx 4$ nm) were synthesized (cf. Section 1.2) and coated with PMA modified with $R_{dye/mon} = 2\%$ tetramethylrhodamine 5-(and-6-) carboxamide cadaverine (TAMRA, no. AS-81506, Anaspec) (cf. Section 6). After their purification using gel electrophoresis (the process has been repeated twice) (cf. Section 7.4), the NPs were concentrated, washed with Milli-Q water, and filtered by passing them through a syringe membrane filter (0.22 μm pore size) (cf. Section 7.2). Cresyl violet perchlorate (CV) dissolved in
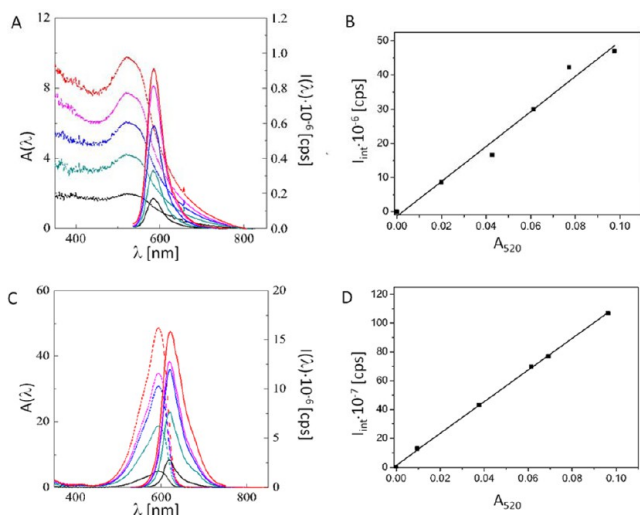
Figure 100. Determination of the quantum yield Φ_{NP} of TAMRA modified Au NPs (top row) and CV (bottom row). The graphs on the left side (A, C) represent the absorption spectra $A(\lambda)$ (dotted line, left y-axis) and emission spectra $I(\lambda)$ (full line, right y-axis) recorded at excitation wavelength λ_{exc} = 520 nm for dilution series of the Au NPs and CV. From each absorption spectrum the absorption A_{520} at 520 nm was determined. From each emission spectrum at 520 nm excitation, the integrated fluorescence intensity I_{int} was determined as the sum of all emitted fluorescence from 530 to 750 nm.

methanol was chosen as the reference dye with a known quantum yield Φ_{CVP} = 0.54 ± 0.03.[152]

To determine the quantum yield, first dilution series of both samples (NPs in water, CV in methanol) were generated. Dilution was quantified by measuring the absorption A_{λ} of the samples at the excitation wavelength λ_{exc} = 520 nm of TAMRA. Note that for the NP sample as for the reference dye absorption needs to be detected at the same wavelength. Ideally, the excitation wavelength of the reference dye should be similar to the fluorescent NP sample. The highest concentration of the absorption series should not exceed an optical density of 0.1, in order to avoid reabsorption and self-quenching of fluorescence, which may occur at high fluorophore concentrations. For each sample within the dilution series the integrated fluorescence emission I_{int} was determined (i.e., the intensity of the whole fluorescence peak was counted), using the excitation wavelength λ_{exc} at which the absorption A_{λ} had been determined before. All fluorescence emission measurements must be made with the same settings of the fluorometer. The recorded absorption $A(\lambda)$ and emission spectra $I(\lambda)$ of the dilution series are shown in Figure 100. From these curves the respective absorption A_{520} at λ_{exc} = 520 nm was determined. The integrated emission I_{int} was obtained as the sum of all fluorescence emission counts in the spectral range from 530 to 750 nm. The resulting $I_{int}(A_{520})$ curves show the linear relation between absorbance and integrated fluorescence intensity. From these graphs the slopes $\Delta I_{int}/\Delta A_{520}$ were derived. In the case of the NP and the CV sample (5.11 ± 10.4) × 10^8 cps and (110 ± 1.31) × 10^8 cps were obtained (cps = counts per second). In order to calculate the quantum yield of the NP sample according to eq 45, the refractive indexes n_{H2O} = 1.333 for water and $n_{methanol}$ = 1.3288 for methanol at 20 °C

were used, yielding $\Phi_{NP} = \Phi_{CVP} \cdot \dfrac{(\Delta I_{int} / \Delta A_{520})_{NP}}{(\Delta I_{int} / \Delta A_{520})_{CV}} \cdot \dfrac{n_{H2O}^2}{n_{methanol}^2} = 0.025$

± 0.008. The error was estimated using Gaussian error propagation.

10. CHARACTERIZATION OF THE COLLOIDAL PROPERTIES OF THE NPs

10.1. UV/Vis Absorption Spectroscopy. The UV/vis absorption spectrum provides a fast and simple quality control measure for the colloidal stability of NPs. Several types of NPs, such as plasmonic NPs and QDs, possess characteristic peaks in their absorption spectrum (cf. Section 9.2) that can provide important information regarding size, shape, surface chemistry, and aggregation state. For example, aggregation of Au NPs is typically associated with a red shift of the SPR (λ_{SPR}) to higher wavelengths and a significant spectral broadening. Most isotropic inorganic NPs absorb in the UV/vis and not in the near IR, unless they have been designed for this purpose (e.g., rod-shaped Au NPs, Au nanostars, IR emitting QDs, etc.). Thus, absorption in the range where NPs do not typically absorb indicates NP aggregation. "Absorption" in this case is mainly light scattering due to NP agglomeration. Figure 101 shows the red shift and broadening of the plasmon absorption spectrum of Au NPs upon salt-induced aggregation.
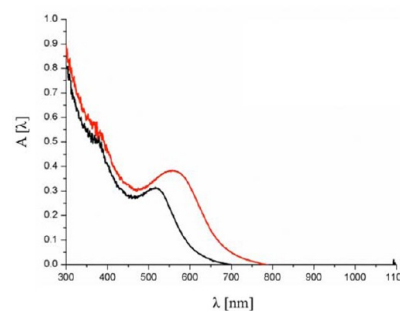

Figure 101. Absorption spectra of 5 nm core diameter Cit-Au NPs (purchased from BBI) as recorded in water (black curve) and in water supplemented with NaCl (red curve). The red shift of the SPR peak to higher wavelength and associated peak broadening is clear upon the addition of NaCl due to NP aggregation and plasmon coupling effect.

Colloidal stability is a critical property for NP dispersions, which can be maintained by ensuring repulsive force (either an electrostatic or a steric repulsion) that outweighs the attractive van der Waals forces between NPs.[5] For example, Cit-Au NPs are stabilized through electrostatic repulsion due to the presence of physically adsorbing citrate ions on the surface of Au NPs (zeta potentials of these NPs are typically negative ∼−30 mV). When salt is added, electrostatic forces are screened by counterion effects and electrostatic double layer compression, and thus NPs tend to aggregate. The higher the charge density of the NP surface, the less prone the NPs are to aggregation. Note that the surface charge of NPs may depend on the pH (cf. Section 10.4). NPs that are stabilized by steric repulsion are typically less prone to aggregation upon the addition of salt. In various biological applications, NPs are expected to be dosed into media with physiological salt levels (150 mM NaCl), and thus colloidal stability should be carefully evaluated.

By titrating the NP suspension against increasing concentrations of NaCl, one can observe the aggregation state by UV/vis absorption measurements. Such measurements in particular allow for observing the NaCl concentration at which the

colloidal stability of the NPs is lost. Figures 102 and 103 show the colloidal stability of Au NPs or Ag NPs with different
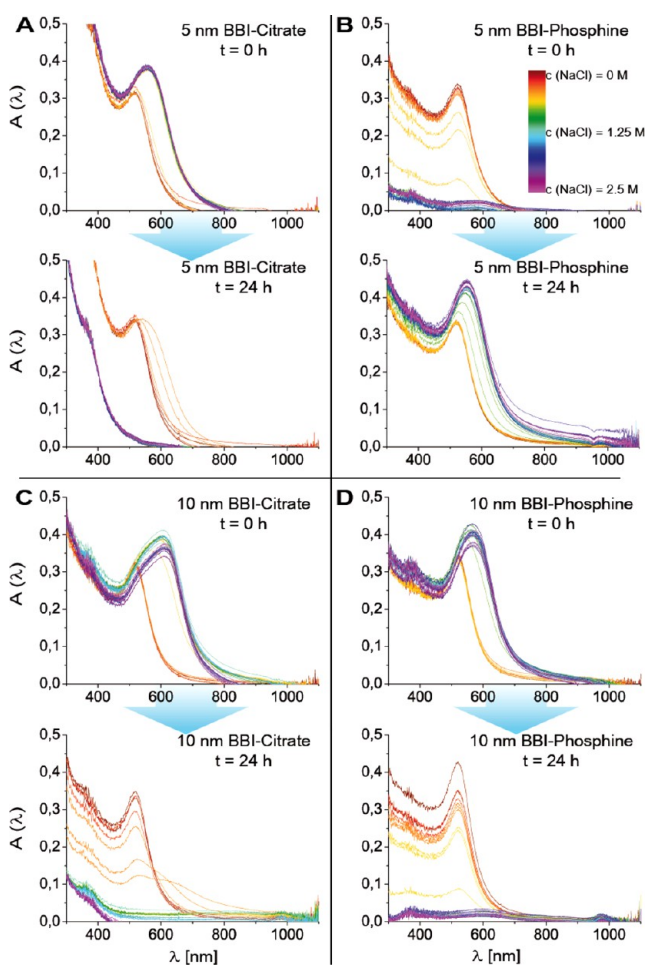

Figure 102. Absorption spectra recorded for different Au NPs in water in the presence of different concentrations of NaCl, recorded after 0 and 24 h, with $c_{NP} \approx 12$ nM. The NaCl concentrations were in the range of 0.0 to 2.5 M as illustrated using a color map. Cuvettes with freshly mixed solutions were measured at $t = 0$ h before incubating overnight at RT and measured again after $t = 24$ h. (A) ≈5 nm core diameter Cit-Au NPs purchased from BBI). (B) ≈5 nm core diameter Cit-Au NPs (purchased from BBI), after ligand exchange to bis(p-sulfonatophenyl)-phenylphosphine (cf. Section 3.2). (C) ≈10 nm core diameter Cit-Au NPs (purchased from BBI). (D) ≈10 nm core diameter Cit-Au NPs (purchased from BBI), after ligand exchange to bis(p-sulfonatophenyl)-phenylphosphine (cf. Section 3.2).

surface coatings, as judged by their UV/vis absorption spectra upon titration with NaCl aqueous solution. As agglomeration is time dependent, these measurements were carried out directly after exposure of the NPs to salt and were then repeated after 24 h. The absorption spectra were measured over a range of 300 to 1100 nm with an Agilent Technologies 8453 UV/vis spectrometer.

In most cases after 24 h the absorption peaks became broader and smaller. The increment in the peak width was due to agglomeration. The reduction in absorption intensity was due to the severe degree of aggregation that decreased the number of individually dispersed NPs due to the significant NP loss via precipitation out from the suspension. Collectively, data in Figures 102 and 103 suggest that PMA is superior to MPA and MUA in protecting NPs against salt-induced aggregation.
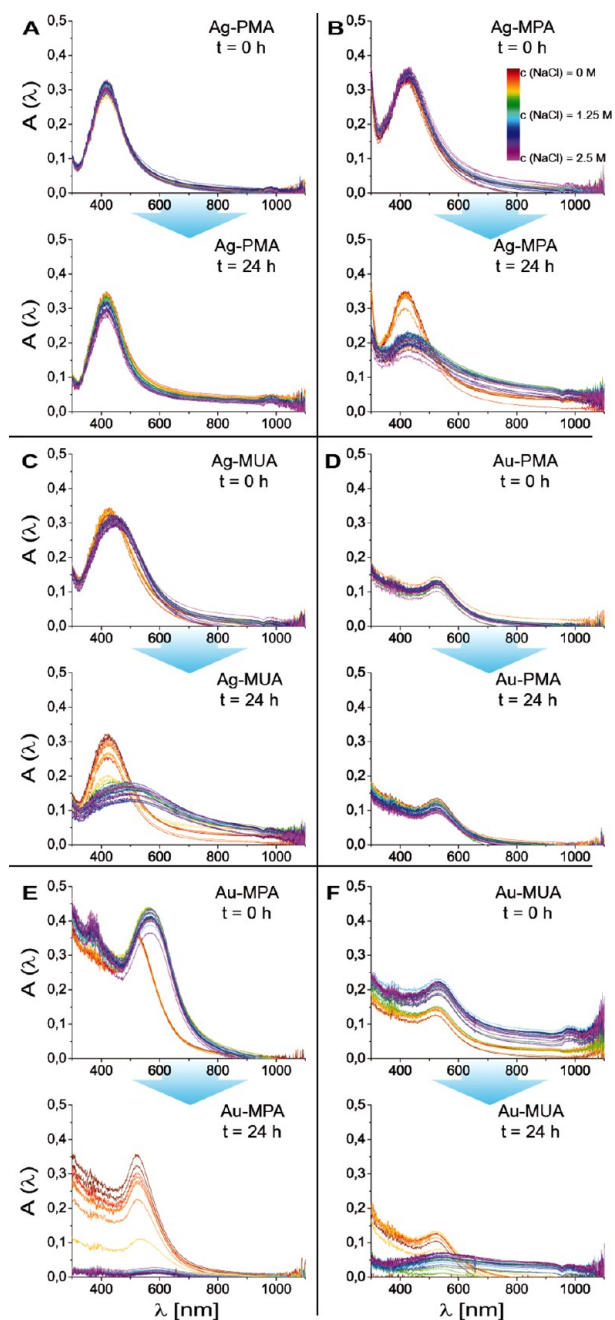

Figure 103. Absorption spectra of different NPs in water in the presence of different concentrations of NaCl recorded after 0 and 24 h, with $c_{NP} \approx 12$ nM. The NaCl concentrations were in the range of 0.0 to 2.5 M as illustrated using a color map. Cuvettes with freshly mixed solutions were measured at $t = 0$ h before incubating overnight at RT and measured again after $t = 24$ h. (A) ≈4 nm core diameter Ag NPs (cf. Section1.3) overcoated with PMA (cf. Section 6.3). (B) ≈4 nm core diameter Ag NPs (cf. Section 1.3) after ligand exchange with mercaptopropionic acid (MPA; cf. Section 5.2). (C) ≈4 nm core diameter Ag NPs (cf. Section 1.3) after ligand exchange with mercaptoundecanoic acid (MUA; cf. Section 5.2). (D) ≈4 nm core diameter Au NPs (cf. Section 1.2) overcoated with PMA (cf. Section 6.3). (E) ≈4 nm core diameter Au NPs (cf. Section 1.2) after ligand exchange with mercaptopropionic acid (MPA; cf. Section 5.2). (F) ≈4 nm core diameter Au NPs (cf. Section 1.2) after ligand exchange with mercaptoundecanoic acid (MUA; cf. Section 5.2).

10.2. Dynamic Light Scattering. There are several techniques available that are able to measure the hydrodynamic

diameter d_h of NPs dispersed in solvent. Hydrodynamic diameters may differ for NPs with different core diameter d_c, capping agents/polymers, solvent, and aggregation state. For example, identical NPs with a PEG shell exhibit different d_h in water versus chloroform due to different hydration/solvation nature and polymer architecture on the NPs in each solvent. In another context, the addition of a high concentration of electrolyte to an aqueous suspension containing charged NPs may decrease the d_h of these NPs due to the counterion effect and thus a compressed electric double layer (Debye length).[153] In addition to measuring the average value of d_h, it is also important to determine the monodispersity of NP suspensions by measuring the so-called polydispersity index (PDI).[154] The PDI is an unitless parameter that measures the heterogeneity (statistical variation from the average value) in the NPs' hydrodynamic diameter in a sample. Values below 0.05 are normally not obtained, meanwhile values higher than 0.7 indicate that the sample has a very broad size distribution.

There are various techniques to measure hydrodynamic diameters of NPs.[94,155] Dynamic light scattering (DLS) is a simple, fast, and common technique to measure the hydrodynamic diameter of NPs and associated PDI.[156−158] DLS records the temporal fluctuations in scattered light, due to diffusion of NPs in solution. Using an autocorrelation function, the diffusion constant of the NPs then can be derived. By applying the Einstein−Stokes relation and using the measured diffusion constant value, the NPs' hydrodynamic diameter d_h can be calculated. Obtaining reliable size measurements of NPs of only a few nanometers in diameter using DLS is a real challenge, since the scattering signal from these small NPs is close to the noise of the detector.

It is worth mentioning that serious error in measuring the absolute size of NPs using DLS may occur and can originate from various reasons such as dirty cuvettes, contaminated solvent, using incorrect values for solvent physical parameters (e.g., viscosity and dielectric constant), improper sample concentration (too high or too low), and unstable samples during measurement. To avoid possible under- or over-estimation of NP hydrodynamic size, an internal calibration with reference NPs is essential.

When carrying out DLS analysis, the obtained distributions of hydrodynamic diameters can be plotted in terms of the number of NPs $N(d_h)$ or the intensity of the scattered light $I(d_h)$ as shown in Figure 104. The intensity distribution $I(d_h)$ considers the scattering intensity of each NP fraction. Since larger NPs scatter much more than smaller NPs, the intensity distribution can provide overestimated values of hydrodynamic diameter. For example, a very low level of aggregates in a Au NP suspension will scatter extensively and thus will result in a
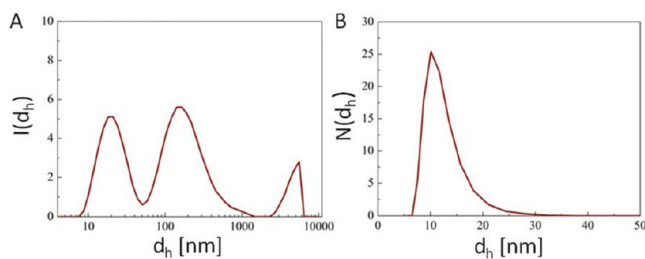
resolved significant peak (second and third peaks in Figure 104A). Applying Mie's theory, the intensity distribution can be converted to volume or number distributions. To do so, there are several assumptions made, including that all NPs are spherical and homogeneous, which in the case of samples with broad size distribution and/or anisotropic NPs is not valid. In the number distribution, the contribution of large NP populations at low level is very minimal and does not dominate, and thus measured d_h values are closer to the d_c values as obtained by TEM. As an example, in Figure 104A, d_h obtained from the intensity distribution (first peak) is 26.07 ± 12.75 nm where d_h obtained from the number distribution in Figure 104B is 11.71 ± 3.29 nm, which is closer to the value obtained by TEM (d_c = 4.3 nm ± 0.4 nm as per Figure 64 plus the addition of the l_{ligand}; (see Figure 63B,C). Commercial DLS setups often assume the presence of several NP populations in solution, and thus fits of even one NP population may result in several distinct sizes. For example, in the intensity distribution shown in Figure 104 three peaks are observed, whereas there is only one peak in the number distribution. In fact, only one NP species is present in solution, and small agglomerates are overestimated in the intensity distribution, which then wrongfully identifies three discrete subspecies.

A significant increase in measured hydrodynamic diameter of NPs as compared to the structural diameter (i.e., $d_h \gg d_c$ for NPs without the presence of thick organic shell) is usually a strong indication of NP aggregation. In the case NPs are aggregated, the measured effective hydrodynamic diameter values describe the diameter of NP agglomerates rather than the diameter of the individual NPs. In Figure 105, aggregation
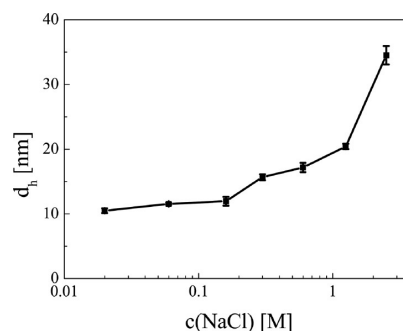

Figure 105. Hydrodynamic diameter (d_h) of 4 nm PMA-Au NPs as a function of NaCl concentration in the NP suspension.

of PMA-Au NPs upon the addition of NaCl is associated with an increase in d_h. Such measurement of hydrodynamic diameters is an essential tool to probe the colloidal stability of NPs in solution.

More examples on the salt-induced aggregation of Ag NPs and Au NPs with differing surface modification and core diameter are provided in Figure 106. Aqueous suspension of the NPs (1.0 mL; c_{NP} = 25 nM) received equal volume of NaCl (aq) (1.0 mL; concentration ranges from 0.0 to 5 M). Obviously the final NaCl concentration was hereby reduced to half of the original concentration upon mixing it with the same amount of NP stock solution. The hydrodynamic diameter d_h was measured immediately after mixing the two solutions and after a 24 h incubation time at RT (since aggregation is a time-dependent process that can be slow but significant). DLS histograms (d_h versus c_{NaCl}) and real photographs of NP suspensions in the cuvettes are shown in Figure 106, in which

Figure 104. (A) DLS histograms of Au NPs of ≈4 nm coated with PMA measured in aqueous solution. (A) Intensity distribution $I(d_h)$ and (B) number distribution $N(d_h)$ of the hydrodynamic diameter d_h.
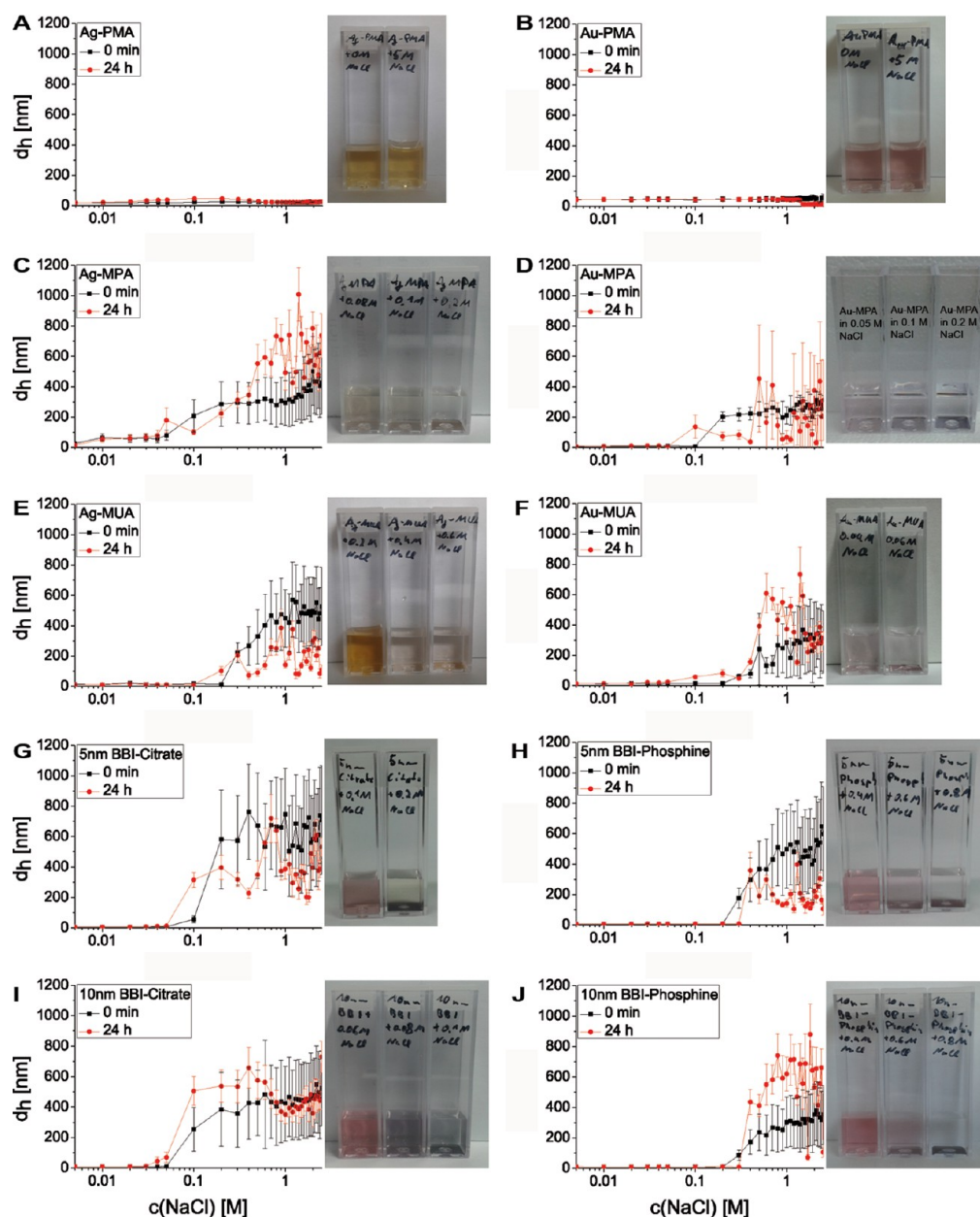
Figure 106. Ag NPs and Au NPs with differing surface modification and core diameter were exposed to different concentrations of NaCl. Hydrodynamic diameter values d_h in aqueous solution were measured directly (0 h; ■) and 24 h (●) after exposure. The behavior of the hydrodynamic diameter d_h is plotted against the NaCl concentration within a range from C_{NaCl} of 0.0 to 2.5 M. The NPs were suspended in Milli-Q water to reach a concentration of 25 nM. DLS measurements were done with a Malvern Zetasizer nano ZS. The cuvette photos represent the relevant concentrations within the range where agglomeration took place. (A) ≈4 nm core diameter Ag NPs (cf. Section 1.3) overcoated with PMA (cf. Section 6.3). (B) ≈4 nm core diameter Au NPs (cf. Section 1.2) overcoated with PMA (cf. Section 6.3). (C) ≈4 nm core diameter Ag NPs (cf. Section 1.3) after ligand exchange with MPA (cf. Section 5.2). (D) ≈4 nm core diameter Au NPs (cf. Section 1.2) after ligand exchange with mercaptopropionic acid (MPA; cf. Section 5.2). (E) ≈4 nm core diameter Ag NPs (cf. Section 1.3) after ligand exchange with MUA (cf. Section 5.2). (F) ≈ 4 nm core diameter Au NPs (cf. Section 1.2) after ligand exchange with MUA (cf. Section 5.2). (G) ≈5 nm core diameter Cit-Au NPs (purchased from BBI). (H) ≈5 nm core diameter citrate coated Au NPs (purchased from BBI), after ligand exchange to bis(p-sulfonatophenyl)-phenylphosphine (cf. Section 3.2). (I) ≈10 nm core diameter Cit-Au NPs (purchased from BBI). (J) ≈10 nm core diameter citrate coated Au NPs (purchased from BBI), after ligand exchange to bis(p-sulfonatophenyl)-phenylphosphine (cf. Section 3.2).

agglomeration can be directly observed by visible color change. In most cases aggregation of NPs at high NaCl concentrations was severe, inducing NP precipitation and sedimentation on the bottom of the cuvette. The results indicated that PMA is superior compared to MPA or MUA in protecting NPs against salt-induced aggregation. PMA coating resulted in constant hydrodynamic diameter values and suspension color even for high NaCl concentrations. Addition of NaCl to MPA or MUA

coated NP resulted in increased hydrodynamic diameter values and change in suspension color, indicating NP aggregation.

Similar to NP aggregation upon salt addition, NP aggregation can be induced by changing the suspension pH. While salt screens the electric charge on the NP surface, pH may suppress ionization and thus decrease the effective surface charge density, resulting in NP aggregation (cf. Section 10.3 and Section 10.4). In Figure 107, examples on pH-induced NP
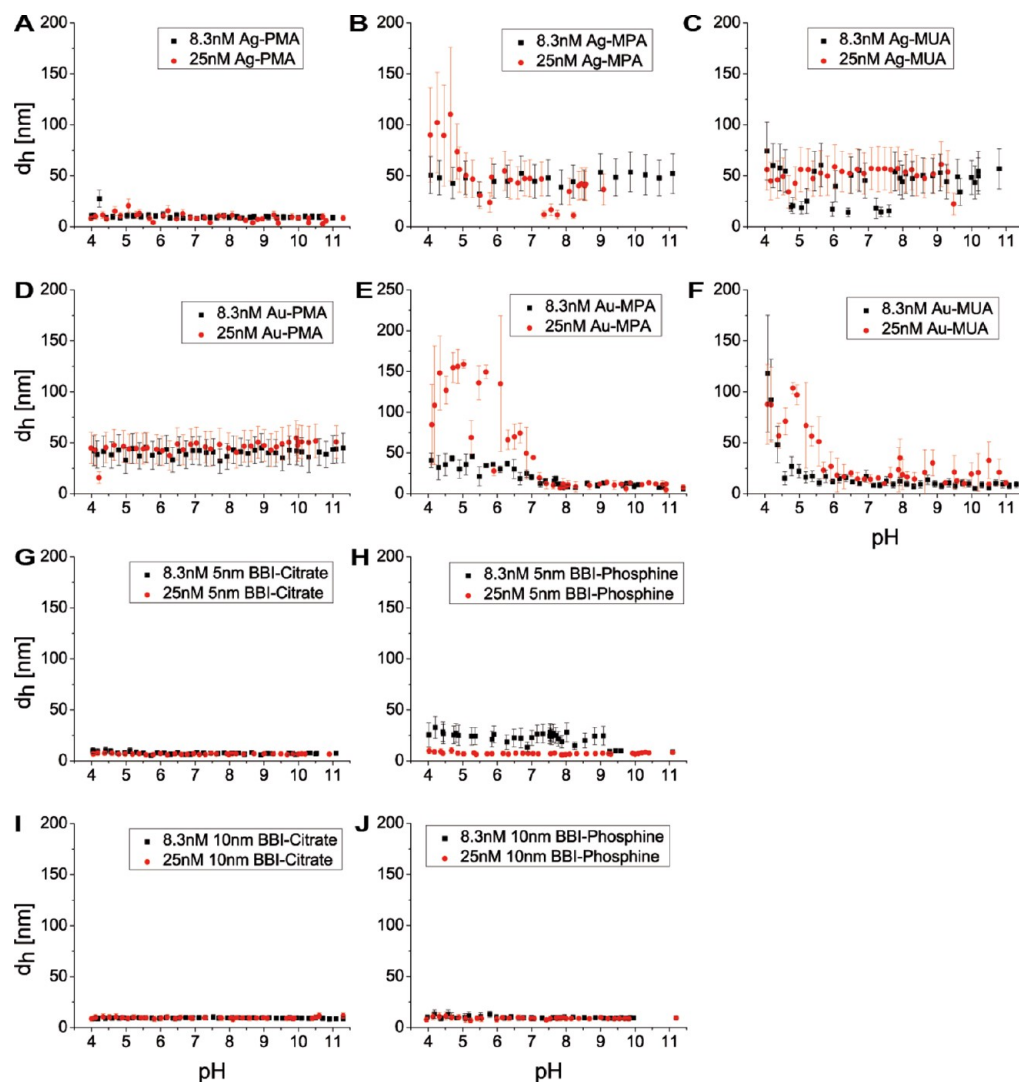
Figure 107. Titration of Ag and Au NPs suspended in 1.5 mM NaOH (aq) with a concentration of c_{NP} = 8.6 nM (■) and c_{NP} = 25 nM (●), with a total volume of 10 mL. HCl (aq) with a concentration of 12 mM was chosen as titrant and was added using a Malvern MPT-2 autotitrator within a pH range from 11 to 4. The hydrodynamic radius d_h is plotted against the pH to detect size-dependent changes and aggregation of the NPs. ≈4 nm core diameter Ag NPs (cf. Section 1.3) (A) overcoated with PMA (cf. Section 6.3), (B) after ligand exchange with MPA (cf. Section 5.2), and (C) after ligand exchange with MUA (cf. Section 5.2). ≈4 nm core diameter Au NPs (cf. Section 1.2) (D) overcoated with PMA (cf. Section 6.3) and (E) after ligand exchange with MPA (cf. Section 5.2). (F) After ligand exchange with MUA (cf. Section 5.2). ≈5 nm core diameter (G) Cit-Au NPs (purchased from BBI) and (H) after ligand exchange to bis(*p*-sulfonatophenyl)-phenylphosphine (cf. Section 3.2). ≈10 nm core diameter (I) Cit-Au NPs (purchased from BBI) and (J) after ligand exchange to bis(*p*-sulfonatophenyl)-phenylphosphine (cf. Section 3.2).

aggregation and the dependence of hydrodynamic diameter from solution pH for anionic charged NPs with different types of surface ligands are shown.

For NPs with ligands containing weak acids, such as carboxylate functional groups ($-COO^-$), the NP effective surface charge decreases at low pH (i.e., high concentration of H^+) due to protonation of the $-COO^-$ groups:

$$R-COOH \leftrightarrow R-COO^- + H^+ \tag{46}$$

This equilibrium is described by the pK_a value.

$$K_a = \frac{c(R-COO^-) \times c(H^+)}{c(R-COOH)} \tag{47}$$

$$pK_a = -\log(K_a) \tag{48}$$

Equations 47 and 48 can be combined with the Henderson–Hasselbalch equation:[159−163]

$$pK_a = -\log(K_a) = -\log\left(\frac{c(R-COO^-) \times c(H^+)}{c(R-COOH)}\right)$$

$$= -\log\left(\frac{c(R-COO^-)}{c(R-COOH)}\right) - \log(c(H^+))$$

$$= -\log\left(\frac{c(R-COO^-)}{c(R-COOH)}\right) + pH$$

leading to

$$pH = pK_a + \log\frac{c(R-COO^-)}{c(R-COOH)} \tag{49}$$

One can thus predict the percent of ionization (J_{R-COO^-}) at certain pH for weak acid as follows:

$$J_{\text{R-COO}^-} = \frac{c(\text{R-COO}^-)}{c(\text{R-COOH}) + c(\text{R-COO}^-)}$$

$$= \frac{1}{\frac{c(\text{R-COOH})}{c(\text{R-COO}^-)} + 1} = \frac{1}{1 + \left(\frac{c(\text{R-COOO}^-)}{c(\text{R-COOH})}\right)^{-1}}$$

$$= \frac{1}{1 + (10^{\text{pH}-\text{p}K_a})^{-1}}$$

leading to

$$J_{\text{R-COO}^-} = \frac{100\%}{1 + 10^{\text{p}K_a - \text{pH}}} \tag{50}$$

Thus, by increasing the NP suspension's pH, the denominator in eq 50 decreases and thus the percent ionized as well as the anionic surface charge density of the NP increases. Instead, by decreasing the NP suspension's pH, the denominator in eq 50 increases, and thus the anionic surface charge density of the NPs decreases. In the latter case, vanishing electrostatic repulsion between NPs induces NP aggregation and increases their effective hydrodynamic diameter at high pH values (cf. Section 10.4).

For NPs with ligands containing weak basic functional groups (e.g., R-NH$_3$), the NP effective surface charge increases at low pH (i.e., high concentration of H$^+$) due to protonation of the amine groups:

$$\text{R-NH}_4^+ \leftrightarrow \text{R-NH}_3 + \text{H}^+ \tag{51}$$

This equilibrium is described by the pK_a value.

$$K_a = \frac{c(\text{R-NH}_3) \times c(\text{H}^+)}{c(\text{R-NH}_4^+)} \tag{52}$$

$$\text{p}K_a = -\log(K_a) \tag{53}$$

This leads to the Henderson–Hasselbalch equation:

$$\text{pH} = \text{p}K_a + \log \frac{c(\text{R-NH}_3)}{c(\text{R-NH}_4^+)} \tag{54}$$

Again, one can predict the percentage of unionization ($J_{\text{R-NH}_3}$) at certain pH values for a weak base as follows:

$$J_{\text{R-NH}_3} = \frac{c(\text{R-NH}_3)}{c(\text{R-NH}_4^+) + c(\text{R-NH}_3)} = \frac{100\%}{1 + 10^{\text{p}K_a - \text{pH}}} \tag{55}$$

Thus, by lowering the pH of suspension containing NPs with a basic functional group, the denominator in eq 55 increases and thus the percent of un-ionized amines decreases (i.e., the ionization and cationic surface charge density of NP increases). Instead, increasing the NP suspension pH, the denominator in eq 55 decreases, and thus the percent un-ionized increases (ionization and cationic surface charge density of NP decreases). In the latter case, vanishing electrostatic repulsion between NPs induces NP aggregation and increases their effective hydrodynamic diameter at high pH values (cf. Section 10.4). There are also charged groups whose charge is independent from the pH. For ammonium salts such as N,N,N-trimethylammonium-2-ethyl methacrylate iodide there is full dissociation, leading to permanent positive surface charges.[114,115]

In Figure 107 the dependence of the hydrodynamic diameter of different negatively charged NPs on the pH of the solution is shown. For this the hydrodynamic diameter d_h of NPs was measured with DLS during a titration with HCl (aq). The NPs were suspended in 1.5 mM NaOH (aq), setting a total volume of 10 mL and concentrations of $c_\text{NP} = 8.3$ or 25 nM. The titrant was aqueous HCl with a concentration of 12 mM. HCl was added using a Malvern MPT-2 autotitrator and the hydrodynamic diameter was measured with a Malvern Zetasizer nano ZS DLS setup.

10.3. Laser Doppler Anemometry. As pointed out in Section 10.1 and Section 10.2, the surface charge of colloidal NPs provides colloidal stability due to electrostatic repulsion forces. Effective surface charge depends on many variables such as solvent type and its pH. In the case of NPs with known surface chemistry and geometry, titration curves (cf. Section 10.4) can be used to estimate the number of charged groups on the surface of a single NP. Alternatively, and most commonly used, the so-called zeta-potential ζ[156,157,164] of the NPs can be measured. The zeta-potential describes the electric potential of the NPs at the distance of the electrostatic screening length (which depends on the ionic strength of the aqueous solution). While in principle electric potential and electric charge are coupled via the Poisson–Boltzmann equation, the complicated geometry of NPs with inorganic core, organic shell, and adsorbed counterions, in general, does not allow for deriving the surface charge from the zeta-potential. However, the sign of the surface charge can be concluded from the sign of the measured zeta-potential. In addition, the magnitude of the zeta-potential provides a good indicator of the NP colloidal stability. Generally, zeta-potential values $|\zeta| > 20–30$ mV are required to maintain colloidal stability and prevent NP aggregation.

One way to measure zeta-potentials is laser Doppler anemometry (LDA). An electric field is applied and the velocity of charged NPs in this field is detected via the Doppler effect. From this the electrophoretic mobility, defined as the quotient of the drift velocity and the applied electric field, can be calculated. By using different models from electrophoretic mobility the zeta-potential can be estimated.[157] Often DLS and LDA are combined in the same setup, such as in the Zetasizer from Malvern. Note that for LDA special cuvettes are required, which comprise electrodes to apply the electric field. Note also that during measurements NP suspensions must cover these electrodes, and thus before measurement it has to be made sure that electrodes are functional, and if required the cuvette needs to be changed. In Figure 108 the distribution of the zeta-potential is shown for PMA-Au NPs. The zeta-potential is then taken as the mean value from the distribution function.

In Figure 109 results for zeta-potential measurements for Au and Ag NPs with different surface coatings at different pH values are shown. Due to the coupled system of an autotitrator and a Zetasizer, it was possible to use the same cuvette for d_h (DLS, cf. Section 10.2) and zeta potential (LDA) measurements before adding more acid and pursue the titration (i.e., lowering of the pH). Thus, the NP concentrations and volumes of added acid are the same as those shown in Section 10.2, as DLS and LDA measurements were performed simultaneously. The data indicate that according to eq 46 at low pH values the negatively charged −COO$^-$ groups get protonated, the zeta-potential thus becomes less negative, and thus the colloidal stability of the NPs is decreased.

10.4. pH Titration. Acid–base titration is a well-established chemical method in which pH is measured as a function of the amount of added acid or base. The resulting plot is called the titration curve, which can be used to determine the pK_a of the
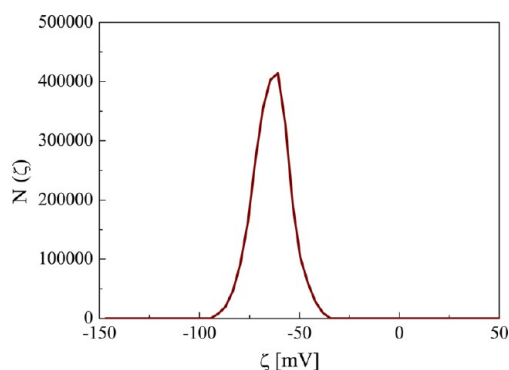
Figure 108. Distribution $N(\zeta)$ of the zeta-potential ζ as measured in water from a sample of ≈4 nm core diameter PMA-Au NPs with c_{NP}= 10 nM. The obtained mean value for the zeta potential is −48.07 ± 1.16 mV.

NPs and, more importantly, the surface density of acidic or basic ligands. Here, the principle is demonstrated for NPs with −COOH groups present on their surface. In order to determine titration curves over a large spectrum and to guarantee fully deprotonated carboxylic moieties, the NPs were first diluted in NaOH (aq) (pH = 11). The basic NP suspension was then titrated using HCl (aq) (cf. Figure 110). First, added H+ (from HCl) can react with free OH− (from NaOH) in suspension. This leads to the first plateau followed by the first steep drop and equivalent point (ep$_1$ in Figure 110). Upon consumption of all free OH− ions, the carboxylates present on the NP surface become protonated, resulting in the second plateau (buffer plateau). Further addition of HCl leads to the second steep drop and equivalent point (ep$_2$ in Figure 110). Further addition of HCl leads to the third plateau at low pH. To determine the pK_a the pH value of the halfway point of the second plateau needs to be considered (∼7 in this case). In
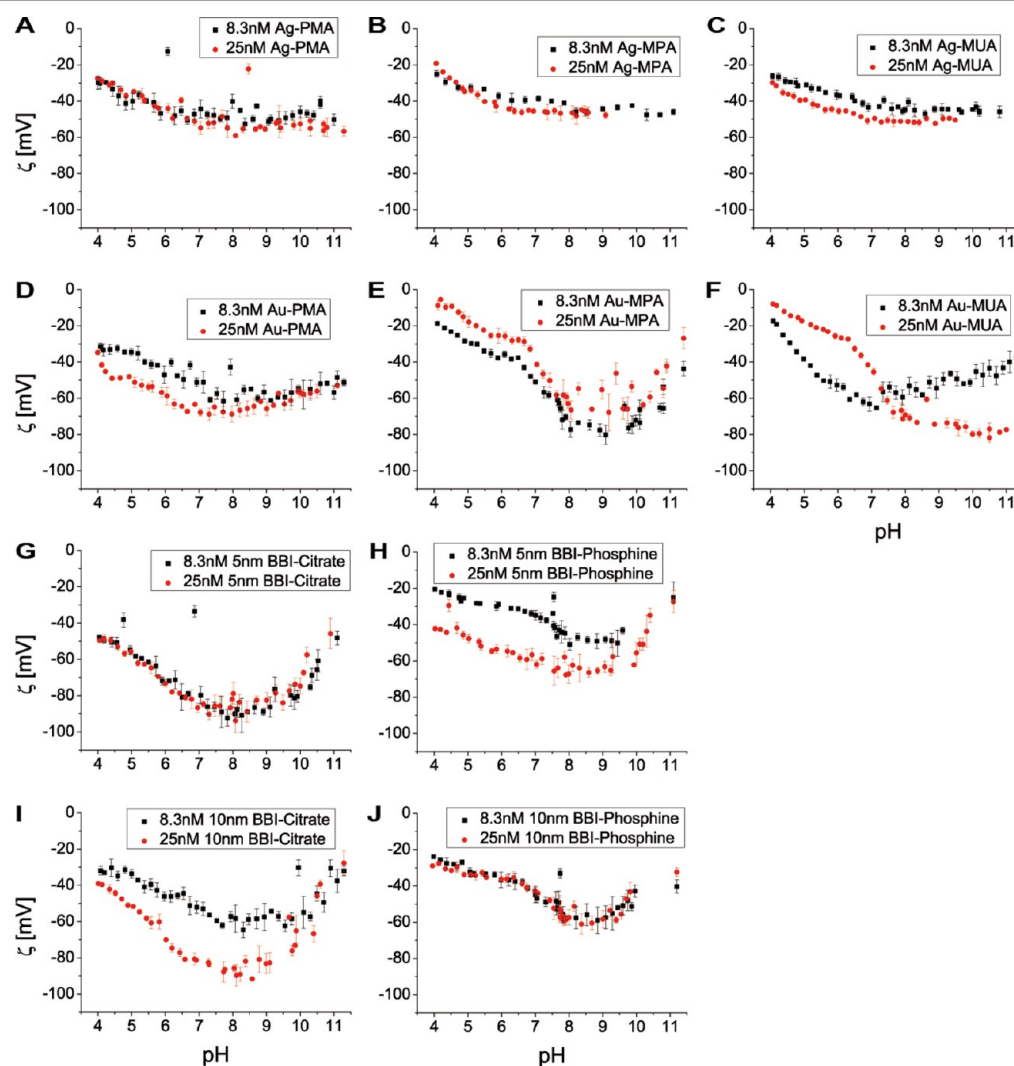

Figure 109. Titration of Ag and Au NPs suspended in 1.5 mM NaOH (aq) with a concentration of c_{NP} = 8.6 nM (■) and c_{NP} = 25 nM (●), with a total volume of 10 mL. HCl (aq) with a concentration of 12 mM was chosen as titrand and was added using a Malvern MPT-2 autotitrator within a pH range from 11 to 4. The zeta-potential ζ is plotted against the pH. These measurements were done simultaneously to the DLS measurements shown in Figure 107. ≈4 nm core diameter Ag NPs (cf. Section 1.3) (A) overcoated with PMA (cf. Section 6.3), (B) after ligand exchange with MPA (cf. Section 5.2), and (C) after ligand exchange with MUA (cf. Section 5.2). ≈4 nm core diameter Au NPs (cf. Section 1.2) (D) overcoated with PMA (cf. Section 6.3), (E) after ligand exchange with MPA (cf. Section 5.2), and (F) after ligand exchange with MUA (cf. Section 5.2). ≈5 nm core diameter (G) Cit-Au NPs (purchased from BBI) and (H) after ligand exchange to bis(p-sulfonatophenyl)-phenylphosphine (cf. Section 3.2). ≈10 nm core diameter (I) Cit-Au NPs (purchased from BBI) and (J) after ligand exchange to bis(p-sulfonatophenyl)-phenylphosphine (cf. Section 3.2).
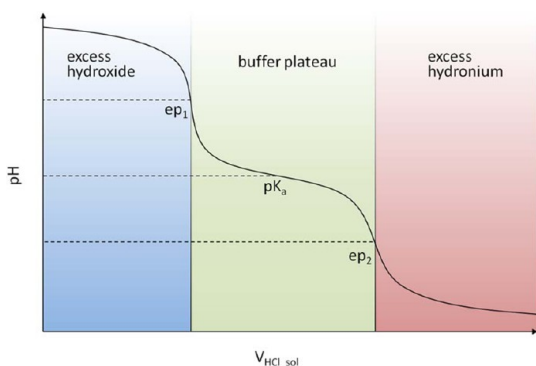
Figure 110. Illustrative titration curve of carboxylate stabilized NPs suspended in NaOH (aq) with the original volume $V_{\text{NaOH\_sol}}$ against HCl (aq), of which the volume $V_{\text{HCl\_sol}}$ has been added. The figure is adapted and modified with permission from Charron et al.[61] Copyright 2012 American Chemical Society.

this experiment, NPs were suspended in aqueous NaOH solution (1.5 mM, $V_{\text{NaOH\_sol}} = 10$ mL) to a concentration of $c_{\text{NP}} = 8.6$ nM. HCl solution (2.5 mM) was added in 100 μL steps to the vigorously stirring NP suspension using the Malvern MPT-2 autotitrator. The resulting volume of the solution is $V_{\text{sol}} = V_{\text{NaOH\_sol}} + V_{\text{HC\_sol}}$. After the addition of each volume of acid the solution was given 5 s to equilibrate, and then the pH was measured using a Sartorius (PP 50) pH meter. The experiments were repeated after 24 h to confirm the data and ensure reproducibility. The pK_a value of the NPs was found to be around ≈ 7 as per the titration curve in Figure 110. By adding more acid the charged groups became saturated with protons, until the pH led to aggregation of the NPs at a pH of around 4−5 due to the loss of surface charge. Examples of titration curves with determined pK_a values for various NPs with different surface chemistries are shown in Figure 111.

If the concentration of NPs (c_{NP}) is known, the number of carboxyl groups on the surface of a single NP can be estimated as described by Charron et al.[61] For example, from Figure 111, the volume of HCl ($\Delta V_{\text{HCl\_sol}}$) used to protonate R−COO$^-$ on the surface of the NPs can be determined as the length of the buffer plateau.

$$\Delta V_{\text{HCl\_sol}} = V_{\text{HCl\_sol}}(\text{ep}_2) - V_{\text{HCl\_sol}}(\text{ep}_1) \qquad (56)$$

Since the concentration of HCl (c_{HCl}) and the volume of initial NP suspension ($V_{\text{NP\_sol}} = V_{\text{NaOH\_sol}}$) are known, the concentration of all carboxylate ions on NPs ($c_{\text{R−COO}^-}$) can be calculated as follows:

$$c_{\text{R−COO}^-} \times V_{\text{NP\_sol}} = c_{\text{HCl}} \times \Delta V_{\text{HCl\_sol}} \qquad (57)$$

The number of acid groups per NP ($N_{\text{R−COO}^-/\text{NP}}$) thus should be

$$N_{\text{R−COO}^-/\text{NP}} = \frac{c_{\text{R−COO}^-}}{c_{\text{NP}}} \qquad (58)$$

In the case of PMA-coated NPs, $N_{\text{R−COO}^-/\text{NP}}$ can be compared with $N_{\text{P/NP}}$ as described in Section 8.6. Each polymer monomer unit in a fully deprotonated state bears one or two negative charges, in the case the PMA backbone is linked to a side chain or hydrolyses, respectively.[114]

$$N_{\text{R−COO}^-/\text{NP}} = (2 - R_{\text{chain/mon}}) \times N_{\text{P/NP}} \qquad (59)$$

While in Figure 111D the second equivalence point is not in the measured pH range, roughly $\Delta V_{\text{HCl\_sol}} \approx 2$ mL. With $c_{\text{HCl}} =$

2.5 mM, $c_{\text{NP}} = 8.6$ nM, and $V_{\text{NP\_sol}} = V_{\text{NaOH\_sol}} = 10$ mL (cf. Figure 111), this leads to $N_{\text{R−COO}^-/\text{NP}} = ((c_{\text{HCl}} \times \Delta V_{\text{HCl\_sol}})/V_{\text{NP\_sol}})/c_{\text{NP}} = ((2.5 \times 10^{-3}$ M $\times 2$ mL$)/10$ mL$)/ 8.6 \times 10^{-9}$ M $\approx 58\,000$. In Section 8.6 TGA analysis of similar PMA-Au NPs (ca. 4 nm core diameter) yielded $N_{\text{P/NP}} = 270$. Thus, with $R_{\text{chain/mon}} = 0.75$, this leads to $N_{\text{R−COO}^-/\text{NP}} = (2 - R_{\text{chain/mon}}) \times N_{\text{P/NP}} = (2 - 0.75) \times 270 \approx 338$. The discrepancy in values can be explained by the different degrees of purification. While the PMA-Au NPs in the case of TGA analysis had been purified by ultracentrifugation ($N_{\text{R−COO}^-/\text{NP}} = 338$), the PMA-Au NPs in the case of titration analysis ($N_{\text{R−COO}^-/\text{NP}} = 58\,000$) had been purified by gel electrophoresis only, which may result in some remaining polymer micelles, which contribute to the amount of COO$^-$ groups. These number examples point out again the necessity of applying different characterization techniques.

CONCLUSIONS

Synthetic protocols in this contribution described the preparation of hydrophobic NPs of different types (Au, Ag, FePt, Fe$_3$O$_4$, Sn, CdSe, and CdSe/ZnS). Moreover, preparation of hydrophilic Au and Ag NPs of various shapes (spheres, rods, stars) and sizes (5−100 nm) are detailed. The prepared NPs showed good monodispersity as evident from the corresponding TEM analysis. Surface functionalization strategies including ligand exchange and polymer overcoating were employed on selected NPs to control their hydrophobicity, hydrophilicity, and colloidal stability. For example, ligand exchange on citrated-capped Au NPs with alkylamine induced phase transfer from water to chloroform. On the other hand, ligand exchange on alkanethiol-capped gold NPs with 3-mercaptopropionic acid molecules facilitated the phase transfer of these NPs into aqueous phase from chloroform. Similarly, a carefully designed amphiphilic polymer was capable of overcoating alkanethiol-capped Au NPs and rendering their surface hydrophilic, allowing facile transfer into aqueous phase from chloroform.

Purification of one type of NPs (namely, PMA-g-dodecyl-capped Au NPs ≈ 4 nm diameter, cf. Section 1.2, Section 6.3) was evaluated using various methods: syringe filtration, ultracentrifugation, size exclusion chromatography, and gel electrophoresis. These results showed different purity levels for different purification methods (for example, ultracentrifugation resulted in fewer free polymer micelles as compared to gel electrophoresis), highlighting the importance of optimizing the purification process for a specific synthesis.

Various characterization techniques confirmed the ability to probe the structural, photophysical, and colloidal properties of NPs. For example, visualization of PEG-capped Au NPs with TEM coupled to negative staining confirmed the NP core dimension and, more importantly, a well-defined polymeric shell surrounding each NP. Thermogravimetric analysis of dodecanethiol-capped Au NPs confirmed the presence of the organic shell on NPs and allowed for quantifying its weight percentage per NP. FTIR and NMR analysis confirmed overcoating of dodecanethiol-capped Au NPs with PMA polymer, highlighting the importance of these analytical techniques to follow surface functionalization of NPs. UV/vis absorption was employed successfully to quantify the concentration of Au NPs, to follow their salt- or pH-induced aggregation by monitoring the plasmon peak shift and broadening and to quantify the loaded dye per single NP. Finally, effective surface charge analysis as measured by laser Doppler anemometry upon acid−base titration allowed for the
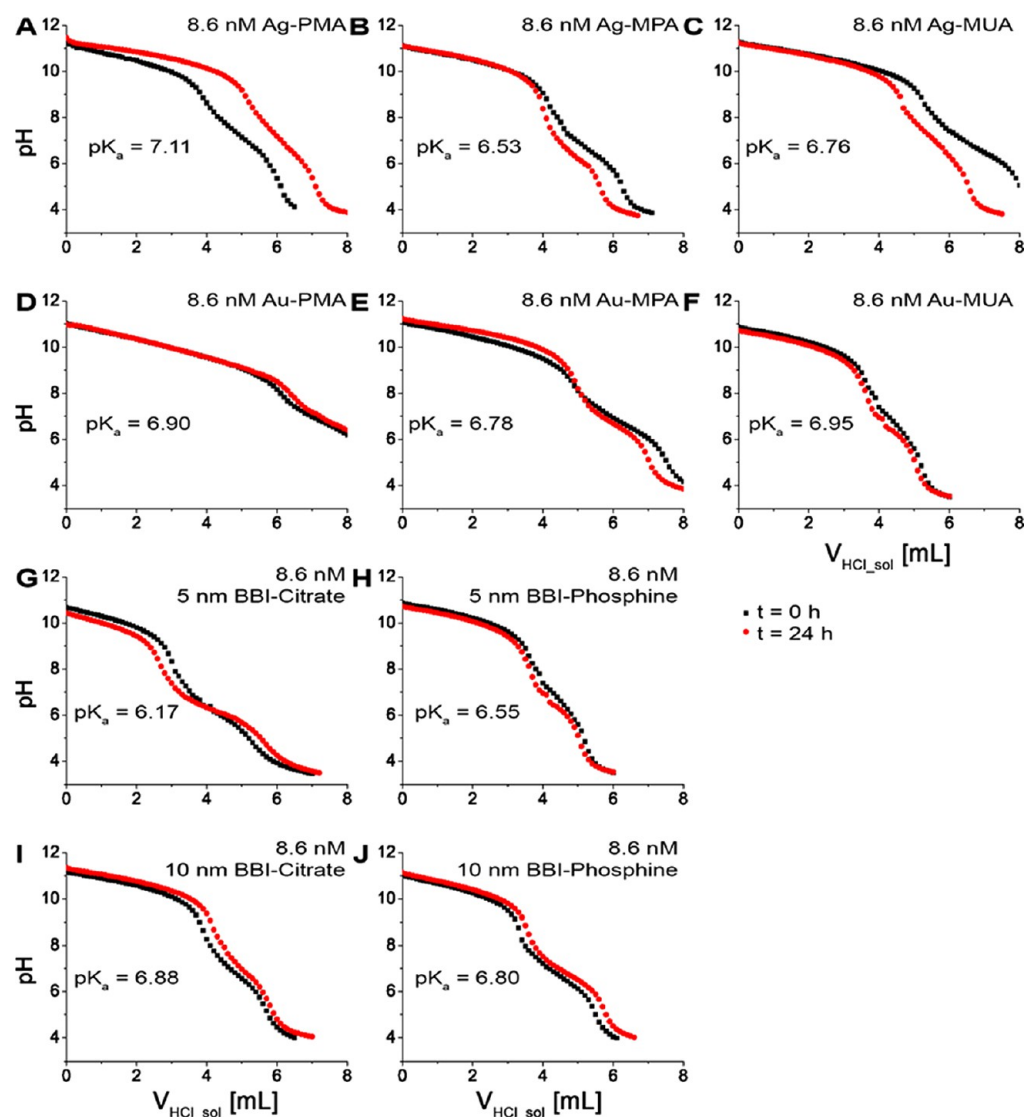
Figure 111. pH titration of Ag and Au NPs with different surface chemistries originally suspended in 1.5 mM NaOH (aq) with a concentration of c_{NP} = 8.6 nM and a total volume of V_{NaOH_sol} = 10 mL. HCl (aq) with a concentration of 2.5 mM was chosen as titrand and was added in steps of ΔV_{HCl_sol} = 100 μL to the NP suspension under vigorous stirring. After the first titration at t = 0 h (■) the experiments were repeated at t = 24 h (●). The NP samples are the same as those used in Figure 107 and Figure 109: ≈4 nm core diameter Ag NPs (cf. Section 1.3) (A) overcoated with PMA (cf. Section 6.3), (B) after ligand exchange with MPA (cf. Section 5.2), and (C) after ligand exchange with MUA (cf. Section 5.2). ≈4 nm core diameter Au NPs (cf. Section 1.2) (D) overcoated with PMA (cf. Section 6.3), (E) after ligand exchange with MPA (cf. Section 5.2), and (F) after ligand exchange with MUA (cf. Section 5.2). ≈5 nm core diameter Au NPs (G) citrate coated (purchased from BBI) and (H) after ligand exchange to bis(p-sulfonatophenyl)-phenylphosphine (cf. Section 3.2). ≈10 nm core diameter Au NPs (I) citrate coated (purchased from BBI) and (J) after ligand exchange to bis(p-sulfonatophenyl)-phenylphosphine (cf. Section 3.2).

determination of the acidity/basicity, pK_a, and number of acidic or basic groups on a single PMA-g-dodecyl-capped Au NP.

On purpose discrepancies in quantitative results as obtained with different characterization techniques are presented. In fact, different characterization techniques analyzed different parameters, and to relate them idealized models, like the sketches in Figure 47, have to be used. Also the degree of purity plays a major role in quantitative analysis.

To the end there is no "optimum" characterization technique. In this contribution an overview was presented about the characterization techniques routinely used in one selected laboratory and which quantitative information can be obtained from them. Collectively, the described details in this contribution should shed light on important corners in the field

of inorganic NP synthesis, characterization, and surface functionalization.

■ ASSOCIATED CONTENT

ⓢ Supporting Information

The Supporting Information is available free of charge on the ACS Publications website at DOI: 10.1021/acs.chemmater.6b04738.

List of symbols used (PDF)

■ AUTHOR INFORMATION

Corresponding Author

*(W.J.P.) E-mail: wolfgang.parak@physik.uni-marburg.de.

ORCID

Pablo del Pino: 0000-0003-1318-6839
Wolfgang J. Parak: 0000-0003-1672-6650

Notes

The authors declare no competing financial interest.

■ REFERENCES

(1) Parak, W. J. Complex Colloidal Assembly. *Science* **2011**, *334*, 1359−1360.

(2) Frens, G. Controlled Nucleation for Regulation of Particle-Size in Monodisperse Gold Solutions. *Nature, Phys. Sci.* **1973**, *241* (105), 20−22.

(3) Bastus, N. G.; Comenge, J.; Puntes, V. Kinetically Controlled Seeded Growth Synthesis of Citrate-Stabilized Gold Nanoparticles of up to 200 nm: Size Focusing versus Ostwald Ripening. *Langmuir* **2011**, *27* (17), 11098−11105.

(4) Bastus, N. G.; Merkoci, F.; Piella, J.; Puntes, V. Synthesis of Highly Monodisperse Citrate-Stabilized Silver Nanoparticles of up to 200 nm: Kinetic Control and Catalytic Properties. *Chem. Mater.* **2014**, *26* (9), 2836−2846.

(5) Pellegrino, T.; Kudera, S.; Liedl, T.; Javier, A. M.; Manna, L.; Parak, W. J. On the Development of Colloidal Nanoparticles towards Multifunctional Structures and their Possible Use for Biological Applications. *Small* **2005**, *1* (1), 48−63.

(6) Sperling, R. A.; Parak, W. J. Surface modification, functionalization and bioconjugation of colloidal inorganic nanoparticles. *Philos. Trans. R. Soc., A* **2010**, *368* (1915), 1333−1383.

(7) Montenegro, J.-M.; Grazu, V.; Sukhanova, A.; Agarwal, S.; de la Fuente, J. M.; Nabiev, I.; Greiner, A.; Parak, W. J. Controlled antibody/(bio-) conjugation of inorganic nanoparticles for targeted delivery. *Adv. Drug Delivery Rev.* **2013**, *65*, 677−688.

(8) Alkilany, A.; Murphy, C. Toxicity and cellular uptake of gold nanoparticles: what we have learned so far? *J. Nanopart. Res.* **2010**, *12* (7), 2313−2333.

(9) Brust, M.; Walker, M.; Bethell, D.; Schiffrin, D. J.; Whyman, R. Synthesis of Thiol-Derivatized Gold Nanoparticles in a 2-Phase Liquid-Liquid System. *J. Chem. Soc., Chem. Commun.* **1994**, No. 7, 801−802.

(10) Lin, C.-A. J.; Sperling, R. A.; Li, J. K.; Yang, T.-Y.; Li, P.-Y.; Zanella, M.; Chang, W. H.; Parak, W. J. Design of an Amphiphilic Polymer for Nanoparticle Coating and Functionalization. *Small* **2008**, *4* (3), 334−341.

(11) Yin, Y.; Alivisatos, A. P. Colloidal nanocrystal synthesis and the organic-inorganic interface. *Nature* **2005**, *437* (7059), 664.

(12) Viswanatha, R.; Santra, P. K.; Dasgupta, C.; Sarma, D. D. Growth mechanism of nanocrystals in solution: ZnO, a case study. *Phys. Rev. Lett.* **2007**, *98* (25), 255501.

(13) Thanh, N. T. K.; Maclean, N.; Mahiddine, S. Mechanisms of Nucleation and Growth of Nanoparticles in Solution. *Chem. Rev.* **2014**, *114* (15), 7610−7630.

(14) Pensa, E.; Cortés, E.; Corthey, G.; Carro, P.; Vericat, C.; Fonticelli, M. H.; Benítez, G.; Rubert, A. A.; Salvarezza, R. C. The Chemistry of the Sulfur−Gold Interface: In Search of a Unified Model. *Acc. Chem. Res.* **2012**, *45*, 1183−1192.

(15) Häkkinen, H. The gold−sulfur interface at the nanoscale. *Nat. Chem.* **2012**, *4*, 443−455.

(16) Fink, J.; Kiely, C. J.; Bethell, D.; Schiffrin, D. J. Self-Organization of Nanosized Gold Particles. *Chem. Mater.* **1998**, *10* (3), 922−926.

(17) Sperling, R. A.; Pellegrino, T.; Li, J. K.; Chang, W. H.; Parak, W. J. Electrophoretic Separation of Nanoparticles with a Discrete Number of Functional Groups. *Adv. Funct. Mater.* **2006**, *16* (7), 943−948.

(18) Ansar, S. M.; Mohammed, F. S.; von White, G., II; Budi, M.; Powell, K. C.; Mefford, O. T.; Kitchens, C. L. Effect of Postsynthesis Purifications on Gold and Silver Nanoparticle Ligand Coverage. *J. Phys. Chem. C* **2016**, *120*, 6842−6850.

(19) Jana, N. R.; Peng, X. Single-Phase and Gram-Scale Routes toward Nearly Monodisperse Au and Other Noble Metal Nanocrystals. *J. Am. Chem. Soc.* **2003**, *125* (47), 14280−14281.

(20) Sun, Y. Controlled synthesis of colloidal silver nanoparticles in organic solutions: empirical rules for nucleation engineering. *Chem. Soc. Rev.* **2013**, *42* (7), 2497−2511.

(21) Mari, A.; Imperatori, P.; Marchegiani, G.; Pilloni, L.; Mezzi, A.; Kaciulis, S.; Cannas, C.; Meneghini, C.; Mobilio, S.; Suber, L. High yield synthesis of pure alkanethiolate-capped silver nanoparticles. *Langmuir* **2010**, *26* (19), 15561−15566.

(22) Sun, S.; Murray, C. B.; Weller, D.; Folks, L.; Moser, A. Monodisperse FePt Nanoparticles and Ferromagnetic FePt Nanocrystal Superlattices. *Science* **2000**, *287*, 1989−1992.

(23) Sun, S.; Zeng, H.; Robinson, D. B.; Raoux, S.; Rice, P. M.; Wang, S. X.; Li, G. Monodisperse MFe_2O_4 (M = Fe, Co, Mn) Nanoparticles. *J. Am. Chem. Soc.* **2004**, *126* (1), 273−279.

(24) Kravchyk, K.; Protesescu, L.; Bodnarchuk, M. I.; Krumeich, F.; Yarema, M.; Walter, M.; Guntlin, C.; Kovalenko, M. V. Monodisperse and inorganically capped Sn and Sn/SnO2 nanocrystals for high-performance Li-ion battery anodes. *J. Am. Chem. Soc.* **2013**, *135* (11), 4199−202.

(25) Peng, Z. A.; Peng, X. Formation of High-Quality CdTe, CdSe, and CdS Nanocrystals Using CdO as Precursor. *J. Am. Chem. Soc.* **2001**, *123* (1), 183−184.

(26) Dabbousi, B. O.; Rodriguez-Viejo, J.; Mikulec, F. V.; Heine, J. R.; Mattoussi, H.; Ober, R.; Jensen, K. F.; Bawendi, M. G. (CdSe)ZnS Core-Shell Quantum Dots: Synthesis and Characterization of a Size Series of Highly Luminescent Nanocrystallites. *J. Phys. Chem. B* **1997**, *101* (46), 9463−9475.

(27) Rizzo, A.; Li, Y. Q.; Kudera, S.; Della Sala, F.; Zanella, M.; Parak, W. J.; Cingolani, R.; Manna, L.; Gigli, G. Blue light emitting diodes based on fluorescent CdSe/ZnS nanocrystals. *Appl. Phys. Lett.* **2007**, *90* (5), 051106.

(28) Song, K.-K.; Lee, S. Highly luminescent (ZnSe)ZnS core-shell quantum dots for blue to UV emission: synthesis and characterization. *Curr. Appl. Phys.* **2001**, *1* (2−3), 169−173.

(29) Yu, W. W.; Qu, L.; Guo, W.; Peng, X. Experimental Determination of the Extinction Coefficient of CdTe, CdSe, and CdS Nanocrystals. *Chem. Mater.* **2003**, *15* (14), 2854−2860.

(30) Bawendi, M. G.; Steigerwald, M. L.; Brus, L. E. The quantum mechanics of large semiconductor clusters ("quantum dots"). *Annu. Rev. Phys. Chem.* **1990**, *41*, 477−496.

(31) Talapin, D. V.; Rogach, A. L.; Kornowski, A.; Haase, M.; Weller, H. Highly Luminescent Monodisperse CdSe and CdSe/ZnS Nanocrystals Synthesized in a Hexadecylamine-Trioctylphosphine Oxide-Trioctylphospine Mixture. *Nano Lett.* **2001**, *1* (4), 207−211.

(32) Xie, R.; Kolb, U.; Li, J.; Basche, T.; Mews, A. Synthesis and Characterization of Highly Luminescent CdSe-Core CdS/Zn0.5Cd0.5S/ZnS Multishell Nanocrystals. *J. Am. Chem. Soc.* **2005**, *127* (20), 7480−7488.

(33) Yu, W. W.; Peng, X. Formation of High-Quality CdS and Other II-VI Semiconductor Nanocrystals in Noncoordinating Solvents: Tunable Reactivity of Monomers. *Angew. Chem., Int. Ed.* **2002**, *41* (13), 2368−2371.

(34) Turkevich, J.; Stevenson, P. C.; Hillier, J. A study of the nucleation and growth processes in the synthesis of colloidal golde. *Discuss. Faraday Soc.* **1951**, *11*, 55−75.

(35) Ye, X.; Jin, L.; Caglayan, H.; Chen, J.; Xing, G.; Zheng, C.; Doan-Nguyen, V.; Kang, Y.; Engheta, N.; Kagan, C. R.; Murray, C. B. Improved Size-Tunable Synthesis of Monodisperse Gold Nanorods through the Use of Aromatic Additives. *ACS Nano* **2012**, *6* (3), 2804−2817.

(36) Li, N.; Zhao, P.; Astruc, D. Anisotropic Gold Nanoparticles: Synthesis, Properties, Applications, and Toxicity. *Angew. Chem., Int. Ed.* **2014**, *53* (7), 1756−1789.

(37) Schulz, F.; Homolka, T.; Bastus, N. G.; Puntes, V.; Weller, H.; Vossmeyer, T. Little Adjustments Significantly Improve the Turkevich Synthesis of Gold Nanoparticles. *Langmuir* **2014**, *30* (35), 10779−10784.

(38) Piella, J.; Bastus, N. G.; Puntes, V. Size-Controlled Synthesis of Sub-10-nanometer Citrate-Stabilized Gold Nanoparticles and Related Optical Properties. *Chem. Mater.* **2016**, *28* (4), 1066−1075.

(39) Scarabelli, L.; Sánchez-Iglesias, A.; Pérez-Juste, J.; Liz-Marzán, L. M. A "Tips and Tricks" Practical Guide to the Synthesis of Gold Nanorods. *J. Phys. Chem. Lett.* **2015**, *6* (21), 4270−4279.

(40) ENUSTUN, B.; TURKEVICH, J. COAGULATION OF COLLOIDAL GOLD. *J. Am. Chem. Soc.* **1963**, *85* (21), 3317−3328.

(41) Zeng, J.; Zheng, Y. Q.; Rycenga, M.; Tao, J.; Li, Z. Y.; Zhang, Q. A.; Zhu, Y. M.; Xia, Y. N. Controlling the Shapes of Silver Nanocrystals with Different Capping Agents. *J. Am. Chem. Soc.* **2010**, *132* (25), 8552.

(42) Li, H. S.; Xia, H. B.; Wang, D. Y.; Tao, X. T. Simple Synthesis of Monodisperse, Quasi-spherical, Citrate-Stabilized Silver Nanocrystals in Water. *Langmuir* **2013**, *29* (16), 5074−5079.

(43) Sondi, I.; Goia, D. V.; Matijevic, E. Preparation of highly concentrated stable dispersions of uniform silver nanoparticles. *J. Colloid Interface Sci.* **2003**, *260* (1), 75−81.

(44) Banerjee, S.; Loza, K.; Meyer-Zaika, W.; Prymak, O.; Epple, M. Structural Evolution of Silver Nanoparticles during Wet-Chemical Synthesis. *Chem. Mater.* **2014**, *26* (2), 951−957.

(45) Ye, X.; Zheng, C.; Chen, J.; Gao, Y.; Murray, C. B. Using Binary Surfactant Mixtures To Simultaneously Improve the Dimensional Tunability and Monodispersity in the Seeded Growth of Gold Nanorods. *Nano Lett.* **2013**, *13* (2), 765−771.

(46) Jana, N. R.; Gearheart, L.; Murphy, C. J. Wet Chemical Synthesis of High Aspect Ratio Cylindrical Gold Nanorods. *J. Phys. Chem. B* **2001**, *105* (18), 4065−4067.

(47) Nikoobakht, B.; El-Sayed, M. A. Preparation and Growth Mechanism of Gold Nanorods (NRs) Using Seed-Mediated Growth Method. *Chem. Mater.* **2003**, *15* (10), 1957−1962.

(48) Murphy, C. J.; Thompson, L. B.; Chernak, D. J.; Yang, J. A.; Sivapalan, S. T.; Boulos, S. P.; Huang, J.; Alkilany, A. M.; Sisco, P. N. Gold nanorod crystal growth: From seed-mediated synthesis to nanoscale sculpting. *Curr. Opin. Colloid Interface Sci.* **2011**, *16* (2), 128−134.

(49) Alkilany, A. M.; Nagaria, P. K.; Hexel, C. R.; Shaw, T. J.; Murphy, C. J.; Wyatt, M. D. Cellular uptake and cytotoxicity of gold nanorods: molecular origin of cytotoxicity and surface effects. *Small* **2009**, *5* (6), 701−8.

(50) Yuan, H.; Fales, A.; Vo-Dinh, T. TAT Peptide-Functionalized Gold Nanostars: Enhanced Intracellular Delivery and Efficient NIR Photothermal Therapy Using Ultralow Irradiance. *J. Am. Chem. Soc.* **2012**, *134* (28), 11358−11361.

(51) Indrasekara, A.; Wadams, R.; Fabris, L. Ligand Exchange on Gold Nanorods: Going Back to the Future. *PARTICLE & PARTICLE SYSTEMS CHARACTERIZATION* **2014**, *31* (8), 819−838.

(52) Pellegrino, T.; Sperling, R. A.; Alivisatos, A. P.; Parak, W. J. Gelelectrophoresis of Gold-DNA Nanoconjugates. *J. Biomed. Biotechnol.* **2007**, *2007*, 26796.

(53) Parak, W. J.; Pellegrino, T.; Micheel, C. M.; Gerion, D.; Williams, S. C.; Alivisatos, A. P. Conformation of oligonucleotides attached to gold nanocrystals probed by gel electrophoresis. *Nano Lett.* **2003**, *3* (1), 33−36.

(54) Lipka, M.; Semmler-Behnke, M.; Sperling, R. A.; Wenk, A.; Takenaka, S.; Schleh, C.; Kissel, T.; Parak, W. J.; Kreyling, W. G. Biodistribution of PEG-modified gold nanoparticles following intratracheal instillation and intravenous injection. *Biomaterials* **2010**, *31* (25), 6574−6581.

(55) Brandenberger, C.; Mühlfeld, C.; Ali, Z.; Lenz, A.-G.; Schmid, O.; Parak, W. J.; Gehr, P.; Rothen-Rutishauser, B. Quantitative Evaluation of Cellular Uptake and Trafficking of Plain and Polyethylene Glycol-Coated Gold Nanoparticles. *Small* **2010**, *6*, 1669−1678.

(56) del Pino, P.; Yang, F.; Pelaz, B.; Zhang, Q.; Kantner, K.; Hartmann, R.; Martinez de Baroja, N.; Gallego, M.; Möller, M.; Manshian, B. B.; Soenen, S. J.; Riedel, R.; Hampp, N.; Parak, W. J. Basic Physicochemical Properties of Polyethylene Glycol Coated Gold Nanoparticles that Determine Their Interaction with Cells. *Angew. Chem., Int. Ed.* **2016**, *55*, 5483−5487.

(57) Soliman, M. G.; Pelaz, B.; Parak, W. J.; del Pino, P. Phase transfer and polymer coating methods toward improving the stability of metallic nanoparticles for biological applications. *Chem. Mater.* **2015**, *27*, 990−997.

(58) Lista, M.; Liu, D. Z.; Mulvaney, P. Phase Transfer of Noble Metal Nanoparticles to Organic Solvents. *Langmuir* **2014**, *30* (8), 1932−1938.

(59) Serrano-Montes, A. B.; Jimenez de Aberasturi, D.; Langer, J.; Giner-Casares, J. J.; Scarabelli, L.; Herrero, A.; Liz-Marzan, L. M. A General Method for Solvent Exchange of Plasmonic Nanoparticles and Self-Assembly into SERS-Active Monolayers. *Langmuir* **2015**, *31* (33), 9205−9213.

(60) Chan, W. C. W.; Nie, S. Quantum Dot Bioconjugates for Ultrasensitive Nonisotopic Detection. *Science* **1998**, *281*, 2016−2018.

(61) Charron, G.; Hühn, D.; Perrier, A.; Cordier, L.; Pickett, C. J.; Nann, T.; Parak, W. J. On the Use of pH Titration to Quantitatively Characterize Colloidal Nanoparticles. *Langmuir* **2012**, *28* (43), 15141−15149.

(62) Caballero-Díaz, E.; Pfeiffer, C.; Kastl, L.; Rivera-Gil, P.; Simonet, B.; Valcárcel, M.; Jiménez-Lamana, J.; Laborda, F.; Parak, W. J. The Toxicity of Silver Nanoparticles Depends on Their Uptake by Cells and Thus on Their Surface Chemistry. *Particle and Particle Systems Characterization* **2013**, *30* (12), 1079−1085.

(63) Wu, M. X.; Liu, H.; Liu, J.; Haley, K. N.; Treadway, J. A.; Larson, J. P.; Ge, N.; Peale, F.; Bruchez, M. P. Immunofluorescent labeling of cancer marker Her2 and other cellular targets with semiconductor quantum dots. *Nat. Biotechnol.* **2002**, *21*, 41−46.

(64) Pellegrino, T.; Manna, L.; Kudera, S.; Liedl, T.; Koktysh, D.; Rogach, A. L.; Keller, S.; Rädler, J.; Natile, G.; Parak, W. J. Hydrophobic Nanocrystals Coated with an Amphiphilic Polymer Shell: A General Route to Water Soluble Nanocrystals. *Nano Lett.* **2004**, *4* (4), 703−707.

(65) Ali, Z.; Abbasi, A. Z.; Zhang, F.; Arosio, P.; Lascialfari, A.; Casula, M. F.; Wenk, A.; Kreyling, W.; Plapper, R.; Seidel, M.; Niessner, R.; Knoll, J.; Seubert, A.; Parak, W. J. Multifunctional Nanoparticles for Dual Imaging. *Anal. Chem.* **2011**, *83* (8), 2877−2882.

(66) Zhang, F.; Lees, E.; Amin, F.; RiveraGil, P.; Yang, F.; Mulvaney, P.; Parak, W. J. Polymer-Coated Nanoparticles: A Universal Tool for Biolabelling Experiments. *Small* **2011**, *7*, 3113−3127.

(67) Pelaz, B.; Del Pino, P.; Maffre, P.; Hartmann, R.; Gallego, M.; Rivera-Fernandez, S.; de la Fuente, J. M.; Nienhaus, G. U.; Parak, W. J. Surface Functionalization of Nanoparticles with Polyethylene Glycol: Effects on Protein Adsorption and Cellular Uptake. *ACS Nano* **2015**, *9* (7), 6996−7008.

(68) Kaiser, U.; Jimenez de Aberasturi, D.; Vazquez-Gonzalez, M.; Carrillo-Carrion, C.; Niebling, T.; Parak, W. J.; Heimbrodt, W. Determining the exact number of dye molecules attached to colloidal

CdSe/ZnS quantum dots in Förster resonant energy transfer assemblies. *J. Appl. Phys.* **2015**, *117*, 024701.

(69) Joris, F.; Valdeperez, D.; Pelaz, B.; Soenen, S.; Manshian, B.; Parak, W.; De Smedt, S.; Raemdonck, K. The impact of species and cell type on the nanosafety profile of iron oxide nanoparticles in neural cells. *J. Nanobiotechnol.* **2016**, *14*, 69.

(70) Kirchner, C.; Liedl, T.; Kudera, S.; Pellegrino, T.; Muñoz Javier, A.; Gaub, H. E.; Stölzle, S.; Fertig, N.; Parak, W. J. Cytotoxicity of Colloidal CdSe and CdSe/ZnS Nanoparticles. *Nano Lett.* **2005**, *5* (2), 331−338.

(71) Riedinger, A.; Zhang, F.; Dommershausen, F.; Röcker, C.; Brandholt, S.; Nienhaus, G. U.; Koert, U.; Parak, W. J. Ratiometric Optical Sensing of Chloride Ions with Organic Fluorophore - Gold Nanoparticle Hybrids: A Systematic Study of Distance Dependency and the Influence of Surface Charge. *Small* **2010**, *6* (22), 2590−2597.

(72) Zhang, F.; Ali, Z.; Amin, F.; Feltz, A.; Oheim, M.; Parak, W. J. IIon and pH Sensing with Colloidal Nanoparticles: Influence of Surface Charge on Sensing and Colloidal Properties. *ChemPhysChem* **2010**, *11*, 730−735.

(73) Abbasi, A. Z.; Amin, F.; Niebling, T.; Friede, S.; Ochs, M.; Carregal-Romero, S.; Montenegro, J. M.; Rivera Gil, P.; Heimbrodt, W.; Parak, W. J. How colloidal nanoparticles could facilitate multiplexed measurements of different analytes with analyte-sensitive organic fluorophores. *ACS Nano* **2011**, *5*, 21−25.

(74) Amin, F.; Yushchenko, D. A.; Montenegro, J. M.; Parak, W. J. Integration of Organic Fluorophores in the Surface of Polymer-Coated Colloidal Nanoparticles for Sensing the Local Polarity of the Environment. *ChemPhysChem* **2012**, *13* (4), 1030−1035.

(75) Soenen, S. J.; Manshian, B.; Montenegro, J. M.; Amin, F.; Meermann, B.; Thiron, T.; Cornelissen, M.; Vanhaecke, F.; Doak, S.; Parak, W. J.; De Smedt, S.; Braeckmans, K. Cytotoxic Effects of Gold Nanoparticles: A Multiparametric Study. *ACS Nano* **2012**, *6* (7), 5767−5783.

(76) Pyell, U.; Jalil, A. H.; Pfeiffer, C.; Pelaz, B.; Parak, W. J. Characterization of gold nanoparticles with different hydrophilic coatings via capillary electrophoresis and Taylor dispersion analysis. Part I: Determination of the zeta potential employing a modified analytic approximation. *J. Colloid Interface Sci.* **2015**, *450*, 288−300.

(77) Pyell, U.; Jalil, A. H.; Pfeiffer, C.; Pelaz, B.; Parak, W. J.; Urban, D. A. Characterization of hydrophilic coated gold nanoparticles via capillary electrophoresis and Taylor dispersion analysis. Part II: Determination of the hydrodynamic radius distribution − Comparison with asymmetric flow field-flow fractionation. *J. Colloid Interface Sci.* **2015**, *457*, 131−140.

(78) Marisca, O. T.; Kantner, K.; Pfeiffer, h.; Zhang, Q.; Pelaz, B.; Leopold, N.; Parak, W. J.; Rejman, J. Comparison of the in Vitro Uptake and Toxicity of Collagen- and Synthetic Polymer-Coated Gold Nanoparticles. *Nanomaterials* **2015**, *5*, 1418−1430.

(79) Menendez-Miranda, M.; Costa-Fernandez, J. M.; Encinar, J. R.; Parak, W. J.; Carrillo-Carrion, C. Determination of the ratio of fluorophore/nanoparticle for fluorescence-labelled nanoparticles. *Analyst* **2016**, *141* (4), 1266−1272.

(80) Sperling, R. A.; Liedl, T.; Duhr, S.; Kudera, S.; Zanella, M.; Lin, C.-A. J.; Chang, W. H.; Braun, D.; Parak, W. J. Size Determination of (Bio-) Conjugated Water-Soluble Colloidal Nanoparticles: A Comparison of Different Techniques. *J. Phys. Chem. C* **2007**, *111* (31), 11552−11559.

(81) Harakeh, S.; Abdel-Massih, R. M.; Rivera Gil, P.; Sperling, R. A.; Meinhardt, A.; Niedwiecki, A.; Rath, M.; Parak, W. J.; Baydoun, E. The effect of PEG-coated gold nanoparticles on the anti-proliferative potential of Specific Nutrient Synergy. *Nanotoxicology* **2010**, *4*, 177−185.

(82) Van Hoecke, K.; De Schamphelaere, K. A. C.; Ali, Z.; Zhang, F.; Elsaesser, A.; Rivera Gil, P.; Parak, W. J.; Smagghe, G.; Janssen, C. R.; Howard, C. V. Ecotoxicity and uptake of polymer coated gold nanoparticles. *Nanotoxicology* **2013**, *7* (1), 37−47.

(83) Soenen, S. J.; Manshian, B. B.; Abdelmonem, A. M.; Montenegro, J.-M.; Tan, S.; Balcaen, L.; Vanhaecke, F.; Brisson, A. R.; Parak, W. J.; De Smedt, S. C.; Braeckmans, K. The Cellular

Interactions of PEGylated Gold Nanoparticles: Effect of PEGylation on Cellular Uptake and Cytotoxicity. *Particle & Particle Systems Characterization* **2014**, *31*, 794−800.

(84) Kantner, K.; Ashraf, S.; Carregal-Romero, S.; Carrillo-Carrion, C.; Collot, M.; del Pino, P.; Heimbrodt, W.; Jimenez de Aberasturi, D.; Kaiser, U.; Kazakova, L. I.; Lelle, M.; Martinez de Baroja, N.; Montenegro, J.-M.; Nazarenus, M.; Pelaz, B.; Peneva, K.; Rivera Gil, P.; Sabir, N.; Schneider, L. M.; Shabarchina, L. I.; Sukhorukov, G. B.; Vazquez, M.; Yang, F.; Parak, W. J. Particle-Based Optical Sensing of Intracellular Ions at the Example of Calcium - What are the Experimental Pitfalls? *Small* **2015**, *11*, 896−904.

(85) Yu, X.; Lei, D. Y.; Amin, F.; Hartmann, R.; Acuna, G. P.; Guerrero-Martínez, A.; Maier, S. A.; Tinnefeld, P.; Carregal-Romero, S.; Parak, W. J. Distance control in-between plasmonic nanoparticles via biological and polymeric spacers. *Nano Today* **2013**, *8* (5), 480−493.

(86) Kaiser, U.; Jimenez de Aberasturi, D.; Malinowski, R.; Amin, F.; Parak, W. J.; Heimbrodt, W. Multiplexed measurements by time resolved spectroscopy using colloidal CdSe/ZnS quantum dots. *Appl. Phys. Lett.* **2014**, *104*, 041901−041904.

(87) Kreyling, W. G.; Abdelmonem, A. M.; Ali, Z.; Alves, F.; Geiser, M.; Haberl, N.; Hartmann, R.; Hirn, S.; de Aberasturi, D. J.; Kantner, K.; Khadem-Saba, G.; Montenegro, J. M.; Rejman, J.; Rojo, T.; de Larramendi, I. R.; Ufartes, R.; Wenk, A.; Parak, W. J. In vivo integrity of polymer-coated gold nanoparticles. *Nat. Nanotechnol.* **2015**, *10* (7), 619−23.

(88) Zyuzin, M. V.; Honold, T.; Carregal-Romero, S.; Kantner, K.; Karg, M.; Parak, W. J. Influence of Temperature on the Colloidal Stability of Polymer-Coated Gold Nanoparticles in Cell Culture Media. *Small* **2016**, *13*, 1723−1731.

(89) Rothen-Rutishauser, B.; Kuhn, D. A.; Ali, Z.; Gasser, M.; Amin, F.; Parak, W. J.; Vanhecke, D.; Fink, A.; Gehr, P.; Brandenberger, C. Quantification of gold nanoparticle cell uptake under controlled biological conditions and adequate resolution. *Nanomedicine* **2014**, *9* (5), 607−621.

(90) Jimenez de Aberasturi, D.; Serrano-Montes, A. B.; Langer, J.; Henriksen-Lacey, M.; Parak, W. J.; Liz-Marzán, L. M. Encoded Gold Nanostars for Multiplexed SERS Cell Differentiation. *Chem. Mater.* **2016**, *28*, 6779−6790.

(91) Manshian, B. B.; Pfeiffer, C.; Pelaz, B.; Heimerl, T.; Gallego, M.; Möller, M.; del Pino, P.; Himmelreich, U.; Parak, W. J.; Soenen, S. J. High-Content Imaging and Gene Expression Approaches To Unravel the Effect of Surface Functionality on Cellular Interactions of Silver Nanoparticles. *ACS Nano* **2015**, *9*, 10431−10444.

(92) Yakovlev, A. V.; Zhang, F.; Zulqurnain, A.; Azhar-Zahoor, A.; Luccardini, C.; Gaillard, S.; Mallet, J. M.; Tauc, P.; Brochon, J. C.; Parak, W. J.; Feltz, A.; Oheim, M. Wrapping Nanocrystals with an Amphiphilic Polymer Preloaded with Fixed Amounts of Fluorophore Generates FRET-Based Nanoprobes with a Controlled Donor/Acceptor Ratio. *Langmuir* **2009**, *25* (5), 3232−3239.

(93) Cywiński, P. J.; Hammann, T.; Hühn, D.; Parak, W. J.; Hildebrandt, N.; Löhmannsröben, H.-G. Europium-quantum dot nanobioconjugates as luminescent probes for time-gated biosensing. *J. Biomed. Opt.* **2014**, *19*, 101506.

(94) Liedl, T.; Keller, S.; Simmel, F. C.; Rädler, J. O.; Parak, W. J. Fluorescent Nanocrystals as Colloidal Probes in Complex Fluids Measured by Fluorescence Correlation Spectroscopy. *Small* **2005**, *1* (10), 997−1003.

(95) Carrillo-Carrion, C.; Parak, W. J. Design of pyridyl-modified amphiphilic polymeric ligands: Towards better passivation of water-soluble colloidal quantum dots for improved optical performance. *J. Colloid Interface Sci.* **2016**, *478*, 88−96.

(96) Niebling, T.; Zhang, F.; Ali, Z.; Parak, W. J.; Heimbrodt, W. Excitation dynamics in polymer-coated semiconductor quantum dots with integrated dye molecules: The role of reabsorption. *J. Appl. Phys.* **2009**, *106*, 104701.

(97) Hsieh, M. F.; Li, J. K. J.; Lin, C. A. J.; Huang, S. H.; Sperling, R. A.; Parak, W. J.; Chang, W. H. Tracking of Cellular Uptake of Hydrophilic CdSe/ZnS Quantum Dots/Hydroxyapatite Composites

Nanoparticles in MC3T3-E1 Osteoblast Cells. *J. Nanosci. Nanotechnol.* **2009**, *9* (4), 2758−2762.

(98) Manshian, B. B.; Abdelmonem, A. M.; Kantner, K.; Pelaz, B.; Klapper, M.; Tirroni, C. N.; Parak, W. J.; Himmelreich, U.; Soenen, S. J. Evaluation of quantum dot cytotoxicity: interpretation of nanoparticle concentrations versus intracellular nanoparticle numbers. *Nanotoxicology* **2016**, *10*, 1318−1328.

(99) Soenen, S. J.; Montenegro, J.-M.; Abdelmonem, A. M.; Manshian, B. B.; Doak, S. H.; Parak, W. J.; De Smedt, S. C.; Braeckmans, K. Corrigendum to "The effect of nanoparticle degradation on poly(methacrylic acid)-coated quantum dot toxicity: The importance of particle functionality assessment in toxicology" [Acta Biomater. 10 (2014) 732−741]. *Acta Biomater.* **2015**, *12*, 362.

(100) Fernández-Argüelles, M. T.; Yakovlev, A.; Sperling, R. A.; Luccardini, C.; Gaillard, S.; Medel, A. S.; Mallet, J.-M.; Brochon, J.-C.; Feltz, A.; Oheim, M.; Parak, W. J. Synthesis and Characterization of Polymer-Coated Quantum Dots with Integrated Acceptor Dyes as FRET-based Nanoprobes. *Nano Lett.* **2007**, *7* (9), 2613−2617.

(101) Kaiser, U.; Sabir, N.; Carrillo-Carrion, C.; del Pino, P.; Bossi, M.; Heimbrodt, W.; Parak, W. J. Förster resonance energy transfer mediated enhancement of the fluorescence lifetime of organic fluorophores to the millisecond range by coupling to Mn-doped CdS/ZnS quantum dots. *Nanotechnology* **2016**, *27*, 055101.

(102) Schrittwieser, S.; Pelaz, B.; Parak, W. J.; Lentijo-Mozo, S.; Soulantica, K.; Dieckhoff, J.; Ludwig, F.; Altantzis, T.; Bals, S.; Schotter, J. Homogeneous Protein Analysis by Magnetic Core−Shell Nanorod Probes. *ACS Appl. Mater. Interfaces* **2016**, *8*, 8893−8899.

(103) Zhang, Q.; Castellanos-Rubio, I.; Munshi, R.; Orue, I.; Pelaz, B.; Gries, K. I.; Parak, W. J.; del Pino, P.; Pralle, A. Model Driven Optimization of Magnetic Anisotropy of Exchange-Coupled Core-Shell Ferrite Nanoparticles for Maximal Hysteretic Loss. *Chem. Mater.* **2015**, *27*, 7380−7387.

(104) Casula, M. F.; Floris, P.; Innocenti, C.; Lascialfari, A.; Marinone, M.; Corti, M.; Sperling, R. A.; Parak, W. J.; Sangregorio, C. Magnetic Resonance Imaging Contrast Agents Based on Iron Oxide Superparamagnetic Ferrofluids. *Chem. Mater.* **2010**, *22* (5), 1739−1748.

(105) Colombo, M.; Mazzucchelli, S.; Montenegro, J. M.; Galbiati, E.; Corsi, F.; Parak, W. J.; Prosperi, D. Protein Oriented Ligation on Nanoparticles Exploiting O6-Alkylguanine-DNA Transferase (SNAP) Genetically Encoded Fusion. *Small* **2012**, *8* (10), 1492−1497.

(106) Schweiger, C.; Hartmann, R.; Zhang, F.; Parak, W. J.; Kissel, T.; Rivera Gil, P. Quantification of the Internalization Patterns of Superparamagnetic Iron Oxide Nanoparticles with Opposite Charge. *J. Nanobiotechnol.* **2012**, *10* (1), 28.

(107) Röcker, C.; Pötzl, M.; Zhang, F.; Parak, W. J.; Nienhaus, G. U. A Quantitative Fluorescence Study of Protein Monolayer Formation on Colloidal Nanoparticles. *Nat. Nanotechnol.* **2009**, *4* (9), 577−580.

(108) Lehmann, A. D.; Parak, W. J.; Zhang, F.; Ali, Z.; Röcker, C.; Nienhaus, G. U.; Gehr, P.; Rothen-Rutishauser, B. Fluorescent-Magnetic Hybrid Nanoparticles Induce a Dose-Dependent Increase in Proinflammatory Response in Lung Cells in vitro Correlated with Intracellular Localization. *Small* **2010**, *6* (6), 753−762.

(109) Mahmoudi, M.; Abdelmonem, A. M.; Behzadi, S.; Clement, J. H.; Dutz, S.; Ejtehadi, M. R.; Hartmann, R.; Kantner, K.; Linne, U.; Maffre, P.; Metzler, S.; Moghadam, M. K.; Pfeiffer, C.; Rezaei, M.; Ruiz-Lozano, P.; Serpooshan, V.; Shokrgozar, M. A.; Nienhaus, G. U.; Parak, W. J. Temperature: The "Ignored" Factor at the NanoBio Interface. *ACS Nano* **2013**, *7* (8), 6555−6562.

(110) Tromsdorf, U. I.; Bigall, N. C.; Kaul, M.; Bruns, O. T.; Nikolic, M. S.; Mollwitz, B.; Sperling, R. A.; Reimer, R.; Hohenberg, H.; Parak, W. J.; Förster, S.; Beisiegel, U.; Adam, G.; Weller, H. Size and Surface Effects on the MRI Relaxivity of Manganese Ferrite Nanoparticle Contrast Agents. *Nano Lett.* **2007**, *7* (8), 2422−2427.

(111) Wilhelm, S.; Kaiser, M.; Wuerth, C.; Heiland, J.; Carrillo-Carrion, C.; Muhr, V.; Wolfbeis, O. S.; Parak, W. J.; Resch-Genger, U.; Hirsch, T. Water dispersible upconverting nanoparticles: effects of surface modification on their luminescence and colloidal stability. *Nanoscale* **2015**, *7* (4), 1403−1410.

(112) Abdelmonem, A. M.; Pelaz, B.; Kantner, K.; Bigall, N. C.; Del Pino, P.; Parak, W. J. Charge and agglomeration dependent in vitro uptake and cytotoxicity of zinc oxide nanoparticles. *J. Inorg. Biochem.* **2015**, *153*, 334−338.

(113) Kim, G.-M.; Wutzler, A.; Radusch, H.-J.; Michler, G. H.; Simon, P.; Sperling, R. A.; Parak, W. J. One-Dimensional Arrangement of Gold Nanoparticles by Electrospinning. *Chem. Mater.* **2005**, *17*, 4949−4957.

(114) Geidel, C.; Schmachtel, S.; Riedinger, A.; Pfeiffer, C.; Müllen, K.; Klapper, M.; Parak, W. J. A General Synthetic Approach for Obtaining Cationic and Anionic Inorganic Nanoparticles *via* Encapsulation in Amphiphilic Copolymers. *Small* **2011**, *7* (20), 2929−2934.

(115) Hühn, D.; Kantner, K.; Geidel, C.; Brandholt, S.; De Cock, I.; Soenen, S. J. H.; Rivera Gil, P.; Montenegro, J.-M.; Braeckmans, K.; Müllen, K.; Nienhaus, G. U.; Klapper, M.; Parak, W. J. Polymer-Coated Nanoparticles Interacting with Proteins and Cells: Focusing on the Sign of the Net Charge. *ACS Nano* **2013**, *7* (4), 3253−3263.

(116) Hagel, L. Gel Filtration. In *Protein Purification. Principles, High Resolution Methods and Applications*, 2nd ed.; Janson, J.-C.; Ryden, L., Eds.; John Wiley & Sons: New York, 1998; pp 79−143.

(117) Amersham_Pharmacia_Biotech. *Gel filtration - Principles and Methods*, 8th ed.; Amersham Pharmacia Biotech: 2001.

(118) Parak, W. J.; Gerion, D.; Zanchet, D.; Woerz, A. S.; Pellegrino, T.; Micheel, C.; Williams, S. C.; Seitz, M.; Bruehl, R. E.; Bryant, Z.; Bustamante, C.; Bertozzi, C. R.; Alivisatos, A. P. Conjugation of DNA to silanized colloidal semiconductor nanocrystaline quantum dots. *Chem. Mater.* **2002**, *14* (5), 2113−2119.

(119) Zanchet, D.; Micheel, C. M.; Parak, W. J.; Gerion, D.; Williams, S. C.; Alivisatos, A. P. Electrophoretic and Structural Studies of DNA-Directed Au Nanoparticle Groupings. *J. Phys. Chem. B* **2002**, *106* (45), 11758−11763.

(120) Harris, J. R. Negative Staining of Thinly Spread Biological Particulates. In *Electron Microscopy Methods and Protocols*; Humana Press: 1999; Vol. 117.

(121) Carpenter, A.; Jones, T.; Lamprecht, M.; Clarke, C.; Kang, I.; Friman, O.; Guertin, D.; Chang, J.; Lindquist, R.; Moffat, J.; Golland, P.; Sabatini, D. CellProfiler: image analysis software for identifying and quantifying cell phenotypes. *Genome Biology* **2006**, *7* (10), R100.

(122) Borchert, H.; Shevchenko, E. V.; Robert, A.; Mekis, I.; Kornowski, A.; Grübel, G.; Weller, H. Determination of Nanocrystal Sizes: A Comparison of TEM, SAXS, and XRD Studies of Highly Monodisperse $CoPt_3$ Particles. *Langmuir* **2005**, *21* (5), 1931−1936.

(123) Dubois, L. H.; Nuzzo, R. G. Synthesis, Structure, and Properties of Model Organic-Surfaces. *Annu. Rev. Phys. Chem.* **1992**, *43*, 437−463.

(124) Fedosyuk, A.; Radchanka, A.; Antanovich, A.; Prudnikau, A.; Kvach, M. V.; Shmanai, V.; Artemyev, M. Determination of Concentration of Amphiphilic Polymer Molecules on the Surface of Encapsulated Semiconductor Nanocrystals. *Langmuir* **2016**, *32* (8), 1955−1961.

(125) Liz-Marzan, L. M. Tailoring surface plasmons through the morphology and assembly of metal nanoparticles. *Langmuir* **2006**, *22* (1), 32−41.

(126) Sepulveda, B.; Angelome, P. C.; Lechuga, L. M.; Liz-Marzan, L. M. LSPR-based nanobiosensors. *Nano Today* **2009**, *4* (3), 244−251.

(127) Barbosa, S.; Agrawal, A.; Rodriguez-Lorenzo, L.; Pastoriza-Santos, I.; Alvarez-Puebla, R. A.; Kornowski, A.; Weller, H.; Liz-Marzan, L. M. Tuning Size and Sensing Properties in Colloidal Gold Nanostars. *Langmuir* **2010**, *26* (18), 14943−14950.

(128) Vial, S.; Pastoriza-Santos, I.; Perez-Juste, J.; Liz-Marzan, L. M. Plasmon coupling in layer-by-layer assembled gold nanorod films. *Langmuir* **2007**, *23* (8), 4606−4611.

(129) Efros, A. L.; Efros, A. L. Interband Absorption of Light in a Semiconductor Sphere. *Sov. Phys. Semicond.-USSR* **1982**, *16* (7), 772−775.

(130) Takagahara, T.; Takeda, K. Theory of the quantum confinement effect on excitons in quantum dots of indirect-gap

materials. *Phys. Rev. B: Condens. Matter Mater. Phys.* **1992**, *46*, 15578−15581.

(131) Vossmeyer, T.; Katsikas, L.; Giersig, M.; Popovic, I. G.; Diesner, K.; Chemseddine, A.; Eychmüller, A.; Weller, H. CdS Nanoclusters: Synthesis, Characterization, Size Dependent Oscillator Strength, Temperature Shift of the Excitonic Transition Energy, and Reversible Absorbance Shift. *J. Phys. Chem.* **1994**, *98*, 7665.

(132) Nirmal, M.; Murray, C. B.; Bawendi, M. G. Fluorescence-line narrowing in CdSe quantum dots: Surface localization of the photogenerated exciton. *Phys. Rev. B: Condens. Matter Mater. Phys.* **1994**, *50* (4), 2293−2300.

(133) Lavallard, P. Excitons in nanocrystals. *J. Cryst. Growth* **1998**, *185*, 352−359.

(134) Peng, X. G.; Manna, L.; Yang, W. D.; Wickham, J.; Scher, E.; Kadavanich, A.; Alivisatos, A. P. Shape control of CdSe nanocrystals. *Nature* **2000**, *404* (6773), 59−61.

(135) Henglein, A. Photo-Degradation And Fluorescence Of Colloidal-Cadmium Sulfide In Aqueous-Solution. *Berichte Der Bunsen-Gesellschaft-Physical Chemistry Chemical Physics* **1982**, *86* (4), 301−305.

(136) Rossetti, R.; Nakahara, S.; Brus, L. E. Quantum Size Effects in the Redox Potentials, Resonance Raman-Spectra, and Electronic-Spectra of Cds Crystallites in Aqueous-Solution. *J. Chem. Phys.* **1983**, *79* (2), 1086−1088.

(137) Ekimov, A. I.; Efros, A. L.; Onushchenko, A. A. Quantum size effect in semiconductor microcrystals. *Solid State Commun.* **1993**, *88*, 947−50.

(138) Alivisatos, A. P. Semiconductor Clusters, Nanocrystals, and Quantum Dots. *Science* **1996**, *271*, 933−937.

(139) Parak, W. J.; Manna, L.; Simmel, F. C.; Gerion, D.; Alivisatos, P. Quantum Dots. In *Nanoparticles - From Theory to Application*, 1st ed.; Schmid, G., Ed.; Wiley-VCH: Weinheim, 2004; pp 4−49.

(140) Segets, D.; Lucas, J. M.; Taylor, R. N. K.; Scheele, M.; Zheng, H.; Alivisatos, A. P.; Peukert, W. Determination of the Quantum Dot Band Gap Dependence on Particle Size from Optical Absorbance and Transmission Electron Microscopy Measurements. *ACS Nano* **2012**, *6* (10), 9021−9032.

(141) Haiss, W.; Thanh, N. T. K.; Aveyard, J.; Fernig, D. G. Determination of Size and Concentration of Gold Nanoparticles from UV-Vis Spectra. *Anal. Chem.* **2007**, *79* (11), 4215−4221.

(142) Striolo, A.; Ward, J.; Prausnitz, J. M.; Parak, W. J.; Zanchet, D.; Gerion, D.; Milliron, D. J.; Alivisatos, A. P. Molecular Weight, Osmotic Second Virial Coefficient, and Extinction Coefficient of colloidal CdSe Nanocrystals. *J. Phys. Chem. B* **2002**, *106* (21), 5500−5505.

(143) Bruchez, M., Jr.; Moronne, M.; Gin, P.; Weiss, S.; Alivisatos, A. P. Semiconductor Nanocrystals as Fluorescent Biological Labels. *Science* **1998**, *281* (5385), 2013−2016.

(144) Lin, C.-A. J.; Yang, T.-Y.; Lee, C.-H.; Huang, S. H.; Sperling, R. A.; Zanella, M.; Li, J. K.; Shen, J.-L.; Wang, H.-H.; Yeh, H.-I.; Parak, W. J.; Chang, W. H. Synthesis, Characterization, and Bioconjugation of Fluorescent Gold Nanoclusters toward Biological Labeling Applications. *ACS Nano* **2009**, *3* (2), 395−401.

(145) Huang, S.; Pfeiffer, C.; Hollmann, J.; Friede, S.; Chen, J. J.-C.; Beyer, A.; Volz, K.; Heimbrodt, W.; Montenegro Martos, J. M.; Chang, W.; Parak, W. J.; Haas, B. Synthesis and Characterization of Colloidal Fluorescent Silver Nanoclusters. *Langmuir* **2012**, *28*, 8915−8919.

(146) Dulkeith, E.; Ringler, M.; Klar, T. A.; Feldmann, J.; Muñoz Javier, A.; Parak, W. J. Gold Nanoparticles Quench Fluorescence by Phase Induced Radiative Rate Suppression. *Nano Lett.* **2005**, *5* (4), 585−589.

(147) Medintz, I. L.; Clapp, A. R.; Mattoussi, H.; Goldman, E. R.; Fisher, B.; Mauro, J. M. Self-Assembled Nanoscale Biosensors Based on Quantum Dot FRET Donors. *Nat. Mater.* **2003**, *2*, 630−638.

(148) Würth, C.; Geissler, D.; Behnke, T.; Kaiser, M.; Resch-Genger, U. Critical review of the determination of photoluminescence quantum yields of luminescent reporters. *Anal. Bioanal. Chem.* **2015**, *407*, 59−78.

(149) Huber, A.; Behnke, T.; Würth, C.; Jaeger, C.; Resch-Genger, U. Spectroscopic Characterization of Coumarin-Stained Beads: Quanti-

fication of the Number of Fluorophores Per Particle with Solid-State 19F-NMR and Measurement of Absolute Fluorescence Quantum Yields. *Anal. Chem.* **2012**, *84* (8), 3654.

(150) Jobin Yvon Horiba. *A Guide to Recording Fluorescence Quantum Yields*; Jobin Yvon Horiba: Stanmore, 2016.

(151) Williams, A. T. R.; Winfield, S. A.; Miller, J. N. Relative Fluorescence Quantum Yields Using a Computer-controlled Luminescence Spectrometer. *Analyst (Cambridge, U. K.)* **1983**, *108* (1290), 1067−1071.

(152) Magde, D.; Brannon, J. H.; Cremers, T. L.; Olmsted, J. Absolute Luminescence Yield of Cresyl Violet - Standard for the Red. *J. Phys. Chem.* **1979**, *83* (6), 696−699.

(153) Rivera Gil, P.; Jimenez de Aberasturi, D.; Wulf, V.; Pelaz, B.; del Pino, P.; Zhao, Y.; de la Fuente, J.; Ruiz de Larramendi, I; Rojo, T.; Liang, X.-J.; Parak, W. J. The Challenge to Relate the Physicochemical Properties of Colloidal Nanoparticles to Their Cytotoxicity. *Acc. Chem. Res.* **2013**, *46* (3), 743−749.

(154) Murdock, R. C.; Braydich-Stolle, L.; Schrand, A. M.; Schlager, J. J.; Hussain, S. M. Characterization of nanomaterial dispersion in solution prior to in vitro exposure using dynamic light scattering technique. *Toxicol. Sci.* **2008**, *101* (2), 239−53.

(155) Roebben, G.; Ramirez-Garcia, S.; Hackley, V. A.; Roesslein, M.; Klaessig, F.; Kestens, V.; Lynch, I.; Garner, C. M.; Rawle, A.; Elder, A.; Colvin, V. L.; Kreyling, W.; Krug, H. F.; Lewicka, Z. A.; McNeil, S.; Nel, A.; Patri, A.; Wick, P.; Wiesner, M.; Xia, T.; Oberdorster, G.; Dawson, K. A. Interlaboratory comparison of size and surface charge measurements on nanoparticles prior to biological impact assessment. *J. Nanopart. Res.* **2011**, *13* (7), 2675−2687.

(156) Bhattacharjee, S. DLS and zeta potential − What they are and what they are not? *J. Controlled Release* **2016**, *235*, 337.

(157) Tay, C. Y.; Setyawati, M. I.; Xie, J.; Parak, W. J.; Leong, D. T. Back to Basics: Exploiting the Innate Physico-chemical Characteristics of Nanomaterials for Biomedical Applications. *Adv. Funct. Mater.* **2014**, *24*, 5936−5955.

(158) Fischer, K.; Schmidt, M. Pitfalls and novel applications of particle sizing by dynamic light scattering. *Biomaterials* **2016**, *98*, 79−91.

(159) Henderson, L. J. Concerning the relationship between the strength of acids and their capacity to preserve neutrality. *Am. J. Physiol.* **1908**, *21* (2), 173−179.

(160) Hasselbalch, K. A. Die Berechnung der Wasserstoffzahl des Blutes aus der freien und gebundenen Kohlensäure desselben, und die Sauerstoffbindung des Blutes als Funktion der Wasserstoffzahl. *Biochem. Z.* **1917**, *78*, 112−144.

(161) Po, H. N.; Senozan, N. M. The Henderson-Hasselbalch Equation: Its History and Limitations. *J. Chem. Educ.* **2001**, *78* (11), 1499.

(162) de Levie, R. The Henderson Approximation and the Mass Action Law of Guldberg and Waage. *Chem. Educ.* **2002**, *7* (3), 132−135.

(163) de Levie, R. The Henderson-Hasselbalch Equation: Its History and Limitations. *J. Chem. Educ.* **2003**, *80* (2), 146.

(164) Doane, T. L.; Chuang, C. H.; Hill, R. J.; Burda, C. Nanoparticle Zeta-Potentials. *Acc. Chem. Res.* **2012**, *45* (3), 317−326.